

## Triplet Dynamics in Crystalline Perylene Diimides

Felter, Kevin

**DOI**

[10.4233/uuid:5137711f-d5e6-41b6-ac7a-34c6c5e29caf](https://doi.org/10.4233/uuid:5137711f-d5e6-41b6-ac7a-34c6c5e29caf)

**Publication date**

2020

**Document Version**

Final published version

**Citation (APA)**

Felter, K. (2020). *Triplet Dynamics in Crystalline Perylene Diimides*. [Dissertation (TU Delft), Delft University of Technology]. <https://doi.org/10.4233/uuid:5137711f-d5e6-41b6-ac7a-34c6c5e29caf>

**Important note**

To cite this publication, please use the final published version (if applicable).  
Please check the document version above.

**Copyright**

Other than for strictly personal use, it is not permitted to download, forward or distribute the text or part of it, without the consent of the author(s) and/or copyright holder(s), unless the work is under an open content license such as Creative Commons.

**Takedown policy**

Please contact us and provide details if you believe this document breaches copyrights.  
We will remove access to the work immediately and investigate your claim.

# **TRIPLET DYNAMICS IN CRYSTALLINE PERYLENE DIIMIDES**



# **TRIPLET DYNAMICS IN CRYSTALLINE PERYLENE DIIMIDES**

## **Proefschrift**

ter verkrijging van de graad van doctor  
aan de Technische Universiteit Delft,  
op gezag van de Rector Magnificus prof. dr. ir. T.H.J.J. van der Hagen,  
voorzitter van het College voor Promoties,  
in het openbaar te verdedigen op  
woensdag 29 januari 2020 om 12:30 uur

door

**Kevin Mitchell FELTER**

Chemisch ingenieur,  
Technische Universiteit Delft, Nederland,  
geboren te Dordrecht, Nederland.



Dit proefschrift is goedgekeurd door de promotoren.

Samenstelling promotiecommissie bestaat uit:

Rector Magnificus,	voorzitter
Dr. F. C. Grozema	Technische Universiteit Delft, promotor
Dr. ir. T. J. Savenije	Technische Universiteit Delft, promotor

*Onafhankelijke leden:*

Prof. dr. S. J. Picken	Technische Universiteit Delft
Prof. dr. P. Dorenbos	Technische Universiteit Delft
Prof. dr. B. Albinsson	Chalmers University of Technology
Prof. dr. D. M. Guldi	Friedrich-Alexander-Universität Erlangen-Nürnberg
Dr. B. Ehrler	AMOLF, Center for Nanophotonics



Het onderzoek dat heeft geleid tot de resultaten die worden beschreven in deze dissertatie is mogelijk gemaakt door een subsidie van de European Research Council Horizon 2020 ERC Grant Agreement no. 648433.

*Sleutelwoorden:* Singlet fission, triplet upconversion, perylene diimides, solid-state packing, microwave conductivity, transient absorption spectroscopy

*Drukkerij:* GVO grafisch bedrijf B.V.

*Omslagontwerp:* Loes van de Kraats - Kema en Kevin Felter

Copyright © 2020 K.M. Felter

ISBN 978-94-6332-591-2

Een elektronische versie van dit proefschrift is beschikbaar op:  
<http://repository.tudelft.nl/>.

# CONTENTS

<b>1</b>	<b>Introduction</b>	<b>1</b>
1.1	Introduction . . . . .	2
1.2	Singlet exciton fission . . . . .	2
1.3	Outline of this thesis . . . . .	13
<b>2</b>	<b>Interplay between charge carrier mobility, exciton diffusion and crystal packing in perylene diimides</b>	<b>19</b>
2.1	Introduction . . . . .	20
2.2	Experimental Section . . . . .	22
2.3	Results and Discussion . . . . .	26
2.4	Conclusions. . . . .	36
<b>3</b>	<b>Relation between molecular packing and singlet fission in thin films of brominated perylenediimides</b>	<b>43</b>
3.1	Introduction . . . . .	44
3.2	Experimental Section . . . . .	45
3.3	Results and Discussion . . . . .	46
3.4	Conclusions. . . . .	56
<b>4</b>	<b>Solid-State Infrared Upconversion in PDIs Followed by Direct Electron Injection</b>	<b>59</b>
4.1	Introduction . . . . .	60
4.2	Experimental Section . . . . .	62
4.3	Results and Discussion . . . . .	62
4.4	Conclusions. . . . .	67
<b>5</b>	<b>Triplet Exciton Diffusion in PDI Thin Films Mediated by Singlet Fission</b>	<b>73</b>
5.1	Introduction . . . . .	74
5.2	Experimental Section . . . . .	75
5.3	Results and Discussion . . . . .	77
5.4	Conclusions. . . . .	85
<b>6</b>	<b>Magnetic Field Effects on Triplet Pair States in Perylene Diimide Thin Films</b>	<b>89</b>
6.1	Introduction . . . . .	90
6.2	Theory . . . . .	91
6.3	Experimental Section . . . . .	93
6.4	Results and Discussion . . . . .	95
6.5	Conclusions. . . . .	100

---

<b>7 Outlook</b>	<b>103</b>
<b>A Appendix Chapter 2</b>	<b>105</b>
<b>B Appendix Chapter 3</b>	<b>115</b>
<b>C Appendix Chapter 4</b>	<b>125</b>
<b>D Appendix Chapter 5</b>	<b>133</b>
<b>Summary</b>	<b>137</b>
<b>Samenvatting</b>	<b>141</b>
<b>Acknowledgements</b>	<b>145</b>
<b>Curriculum Vitae</b>	<b>149</b>
<b>List of Publications</b>	<b>151</b>

# 1

## INTRODUCTION

---

Parts of this chapter are based on: Felter, K. M. and Grozema, F. C. (2019). *Singlet Fission in Crystalline Organic Materials: Recent Insights and Future Directions*. *The Journal of Physical Chemistry Letters*, 10(22), 7208-7214.

## 1.1. INTRODUCTION

Conjugated organic materials have been studied widely over the last few decades because of their potential application in optoelectronic devices. Two of the breakthrough discoveries in this sense are the observation of electrical conductance in polydiacetylene in 1977 by Shirakawa, MacDiarmid and Heeger<sup>1</sup> in 1977 for which they were awarded the Nobel prize in 2000 and the observation of electroluminescence by Burroughes et al.<sup>2</sup> These discoveries set off a whole field of research where organic materials are considered as the active material in a wide variety of devices, including transistors, light-emitting diodes and lasers, photodetectors, and solar cells. Conjugated organic materials have several advantageous properties that make them interesting for such application, including light weight, mechanical flexibility and a low processing cost. In addition, organic chemistry allows a wide tunability in the properties of the materials, including the optical absorption and emission properties and the ability to transport charge. A particularly interesting aspect of conjugated organic molecules is that they can also be designed to exhibit uncommon photophysical processes such as singlet fission and the reverse process, triplet-triplet annihilation upconversion. These uncommon processes involving triplet excited states are the focus of this thesis.

In this chapter we give a brief overview of the field of singlet fission and upconversion and discuss some other relevant processes that are related such as triplet energy transfer and diffusion. Finally, a brief outline of this thesis will be given.

## 1.2. SINGLET EXCITON FISSION

Singlet exciton fission (SF) is a photophysical process by which a singlet excited state is converted into two triplet excited states, each with about half of the energy of the initial singlet. SF was initially described in the 1960s and 1970s as an explanation for the observed delayed fluorescence in acene crystals.<sup>3,4</sup> In the early 2000's the interest in singlet fission was renewed as it was realised that it could be exploited as a route to increase the photon-to-electricity efficiency of organic photovoltaic devices (OPV). Incorporation of singlet fission into OPV devices can boost its maximum attainable photon-to-electricity efficiency from 33 to 47% by minimizing the thermal relaxation losses included in the Shockley-Queisser limit.<sup>5</sup> Such increases will be hard to reach in practice, but simulations have indicated that combining a SF layer with a state-of-the-art silicon solar cell can increase the efficiency by up to 4.2% absolute.<sup>6</sup>

In order to capitalize on the promise of singlet fission for improving the efficiency of organic solar cells both the yield of SF itself and the separation of the generated triplets into charge carriers are essential requirements. Currently, efficient extraction of charges after singlet fission has been demonstrated in only a few systems, with low efficiency or limited to very specific excitation wavelengths.<sup>7-9</sup> Most work on such devices and other more fundamental SF research is done on molecules that belong to the acene family. However, these acenes do not possess all the characteristics that are optimal when considering SF-based OPV devices.<sup>10</sup> A specific problem related to acenes is that they are particularly prone to photodegradation.<sup>11</sup> Therefore, fundamental knowledge on the mechanism and dynamics of SF in solid-state systems is essential in establishing guidelines for the design of chromophores that do possess optimal SF characteristics. These

characteristics include minimally exoergic, ultrafast and highly efficient but displaying good charge transport properties.<sup>12</sup> Important electronic and structural conditions that play a role in attaining optimal SF characteristics include (1) fulfilment of adiabatic energy conditions  $E(T_2) - E(S_0) > E(S_1)$  and,  $E(S_1) - E(S_0) \geq 2[E(T_1) - E(S_0)]$ , (2) a suitable molecular packing that optimizes the intermolecular electronic coupling for SF but at the same time minimizes competitive singlet deactivation pathways and (3) efficient separation of triplet excited states into free charges.

These electronic and structural conditions for SF have been explored in a multitude of theoretical studies. First of all, electronic structure calculations by time-dependent density functional theory or configuration interaction-based methods from which accurate  $S_1$ ,  $S_2$ ,  $T_1$  and  $T_2$  energies are obtained allowed the identification of SF candidates based on the adiabatic energy conditions.<sup>13,14</sup> Second, calculations of the electronic coupling for singlet fission have been mostly calculated in dimer systems, revealing that the molecular packing strongly affects the fission rate and yield. In order to study the dynamics of fission and explore the importance of different pathways, density matrix propagation methods have been used. The latter have also emphasized the role of vibronic coupling in the singlet fission process.<sup>15</sup> These theoretical studies on SF in dimers have resulted in many new insights, however, the subsequent processes, such as the dissociation of the correlated triplet pair into free triplets, the diffusion of triplets and their separation into free charges, have remained largely unexplored. The latter processes are of pivotal importance when SF compounds are to be applied in the solid-state in actual devices.

Crystalline organic materials offer an ideal platform for experimental studies on SF dynamics as the intermolecular packing in the solid can be controlled by altering the chemical structure of the individual molecules. Moreover, they naturally consist of extended arrays of molecules where the coherent triplet pair state can separate into uncoupled triplets.<sup>16</sup> Furthermore, the solid-state structure allows the study of the relation between the nature of the excited state, and exciton transport and charge separation.<sup>17</sup> It should be noted that efficient SF has also been reported for polycrystalline and amorphous materials with high efficiency, showing that sufficiently strong electronic interactions exist in such systems.<sup>18,19</sup> The drawback of such systems is that they are less well-defined and hence it is more difficult to derive detailed structure-property relations.

## BASIC QUANTUM CHEMICAL DESCRIPTION OF SF

A first order picture of the states involved in transforming a singlet into a combination of two triplets is given in Figure 1.1 where the SF process starts from the  $S_1$  state. This  $S_1$  excited state is, in first approximation, considered to be localized on a single molecule, but can also be a delocalized exciton state. After the initial excitation, the multi-exciton triplet state or correlated triplet pair state  $^1(TT)$  can be formed via the direct pathway (blue arrow). Alternatively, SF may proceed through virtual intermediate states that have charge transfer (CT) character, provided that these states are not too high in energy (green and orange arrow).<sup>10</sup> These different energy states of the system involving two molecules A and B can be expressed in a 'basis' of diabatic states in the singlet ground-state  $S_0^A S_0^B$ , localized excited singlets  $S_1^A S_0^B$  and  $S_0^A S_1^B$ , a lowest energy triplet pair or correlated triplet pair  $^1(T_1^A T_1^B)$  and the charge transfer states  $^1(C^+ A^- B)$  and  $^1(A^- A^+ C^+ B)$ . In

this description  $C^+$  represents the ground-state of a radical cation while  $A^-$  represents the ground-state of the respective radical anion. In the following discussion we will omit the superscripts A and B that denote the SF dimer components for clarity. Using these diabatic basis states we can write the rate of the singlet fission process in terms of the electronic Hamiltonian operator  $H_{el}$ .

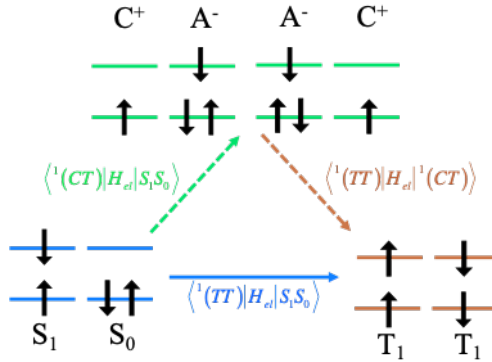


Figure 1.1: Schematic representation of the direct (blue lines) and indirect, CT-state mediated (green and orange) singlet fission mechanism. The matrix elements are shown in bracket notation that represent the electronic coupling involved in the mechanism steps.

The simplest quantum mechanical description of the SF rate,  $w(SF)$ , via the direct pathway is governed by the electronic coupling between  $S_1 S_0$  and  ${}^1(TT)$ ,  $\langle {}^1(TT) | H_{el} | S_1 S_0 \rangle$  and in a first order perturbation theory approximation is given by

$$w(SF) = \left( \frac{2\pi}{\hbar} \right) \left| \langle {}^1(TT) | H_{el} | S_0 S_1 \rangle \right|^2 \rho[E] \quad (1.1)$$

where  $\rho[E]$  is the Franck-Condon weighed density of states at  $E = E(S_0 S_1) = E({}^1(TT))$ . The matrix element for this direct pathway,  $\langle {}^1(TT) | H_{el} | S_1 S_0 \rangle$ , is usually very small, even though energetically this is the most favourable process and the expression for  $w(SF)$  improves by incorporating terms from additional electronic states. Incorporating pathways due to additional electronic states such as charge transfer states can significantly increase the SF rate from that of the simple direct pathway in Equation 1.1, depending on the energy of these states. Important virtual states that play a role are low energy CT-states and result in additional matrix terms  $\langle {}^1(CA) | H_{el} | S_1 S_0 \rangle$ ,  $\langle {}^1(AC) | H_{el} | S_1 S_0 \rangle$  and  $\langle {}^1(TT) | H_{el} | {}^1(AC) \rangle$ ,  $\langle {}^1(TT) | H_{el} | {}^1(CA) \rangle$  from interaction with the  $S_0 S_1$  and TT states. A simplified Hamiltonian matrix for a dimer system in terms of the singlet CT and triplet pair states is, given in Equation 1.2, with the excited states energies on the diagonal and the electronic coupling between the different states on the off-diagonals. The blue elements are involved in the direct pathway, while the green and orange matrix elements are involved in the virtual intermediate pathway.

$$H_{el} = \begin{pmatrix} E(S_0S_1) & 0 & t_{LL} & -t_{HH} & t_{2e} \\ 0 & E(S_1S_0) & -t_{HH} & t_{LL} & t_{2e} \\ t_{LL} & -t_{HH} & E(CT) & 0 & \sqrt{\frac{3}{2}}t_{LH} \\ -t_{HH} & t_{LL} & 0 & E(CT) & \sqrt{\frac{3}{2}}t_{HL} \\ t_{2e} & t_{2e} & \sqrt{\frac{3}{2}}t_{LH} & \sqrt{\frac{3}{2}}t_{HL} & E(T_1T_1) \end{pmatrix} \quad (1.2)$$

The matrix elements that make up the Hamiltonian in Equation 1.2 are strongly dependent on the mutual orientation and distance of neighbouring molecules, which is intricately linked to the nodal structure of the frontier molecular orbitals. A typical example orbital schematic is shown in Figure 1.2 for the charge transfer coupling matrix element,  $t_{HL}$ , which involves coupling between the HOMO (h) and LUMO (l) orbitals on molecules A and B. In this case, in a perfect face-to-face stacking arrangement the coupling is exactly zero, while a slip-stacked geometry leads to a maximum in the coupling. A similar picture exists for the electronic coupling of the direct process,  $t_{2e}$ , however the maximum coupling will occur at a different displacement.

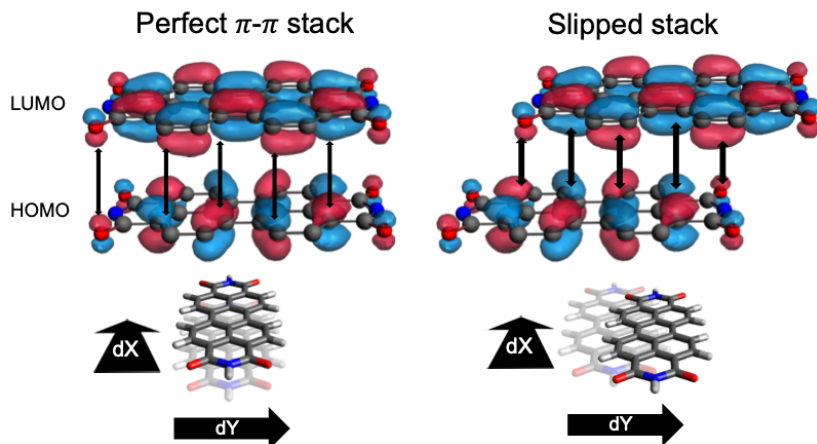


Figure 1.2: Schematic representation of frontier molecular orbitals (HOMO and LUMO) and their overlaps for a perfect stacking and slipped stack configuration of two PDI molecules. The slipping directions along the long axis (x) and short axis (y) are indicated as used in Figure 1.3.

The strong connection between the stacking geometry in the crystal and magnitude and sign of the coupling matrix elements directly points to ways to optimize the initial step in singlet fission. If the mutual orientation, or the degree of 'slipping' in a slip-stacked structure can be controlled it is possible to systematically study the relation between structure and SF efficiency. An example of a class of materials where this is possible are perylenediimides, where the crystal structure can be tuned to a large extent by varying the substituents on the imid position.<sup>20</sup> Using the geometry dependent electronic coupling matrix elements, we have shown recently that strong differences are to be expected for different PDI derivatives.<sup>21</sup> Using the Hamiltonian matrix in Equation 1.2 in a Redfield density matrix propagation study, insight was obtained in the dynamics



of the initial fission process for different geometries.<sup>15,21</sup> A map of the resulting rates for different geometries, shown in Figure 1.3a shows a strong dependence of the SF rate on geometry. In addition, in such a model-Hamiltonian study it is possible to look at the contributions of the individual pathways, *i.e.* direct vs. CT-mediated. In this particular example the geometry dependence of these two pathways is markedly different as shown in Figure 1.3a, but it is also clear that the overall process is dominated by the CT-mediated contribution.<sup>15,21</sup> Experimentally, the strong effect of the molecular packing on SF dynamics was confirmed by femtosecond transient absorption experiments,<sup>22–24</sup> although the described rates are of a different order of magnitude as shown in Figure 1.3c. The latter can be due to assumptions made on the energy of the different states involved. A similar correlation between structure and SF dynamic has been described for the acene family where slip stacking is also shown to benefit SF in tetracene and pentacene making it faster and more efficient when compared to less ordered derivative structures.<sup>22,25–27</sup>

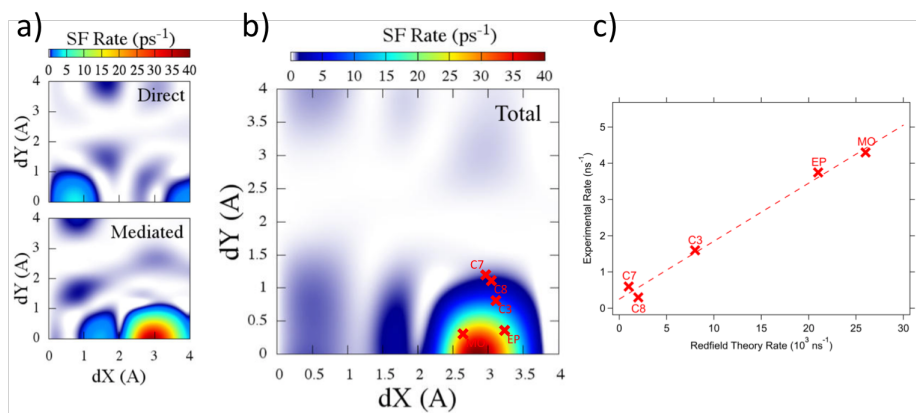


Figure 1.3: a) Singlet fission rates as obtained via the direct and CT-mediated pathways (a) and the overall SF rate as a function of translation along the short (y) and long axis as indicated in Figure 1.2 (b). (c) Comparison of the calculated and experimental SF rates.

All examples mentioned here primarily relate to the initial fission process in a dimer picture and in a simplified basis with very few states involved. In reality, the relevant states are not so rigorously disconnected and mixed states exist. This is for instance evident from configuration interaction calculations where it is shown that the coherent triplet pair state often has a complex composition, including also CT determinants and mixing of singlet and quintet character.<sup>28–30</sup> This has also been shown experimentally.<sup>31</sup>

In the large majority of theoretical studies, the focus is on the initial triplet pair state in a dimer. However, if the energy of the two triplets is to be harvested efficiently, the subsequent process where this pair state is split up into two individual triplets that can freely diffuse is essential. This requires extended systems with a detailed description of decoherence, which is a challenge for theoretical work in this field.

## ELECTRON - PHONON INTERACTION: VIBRONIC COUPLING

Apart from the electronic coupling there is substantial evidence from experiments and theory that the interaction of the exciton with inter- and intramolecular vibrational modes significantly affects singlet fission.<sup>32</sup> This can be due to energy provided to bring the singlet and triplet state in resonance or due to fluctuations in the electronic coupling matrix elements.<sup>33</sup> This electron-phonon (vibronic) coupling can be referred to as Peierls and Holstein for defining exciton coupling with intermolecular and intramolecular vibrational modes, respectively.

Following the Redfield density matrix study on SF dynamics in PDI molecules, the inclusion of Peierls vibrational coupling in the simulation was shown to result in accelerated triplet pair state formation from a picosecond to sub-picosecond time scale.<sup>15</sup> The rate acceleration was shown to be unaffected by the CT-state level energy from which the authors deduced that the CT-state acts as a virtual intermediate in a superexchange singlet fission mechanism. Similar findings were reported for acenes, where Holstein vibronic coupling increased the singlet and triplet pair state coupling in tetracene.<sup>34</sup> Secondly, in pentacene the incorporation of coherent vibrational mixing was found to accelerate SF.<sup>35,36</sup>

These vibronic effects cannot be measured directly in linear transient absorption measurements, but such techniques do allow the detection of coherent phonons from the presence of strong oscillations at early times (one ps) in photoinduced absorption or emission measurements.<sup>37-41</sup> The frequency of such oscillations can be compared to FT Raman spectra of the same material to confirm that these coherent phonon signatures are indeed related to specific vibrational modes that influence different excited state processes. Relating these vibronic coupling effects to different excitonic states can be achieved with complex two-dimensional spectroscopic techniques such as four-wave mixing. Two-dimensional spectroscopy allows monitoring both the electronic and electron-phonon coupling between electronic states and the excitation pathway by which they are created.<sup>42</sup> Normally the triplet pair state cannot be directly observed due to its low oscillator strength and needs to be obtained from a SF global or target analysis model<sup>31,43,44</sup>, although very recently ultrafast mid-IR spectroscopy did allow the direct observation of triplet pair states.<sup>45,46</sup>

One example of a four-wave mixing technique that is used for studying singlet fission is two-dimensional electronic photon-echo spectroscopy (2DES).<sup>37,47</sup> A 2DES study on thin films of pentacene and derivatives, revealed the presence of an otherwise dark triplet pair state. This observation was possible due to the increased sensitivity of the 2DES technique, in comparison to regular pump-probe absorption spectroscopy.<sup>37</sup> Furthermore, quantum beating signatures were observed in the kinetic traces of singlet and triplet pair states that corresponded to vibronic modes observed in Raman spectra. These vibronic modes were found to be present in both the spectral region of the singlet exciton and triplet pair state, indicating their influence in mixing the two states.

## A COHERENT AND INCOHERENT SINGLET FISSION MECHANISM

The relevance of vibrational mode coupling and CT-state intermediate mixing in accelerating intermolecular singlet fission is generally accepted.<sup>32</sup> However, the extent to which both factors are involved depends on the singlet fission mechanism that one follows. A schematic representation for the singlet fission process is shown in Figure 1.4a where the singlet excited state  $S_1$  can form an electronically coupled (electronically coherent) triplet pair state or an electronically decoupled (electronically decoherent) triplet pair state.<sup>48</sup> The formation of the electronically coherent triplet pair state can be described by a coherent quantum mechanism as described above, or by an incoherent mechanism that allows a classical kinetic treatment. In the incoherent mechanism, a photoexcited singlet state (1) evolves into a triplet pair state  $^1(TT)$  (1) as the electronic coupling between  $S_1$  and  $^1(TT)$  is weaker than their coupling to the phonon bath and is therefore a thermally assisted process. On the other hand, in the coherent mechanism the photoexcitation creates an excited state that is a superposition of singlet, CT and  $^1(TT)$  (2). Recent experiments<sup>38–40</sup> show that both mechanisms occur concurrently during the singlet fission process at different time scales. The observation of such a dual mechanism can be expected as photoexcitation generates a superposition of a singlet excited state, triplet pair states and CT intermediate states. Such superposition states created by coherent excitations can explain ultrafast femtosecond time scale SF rates. The extent to which these different species are formed within the superposition depends on the excited state energetics which in turn is dictated by the singlet fission chromophore and its molecular packing.<sup>32</sup> Furthermore, quantum calculations show that such coherent excitations are only possible when a conical intersection exists between singlet and triplet pair state<sup>39</sup> as described earlier.<sup>41</sup> The slower SF component, on the order of hundreds of femtoseconds, may then come from the incoherent mechanism for forming  $^1(TT)$ . The loss in electronic coherence of  $^1(TT)$  to form two spin entangled but electronically decoupled triplets  $^1(T\cdots T)$  can occur by coupling to the phonon bath, *i.e.* vibronic coupling and by physical separation occurring via triplet energy transfer that is driven by enthalpic and entropic driving forces (3). Finally, the loss in spin coherence or spin coupling between triplets can occur slowly on nanosecond to microsecond time scale (4).

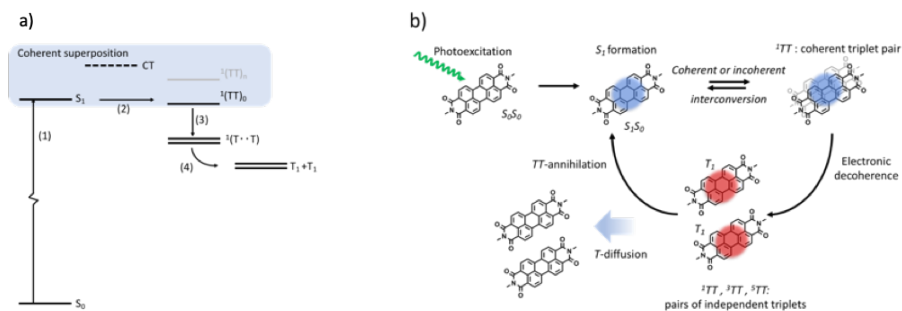


Figure 1.4: a) Schematic energy diagram illustrating the different electronic processes and states involved in SF: Photoexcitation from the ground-state (1) creates a superposition state of  $S_1$ , CT and  $^1(TT)_0$  involving interstate conversion between  $S_1$  and  $^1(TT)_0$  (2). Subsequently,  $^1(TT)_0$  loses electronic coupling during physical triplet state separation and phonon bath interaction and forms  $^1(T\cdot T)$  (3). The final step is the spin decoherence resulting in the formation of free triplets (4). b) Schematic representation of triplet exciton formation from singlet fission. The photoexcited superposition state is composed of  $S_1S_0$ , CT and  $^1(TT)$  state whose formation rate depends on the state mixing. The  $^1(TT)$  state can electronically and spin decohere to form individual separate triplet that can diffuse.

### TRIPLET-TRIPLET ANNIHILATION UPCONVERSION

As shown in Figure 1.4b, the process opposite to SF is triplet-triplet annihilation upconversion (TTA-UC) where one high-energy excited state is generated from annihilation of two triplets. This process can in principle be used to harvest low energy photons that are normally not absorbed in a solar cell. TTA-UC typically involves a combination of two chromophores, a triplet sensitizer that absorbs light and efficiently converts it into triplets, and an triplet acceptor or upconverter in which the triplet-triplet annihilation process takes place.

TTA-UC can be achieved by a sequence of processes that is schematically outlined in Figure 1.1. This sequence starts with the absorption of light in the near-infrared region, between 700 and 1000 nm, by a triplet sensitizer (TS). The singlet excited state that is formed upon absorption should be efficiently transformed into a triplet excited state by inter-system crossing. The lifetime of this triplet state has to be long, in the range of microseconds or beyond, because it should eventually diffuse and transfer its energy to a triplet acceptor (TA). This diffusion process can be either through molecular diffusion in a liquid or by triplet energy transfer in solid materials. When multiple triplet excited states are present close together in the TA material, two of them can combine into a singlet excited state by so-called triplet-triplet annihilation, resulting in a singlet. Finally, this singlet excited state can fluoresce in the visible region, which effectively concludes the process of converting infrared photons into visible light that can be used in a variety of application. The presence of the TA materials is critical in this sequence because triplet-triplet annihilation in the TS material would lead to higher excited state that relaxes and will eventually become a triplet again by intersystem crossing. In all the outlined here processes the energies of the different species and their ability to migrate are important issues and there are several requirements for the combination of molecules that are used to achieve upconversion:

- TS should absorb in the IR and efficiently convert the singlet excited state into

triplets.

- The triplet excited state of TS should have a long lifetime.
- The triplet diffusion toward TA should be efficient.
- Triplet-triplet annihilation to form a singlet should be efficient.
- The singlet state formed should fluoresce with a high quantum yield.

These requirements also summarize the relevant underlying processes that should be optimized to arrive at a material that efficiently upconverts infrared photons. In the project proposed here these processes will be studied by time-resolved spectroscopic techniques.

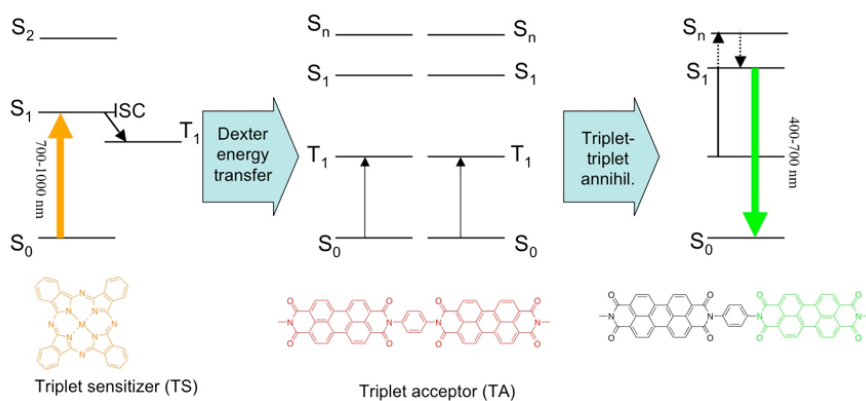


Figure 1.5: Schematic overview of the TTA-UC process where initial absorption of a low energy photon in the triplet acceptor leads to a singlet excited state that is quickly converted into a triplet state by intersystem crossing (ISC). This triplet excited state is subsequently transferred to the triplet acceptor by Dexter energy transfer where triplet-triplet annihilation takes place. This can either be followed by emission or by injection into an electron accepting substrate such as  $\text{TiO}_2$ .

While this general principle has been shown in solution<sup>49</sup> and in glassy polymer matrices,<sup>50</sup> this project aims to take it a substantial step forward by utilizing true solid-state processes rather than relying on molecular diffusion as in earlier examples. A possibly improved implementation is to use a full solid-state device where the annihilation process does not involve molecular diffusion in solution of glassy matrices but the triplets move by Dexter energy transfer through the crystalline material. This possibility will be explored in Chapter 4.

## TRIPLET DIFFUSION

As mentioned above, one requirement for application of SF chromophores in photovoltaics is to have a sufficiently high triplet diffusion coefficient. In this context one can perceive triplet diffusion as the diffusion of individual triplet states that may interconvert to singlet states via the triplet-triplet annihilation pathway as represented in Figure 1.4b.<sup>51</sup> Alternatively, triplet diffusion can be understood as correlated triplet pair diffusion where the triplets have mixed singlet-triplet character.<sup>17,52</sup> In order to gain more insight into the exact nature of mixed singlet triplet character and its diffusion we treat the definitions of pure singlet and triplet energy transfer.

## SINGLET AND TRIPLET ENERGY TRANSFER

Energy transfer involves the movement of an electronically excited state from one molecular entity to another. The description of energy transfer In general the description of these processes proceeds from Fermi's Golden Rule, where the rate of transfer,  $k$ , is given by:

$$k = \frac{2\pi}{\hbar} V_{EnT}^2 \rho \quad (1.3)$$

where  $V_{EnT}$  is the electronic coupling matrix element and  $\rho$  is the vibrational density of states. The value of  $V_{EnT}$  is the main factor in determining how the rate of energy transfer depends on the nature of the excited state (singlet vs. triplet) and on the mutual distance and orientation of the two chromophores between which energy transfer takes place. For the transfer of singlet excited states the electronic coupling matrix element can be expressed in terms of the transition dipole moments of the optical transitions localized on the individual chromophores according to the Förster model:

$$|V_{EnT}| = \frac{|\kappa| |\vec{\mu}_D| |\vec{\mu}_A|}{4\pi\epsilon_0 R_{DA}^3} \quad (1.4)$$

Where  $|\vec{\mu}_D|$  and  $|\vec{\mu}_A|$  are the transition dipole moments for transitions on the two individual chromophores between which the energy transfer takes place,  $R_{DA}$  is the center-to-center distance between the two chromophores and  $\kappa$  is the orientation factor given by

$$\kappa = \vec{e}_D \cdot \vec{e}_A - 3(\vec{e}_D \cdot \vec{r}_{DA})(\vec{e}_A \cdot \vec{r}_{DA}) \quad (1.5)$$

Where  $\vec{e}_D$  and  $\vec{e}_A$  are unit vectors along the transition dipole moment of the donor and acceptor, and  $\vec{r}_{DA}$  is a unit vector along the direction connecting the centers of the two chromophores.

Including this expression for  $V_{EnT}$  in Fermi's Golden Rule leads, to the overall expression of the Förster energy transfer rate in terms of the transition dipole moments:

$$k_{Förster} = \frac{|\kappa|^2 |\vec{\mu}_D|^2 |\vec{\mu}_A|^2}{8\hbar\pi\epsilon_0^2 R_{DA}^6} \int F_D(E) A_A(E) dE \quad (1.6)$$

Where  $F_D$  and  $A_A$  are the line shape of the donor emission and the acceptor absorption spectrum, respectively. Conceptually, the overall process can be seen as the emission of a 'virtual' photon from the energy donor, followed by reabsorption of that photon by the energy acceptor.

For triplet excited states, the transition dipole moments from the ground to the excited state are zero by definition, meaning that according to the approximations made in the derivation of the Förster model, energy transfer is completely forbidden. Dexter mechanism, where less severe approximations are made since the exchange coupling between the chromophores is not neglected, is generally invoked to describe transfer of triplet excited states. The Dexter rate is given by:

$$k_{Dexter} = \frac{2\pi}{\hbar} K \int F_D(E) A_A(E) dE \exp\left(\frac{-2R_{DA}}{L}\right) \quad (1.7)$$

Where  $K$  is a parameter that describes tunnelling of electrons between the two chromophores and  $L$  is the sum of the Van der Waals radii of the two chromophores. Conceptually, in the Dexter model, the transfer of triplet excited states can be seen as simultaneous transfer of two electrons and decays much faster with distance than Förster energy transfer. The rate of triplet energy transfer is generally several orders of magnitude lower than from singlet excited states.

## EXPERIMENTAL APPROACHES TO STUDY TRIPLET DIFFUSION

A variety of experimental techniques allow the study of triplet diffusion in solid-state materials such as transient absorption spectroscopy, photoluminescence and microwave conductivity.<sup>53</sup> These studies are necessary as molecular packing and macroscale crystalline domain size are important factors that determine diffusion properties and cannot (easily) be modelled theoretically or studied in solution.<sup>54</sup> However, these techniques are either limited to measuring the ensemble sample morphology (as is the case in transient absorption) or are limited by the spectral features necessary to determine specific exciton species. A recently developed optical measurement technique that tackles both issues is transient absorption microscopy. This measurement technique allows ultrafast (200 fs time resolution) and spatial optical probing of excitons on a micro- and macroscale with a 50 nm spatial resolution.<sup>17</sup> As such, the investigators were able to study triplet exciton diffusion in a variety of singlet fission chromophores and found that singlet-mediated triplet transport, *i.e.* exciton with mixed singlet-triplet character increases the triplet diffusion coefficient by more than an order of magnitude. In a follow-up study the same group found a correlation between the SF endothermicity and the triplet diffusion length of several acene molecules that was attributed to an increasing singlet-mediated SF pathway.<sup>52</sup> What remains unknown from this study is which triplet pair state is responsible for the singlet mediated diffusion. The identification of specific triplet pair states formed during singlet fission was performed recently in photoluminescence measurements at high magnetic field.<sup>55</sup> The investigators use the magnetic field to tune the otherwise dark triplet pair state into resonance with the optically bright singlet state thereby decreasing the photoluminescence. As a result, dips in the photoluminescence emerge at specific magnetic field strengths that correspond to specific triplet pair exchange-coupling strengths. The investigators argue that this resonance ex-

citation technique may supplement to transient microscopy absorption measurement in identifying triplet pair state specific diffusion.

In this thesis we study the diffusion of triplets in an alternative way, by performing photoconductivity experiments using time-resolved microwave conductivity technique. In these experiments, we monitor the injection of electrons into an inorganic  $\text{TiO}_2$  substrate that acts as an antenna layer. By determining how many electrons are injected into this antenna layer for a specific layer thickness and excitation density it is possible to determine the exciton diffusion length and the diffusion coefficient, as will be shown in Chapter 2.

### 1.3. OUTLINE OF THIS THESIS

The focus of this thesis is on the fundamental understanding of the relation between the packing of conjugated organic molecules and the efficiency of the singlet fission and triplet-triplet annihilation upconversion and the diffusion of triplet excited states. The efficient exploitation of singlet exciton fission and triplet-triplet annihilation upconversion in organic solar cell devices requires that all these processes occur with a reasonable efficiency.

In **Chapter 2** we describe a study of the interplay between charge carrier mobility, exciton diffusion and the packing of perylene diimide molecules in the solid-state by using time-resolved microwave conductivity experiments.

In **Chapter 3** we study the relation between molecular packing and singlet fission in a series of perylene diimide molecules that are substituted in the bay area of the molecule, which has a pronounced effect on the stacking of the molecules on top of each other. Time-resolved optical absorption measurements on the nanosecond and femtosecond time scales show that this indeed has a pronounced effect on the rate of the singlet fission process.

In **Chapter 4** we explore the possibility of implementing the triplet-triplet annihilation upconversion process in a fully solid-state setting relying on triplet energy transfer rather than molecular diffusion and in which the singlet excited state directly injects an electron rather than photon emission and reabsorption. The injection of charge formed by TTA-UC is studied by microwave conductivity techniques.

In **Chapter 5** we use temperature dependent microwave conductivity experiments to study the nature of triplet diffusion in crystalline perylene diimide layers. It is shown that there is a distinct effect of temperature, indicating a thermally activated mechanism for triplet diffusion.

In **Chapter 6** we describe our initial attempts to study the effect of external magnetic fields to study the dynamics of singlet fission and the subsequent decoherence of the coupled triplet pairs that are formed in perylene diimides. These measurements show clear effects of magnetic field on the processes but more detailed studies are needed to get a full picture.

Finally, in **Chapter 7** we give a brief outlook where, based on the results in this thesis and other results in literature, we give some directions for future work.





## REFERENCES

- (1) Shirakawa, H.; Louis, E. J.; MacDiarmid, A. G.; Chiang, C. K.; Heeger, A. J. Synthesis of electrically conducting organic polymers: halogen derivatives of polyacetylene, (CH)<sub>x</sub>. *J. Chem. Soc. Chem. Comm.* **1977**, *16*, 578–580.
- (2) Burroughes, J. H.; Bradley, D. D.; Brown, A.; Marks, R.; Mackay, K. and Friend, R. H.; Burns, P.; Holmes, A. Light-emitting diodes based on conjugated polymers. *Nature* **1990**, *347*, 539.
- (3) Singh, S.; Jones, W.; Siebrand, W.; Stoicheff, B. P.; Schneider, W. G. Laser generation of excitons and fluorescence in anthracene crystals. *J. Chem. Phys.* **1965**, *42*, 330–342.
- (4) Swenberg, C.; Stacy, W. Bimolecular radiationless transitions in crystalline tetracene. *Chem. Phys. Lett.* **1968**, *2*, 327–328.
- (5) Hanna, M. C.; Nozik, A. Solar conversion efficiency of photovoltaic and photoelectrolysis cells with carrier multiplication absorbers. *J. Appl. Phys.* **2006**, *100*, 074510.
- (6) Futscher, M. H.; Rao, A.; Ehrler, B. The Potential of Singlet Fission Photon Multipliers as an Alternative to Silicon-Based Tandem Solar Cells. *ACS Energ. Lett.* **2018**, *3*, 2587–2592.
- (7) Pace, N. A.; Arias, D. H.; Granger, D. B.; Christensen, S.; Anthony, J. E.; Johnson, J. C. Dynamics of singlet fission and electron injection in self-assembled acene monolayers on titanium dioxide. *Chem. Sci.* **2018**, *9*, 3004–3013.
- (8) Congreve, D. N.; Lee, J.; Thompson, N. J.; Hontz, E.; Yost, S. R.; Reuswig, P. D.; Bahlke, M. E.; Reineke, S.; Van Voorhis, T.; Baldo, M. A. External quantum efficiency above 100% in a singlet-exciton-fission-based organic photovoltaic cell. *Science* **2013**, *340*, 334–337.
- (9) Pazos-Outón, L. M.; Lee, J. M.; Futscher, M. H.; Kirch, A.; Tabachnyk, M.; Friend, R. H.; Ehrler, B. A Silicon–Singlet Fission Tandem Solar Cell Exceeding 100% External Quantum Efficiency with High Spectral Stability. *ACS Energ. Lett.* **2017**, *2*, 476–480.
- (10) Smith, M. B.; Michl, J. Singlet fission. *Chem. Rev.* **2010**, *110*, 6891–6936.
- (11) Sullivan, P.; Jones, T. S. Pentacene/Fullerene (C60) Heterojunction Solar Cells: Device Performance and Degradation Mechanisms. *Org. Electron.* **2008**, *9*, 656–660.
- (12) Smith, M. B.; Michl, J. Recent advances in singlet fission. *Annu. Rev. Phys. Chem.* **2013**, *64*, 361–386.
- (13) Wen, J.; Havlas, Z.; Michl, J. Captodatively stabilized biradicaloids as chromophores for singlet fission. *J. Am. Chem. Soc.* **2014**, *137*, 165–172.
- (14) Grotjahn, R.; Maier, T. M.; Michl, J.; Kaupp, M. Development of a TDDFT-Based Protocol with Local Hybrid Functionals for the Screening of Potential Singlet Fission Chromophores. *J. Chem. Theory Comput.* **2017**, *13*, 4984–4996.
- (15) Renaud, N.; Grozema, F. C. Intermolecular vibrational modes speed up singlet fission in perylene diimide crystals. *J. Phys. Chem. Lett.* **2015**, *6*, 360–365.

- (16) Scholes, G. D. Correlated Pair States Formed by Singlet Fission and Exciton–Exciton Annihilation. *J. Phys. Chem. A* **2015**, *119*, 12699–12705.
- (17) Wan, Y.; Guo, Z.; Zhu, T.; Yan, S.; Johnson, J.; Huang, L. Cooperative singlet and triplet exciton transport in tetracene crystals visualized by ultrafast microscopy. *Nat. Chem.* **2015**, *7*, 785.
- (18) Johnson, J. C.; Nozik, A. J.; Michl, J. High Triplet Yield from Singlet Fission in a Thin Film of 1,3-Diphenylisobenzofuran. *J. Am. Chem. Soc.* **2015**, *132*, 785.
- (19) Piland, G. B.; Burdett, J. J.; Kurunthu, D.; Bardeen, C. J. Magnetic field effects on singlet fission and fluorescence decay dynamics in amorphous rubrene. *J. Phys. Chem. C* **2013**, *117*, 1224–1236.
- (20) Delgado, M. C. R.; Kim, E. G.; da Silva, D. A.; Bredas, J. L. Tuning the Charge-Transport Parameters of Perylene Diimide Single Crystals Via End and/or Core Functionalization: A Density Functional Theory Investigation. *J. Am. Chem. Soc.* **2010**, *132*, 3375–3387.
- (21) Mirjani, F.; Renaud, N.; Gorczak, N.; Grozema, F. C. Theoretical Investigation of Singlet Fission in Molecular Dimers: The Role of Charge Transfer States and Quantum Interference. *J. Phys. Chem. C* **2014**, *118*, 14192–14199.
- (22) Aulin, Y. V.; Felter, K. M.; Gunbas, D.; Dubey, R. K.; Jager, W. F.; Grozema, F. Morphology independent efficient singlet exciton fission in perylenediimide thin films. *ChemPlusChem*.
- (23) Eaton, S. W.; Shoer, L. E.; Karlen, S. D.; Dyar, S. M.; Margulies, E. A.; Veldkamp, B. S.; Ramanan, C.; Hartzler, D. A.; Savikhin, S.; Marks, T. J. Singlet exciton fission in polycrystalline thin films of a slip-stacked perylenediimide. *J. Am. Chem. Soc.* **2013**, *135*, 14701–14712.
- (24) Le, A. K.; Bender, J. A.; Arias, D. H.; Cotton, D. E.; Johnson, J. C.; Roberts, S. T. Singlet Fission Involves an Interplay between Energetic Driving Force and Electronic Coupling in Perylenediimide Films. *J. Am. Chem. Soc.* **2018**, *140*, 814–826.
- (25) Arias, D. H.; Ryerson, J. L.; Cook, J. D.; Damrauer, N. H.; Johnson, J. C. Polymorphism influences singlet fission rates in tetracene thin films. *Chem. Sci.* **2016**, *7*, 1185–1191.
- (26) Piland, G. B.; Bardeen, C. J. How morphology affects singlet fission in crystalline tetracene. *J. Phys. Chem. Lett.* **2015**, *6*, 1841–1846.
- (27) Yost, S. R.; Lee, J.; Wilson, M. W. B.; Wu, T.; McMahon, D. P.; Parkhurst, R. R.; Thompson, N. J.; Congreve, D. N.; Rao, A.; Johnson, K. A transferable model for singlet-fission kinetics. *Nat. Chem.* **2014**, *6*, 492.
- (28) Wibowo, M.; Broer, R.; Havenith, R. W. A rigorous nonorthogonal configuration interaction approach for the calculation of electronic couplings between diabatic states applied to singlet fission. *Comput. Theor. Chem.* **2017**, *1116*, 190–194.
- (29) Havenith, R. W. A.; de Gier, H. D.; Broer, R. Explorative computational study of the singlet fission process. *Mol. Phys.* **2012**, *110*, 2445–2454.
- (30) Casanova, D. Theoretical modelling of singlet fission. *Chem. Rev.* **2018**, *118*, 7164–7207.
- (31) Basel, B. S.; Zirzmeier, J.; Hetzer, C.; Phelan, B. T.; Krzyaniak, M. D.; Reddy, S. R.; Coto, P. B.; Horwitz, N. E.; Young, R. M.; White, F. J. Unified model for singlet fis-

- sion within a non-conjugated covalent pentacene dimer. *Nat. Commun.* **2017**, *8*, 15171.
- (32) Ito, S.; Nagami, T.; Nakano, M. Molecular design for efficient singlet fission. *J. Photoch. Photobio. C* **2018**.
- (33) Berkelbach, T. C.; Hybertsen, M. S.; Reichman, D. R. Microscopic theory of singlet exciton fission. II. Application to pentacene dimers and the role of superexchange. *J. Chem. Phys.* **2013**, *138*, 114103.
- (34) Morrison, A. E.; Herbert, J. M. Evidence for Singlet Fission Driven by Vibronic Coherence in Crystalline Tetracene. *J. Phys. Chem. Lett.* **2017**, *8*, 1442–1448.
- (35) Wilson, M. W. B.; Rao, A.; Ehrler, B.; Friend, R. H. Singlet exciton fission in polycrystalline pentacene: from photophysics toward devices. *Accounts Chem. Res.* **2013**, *46*, 1330–1338.
- (36) Elenewski, J. E.; Cubeta, U. S.; Ko, E.; Chen, H. Computer Simulation of Singlet Fission in Single Crystalline Pentacene by Functional Mode Vibronic Theory. *J. Phys. Chem. C* **2017**, *121*, 11159–11165.
- (37) Bakulin, A. A.; Morgan, S. E.; Kehoe, T. B.; Wilson, M. W.; Chin, A. W.; Zigmantas, D.; Egorova, D.; Rao, A. Real-time observation of multiexcitonic states in ultrafast singlet fission using coherent 2D electronic spectroscopy. *Nat. Chem.* **2016**, *8*, 16.
- (38) Stern, H. L.; Cheminal, A.; Yost, S. R.; Broch, K.; Bayliss, S. L.; Chen, K.; Tabachnyk, M.; Thorley, K.; Greenham, N.; Hodgkiss, J. M. Vibronically coherent ultrafast triplet-pair formation and subsequent thermally activated dissociation control efficient endothermic singlet fission. *Nat. Chem.* **2017**, *9*, 1205.
- (39) Miyata, K.; Kurashige, Y.; Watanabe, K.; Sugimoto, T.; Takahashi, S.; Tanaka, S.; Takeya, J.; Yanai, T.; Matsumoto, Y. Coherent singlet fission activated by symmetry breaking. *Nat. Chem.* **2017**, *9*, 983.
- (40) Monahan, N. R.; Sun, D.; Tamura, H.; Williams, K. W.; Xu, B.; Zhong, Y.; Kumar, B.; Nuckolls, C.; Harutyunyan, A. R.; Chen, G. Dynamics of the triplet-pair state reveals the likely coexistence of coherent and incoherent singlet fission in crystalline hexacene. *Nat. Chem.* **2017**, *9*, 341.
- (41) Musser, A. J.; Liebel, M.; Schnedermann, C.; Wende, T.; Kehoe, T. B.; Rao, A.; Kukura, P. Evidence for conical intersection dynamics mediating ultrafast singlet exciton fission. *Nat. Phys.* **2015**, *11*, 352.
- (42) Jonas, D. M. Two-dimensional femtosecond spectroscopy. *Annu. Rev. Phys. Chem.* **2003**, *54*, 425–463.
- (43) Pensack, R. D.; Ostroumov, E. E.; Tilley, A. J.; Mazza, S.; Grieco, C.; Thorley, K. J.; Asbury, J. B.; Seferos, D. S.; Anthony, J. E.; Scholes, G. D. Observation of two triplet-pair intermediates in singlet exciton fission. *J. Phys. Chem. Lett.* **2016**, *7*, 2370–2375.
- (44) Pensack, R. D.; Tilley, A.; Grieco, C.; Purdum, G.; Ostroumov, E.; Granger, D. B.; Oblinsky, D.; Dean, J.; Doucette, G.; Asbury, J. Striking the right balance of intermolecular coupling for high-efficiency singlet fission. *Chem. Sci.* **2018**.
- (45) Grieco, C.; Kennehan, E. R.; Kim, H.; Pensack, R. D.; Brigeman, A. N.; Rimshaw, A.; Payne, M. M.; Anthony, J. E.; Giebink, N. C.; Scholes, G. D. Direct Observation of Correlated Triplet Pair Dynamics during Singlet Fission Using Ultrafast Mid-IR Spectroscopy. *J. Phys. Chem. C* **2018**, *122*, 2012–2022.

- (46) Chen, M.; Bae, Y. J.; Mauck, C. M.; Mandal, A.; Young, R. M.; Wasielewski, M. R. Singlet fission in covalent terrylenediimide dimers: probing the nature of the multiexciton state using femtosecond mid-infrared spectroscopy. *J. Am. Chem. Soc.* **2018**, *140*, 9184–9192.
- (47) Mandal, A.; Chen, M.; Foszcz, E. D.; Schultz, J. D.; Kearns, N. M.; Young, R. M.; Zanni, M. T.; Wasielewski, M. R. Two-Dimensional Electronic Spectroscopy Reveals Excitation Energy-Dependent State Mixing during Singlet Fission in a Terrylenediimide Dimer. *J. Am. Chem. Soc.* **2018**, *140*, 17907–17914.
- (48) Miyata, K.; Conrad-Burton, F. S.; Geyer, F. L.; Zhu, X. Y. Triplet Pair States in Singlet Fission. *Chem. Rev.* **2019**.
- (49) Singh-Rachford, T. N.; Castellano, F. N. Photon upconversion based on sensitized triplet–triplet annihilation. *Coordin. Chem. Rev.* **2010**, *254*, 2560–2573.
- (50) Monguzzi, A.; Tubino, R.; Meinardi, F. Multicomponent polymeric film for red to green low power sensitized upconversion. *J. Phys. Chem. A* **2009**, *113*, 1171–1174.
- (51) Grieco, C.; Doucette, G. S.; Pensack, R. D.; Payne, M. M.; Rimshaw, A.; Scholes, G. D.; Anthony, J. E.; Asbury, J. B. Dynamic exchange during triplet transport in nanocrystalline tips-pentacene films. *J. Am. Chem. Soc.* **2016**, *138*, 16069–16080.
- (52) Zhu, T.; Wan, Y.; Guo, Z.; Johnson, J.; Huang, L. Two Birds with One Stone: Tailoring Singlet Fission for Both Triplet Yield and Exciton Diffusion Length. *Adv. Mater.* **2016**, *28*, 7539–7547.
- (53) Mikhnenko, O. V.; Blom, P. W.; Nguyen, T.-Q. Exciton diffusion in organic semiconductors. *Energ. Environ. Sci.* **2015**, *8*, 1867–1888.
- (54) Lunt, R. R.; Benziger, J. B.; Forrest, S. R. Relationship between crystalline order and exciton diffusion length in molecular organic semiconductors. *Adv. Mater.* **2010**, *22*, 1233–1236.
- (55) Bayliss, S. L.; Weiss, L. R.; Mitioglu, A.; Galkowski, K.; Yang, Z.; Yunusova, K.; Surrente, A.; Thorley, K. J.; Behrends, J.; Bittl, R. Site-selective measurement of coupled spin pairs in an organic semiconductor. *Proc. Natl. Acad. Sci.* **2018**, *115*, 5077–5082.

# 2

## INTERPLAY BETWEEN CHARGE CARRIER MOBILITY, EXCITON DIFFUSION AND CRYSTAL PACKING IN PERYLENE DIIMIDES

*Two of the key parameters that characterize the usefulness of organic semiconductors for organic or hybrid organic/inorganic solar cells are the mobility of charges and the diffusion length of excitons. Both parameters are strongly related to the supramolecular organization in the material. In this work we have investigated the relation between the solid-state molecular packing and the exciton diffusion length, charge carrier mobility, and charge carrier separation yield using two perylene diimide (PDI) derivatives which differ in their substitution. We have used the time resolved microwave conductivity technique and measured charge carrier mobilities of 0.32 and 0.02 cm<sup>2</sup>/Vs and determined exciton diffusion lengths of 60 nm and 18 nm for octyl- and bulky hexylheptyl-imide substituted PDIs, respectively. This diffusion length is independent of substrate type and aggregate domain size. The differences in charge carrier mobility and exciton diffusion length clearly reflect the effect of solid-state packing of PDIs on their opto-electronic properties and show that significant improvements can be obtained by effectively controlling the solid-state packing.*

---

This chapter is based on: Felzer, K. M., Caselli, V. M., Günbaş, D. D., Savenije, T. J., and Grozema, F. C. (2019). *Interplay between charge carrier mobility, exciton diffusion, crystal packing and charge separation in perylene diimide-based heterojunctions*. ACS Applied Energy Materials, 2(11), 8010-8021.

## 2.1. INTRODUCTION

Perylene diimides (PDIs) are attractive organic semiconductors for opto-electronic studies and organic photovoltaic technologies owing to their high optical absorption and fluorescence yield, high photo-chemical stability<sup>1</sup> and strong electron accepting properties. Among the most appealing characteristics of PDIs is the possibility to control the electronic structure and molecular packing by chemically functionalizing the molecule with a large variety of side-groups. As such, they are often used to study energetic and molecular packing effects in connection to organic semiconductor device performance.<sup>2</sup> These electron acceptor molecules also offer an attractive alternative to fullerene acceptor molecules that are predominantly used in organic photovoltaic devices.<sup>3</sup> An additional aspect of this is that PDIs display unconventional processes such as singlet exciton fission with high efficiency and rate that can ultimately lead to device efficiencies surpassing the Shockley-Queisser limit.<sup>4-6</sup> The reverse process, triplet-triplet annihilation up-conversion has also been demonstrated in PDIs.<sup>7,8</sup> Both processes can be used to boost organic photovoltaic device efficiencies.

Two key parameters that determine the performance of organic semiconductors in opto-electronic applications are the charge carrier mobility and the exciton diffusion length. However, only a few reports exist on experimentally determined PDI diffusion characteristics. To our knowledge there are only three previously published studies on the PDI exciton diffusion length  $\Lambda_{EXC}$ . The  $\Lambda_{EXC}$  values in solid-state thin films of phenylethyl imid substituted PDI vary from 50-500 nm (with a 50 nm resolution)<sup>9</sup> to  $2.5 \pm 0.5 \mu\text{m}$ <sup>10</sup>. In addition, two studies on J-aggregates of PDIs in solution reported values of  $\Lambda_{EXC} = 70 \text{ nm}$ <sup>11</sup> and  $\Lambda_{EXC} = 96 \text{ nm}$ <sup>12</sup>. These values are in agreement with that of a related perylene compound, perylene tetracarboxyl dianhydride.<sup>13</sup> In a study on this material it was shown how the grain diameter strongly affects the non-radiative decay rate. In turn, the exciton diffusion length determination via photoluminescence quenching was shown to result in  $\Lambda_{EXC} = 6.5 \pm 1.0 \text{ nm}$  for a grain diameter of  $\pm 5 \text{ nm}$  to  $\Lambda_{EXC} = 21.5 \pm 2.5 \text{ nm}$  for  $\pm 400 \text{ nm}$  grain sizes.<sup>13</sup> Some of these singlet exciton diffusion lengths are unusually long, considering that for most organic semiconductors singlet exciton diffusion lengths are in the range of 2-15 nm.<sup>14</sup> Therefore, the electronic and structural origins of the large singlet exciton diffusion lengths are interesting to study in PDIs. The second important electronic characteristic of organic semiconductors is the charge carrier mobility. There are several theoretical<sup>15-18</sup> and experimental<sup>16-21</sup> studies on PDIs reporting electron mobilities  $\mu_{e^-}$  ranging from 0.1 to 2  $\text{cm}^2/\text{Vs}$ . Some of these studies indicate that intermolecular orientation and distance strongly influence charge carrier mobility. This was explained by differences in molecular orbital overlap that affect the effective charge transfer integral between neighbouring molecules.

The aim of this study is to investigate the interplay between morphology and opto-electronic properties which is highly relevant considering the aforementioned renewed interest in PDI molecules as electron acceptors and the possible exploitation of singlet fission<sup>6,22</sup> and up-conversion in organic photovoltaic devices.<sup>23,24</sup> However, while the optical, and charge carrier properties have been reported separately,<sup>10,17,25-27</sup> no integrated study has been performed, reporting on exciton diffusion and charge carrier dynamics using the same experimental technique, *i.e.* time resolved microwave conductivity. In fact, simultaneous knowledge on all these properties is essential for designing

better chromophore systems for organics based opto-electronic devices. To this end we examine thin films of octyl (PDI-octyl) and hexylheptyl (PDI-hexhep) imid substituted PDIs shown in Figure 2.1. PDI-octyl is a commonly used PDI for organic electronics related studies and has been shown to form large crystalline aggregates.<sup>28–31</sup> PDI-hexhep is substituted with a branched alkyl chain that is commonly used to improve solubility by decreasing intermolecular  $\pi - \pi$  stacking between PDI cores.<sup>28</sup> The decreased electronic interaction between the  $\pi$  systems should provide clear differences in opto- electronic behaviour between PDI-hexhep and PDI-octyl. Using electron and laser pulsed time resolved microwave conductivity (TRMC) measurements we determined charge carrier mobilities of 0.32 and 0.02  $\text{cm}^2/\text{Vs}$  and corresponding exciton diffusion lengths of 60 and 20 nm for PDI-octyl and PDI-hexhep, respectively. These studies were performed on planar heterojunction systems of PDIs with zinc phthalocyanine (ZnPc) and polycrystalline titanium dioxide ( $\text{TiO}_2$ ) of which the electronic diagram is depicted in Figure 2.1.

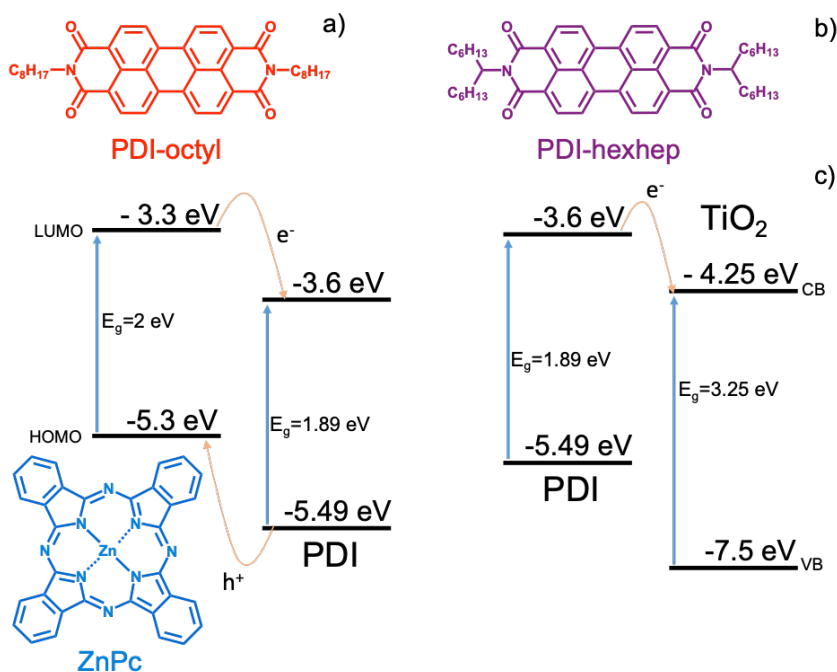


Figure 2.1: Chemical structure of a) PDI-octyl and b) PDI-hexhep and ZnPc and c) energy diagrams for the fully organic PDI/ZnPc and  $\text{TiO}_2$ /PDI planar heterojunction used in this study to investigate charge carrier kinetics and exciton diffusion.



## 2.2. EXPERIMENTAL SECTION

### SAMPLE PREPARATION AND CHARACTERIZATION

PDI-octyl (N,N'-dioctyl-3,4,9,10-perylenedicarboximide) and PDI-hexhep (N'-hexyl-heptyl-3,4,9,10-perylenedicarboximide) were synthesized from perylene-3,4,9,10-tetracarboxylic acid dianhydride as purchased from Sigma-Aldrich according to procedures published elsewhere.<sup>32</sup> The ZnPc powder was purchased from TCP and used without further modification. The polycrystalline TiO<sub>2</sub> coated fused silica substrates (~90 nm thickness) were purchased from *Everest Coatings Inc.* and treated at 450°C for two hours in a furnace. Pulse radiolysis time resolved microwave conductivity (PR-TRMC) measurements were performed on PDI powders and flash photolysis TRMC measurements were carried out on thin films. Thin films of PDI and ZnPc powders were deposited on fused silica substrates by thermal evaporation in an *AJA ATC Orion evaporator*. Prior to deposition, the substrates (*ESCO, 12 x 25 x 1 mm*) underwent an air plasma treatment (2 min, 1000 mtorr) to clean and charge the substrate surface. During deposition, the powders were heated to their sublimation temperature (180-230°C) under high vacuum conditions (10<sup>-7</sup>-10<sup>-6</sup> mbar) and heated further until the desired evaporation rate was reached (0.3Å/s). The deposition rate was monitored using a quartz micro-crystal balance. The fused silica substrates were heated to 150°C during PDI deposition to promote crystallization and were brought back to room temperature prior to ZnPc evaporation in order to prevent blending of the organic layers. TiO<sub>2</sub> thin films on fused silica underwent the same processing to fabricate the TiO<sub>2</sub>/PDI planar heterojunctions but now without heating the substrate. During deposition the substrate holder rotated the substrates at 25 rpm to ensure film homogeneity. The thin film surface morphology was imaged using an Extreme-Resolution Analytical Field Emission *SEM JEOL-7800F Prime Extreme*. The images were recorded under high vacuum with an upper electron detector (UED) and a lower electron detector (LED) to measure secondary and backscattered electrons. The resolution of the images was enhanced by occasionally sputtering the organic films with a 5 nm thick Pt layer (*sputter coater Leica EM ACE600*). The film thickness was determined using a step-profilometer (*Veeco Dektak 8 Stylus step-profilometer*) and are listed in Table A.1. X-ray diffractograms were acquired using a Brüker D8 X-ray diffractometer (Co K $\alpha$ 1 radiation,  $\alpha = 1.79 \text{ \AA}$ ) and analysed with the Brüker program *EVA*. Steady state absorption spectra were obtained using a *Perkin Elmer Lambda 1050* spectrometer with the sample placed inside and in front of an integrating sphere to measure attenuation and transmission, respectively. Emission and excitation spectra of solutions and thin films were recorded with a *FLS980 Edinburgh Instruments spectrometer*. Time resolved photoluminescence experiments were performed with a *Hamamatsu C5680* streak camera coupled to a *Princeton Instruments* spectrograph. The excitation wavelength was created via frequency doubling using a *Coherent Chameleon* oscillator operating at a repetition rate of 80 MHz.

### PULSE RADIOLYSIS MICROWAVE CONDUCTIVITY

The PDI charge carrier mobilities were measured in pulse radiolysis TRMC measurements. An extensive description of the PR-TRMC technique and its capabilities can be found elsewhere.<sup>33,34</sup> In this technique the powder sample is irradiated with a 1-50 ns duration pulse of high-energy electrons (3 MeV) generated by a Van de Graaff accelerator that creates low concentration (micro-molar) but uniformly distributed positive and negative carrier densities. Subsequently, the time-resolved conductivity of the sample is probed by monitoring the attenuation of reflected microwave power (frequency 28-38 GHz, maximum electric field strength in the sample is 10 V/m). The fractional change in microwave power reflected by the cell ( $\Delta P(t)/P$ ) relates to the change in conductivity  $\Delta\sigma(t)$  as

$$\frac{\Delta P(t)}{P} = A\Delta\sigma(t) \quad (2.1)$$

The initial concentration of charge carrier pairs, *i.e.* electrons and holes  $n_p$  can be estimated using dosimetry measurements combined with a charge-scavenging model. From this estimate of the carrier concentration, a summed charge carrier mobility  $\Sigma\mu_{TRMC}$  can be calculated according to

$$\Delta\sigma(t) = en_p \Sigma\mu_{TRMC} \quad (2.2)$$

where  $\Sigma\mu_{TRMC}$  is the sum of electron and hole mobility that both contribute to the conductivity and are indistinguishable in the experiment. Almost all known crystal structures show that PDIs preferentially stack in a one-dimensional columnar geometry. Therefore, we derive an intra columnar mobility that equals three times the isotropic value obtained from the TRMC conductivity measurements

$$\Sigma\mu_{1D} = 3 \Sigma\mu_{TRMC} \quad (2.3)$$

The measured mobility values in PR-TRMC are related to the charge transfer rate between PDI molecules in the ordered crystallite. An expression for the charge transfer rate  $\nu$ , between PDI molecules is provided by Marcus theory<sup>35,36</sup>

$$\nu = \frac{J_{eff}^2}{\hbar} \sqrt{\frac{\pi}{\lambda k_B T}} e^{\frac{-\lambda}{4k_B T}} \quad (2.4)$$

where  $J_{eff}$  is the effective charge transfer integral between neighbouring molecules that depends on the mutual orientation and distance,  $\lambda$  is the reorganization energy,  $T$  is the temperature and  $k_B$  is Boltzmann's constant. Provided that the PDIs self-assemble in columnar crystalline stacks without structural fluctuations, the charge transfer integrals for PDI molecules in such a stack are identical and the charge carrier mobility in the direction along the stack  $\mu_{1D}$  can be calculated according to the relation involving an expression for the charge carrier diffusion coefficient  $D_{CHARGE} = \nu d^2$ <sup>37</sup>

$$\mu_{1D} = \frac{e}{k_B T} \nu d^2 \quad (2.5)$$

In equation 2.5,  $d$  is the intermolecular distance in a PDI stack. Note that for a given value of the charge transfer rate,  $\nu$ , the charge carrier mobility scales with the square

of  $d$ , however, for large values of  $d$  the charge transfer integral,  $J_{eff}$  and hence  $v$ , will be smaller, see equation 2.4. The charge carrier mobility can be used to provide an estimate of the charge carrier diffusion coefficient  $D_{CHARGE}$  according to the Einstein-Smoluchowski relation

$$D_{CHARGE} = \frac{\mu_{1D} k_B T}{q} \quad (2.6)$$

where  $q$  is the elementary charge.

### FLASH PHOTOLYSIS MICROWAVE CONDUCTIVITY

The diffusion length of the PDIs were studied with the laser pulsed TRMC technique. These TRMC measurements were performed on a home-built setup of which the operating principles are described elsewhere.<sup>38</sup> In this technique, optical excitation of the sample occurs via 3 ns full width half maximum (FWHM) laser pulses ( $\lambda = 240\text{-}2200$  nm). The sample is probed by continuous X-band microwaves ( $\sim 8.4$  GHz) in a microwave resonant cavity cell, that defines the instrument response function to 18 ns. The fractional change in microwave power reflected ( $\Delta P/P$ ) is related to a change in photoconductance,  $\Delta G(t)$ , as:

$$\frac{\Delta P(t)}{P} = -K \Delta G(t) \quad (2.7)$$

In equation 2.7,  $K$  is the microwave frequency dependent sensitivity factor that has a predetermined value of  $40 \cdot 10^3 \text{ S}^{-1}$  for the current experimental conditions.<sup>39</sup>  $\Delta G(t)$  is directly proportional to the product of the charge carrier density  $n_i$  and mobility  $\mu_i$  according to:

$$\Delta G(t) = e\beta L \sum_i n_i(t) \mu_i \quad (2.8)$$

In equation 2.8,  $e$  is the elementary charge,  $L$  the film thickness and  $\beta$  the ratio between the inner width and length dimensions of the microwave waveguide. The index ' $i$ ' runs over all charged species present, *i.e.* electrons and holes, that both contribute to the photoconductance. The photoconductance transients can be deconvoluted for the instrumental response function using the cavity response function profile ( $LP(t)$ ):

$$\Delta G_{exp}(t) - LP(t) \otimes \Delta G_0 \left( \sum_i c_i e^{-\frac{t}{\tau_i}} \right) \quad (2.9)$$

In equation 2.9,  $\Delta G_0$  is the initial photoconductance prior to charge carrier decay and  $\otimes$  indicates the convolution between  $LP(t)$  and  $\Delta G_0$ .  $c_i$  and  $\tau_i$  are the exponent and decay time characteristic of the  $i$ -th transient decay component. The sum of all decay components account for all recombination processes occurring in the sample.  $\Delta G_0$  can be used to obtain a value for the product of the incident photon to charge carrier generation yield,  $\eta_0$ , and the sum of electron and hole mobility,  $\Sigma\mu$ , as<sup>40</sup>

$$\eta_0 \Sigma\mu = \frac{\Delta G_0}{e\beta I_0 (1 - F_R)} \quad (2.10)$$

In equation 2.10,  $I_0$  is the measured incident photon fluence and  $F_R$  the fraction of reflected incident photons as deduced from attenuation and transmission measurements. The applied fitting function to determine the exciton diffusion length  $\Lambda_{EXC}$  was described by Kroeze et al. for steady state illumination and has since been applied to study singlet and triplet exciton diffusion for organic semiconductors in various heterojunction systems.<sup>41–44</sup> Such function is used to fit the experimentally measured  $\eta_0 \Sigma \mu$  and has the following general form:

$$\eta_0 \Sigma \mu = (1 - F_R) S(\alpha, L, \Lambda_{EXC}) \phi_{CS} \Sigma \mu \quad (2.11)$$

In equation 2.11,  $\phi_{CS}$  is the interfacial charge separation yield that is a function of  $S$ , the fraction of charges that reaches the interface. The expression for  $S$  provided in equations A.2-A.5, shows its dependence on the absorption coefficient  $\alpha$ ,  $L$  and  $\Lambda_{EXC}$ . It should be noted that  $\phi_{CS}$  can only be disentangled from the product  $\eta_0 \Sigma \mu$  if the mobility of the generated charge carriers is known. For the bilayers with  $\text{TiO}_2$  this approach is discussed below. However, for the PDI-ZnPc bilayers this is not possible. Nevertheless,  $\Lambda_{EXC}$  can be determined independent of the mobility and can be directly obtained from the thickness dependence, as discussed below. The expression for  $S$  is provided in the SI and depends on the illumination side (front side (FS) and back side (BS)) and whether exciton reflection or quenching occurs at the non-heterojunction interface of the system. To determine  $\Lambda_{EXC}$ , planar heterojunction systems were measured by front side and back side illumination and by varying the PDI film thickness  $L$ . The measured values for  $\eta_0 \Sigma \mu$  are fitted with equations 2.11 and A.2-A.3 using a predetermined value for  $\alpha$  to obtain the indistinguishable product term  $\phi_{CS} \Sigma \mu$  and  $\Lambda_{EXC}$ . Similar fitting functions, *i.e.* equations 2.11 and A.4-A.5, were applied to  $\text{TiO}_2/\text{PDI}$  heterojunctions. However, instead of varying the PDI layer thickness, an action spectrum was measured acting to vary  $\alpha$ . The singlet exciton diffusion coefficient  $D_{EXC}$  can be calculated using the following relation

$$\Lambda_{EXC} = \sqrt{D_{EXC} \tau_{EXC}} \quad (2.12)$$

Where  $\tau_{EXC}$  is the singlet exciton lifetime obtained from photoluminescence measurements.

## 2.3. RESULTS AND DISCUSSION

### CRYSTALLINITY AND CHARGE CARRIER TRANSPORT IN PDI POWDERS

We first investigate the effect of the PDI imid substitution on molecular packing using X-ray powder diffraction and the resulting charge carrier mobility using pulse radiolysis conductivity experiments. The X-ray diffractograms of PDI-octyl and PDI-hexhep powders in Figure 2.2a display strong differences in reflection intensity. PDI-octyl has a pronounced [001] reflection that is consistent with the known crystal structure<sup>30,31</sup>, contrary to the less well resolved PDI-hexhep diffractogram that indicates rather poor crystallinity. This is consistent with the expected effect of the branched side chains that disrupts the solid-state packing. The radiation induced conductivity transients obtained from PR-TRMC measurement on PDI-octyl and PDI-hexhep powders are shown in Figure 2.2b. During the 10 ns electron pulse, the conductivity increases linearly with time due to the formation of mobile charge carriers. Subsequently, recombination of electrons and holes or trapping of charges at impurities cause the conductivity to decay. The conductivity of PDI-octyl is an order of magnitude higher than that of PDI-hexhep. The sum of the electron and hole mobility  $\Sigma\mu$  derived from these transients are  $\Sigma\mu_{1D} = 0.32$  for PDI-octyl and  $0.02 \text{ cm}^2/\text{Vs}$  for PDI-hexhep. According to estimates based on Marcus theory made by Delgado et al. for PDI-pentyl, which has a similar crystal packing as PDI-octyl, the values of the electron and hole mobility of PDI-octyl are  $\mu_{e^-} = 0.1 \text{ cm}^2/\text{Vs}$  and  $\mu_{h^+} = 2.1 \text{ cm}^2/\text{Vs}$ , respectively. These values are larger than what we find experimentally for PDI-octyl, but this can easily be understood by realising that the calculated values do not account for any static or dynamic structural disorder.<sup>15,16</sup> For PDI-hexhep such calculations are not possible since no crystal structure is known. The mobility of PDI-octyl is among the highest values obtained for perylene diimides<sup>45</sup> and is attributed to columnar packed PDI units. Such columnar structures are also observed in XRD and SEM measurements of the thin films shown later. The more ordered structure of PDI-octyl, as shown in Figure A.1, compared to PDI-hexhep leads to a larger effective orbital overlap and thus higher mobility values.<sup>15</sup>

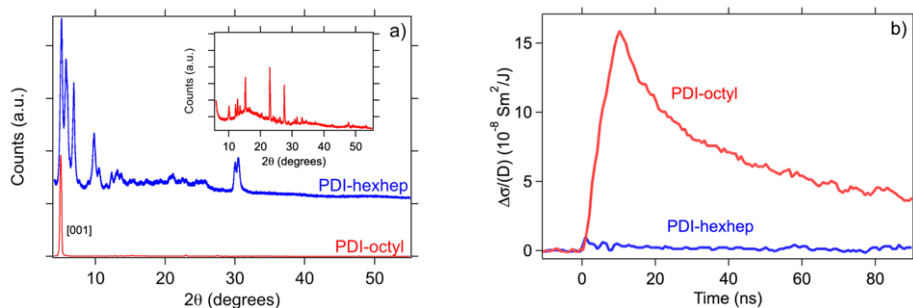


Figure 2.2: a) Powder X-ray diffractograms of PDI-octyl and PDI-hexhep with the pronounced [001] reflection of PDI-octyl and a 4500x zoomed-in view in the inset. b) Dose normalized radiation induced conductivity transients for PDI-octyl and PDI-hexhep at room temperature using a 10 ns electron pulse.

### SOLID-STATE PACKING AND THIN FILM MORPHOLOGY

The X-ray diffractograms of PDI films in Figure 2.3 reveal one reflection for PDI-octyl at  $5.1^\circ$  and PDI-hexhep at  $5.86^\circ$ . This corresponds to intercolumnar spacings of  $20.1 \text{ \AA}$  and  $17.5 \text{ \AA}$ , respectively. The preferential crystal orientation of PDI-octyl and -hexhep are in accordance with literature.<sup>19,30,45</sup> Comparison of the powder with the thin film diffractograms shows the preferred crystal orientation in the thin film since it only has one reflection, in contrast to the powder spectrum. The extent of crystallization of PDI-octyl does not seem to be larger than in PDI-hexhep. This observation is supported by an estimation of the crystallite domain size (provided in Table A.2) using the Scherrer equation. The estimate shows that PDI-hexhep has similar crystalline domains ranging from 29 to 131 nm and in PDI-octyl it ranges from 28 to 97 nm.

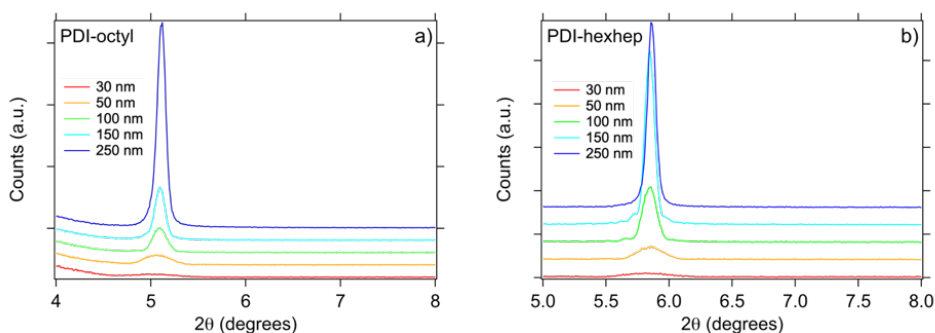


Figure 2.3: X-ray diffractograms for annealed ( $150^\circ\text{C}$ ) single layer thin films on fused silica of a) PDI-octyl and b) PDI-hexhep with thicknesses ranging from 15-500 nm.

Previous studies have shown that the formation of organic thin films depends on the substrate properties.<sup>20,31,46</sup> We use fused silica and  $\text{TiO}_2$  as a substrate to investigate a possible relation between substrate type and the solid-state packing of the PDIs. In Figure 2.4 SEM images are displayed of the PDI film surface morphology on both fused silica and  $\text{TiO}_2$ . The films are not annealed and are carefully coated with a Pt layer (3 nm) to allow better imaging. The PDI-octyl layer on fused silica is composed of rod like domains with lengths up to 500 nanometres. Similar but rougher structures exist on  $\text{TiO}_2$  owing to the rougher  $\text{TiO}_2$  surface (Figure A.3). The PDI-hexhep layer on fused silica lacks structure while on  $\text{TiO}_2$  we do observe irregular shaped features with diameters up to hundreds of nanometres. The similarity between PDI surface morphology on fused silica and  $\text{TiO}_2$  is substantiated by an identical position and width of the reflection in the XRD diffractogram of PDI-octyl and PDI-hexhep on fused silica and  $\text{TiO}_2$  (Figure A.4). Upon annealing the film, PDI-octyl and -hexhep both form large rod-like filaments of lengths exceeding a micrometer, as displayed in Figure A.2. As mentioned, the annealed films were used in the PDI/ZnPC heterojunctions, while the unannealed variants in Figure 2.4 were used in the  $\text{TiO}_2$ /PDI heterojunctions. We observe similar sizes of filamental structures in all film thicknesses although the film surface roughens (Figure A.2).

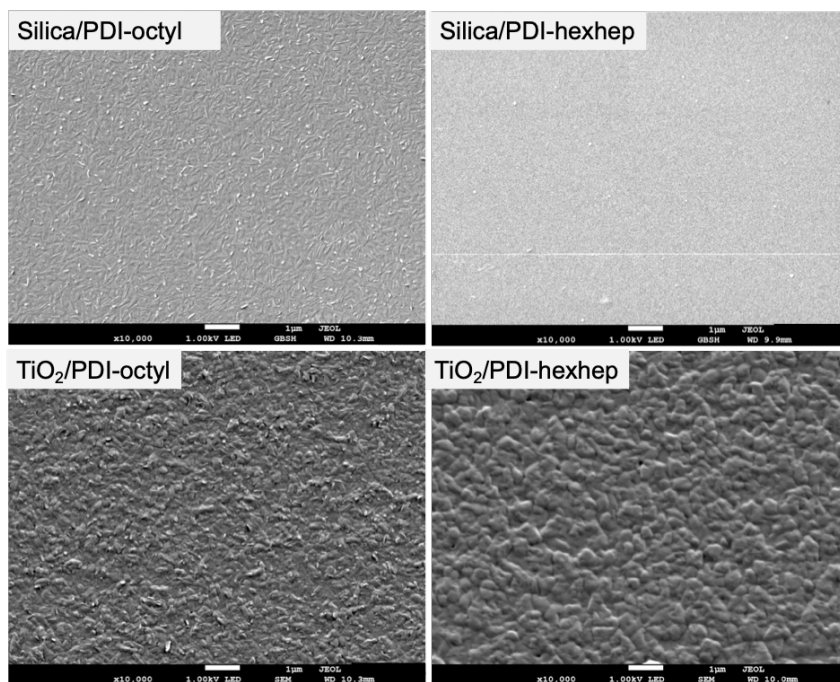


Figure 2.4: Scanning electron microscope images for 100 nm thick films of PDI-octyl (left) and PDI-hexhep (right) on fused silica and  $\text{TiO}_2$  substrates. Scale bars indicate the size of the features at 10,000X magnification.

## OPTICAL PROPERTIES OF THIN FILMS

In Figure 2.5a we display the absorption spectra of films of PDI-octyl and PDI-hexhep on fused silica and PDI-octyl in solution. In solution, the absorption spectrum of both PDIs is identical (Figure A.3) and shows the characteristic PDI absorption in the 450-550 nm region with three bands centred at 460, 490 and 530 nm that belong to the  $\pi - \pi^*$  transition of the PDI aromatic core involved in the vibronic progression of the  $S_0 - S_1$  excitation.<sup>26,27</sup> In the solid-state, PDI-octyl and PDI-hexhep form H-type aggregates as visible from the 550 nm absorption shoulder.<sup>26,47,48</sup> The stronger red shift in the absorption onset of PDI-octyl (570 nm) than -hexhep (540 nm) indicates stronger excitonic interaction in PDI-octyl.<sup>27</sup> The shape of the absorption spectrum of PDI-octyl and PDI-hexhep resembles that of their excitation spectrum. However, the emission intensity of PDI-octyl is less at lower wavelength, which points to the presence of a non-radiative decay pathway. The effect of solid-state packing is also visible in the emission spectra shown in Figure 2.5b. The PDI emission spectrum in solution has three distinct emission features while in the thin films these features broadened strongly and an overall emission redshift is observed. This redshift in the emission in PDIs is commonly attributed to the presence of emissive excimer states that form upon aggregation.<sup>49,50</sup> We recently carried out a study in which we showed that bromination in the bay area prevents the formation of excimer states that are a competing decay channel for singlets, next to singlet fission.<sup>51</sup> The thin film photoluminescence lifetime of PDI-octyl and PDI-hexhep are



$\tau_{EXC} = 0.55$  ns and  $\tau_{EXC} = 1.13$  ns, respectively, as determined from a mono-exponential decay fit on fluorescence decays as shown in Figure 2.5c. In our previous study we estimated an  $\tau_{EXC} = 890$  ps for PDI-octyl which was longer than in the present study, as we presently used a streak camera setup that has a faster detection limit. The shorter fluorescence lifetime of excitons in PDI-octyl may be another indication of its improved packing as PDI-hexhep has a fluorescence lifetime that is more similar to that in solution ( $\tau_{EXC} = 4.5$  ns).<sup>4</sup>

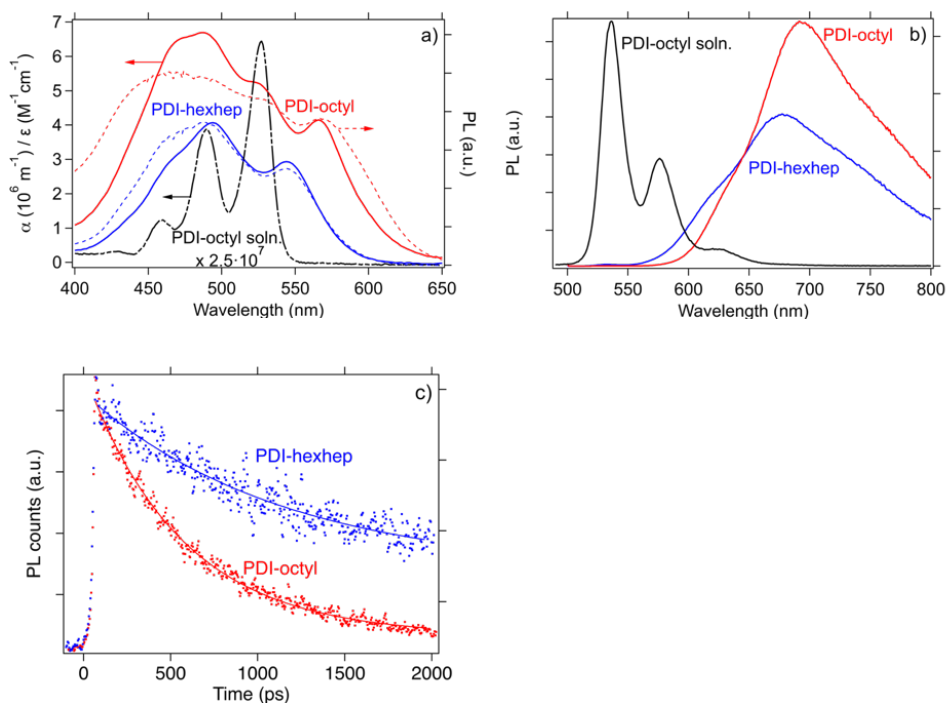


Figure 2.5: a) Absorption spectra ( $\alpha$  on left axis) and fluorescence excitation spectra (right axis) of PDI-octyl and PDI-hexhep films and b) emission spectra thin films. The absorption ( $\epsilon$  on left axis) and emission spectra of PDI-octyl in  $1 \cdot 10^{-5}$  M  $\text{CHCl}_3$  solution has also been added in blue. c) Fluorescence decays of annealed thin films of PDI-octyl (emission at 687 nm) and PDI-hexhep (emission at 630 nm) (dots) upon 460 nm photoexcitation (300  $\mu\text{W}$ ) and their monoexponential fit (solid lines).

In Figure 2.6 we show the effect of the substrate on the PDI absorption. For unannealed PDI-octyl on  $\text{TiO}_2$  we observe absorption features that are more similar to those in solution. In contrast, the optical absorption of PDI-hexhep lacks a strong substrate dependence shown in Figure 2.6b. The effect on PDI-octyl may be explained by the rougher  $\text{TiO}_2$  topology and/or different interfacial tension that negatively affects close packing, although no strong differences are observed in domain sizes. Since PDI-hexhep did not display strong aggregation on fused silica, the difference with  $\text{TiO}_2$  may be expected to be smaller. XRD measurements confirm that aggregates of PDI-octyl and PDI-hexhep are formed to the same extent on both substrate types with identical crystal phase (Figure A.5). We therefore expect little effect of the substrate on the charge carrier and exciton



transport properties.

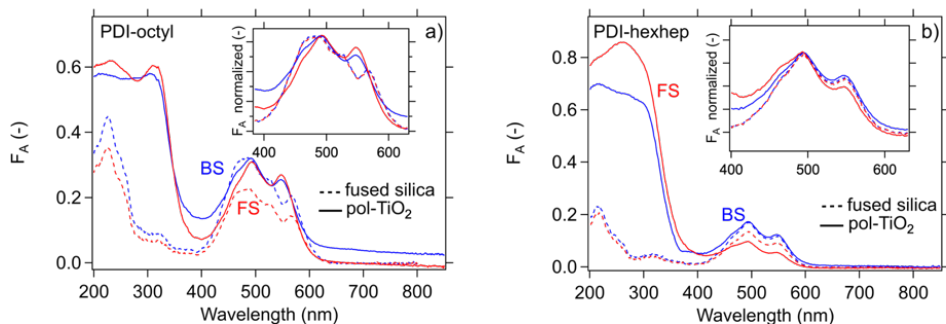


Figure 2.6: a) Absorbance spectra of unannealed 50 nm PDI-octyl thin film on uncoated fused silica and  $\text{TiO}_2$  and b) a similar plot for a 50 nm PDI-hexhep thin film upon front side (FS) and back side excitation (BS). The insets show the absorbance spectra normalized to the absorption maximum at around 490 nm. They show the difference and spectral similarity for PDI-octyl and PDI-hexhep, respectively.

### EXCITON DIFFUSION IN PDI/ZnPC PLANAR HETEROJUNCTIONS

In order to gain insight in the diffusion of excitons in PDI-octyl and PDI-hexhep we have performed TRMC photoconductivity measurements as shown in Figure 2.7a. In Figure 2.7a the photoconductance transients obtained upon photoexciting bilayers of PDI-octyl/ZnPc and PDI-hexhep/ZnPc (50/30 nm) are compared with the photoconductance of the PDI-octyl and ZnPc layers. There is negligible photoconductivity in these single layers. However, the photoconductance maximum increases by a factor forty and four upon forming the PDI-octyl/ZnPc and PDI-hexhep/ZnPc bilayers, respectively. This can be explained by considering the energy diagram shown in Figure 2.1. The energy difference between the LUMO of ZnPc and PDI is 0.3 eV and that between the HOMO of ZnPc and PDI is 0.19 eV. The LUMO offset is significantly larger than the typical binding energy of singlet excitons in organic solids (0.06 eV).<sup>52,53</sup> Therefore all singlet excitons reaching the interface will dissociate, which cannot happen in a single layer structure. However, the 0.3 eV offset is likely not enough for triplet excitons to charge separate as their binding energy is higher than that of singlets due to the exchange energy.<sup>14,53</sup>

The charge carrier lifetime exceeds a microsecond. We fit the bilayer transients using the triexponential decay function described in equation 2.9 represented by the solid lines in Figure 2.7a. The photoconductance prior to electron-hole recombination  $\Delta G_0$  and carrier kinetics obtained from the fitting are provided in Table A.3 and are comparable to values found in an earlier TRMC study on thin film bulk heterojunction systems of soluble PDIs and copper phthalocyanine.<sup>25</sup> Using equation 2.10,  $\Delta G_0$  is converted to  $\eta_0 \Sigma \mu$  and shown in Figure 2.7b as function of the incident photon fluence  $I_0$ . We observe a fluence independent photoconductance regime below an  $I_0$  of  $2 \cdot 10^{12}$  photons/cm<sup>2</sup> for PDI-octyl, while due to the low signal-to-noise ratio in the PDI-hexhep/ZnPc bilayer it was not possible to measure photoconductivity below  $1 \cdot 10^{13}$  photons/cm<sup>2</sup>. The low photoconductivity of the PDI-hexhep/ZnPc bilayer may be due to a low charge carrier mobility and/or charge separation yield. We observe a decrease in photoconductance for both bilayers at fluences that are higher than  $2 \cdot 10^{12}$  photons/cm<sup>2</sup> that we attribute

to second-order charge recombination<sup>40</sup> which we kept to a minimum during our measurements. The low photoconductivity in the single layers is caused by negligible exciton dissociation and therefore a low yield of free and mobile charge carriers. However, in the bilayer heterojunction the charges can separate at the ZnPc-PDI interface between ZnPc and PDI. In this situation, the hole localizes in the ZnPc and the electron in the PDI. Possible reasons for the higher photoconductivity of the PDI-octyl bilayer than the PDI-hexhep bilayer are a higher PDI-octyl electron mobility and a higher yield of free and mobile charge carriers upon photon absorption. The tenfold higher charge carrier mobility of PDI-octyl found in the pulse radiolysis measurements described above is in agreement with this difference in the photoconductivity.

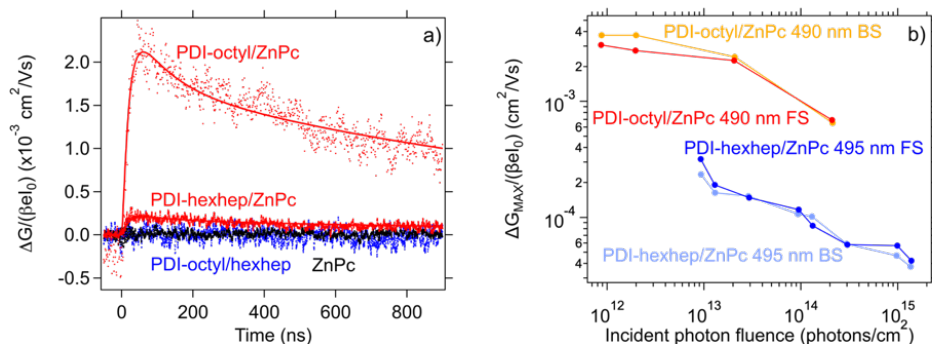


Figure 2.7: a) Photoconductance transients are shown for a 50 nm PDI and 30 nm ZnPc single film and 50/30 nm bilayer at an incident photon fluence of  $1 \cdot 10^{13}$  -  $1 \cdot 10^{14}$  photons/cm<sup>2</sup> upon 490/495 nm excitation for both PDI-octyl and PDI-hexhep (dots). The solid lines represent the tri-exponential function of equation 9 that is applied to fit the transients. b) The photon fluence dependence of  $\eta_0 \Sigma \mu$  is represented for a 50/30 nm PDI-octyl/ZnPc (490 nm) and PDI-hexhep/ZnPc bilayer (495 nm) upon FS and BS excitation.

In Figure 2.8a we show  $\eta_0 \Sigma \mu$  in the fluence independent photoconductance regime of the PDI-octyl/ZnPc bilayers as function of PDI film thickness. Upon front side illumination at 490 nm we observe an increasing  $\eta_0 \Sigma \mu$  that saturates at 100 nm. In contrast, upon back side bilayer illumination  $\eta_0 \Sigma \mu$  reaches a maximum at 50 nm and decreases at higher PDI thicknesses. We explain these trends as follows using the schematic representation shown in Figure 2.8b. Upon front side (FS) illumination, light is absorbed by both the ZnPc (30 nm thickness) and the PDI where excitons are generated in both materials thus contributing to the photoconductance. These excitons form charge transfer excitons that dissociate at the interface by transferring electrons to the PDI (LUMO offset 0.3 eV) and holes to the ZnPc (HOMO offset 0.19 eV) that are responsible for the photoconductance.<sup>54</sup> As the PDI thickness increases, more excitons are created and  $\eta_0 \Sigma \mu$  increases. At a PDI thickness of 50 nm the linear trend in photoconductance as function of PDI thickness becomes sublinear as only a fraction of the excitons created beyond 50 nm is capable of diffusing towards the interface and charge separate while the rest of these excitons undergo recombination. Therefore, the gain in free charge carriers diminishes upon increasing the PDI thickness and the photoconductance trend saturates. Consequently, the exciton diffusion length plays a pivotal role in the observed photoconductive behaviour. Moreover, when the PDI excitons are primarily generated

near the PDI/substrate interface, most excitons need to diffuse to the heterojunction interface in order to charge separate. Indeed, upon back side (BS) illumination the photoconductance follows a similar trend as in FS illumination up until 50 nm where exciton diffusion is not limiting the charge carrier yield. Beyond this length a decreasing amount of PDI excitons reach the PDI/ZnPc interface and less excitons are generated within the ZnPc such that that  $\eta_0 \Sigma \mu$  decreases beyond 50 nm and eventually reduces to zero. We fit the data points in Figure 2.8 with the exciton model described by equations 2.11 and A.2- A.3 and find  $\phi_{CS} \Sigma \mu = 0.0152 \text{ cm}^2/\text{Vs}$  and  $\Lambda_{EXC} = 59.91 \text{ nm}$  for PDI-octyl using  $\alpha = 7.96 \cdot 10^6 \text{ m}^2$  (at 490 nm). If we assume a unity yield of charge separation,  $\phi_{CS}$ , then the charge carrier mobility  $\Sigma \mu$  in the thin film would be a factor fifty lower than in the powder as determined from PR-TRMC. However, a unity  $\phi_{CS}$  is unlikely since exciton recombination and geminate interfacial charge recombination are likely to happen. Selective excitation of ZnPc in the PDI-octyl/ZnPc show similar  $\eta_0 \Sigma \mu$  trends and values as PDI excitation close to the interface. The similarity in  $\eta_0 \Sigma \mu$  values points to equal charge separation efficiency when exciting either ZnPc or PDI. We did not carry out the diffusion length determination for PDI-hexhep due to the low signal-to-noise ratio in the PDI-hexhep bilayers.

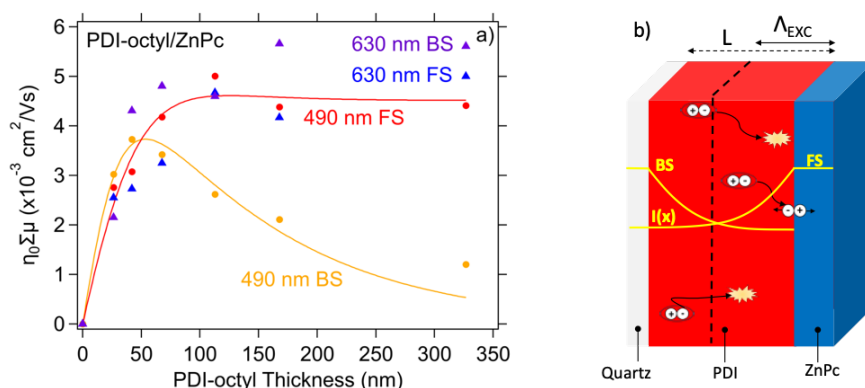


Figure 2.8: a)  $\eta_0 \Sigma \mu$  values as function of PDI thickness of PDI-octyl/ZnPc bilayers (fixed ZnPc thickness of 30 nm). The data are shown for all excitation conditions together with a fit obtained after applying the exciton diffusion model. b) Schematic representation of the planar heterojunction samples on fused silica. The samples are photo excited with laser pulses from the front side (FS) or back side (BS). The yellow profile represents the PDI excitation profile  $I(x)$  in the sample and depends on the absorption coefficient. Excitons created further away from the heterojunction interface have to diffuse to the interface via exciton hopping. During diffusion they can recombine, process that limits their lifetime and diffusion length  $\Lambda_{EXC}$ .

### EXCITON DIFFUSION IN $\text{TiO}_2$ /PDI PLANAR HETEROJUNCTIONS

In order to examine a possible relationship between substrate and PDI supramolecular packing and exciton diffusion length, we deposit the PDIs on polycrystalline  $\text{TiO}_2$  coated fused silica.  $\text{TiO}_2$  forms a functional inorganic/organic heterojunction with PDI, where PDI acts as electron donor and injects electrons into the  $\text{TiO}_2$  conduction band upon photoexcitation and is used to study the exciton diffusion length in the same manner as in the PDI/ZnPc bilayers. However, the added benefit of using  $\text{TiO}_2$  over ZnPc is the higher  $\text{TiO}_2$  electron mobility ( $\mu_{e^-} = 1 \text{ cm}^2/\text{Vs}$ ) and long charge carrier lifetime ( $\mu\text{s}-\text{ms}$ )<sup>55</sup>

that is beneficial for the photoconductivity. In Figures 2.9a (2.9b) and 2.9c (2.9d) we show the photoconductance transients for single layered films of TiO<sub>2</sub>, PDI-octyl (-hexhep) and a TiO<sub>2</sub>/PDI-octyl (-hexhep) bilayer, respectively, upon selectively photoexciting the PDI. We observe a tenfold and six-fold increase in peak photoconductivity upon combining TiO<sub>2</sub> and PDI-octyl and PDI-hexhep when compared to that of the single layer films. In Figures 2.9b and 2.9d we show the action spectrum for the TiO<sub>2</sub>/PDI-octyl and TiO<sub>2</sub>/PDI-hexhep bilayer, respectively. The action spectrum contains values for  $\eta\Sigma\mu$  as function of excitation wavelength and is plotted together with the bilayer absorbance spectrum. Since TiO<sub>2</sub> is a wide bandgap semiconductor its absorption in the visible part of the spectrum is negligible such that PDI is the primary absorbing species. A minor absorption by TiO<sub>2</sub> intrabandgap states occurs in the visible. The photoconductivity of TiO<sub>2</sub> due to intrabandgap state absorption can be measured and it is subtracted from that of the bilayer response as detailed elsewhere.<sup>55</sup> The bilayer photoconductivity is higher when light enters the sample at the heterojunction interface (BS) compared to when it enters the sample at the PDI-air interface (FS). Furthermore, the trend displayed  $\eta\Sigma\mu$  as function of excitation wavelength matches that of the absorption spectrum when the bilayer is excited near the heterojunction interface. We attribute this agreement to selective PDI excitation and subsequent charge separation and electron injection at the TiO<sub>2</sub>/PDI interface. The mismatch in trend between  $\eta\Sigma\mu$  and absorbance can be explained by a relatively lower number of injected electrons in TiO<sub>2</sub> since the majority of the excitons have decayed due to the limited exciton diffusion length as we described for the PDI/ZnPc bilayers. We apply the same exciton diffusion model used to model the PDI/ZnPc bilayers described by equations 2.11 and A.2-A.3 to estimate an exciton diffusion length for PDI-octyl and PDI-hexhep of which we outline the procedure in the Supplementary Information. For PDI-octyl we obtain  $\phi_{CS}\Sigma\mu = 0.04 \text{ cm}^2/\text{Vs}$  and  $\Lambda_{EXC} = 48.05 \text{ nm}$  and for PDI-hexhep a  $\phi_{CS}\Sigma\mu = 0.064 \text{ cm}^2/\text{Vs}$  and  $\Lambda_{EXC} = 19.6 \text{ nm}$ . In the model we fixed  $L$  ( $L = 100 \text{ nm}$  for PDI-octyl and  $L = 30 \text{ nm}$  for PDI-hexhep). The fit parameters together with the charge carrier mobilities and exciton diffusion length from the PDI-octyl/ZnPc bilayer are listed in Table 2.1.

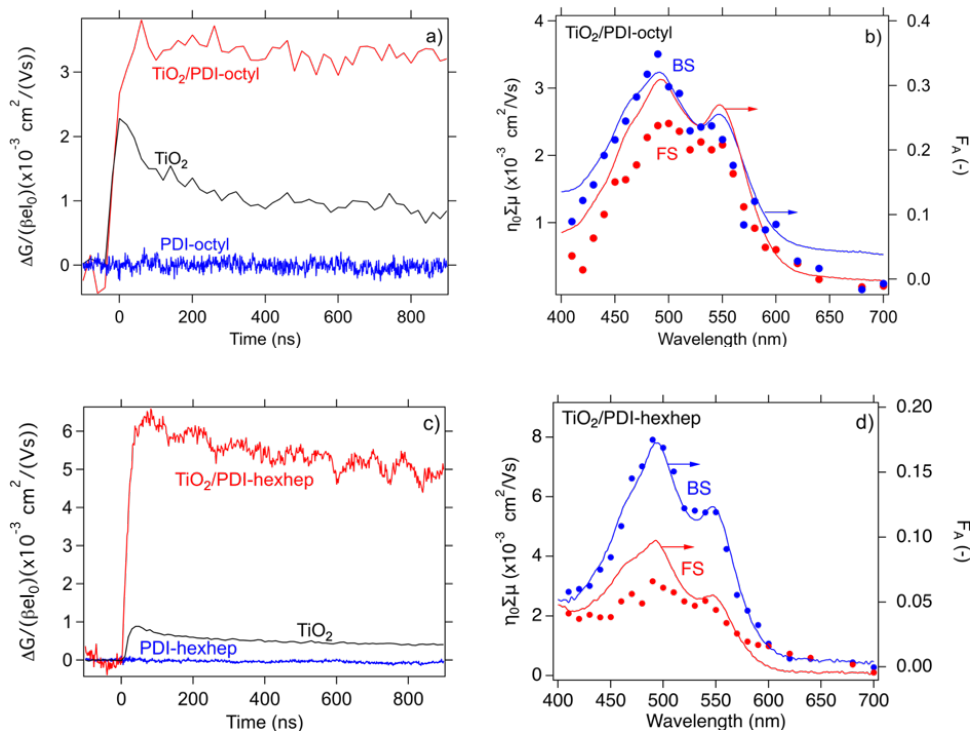


Figure 2.9: a) Photoconductivity transients of a single layer film of pol-TiO<sub>2</sub>, PDI-octyl (50 nm) and a TiO<sub>2</sub>/PDI-octyl (50 nm) bilayer at  $I_0 = 2.3 \cdot 10^{12}$  photons/cm<sup>2</sup> upon BS excitation. b) Action spectrum of  $\eta_0 \Sigma \mu$  and attenuation spectrum vs. excitation wavelength for the TiO<sub>2</sub>/PDI-octyl (50 nm) bilayer. c) Photoconductivity transients for a single layer film of pol-TiO<sub>2</sub> and PDI-hexhep (38 nm) and a TiO<sub>2</sub>/PDI-hexhep (38 nm) bilayer at  $I_0 = 2.3 \cdot 10^{12}$  photons/cm<sup>2</sup> upon BS excitation. Similar to b), d) contains the action spectrum for the TiO<sub>2</sub>/PDI-hexhep (38 nm) bilayer.

We use the TiO<sub>2</sub> film specific electron mobility to calculate an incident photon to charge separation efficiency  $\phi_{CS}$  of 0.64% and 3.5% for PDI-octyl and PDI-hexhep, respectively, averaged over front- and backside excitation. These efficiencies are similar to those found for electron injection from porphyrins into TiO<sub>2</sub> using the same experimental setup. The relatively low  $\phi_{CS}$  values can be due to various loss mechanisms.<sup>43,44</sup> The first is inefficient coupling between the organic materials and the TiO<sub>2</sub> layer because of strong crystallization of PDI, possibly resulting in a barrier of alkyl chains at the interface.<sup>56</sup> This small resulting injection rate gives dominance to alternative decay processes in the PDI. Additionally, if charge injection is followed by fast recombination at the interface, this results in a reduced observed  $\phi_{CS}$ . The mobility of charges in TiO<sub>2</sub> is not affected by these processes and has been independently determined as discussed in the Supporting Information. The magnitude of  $\Lambda_{EXC}$  of PDI-octyl that we find for the PDI-octyl/ZnPc and TiO<sub>2</sub>/PDI-octyl heterojunction is very similar (< 10% difference), indicating that the intrinsic  $\Lambda_{EXC}$  is specific for the material and not affected by the interface. This observation is notable considering the difference in aggregate size in the two systems. One would expect a larger diffusion length for larger domain size as the

limiting step in the transport is likely to be the inter-domain hopping. If the distance between interdomain hops decreases a larger overall diffusion length would be expected. Interestingly, in this case such a difference is not observed, indicating that inter-domain transport is not limiting transport in this case.<sup>57,58</sup>

One estimate for the singlet exciton diffusion coefficient  $D_{EXC}$  can be obtained using equation 2.12 and assuming pure singlet character transport of our excitons. In this calculation we use our estimate of the exciton diffusion length and exciton lifetime ( $\tau_{EXC} = 550$  ps and 1.13 ns for PDI-octyl and PDI-hexhep, see Figure 2.5c) of the thin film, resulting in  $D_{EXC} = 6.47 \cdot 10^{-2} - 7.04 \cdot 10^{-2}$  cm<sup>2</sup>/s and  $D_{EXC} = 2.87 \cdot 10^{-3}$  cm<sup>2</sup>/s for PDI-octyl and PDI-hexhep, respectively. Using the Einstein-Smoluchowski relation (equation 2.6) and mobility values from the TRMC measurements on PDI powders we estimate a charge carrier diffusion coefficient  $D_{CHARGE} = 8.23 \cdot 10^{-3}$  cm<sup>2</sup>/s and  $D_{CHARGE} = 5.14 \cdot 10^{-4}$  cm<sup>2</sup>/s for PDI-octyl and PDI-hexhep, respectively. The ratio of these two charge carrier diffusion coefficients is 16, which is similar to the ratio of the exciton diffusion coefficients discussed above (22.6). If the exciton diffusion is governed by the Förster mechanism a smaller dependence on distance would be expected. A relevant aspect here is the partial triplet character of the excitons as shown by transient absorption studies that confirm the presence of singlet fission in PDI-octyl.<sup>4,6</sup> The triplet character results in much longer exciton lifetimes than for pure singlet species, and the Dexter transfer mechanism for triplets can be considered as a double electron transfer process, making it similar to electron and hole transfer. However, this particular study did not involve in the discrimination of these contributions and conclude that the studied excitons are singlets with possibly a certain amount triplet contribution.

Table 2.1: Charge carrier and exciton diffusion parameters for PDI-octyl and -hexhep as obtained from analysis of PR- and FP-TRMC experiments.  $\phi_{CS}\Sigma\mu$  and  $\Lambda_{EXC}$  were obtained upon application of the exciton diffusion model described by equations 2.11, A.2-A.3 and A.4-A.5.

	$\Sigma\mu lD$ (cm <sup>2</sup> /vs)	$\alpha$ (m <sup>2</sup> )	PDI/ZnPc		TiO <sub>2</sub> /PDI		
			$\phi_{CS}\Sigma\mu$ (cm <sup>2</sup> /vs)	$\Lambda_{EXC}$ (nm)	$\phi_{CS}\Sigma\mu$ (cm <sup>2</sup> /vs)	$\phi_{CS*}$ (%)	$\Lambda_{EXC}$ (nm)
<b>PDI-octyl</b>	0.32	7.96·10 <sup>6</sup>	1.5·10 <sup>-2</sup>	59.90	FS 1.3·10 <sup>-2</sup> BS 1.5·10 <sup>-2</sup> avg.1.4·10 <sup>-2</sup>	FS 0.55 BS 0.73 avg. 0.64	FS 64 BS 61 avg. 62.5
<b>PDI-hexhep</b>	0.02	4.40·10 <sup>6</sup>	-	-	FS 6.6·10 <sup>-2</sup> BS 8.3·10 <sup>-2</sup> avg.7.4·10 <sup>-2</sup>	FS 3.1 BS 3.9 avg. 3.5	FS 18 BS 18 avg. 18

\* $\mu_e = 2.24$  and  $2.14$  cm<sup>2</sup>/Vs for TiO<sub>2</sub>/PDI-octyl and TiO<sub>2</sub>/PDI-hexhep, respectively.

## 2.4. CONCLUSIONS

In this study we investigated the effect of imid substitution in PDIs on their solid-state packing and opto-electronic properties. We found a strong influence of the imid substituent on the intermolecular packing of the molecules in the solid-state. The variation in side-chain substitution affected the extent of crystallization in the powder, but is less significant in vacuum deposited thin films. In these films, macromolecular organization forming fibrous structures occurred for both PDIs. However, an order of magnitude difference in charge carrier mobility was found that can be related to differences in electronic coupling values. We measured an order of magnitude difference in maximum photoconductance  $\Delta G_{MAX}/\beta e I_0$  in bilayer heterojunctions of PDI-octyl/ZnPc and PDI-hexhep/ZnPc, owing to the difference in intrinsic charge carrier mobility and lower exciton diffusion length. Using TRMC measurements on PDI/ZnPc heterojunctions with different PDI-octyl thicknesses, we could determine an exciton diffusion length of 60 nm that agrees with earlier found values for related PDIs and structures. Using TiO<sub>2</sub> as underlayer for the PDI film instead of fused silica did not strongly affect solid-state packing for the PDIs. Using TiO<sub>2</sub> we determined a singlet exciton diffusion length of 18 nm for PDI-hexhep which is a factor three lower than observed for PDI-octyl and confirmed the same exciton diffusion length for PDI-octyl found from the study on the PDI/ZnPc bilayer. The charge separation efficiencies for PDI-octyl and PDI-hexhep are 0.64 and 3.5%. This study serves to show how different molecular packings of electronically similar molecules can lead to strong differences in charge carrier mobilities, while having a surprisingly small effect on the exciton diffusion length. These results offer a complete view of intrinsic organic chromophore properties relevant to opto-electronic devices.

## REFERENCES

- (1) Herbst, W.; Hunger, K., *Industrial organic pigments: production, properties, applications*; John Wiley and Sons: 2006.
- (2) Würthner, F.; Saha-Möller, C. R.; Fimmel, B.; Ogi, S.; Leowanawat, P.; Schmidt, D. Perylene bisimide dye assemblies as archetype functional supramolecular materials. *Chem. Rev.* **2015**, *116*, 962–1052.
- (3) Zhang, G.; Zhao, J.; Chow, P. C.; Jiang, K.; Zhang, J.; Zhu, Z.; Zhang, J.; Huang, F.; Yan, H. Nonfullerene acceptor molecules for bulk heterojunction organic solar cells. *Chem. Rev.* **2018**, *118*, 3447–3507.
- (4) Aulin, Y. V.; Felter, K. M.; Günbas, D.; Dubey, R. K.; Jager, W. F.; Grozema, F. Morphology independent efficient singlet exciton fission in perylenediimide thin films. *ChemPlusChem* **2018**, *83*, 230–238.
- (5) Eaton, S. W.; Shoer, L. E.; Karlen, S. D.; Dyar, S. M.; Margulies, E. A.; Veldkamp, B. S.; Ramanan, C.; Hartzler, D. A.; Savikhin, S.; Marks, T. J. Singlet exciton fission in polycrystalline thin films of a slip-stacked perylenediimide. *J. Am. Chem. Soc.* **2013**, *135*, 14701–14712.
- (6) Le, A. K.; Bender, J. A.; Arias, D. H.; Cotton, D. E.; Johnson, J. C.; Roberts, S. T. Singlet Fission Involves an Interplay Between Energetic Driving Force and Electronic Coupling in Perylenediimide Films. *J. Am. Chem. Soc.* **2017**.
- (7) Singh-Rachford, T. N.; Nayak, A.; Muro-Small, M. L.; Goeb, S.; Therien, M. J.; Castellano, F. N. Supermolecular-chromophore-sensitized near-infrared-to-visible photon upconversion. *J. Am. Chem. Soc.* **2010**, *132*, 14203–14211.
- (8) Deng, F.; Sommer, J. R.; Myahkostupov, M.; Schanze, K. S.; Castellano, F. N. Near-IR phosphorescent metalloporphyrin as a photochemical upconversion sensitizer. *Chem. Commun.* **2013**, *49*, 7406–7408.
- (9) Adams, D. M.; Kerimo, J.; O'Connor, D. B.; Barbara, P. F. Spatial imaging of singlet energy migration in perylene bis(phenethylimide) thin films. *J. Phys. Chem. A* **1999**, *103*, 10138–10143.
- (10) Gregg, B. A.; Sprague, J.; Peterson, M. W. Long-range singlet energy transfer in perylene bis(phenethylimide) films. *J. Phys. Chem. B* **1997**, *101*, 5362–5369.
- (11) Lin, H.; Camacho, R.; Tian, Y.; Kaiser, T. E.; Würthner, F.; Scheblykin, I. G. Collective fluorescence blinking in linear J-aggregates assisted by long-distance exciton migration. *Nano Lett.* **2009**, *10*, 620–626.
- (12) Marciniak, H.; Li, X.-Q.; Würthner, F.; Lochbrunner, S. One-dimensional exciton diffusion in perylene bisimide aggregates. *J. Phys. Chem. A* **2010**, *115*, 648–654.
- (13) Lunt, R. R.; Benziger, J. B.; Forrest, S. R. Relationship between crystalline order and exciton diffusion length in molecular organic semiconductors. *Adv. Mater.* **2010**, *22*, 1233–1236.
- (14) Mikhnenko, O. V.; Blom, P. W. M.; Nguyen, T.-Q. Exciton diffusion in organic semiconductors. *Energ. Environ. Sci.* **2015**, *8*, 1867–1888.



- (15) Delgado, M. C. R.; Kim, E.-G.; Filho, D. A. d. S.; Bredas, J.-L. Tuning the charge-transport parameters of perylene diimide single crystals via end and/or core functionalization: a density functional theory investigation. *J. Am. Chem. Soc.* **2010**, *132*, 3375–3387.
- (16) Vura-Weis, J.; Ratner, M. A.; Wasielewski, M. R. Geometry and Electronic Coupling in Perylenediimide Stacks: Mapping Structure-Charge Transport Relationships. *J. Am. Chem. Soc.* **2010**, *132*, 1738–1739.
- (17) Marcon, V.; Breiby, D. W.; Pisula, W.; Dahl, J.; Kirkpatrick, J.; Patwardhan, S.; Grozema, F.; Andrienko, D. Understanding structure- mobility relations for perylene tetracarboxydiimide derivatives. *J. Am. Chem. Soc.* **2009**, *131*, 11426–11432.
- (18) May, F.; Marcon, V.; Hansen, M. R.; Grozema, F.; Andrienko, D. Relationship between supramolecular assembly and charge-carrier mobility in perylenediimide derivatives: The impact of side chains. *J. Mater. Chem.* **2011**, *21*, 9538–9545.
- (19) Tatemichi, S.; Ichikawa, M.; Koyama, T.; Taniguchi, Y. High mobility n-type thin-film transistors based on N, N'-ditridecyl perylene diimide with thermal treatments. *Appl. Phys. Lett.* **2006**, *89*, 112108.
- (20) Briseno, A. L.; Mannsfeld, S. C.; Reese, C.; Hancock, J. M.; Xiong, Y.; Jenekhe, S. A.; Bao, Z.; Xia, Y. Perylenediimide nanowires and their use in fabricating field-effect transistors and complementary inverters. *Nano Lett.* **2007**, *7*, 2847–2853.
- (21) Chesterfield, R. J.; McKeen, J. C.; Newman, C. R.; Frisbie, C. D.; Ewbank, P. C.; Mann, K. R.; Miller, L. L. Variable temperature film and contact resistance measurements on operating n-channel organic thin film transistors. *J. Appl. Phys.* **2004**, *95*, 6396–6405.
- (22) Mirjani, F.; Renaud, N.; Gorczak, N.; Grozema, F. C. Theoretical investigation of singlet fission in molecular dimers: the role of charge transfer states and quantum interference. *J. Phys. Chem. C* **2014**, *118*, 14192–14199.
- (23) Rao, A.; Friend, R. H. Harnessing singlet exciton fission to break the Shockley–Queisser limit. *Nat. Rev. Mater.* **2017**, *2*, 17063.
- (24) Einzinger, M.; Wu, T.; Kompalla, J. F.; Smith, H. L.; Perkinson, C. F.; Nienhaus, L.; Wieghold, S.; Congreve, D. N.; Kahn, A.; Bawendi, M. G. Sensitization of silicon by singlet exciton fission in tetracene. *Nature* **2019**, *571*, 90.
- (25) Günbaş, D. D.; Xue, C.; Patwardhan, S.; Fravventura, M. C.; Zhang, H.; Jager, W. F.; Sudhölter, E. J.; Siebbeles, L. D.; Savenije, T. J.; Jin, S. High charge carrier mobility and efficient charge separation in highly soluble perylenetetracarboxyl-diimides. *Chem. Commun.* **2014**, *50*, 4955–4958.
- (26) Ghosh, S.; Li, X.; Stepanenko, V.; Würthner, F. Control of H- and J-Type  $\pi$  Stacking by Peripheral Alkyl Chains and Self-Sorting Phenomena in Perylene Bisimide *Homo- and Heteroaggregates*. *Chemistry* **2008**, *14*, 11343–11357.
- (27) Chen, Z.; Stepanenko, V.; Dehm, V.; Prins, P.; Siebbeles, L. D. A.; Seibt, J.; Marquetand, P.; Engel, V.; Würthner, F. Photoluminescence and Conductivity of Self-Assembled  $\pi$ - $\pi$  Stacks of Perylene Bisimide Dyes. *Chemistry* **2007**, *13*, 436–449.
- (28) Chen, S.; Slattum, P.; Wang, C.; Zang, L. Self-assembly of perylene imide molecules into 1D nanostructures: methods, morphologies, and applications. *Chem. Rev.* **2015**, *115*, 11967–11998.

- (29) O'Brien, D. B.; Anglin, T. C.; Massari, A. M. Surface chemistry and annealing-driven interfacial changes in organic semiconducting thin films on silica surfaces. *Langmuir* **2011**, *27*, 13940–13949.
- (30) Kish, E. R.; Nahm, R. K.; Woll, A. R.; Engstrom, J. R. When the sequence of thin film deposition matters: Examination of organic-on-organic heterostructure formation using molecular beam techniques and in situ real time x-ray synchrotron radiation. *J. Phys. Chem. C* **2016**, *120*, 6165–6179.
- (31) Krauss, T. N.; Barrera, E.; de Oteyza, D. G.; Zhang, X. N.; Major, J.; Dehm, V.; Würthner, F.; Dosch, H. X-ray/atomic force microscopy study of the temperature-dependent multilayer structure of PTCDI-C8 films on SiO<sub>2</sub>. *J. Phys. Chem. C* **2009**, *113*, 4502–4506.
- (32) Duff, J.; Hor, A.-M.; Melnyk, A. R.; Teney, D. Spectral response and xerographic electrical characteristics of some perylene bisimide pigments. *Proc. SPIE* **1990**, *1253*, 183.
- (33) Warman, J. M.; de Haas, M. P.; Dicker, G.; Grozema, F. C.; Piris, J.; Debije, M. G. Charge mobilities in organic semiconducting materials determined by pulse-radiolysis time-resolved microwave conductivity:  $\pi$ -bond-conjugated polymers versus  $\pi$ - $\pi$ -stacked discotics. *Chem. Mater.* **2004**, *16*, 4600–4609.
- (34) Warman, J. M.; Gelinck, G. H.; de Haas, M. P. The mobility and relaxation kinetics of charge carriers in molecular materials studied by means of pulse-radiolysis time-resolved microwave conductivity: dialkoxy-substituted phenylene-vinylene polymers. *J. Phys.-Condens. Mat.* **2002**, *14*, 9935.
- (35) Marcus, R. A.; Sutin, N. Electron transfers in chemistry and biology. *Biochim. Biophys. Acta* **1985**, *811*, 265–322.
- (36) Mikkelsen, K. V.; Ratner, M. A. Electron tunneling in solid-state electron-transfer reactions. *Chem. Rev.* **1987**, *87*, 113–153.
- (37) England, S. J.; Kathirgamanathan, P.; Rosseinsky, D. R. Perturbation calculation from the charge-transfer spectrum data of intervalence site-transfer DC conductivity in Prussian Blue. *J. Chem. Soc. Chem. Comm.* **1980**, 840–841.
- (38) De Haas, M. P.; Warman, J. M. Photon-induced molecular charge separation studied by nanosecond time-resolved microwave conductivity. *Chem. Phys.* **1982**, *73*, 35–53.
- (39) Infelta, P. P.; De Haas, M. P.; Warman, J. M. The study of the transient conductivity of pulse irradiated dielectric liquids on a nanosecond timescale using microwaves. *Radiat. Phys. Chem.* **1977**, *10*, 353–365.
- (40) Savenije, T. J.; Ferguson, A. J.; Kopidakis, N.; Rumbles, G. Revealing the dynamics of charge carriers in polymer: fullerene blends using photoinduced time-resolved microwave conductivity. *J. Phys. Chem. C* **2013**, *117*, 24085–24103.
- (41) Fravventura, M. C.; Hwang, J.; Suijkerbuijk, J. W.; Erk, P.; Siebbeles, L. D.; Savenije, T. J. Determination of singlet exciton diffusion length in thin evaporated C60 films for photovoltaics. *J. Phys. Chem. Lett.* **2012**, *3*, 2367–2373.
- (42) Kroeze, J. E.; Savenije, T. J.; Vermeulen, M. J. W.; Warman, J. M. Contactless determination of the photoconductivity action spectrum, exciton diffusion length, and charge separation efficiency in polythiophene-sensitized TiO<sub>2</sub> bilayers. *J. Phys. Chem. B* **2003**, *107*, 7696–7705.

- (43) Huijser, A.; Savenije, T. J.; Kroeze, J. E.; Siebbeles, L. D. Exciton Diffusion and Interfacial Charge Separation in *m* *eso*-Tetraphenylporphyrin/TiO<sub>2</sub> Bilayers: Effect of Ethyl Substituents. *J. Phys. Chem. B* **2005**, *109*, 20166–20173.
- (44) Huijser, A.; Suijkerbuijk, B. M. J. M.; Klein Gebbink, R. J. M.; Savenije, T. J.; Siebbeles, L. D. A. Efficient exciton transport in layers of self-assembled porphyrin derivatives. *J. Am. Chem. Soc.* **2008**, *130*, 2485–2492.
- (45) Sergeev, S.; Pisula, W.; Geerts, Y. H. Discotic liquid crystals: a new generation of organic semiconductors. *Chem. Soc. Rev.* **2007**, *36*, 1902–1929.
- (46) Jones, B. A.; Facchetti, A.; Wasielewski, M. R.; Marks, T. J. Tuning orbital energetics in arylene diimide semiconductors. Materials design for ambient stability of n-type charge transport. *J. Am. Chem. Soc.* **2007**, *129*, 15259–15278.
- (47) Gregg, B. A. Evolution of photophysical and photovoltaic properties of perylene bis (phenethylimide) films upon solvent vapor annealing. *J. Phys. Chem.* **1996**, *100*, 852–859.
- (48) Balakrishnan, K.; Datar, A.; Naddo, T.; Huang, J.; Oitker, R.; Yen, M.; Zhao, J.; Zang, L. Effect of side-chain substituents on self-assembly of perylene diimide molecules: morphology control. *J. Am. Chem. Soc.* **2006**, *128*, 7390–7398.
- (49) Kaufmann, C.; Kim, W.; Nowak-Król, A.; Hong, Y.; Kim, D.; Würthner, F. Ultrafast exciton delocalization, localization, and excimer formation dynamics in a highly defined perylene bisimide quadruple  $\pi$ -stack. *J. Am. Chem. Soc.* **2018**, *140*, 4253–4258.
- (50) Margulies, E. A.; Shoer, L. E.; Eaton, S. W.; Wasielewski, M. R. Excimer formation in cofacial and slip-stacked perylene-3, 4: 9, 10-bis (dicarboximide) dimers on a redox-inactive triptycene scaffold. *Phys. Chem. Chem. Phys.* **2014**, *16*, 23735–23742.
- (51) Felter, K. M.; Dubey, R. K.; Grozema, F. C. Relation between molecular packing and singlet fission in thin films of brominated perylenediimides. *J. Chem. Phys.* **2019**, *151*.
- (52) Rita Narayan, M.; Singh, J. Study of the mechanism and rate of exciton dissociation at the donor-acceptor interface in bulk-heterojunction organic solar cells. *J. Appl. Phys.* **2013**, *114*, 073510.
- (53) Singh, J.; Narayan, M.; Ompong, D.; Zhu, F. Dissociation of charge transfer excitons at the donor-acceptor interface in bulk heterojunction organic solar cells. *J. Mater. Sci.-Mater. El.* **2017**, *28*, 7095–7099.
- (54) Narayan, M.; Singh, J. Photovoltaic contribution of photo-generated excitons in acceptor material of organic solar cells. *J. Mater. Sci.-Mater. El.* **2017**, *28*, 7070–7076.
- (55) Kroeze, J. E.; Savenije, T. J.; Warman, J. M. Contactless determination of the efficiency of photo-induced charge separation in a porphyrin-TiO<sub>2</sub> bilayer. *J. Photoch. Photobio. A* **2002**, *148*, 49–55.
- (56) Adams, D. M.; Kerimo, J.; Olson, E. J.; Zaban, A.; Gregg, B. A.; Barbara, P. F. Spatially-resolving nanoscopic structure and excitonic-charge-transfer quenching in molecular semiconductor heterojunctions. *J. Am. Chem. Soc.* **1997**, *119*, 10608–10619.

- (57) Ye, T.; Singh, R.; Butt, H.-J.; Floudas, G.; Keivanidis, P. E. Effect of local and global structural order on the performance of perylene diimide excimeric solar cells. *ACS Appl. Mater. Inter.* **2013**, *5*, 11844–11857.
- (58) Singh, R.; Giussani, E.; Mróz, M. M.; Di Fonzo, E.; Fazzi, D.; Cabanillas-González, J.; Oldridge, L.; Vaenas, N.; Kontos, A. G.; Falaras, P. On the role of aggregation effects in the performance of perylene-diimide based solar cells. *Org. Electron.* **2014**, *15*, 1347–1361.



# 3

## RELATION BETWEEN MOLECULAR PACKING AND SINGLET FISSION IN THIN FILMS OF BROMINATED PERYLENEDIIMIDES

*Perylene diimides (PDIs) are attractive chromophores that exhibit singlet exciton fission (SF) and have several advantages over traditional SF molecules such as tetracene and pentacene, however, their photophysical properties relating to SF have received only limited attention. In this study we explore how introduction of bulky bromine atoms in the so-called bay-area PDIs, resulting in a non-planar structure, affects the solid-state packing and efficiency of singlet fission. We found that changes in the molecular packing have a strong effect on the temperature dependent photoluminescence, expressed as an activation energy. These effects are explained in terms of excimer formation for PDIs without bay-area substitution, which competes with singlet fission. Introduction of bromine atoms in the bay-positions strongly disrupts the solid-state packing leading to strongly reduced excitonic interactions. Surprisingly, these relatively amorphous materials with weak electronic coupling exhibit stronger formation of triplet excited states by SF because the competing excimer formation is suppressed here. Furthermore, we showed that bromination does not increase intersystem crossing.*

---

This chapter is based on: Felter, K. M., Dubey, R. K., Grozema, F. C. (2019). *Relation between molecular packing and singlet fission in thin films of brominated perylenediimides*. The Journal of chemical physics, 151(9), 094301.

### 3.1. INTRODUCTION

Perylene diimides (see Figure 3.1) are exceptionally photo-stable conjugated organic dye molecules that are attractive for application in opto-electronic devices such as solar cells. Apart from their strong electron accepting nature and their favourable charge transport properties they have also been shown to exhibit singlet exciton fission (SF). SF is a spin-conserved process in which a singlet excited state shares its energy with a neighbouring molecule to form a doubly excited state that consists of two coupled triplet excited states.<sup>1-3</sup> In addition, it has also been shown to undergo the inverse process, triplet-triplet annihilation up-conversion.<sup>4</sup> SF is envisioned to be a viable approach to increase the power conversion efficiency of solar cells by using the excess energy in blue photons that is generally not used efficiently because of thermalization.<sup>5</sup> In order to fully exploit SF in photovoltaic applications, a fundamental understanding of the process is of prime importance. Specifically, as SF chromophores are generally applied in solid state devices, the relation between the dynamics of SF and the molecular packing and excited state energetics of the chromophores. The effect of molecular packing on singlet fission has previously been studied in acene chromophores. Theoretical<sup>6</sup> and experimental results have been reported for tetracene<sup>7</sup>, covalent dimers of pentacene<sup>8</sup> in solution and terrylene diimides<sup>9</sup>. The general conclusion from these studies is that SF rates and efficiencies can be optimized by optimizing the electronic coupling via the molecular organization in the solid state. Perylene diimides (PDIs) offer a unique opportunity to study the effect of molecular organization and energetics on singlet fission since variations in the substituents of the chromophore lead to changes in the solid state packing and excited state energetics. Computational and experimental studies have shown that changes in the molecular packing induced by imide-substituted PDIs indeed have a strong impact on the rate and efficiency of SF.<sup>3,10,11</sup> While the effect of imide-substitution of PDIs on their opto-electronic properties has been studied widely owing to the relatively accessible synthesis, only few studies exist on the impact of substitution on the bay area, especially in relation to SF. It has been shown that PDIs substituted with halogens in the bay area (see Figure 3.1) exhibit changes in the singlet and triplet state excited state energetics. This is due to the sterically induced twisting of the conjugated core of the PDI, as compared to their non-bay-area substituted analogues.<sup>12,13</sup> Moreover, bay-area substitution leads to greatly improved solubility in common organic solvents, which is a desirable characteristic for eventual device applications.

In this study we investigate how halogen substitution in the bay-area of PDIs affects the molecular packing and excitonic interactions in the solid state and how this affects the singlet fission dynamics in thin films of methyl (PDI-C1) and octyl (PDI-C8) imide-substituted PDIs. To achieve this, two or four bromide atoms have been introduced at the bay position of the PDI core as shown in Figure 3.1. Steady state optical absorption and emission measurements on thin films revealed that bay-area bromination significantly reduces the excitonic interactions in the solid state. Nevertheless, from transient-absorption measurements we clearly observe the formation of triplet excited states with efficiencies comparable to their unsubstituted analogues. This indicates that the reduced excitonic interaction does not prohibit SF. Furthermore, we have studied the temperature dependence of the optical absorption, emission and photoluminescence (PL) lifetime. Only small differences in the optical absorption upon cooling were found,

indicating a stable molecular arrangement. However, at the same time strong increases in both PL intensity and lifetime were observed, proving the existence of a thermally activated PL competitive process. The detailed analysis of the effect of bay-area substitution on the excitonic interactions and SF dynamics presented in this work shows bay area substitution offers an additional handle to tune the SF properties of PDI chromophores.

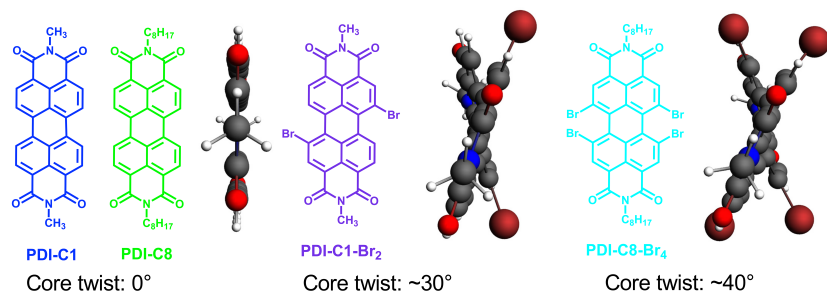


Figure 3.1: Chemical structures of the perylene diimide molecules of interest in this study with different imide- and bay- substitution. The ball-and-stick structures display the twisted perylene core structure upon bromination in side view. The twist angle as determined from TDDFT is mentioned below.

## 3.2. EXPERIMENTAL SECTION

### SAMPLE PREPARATION AND CHARACTERIZATION

The chemical structures of the PDI derivatives investigated in this work are shown in Figure 3.1. PDI-C1 (N,N'-dimethyl-3,4,9,10-perylenedicarboximide) and PDI-C8 (N,N'-dioctyl-3,4,9,10-perylenedicarboximide) were synthesized from perylene-3,4,9,10 tetracarboxylic acid dianhydride as purchased from Sigma-Aldrich using procedures published elsewhere.<sup>14</sup> PDI-PPh-Br<sub>2</sub> (N,N'-Bis(2,6-diisopropylphenyl)-1,7-dibromoperylene-3,4,9,10-tetracarboxybismide) PDI-C1-Br<sub>2</sub> and PDI-C8-Br<sub>4</sub> were synthesized from 1,7-di-bromoperylene dianhydride and 1,6,7,12-tetrabromo-perylene dianhydride, respectively, as described in the Supporting Information.<sup>15,16</sup> The powders of PDI-C1, PDI-C8 and PDI-C1-Br<sub>2</sub> were thermally evaporated (using an *AJA evaporator*) to make thin films on air plasma cleaned 1x2 cm fused silica (also termed quartz) and sapphire substrates (ESCO). The evaporated films were not annealed during or after deposition. Thin films of PDI-C8-Br<sub>4</sub> were spincoated from a saturated chloroform solution. The spincoated film was annealed at 60°C in a N<sub>2</sub> atmosphere to remove any solvents and improve the crystallization. The film thicknesses were measured using a *Dektak profilometer* and are provided in Table B.1.

### METHODS

Temperature-dependent steady state absorption and emission spectra of the thin films were measured in a home-built He-cryostat spectroscopy setup. The sample is placed in a vacuum chamber (10<sup>-7</sup> mbar) of which the temperature is controlled using an *APD-cryogenics* helium cryostat in the range 300-12 K. The optical absorption spectra were measured using the halogen lamp output of a *DH-200 Mikropack UV-VIS-NIR light source*



and a *Maya2000 Pro Ocean Optics* spectrometer detector. The fluorescence emission spectra were measured using 3.15 mW (405 nm) laser pulses of a *CPS405 ThorLabs* laser diode and a *FLAME-S-VIS-NIR Ocean Optics* spectrometer. Exposure of the sample to air was minimized by storing them in an N<sub>2</sub> glovebox and by flushing the sample chamber with N<sub>2</sub> during sample loading. Steady state absorption spectra of the thin films at room temperature were measured with a *Perkin Elmer Lambda 1050* spectrophotometer with the sample placed inside an integrating sphere to measure the attenuation.

Time-resolved photoluminescence measurements were performed with a *Lifespec-ps* fluorescence spectrophotometer (Edinburgh Instruments) using time-correlated single photon counting. The sample was photoexcited using 12.4 pJ (404 nm, 1 MHz) laser pulses from a *M8903-01 Hamamatsu* laser unit. In order to minimize laser scattering, a 425 nm long-pass filter was placed in front of the detector. The sample was loaded in an *Optistat DN* cryostat (*Oxford Instruments*) in an N<sub>2</sub> exchange gas environment. Excitation density effects were examined by placing a neutral density filter (optical density =1) after the laser diode unit to exclude the presence of exciton-exciton annihilation. The thin film topology was measured using atomic force microscopy and the crystallinity was studied using X-ray diffraction using a *Brüker D8* X-ray diffractometer (Co K $\alpha$ 1 radiation,  $\lambda = 1.79 \text{ \AA}$ ) and analysed with the Brüker program *EVA*.

Transient absorption measurements were performed using a *Helios* spectrometer (Ultrafast Systems) where the samples were excited with 180 fs pulses (2.5 kHz) from a *Pharos Yb:KGW* laser system (Light Conversion) via an *Orpheus* optical parametric amplifier (Light Conversion). The probe pulse consisted of supercontinuum light generated by focussing a part of the fundamental laser beam (1030 nm) in either a CaF<sub>2</sub> or sapphire crystal, depending on the required probe wavelength range. ns-time resolved emission and transient absorption spectra were acquired using an *LP920* transient absorption spectrophotometer (Edinburgh Instruments) with pulsed probe light (7 ms) produced by a Xe lamp. The samples were excited by 4 ns (FWHM) laser pulses produced by an *Ekspla NT 342B* OPO pumped by a Q-switched Nd:YAG laser.

The effect of the bay-area substitution with Br atoms on the geometry and electronic structure was studied by density functional theory and semiempirical calculations. The ground state geometries were optimized using the Becke-Perdew (BP86) exchange correlation (XC) functional with a DZP-type basis set consisting of Slater-functions. Using this geometry, the vertical singlet and triplet excitation energies were calculated by TDDFT calculations in the same basis set and XC functional.

An approximate geometry for the lowest triplet state (the triplet ground state) was optimized by performing an open shell triplet ground state calculation, using the BP86 functional with a DZP-type basis set. The absorption spectrum of this triplet ground state was calculated by an unrestricted TDDFT calculation. All calculations were done using the Amsterdam Density Functional software suite.

### 3.3. RESULTS AND DISCUSSION

To gain insight in the effect of bromination of the PDI core on the geometrical and basic photophysical properties we have performed electronic structure calculations using Density Functional Theory (DFT) methods as described in the Experimental section. The results are summarized in Table 3.1. Ground state geometry optimizations show

that bromination leads to a distinct deviation from the planar PDI geometry that is obtained without bromines attached. For PDI-Br<sub>2</sub>, a twist angle of 29.2° was obtained, while for PDI-Br<sub>4</sub> an even larger twist angle of 39.1° was found. Twisting of the core is predicted to have a pronounced effect on the optical properties as can be derived from Table 3.1. TDDFT calculations show that the energy difference between the ground state and the lowest singlet excited state S<sub>1</sub> decreases from 2.16 eV for the planar PDI-H<sub>4</sub>, but decreases significantly to 2.01 eV and 1.95 eV for PDI-Br<sub>2</sub> and PDI-Br<sub>4</sub>, respectively. Interestingly, the energy difference between the ground state and the lowest (vertical) triplet state remains almost unchanged upon bromination.

Table 3.1: Summary of the calculated optical properties of bay area substituted PDIs using DFT.

PDI	Ground State			T <sub>1</sub> State	
	Angle (°)	ES <sub>1</sub> (eV)	ET <sub>1</sub> (eV)	Twist (°)	T <sub>1</sub> -T <sub>n</sub> (nm)
PDI-H <sub>2</sub>	0	2.16	1.33	0	536 (2.31 eV)
PDI-Br <sub>2</sub>	29.2	2.01	1.33	22.3	566 (2.19 eV)
PDI-Br <sub>4</sub>	39.1	1.95	1.32	31.1	579 (2.14 eV)

### EFFECT OF BROMINATION ON PDI OPTICAL PROPERTIES

The attenuation and emission spectra of the different PDIs in solution and in the solid state are shown in Figure 3.2. In solution, the absorption spectra of the PDIs with and without bromines exhibit the characteristic PDI S<sub>0</sub> → S<sub>1</sub> absorption with vibronic peaks at 475, 490 and 520 nm. Halogenation in the bay-area increases the absorption between 420 nm and 460 nm corresponding to the S<sub>0</sub> → S<sub>2</sub> transition. TDDFT calculations show that the S<sub>0</sub> → S<sub>2</sub> transition is symmetry forbidden for planar PDIs without bay area substitution but is partially allowed in the strongly twisted bay area substituted PDI-C8-Br<sub>4</sub>.<sup>12,17</sup> The steady state emission spectra in solution display Stokes shifts of only a few nanometres for PDI-C1 and -C8. The Stokes shift increases to almost 50 nm for PDI-C8-Br<sub>4</sub> indicating a larger excited state geometry relaxation.<sup>12</sup> In addition, the vibronic structure becomes less pronounced upon bromination as a result of the loss of the planarity of the PDI core and the broken symmetry.<sup>17</sup> The impact of bay-area substitution on the molecular packing in the solid state can be observed by comparing the steady state absorption and emission spectra of the thin films with the respective solutions. A strong broadening and red-shift of the absorption features are observed for PDI-C1 and PDI-C8, reflecting close packing, accompanied by strong excitonic coupling.<sup>18</sup> For the brominated samples these effects are much less pronounced. Similar to PDI-C1-Br<sub>2</sub>, for PDI-C8-Br<sub>4</sub> there is a small reorganization of the molecules upon going from solution to the solid state, indicating weak crystal packing. Moreover, the emission spectra of PDI-C1 and -C8 have a strong Stokes shift of 204 and 200 nm respectively, which is typical of excimer emission.<sup>19-21</sup> The reduced excitonic interactions can be traced back to a lack of crystallization and hindered solid state packing in the brominated samples in comparison to PDI-C1 and PDI-C8 as substantiated by the absence of reflections in X-ray diffractograms (Figure B.3a) for PDI-C8-Br<sub>4</sub> thin films. However, the powders of all four PDIs show strong reflections, indicating the possibility to crystallize as shown in Figure

B.3b.

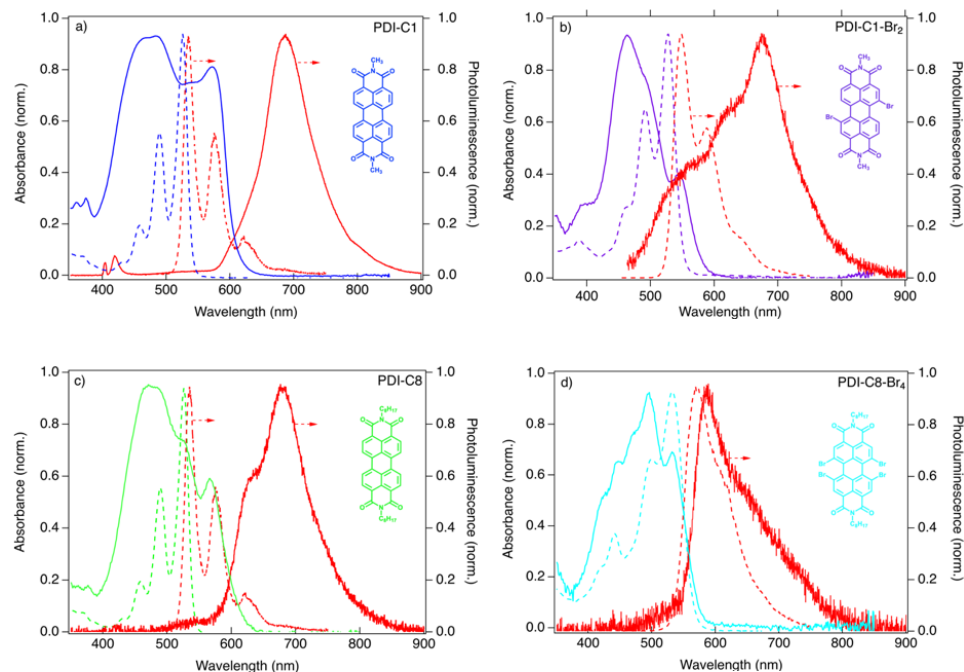


Figure 3.2: Room temperature normalized steady state absorption and emission spectra for a) PDI-C1, b) PDI-C1-Br<sub>2</sub>, c) PDI-C8 and d) PDI-C8-Br<sub>4</sub> thin films (solid lines). The solution spectra (dashed lines) shown in a) and c) come from dissolved PDI-C8 in chloroform, while for b) and d), PDI-PPh-Br<sub>2</sub> and PDI-C8-Br<sub>4</sub> dissolved in chloroform were used, respectively.

As shown in Figure 3.3a, at 300 K the photoluminescence lifetimes in thin films (obtained from fitting the decay in the first two nanoseconds) vary from 700 ps for PDI-C1 to 890 ps for PDI-C8, which is typical of singlet exciton emission. These lifetimes are much shorter than for triplet excitons that typically have lifetimes of a few microseconds in PDI thin films.<sup>2,12</sup> The fluorescence lifetimes in these solid films are considerably smaller than in chloroform solutions ( $\tau = 4.5$  ns, Figure 3.3b), indicating the presence of competing non-radiative decay processes in the solid. A possible cause of the reduced fluorescence lifetime due to closer packing, and thus enhanced electronic coupling between molecules in solid state, is the occurrence of SE.<sup>1-3</sup> An alternative explanation is the formation of non-emissive excimer states. While intersystem crossing can be a third possible explanation for the reduced emission lifetime, this can be ruled out since the fluorescence lifetime of the PDIs in solution, shown in Figure 3.3b, is unaffected by the bromination. This is consistent with previous studies.<sup>12</sup>

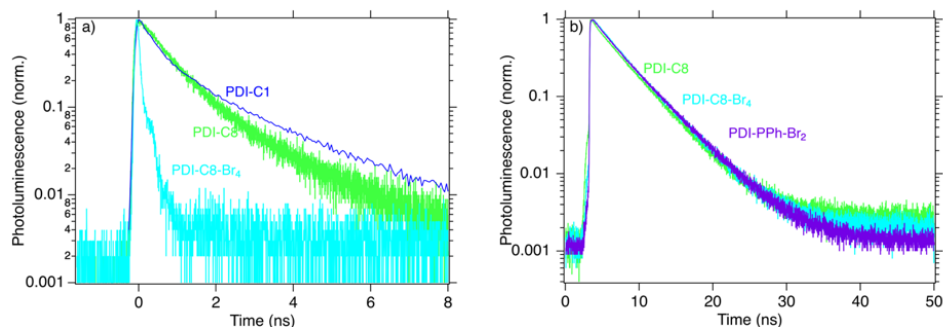


Figure 3.3: a) Time-resolved PL in thin films of PDI-C1, -C8 and -C8-Br<sub>4</sub>. b) Emission spectra of PDI-C8 (with identical behaviour for PDI-C1), PDI-PPh-Br<sub>2</sub> (identical behaviour for PDI-C1-Br<sub>2</sub>) and PDI-C8-Br<sub>4</sub> in solution.

### EFFECT OF TEMPERATURE ON PDI THIN FILM OPTICAL PROPERTIES

In order to gain more insight into the excited state dynamics and decay pathways in these materials, we have performed temperature dependent optical absorption, emission and time-resolved PL measurements at temperatures ranging from 300 K to 12 K. The temperature dependent steady state absorption spectra are shown in Figure B.4. The changes in the optical absorption spectra of the thin films occurring upon cooling to liquid helium temperatures (12 K) are small. This indicates that the molecular packing is stable and no phase change occurs. In contrast, cooling results in significant changes in the emission spectra as shown in Figure 3.4 in two ways. Firstly, the emission intensity, and thus the fluorescence quantum yield, increases upon lowering the temperature, by two orders of magnitude in the case of PDI-C8. Secondly, the shape of the emission spectra changes, exhibiting stronger emission at higher energies. The narrowing of the emission band on the blue side may signify a weaker intermolecular interaction.<sup>18</sup> Furthermore, at 93 K the PL lifetime increases to 1.2 ns and 4.1 ns for PDI-C1 and -C8, respectively, while the lifetime of the brominated PDIs is virtually unaffected upon decreasing the temperature as shown in Figure B.5.

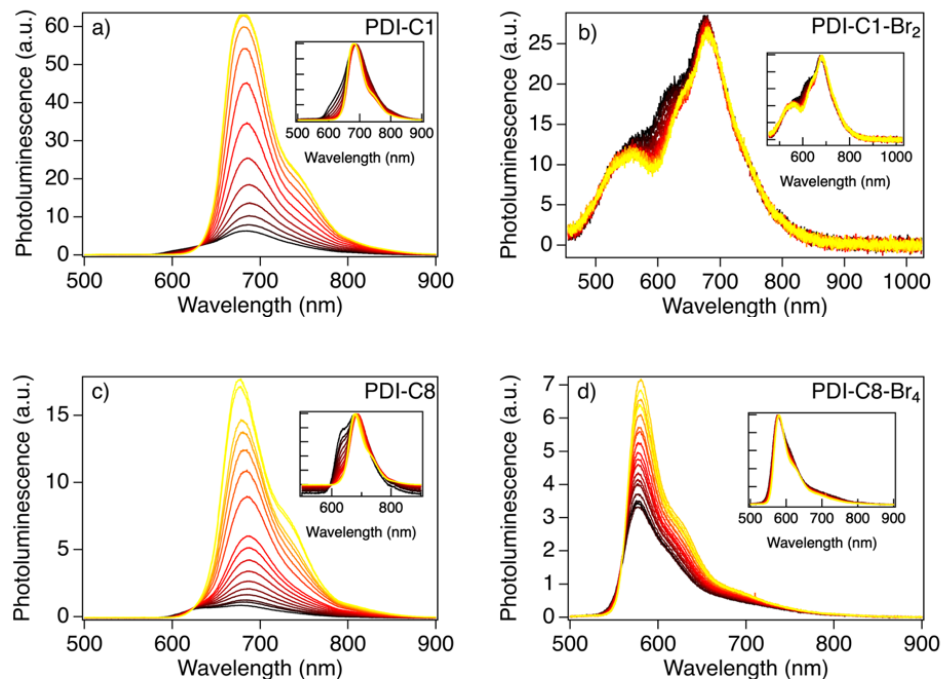


Figure 3.4: Temperature dependent emission spectra measurements of thin films of a) PDI-C1, b) PDI-C1-Br<sub>2</sub>, c) PDI-C8 and d) PDI-C8-Br<sub>4</sub> as measured in the home build helium cryostat setup. The temperatures vary from 13 K (yellow) to maximally 333 K (black). The insets show emission spectra normalized at the peak emission wavelength.

The increase in PL quantum yield and lifetime are both indicative of an thermally activated non-radiative decay pathway that outcompetes fluorescence at room temperature. The activation energies,  $E_A$ , for such a thermally activated process have been obtained by plotting the natural logarithm of the photoluminescence decay rate,  $\ln(k_{PL})$ , as function of the inverse temperature and by fitting the trend with an Arrhenius relation as shown in Figure 3.5. From these fits we obtained activation energies of  $E_A = 66$  meV and 24 meV for PDI-C1 and PDI-C8, respectively. The different energies point to the relevance of subtle changes in film packing on exciton dynamics. These values are of the same magnitude as those reported for strongly coupled chromophores.<sup>5</sup> In the case of tetracene<sup>22</sup> and rubrene<sup>23</sup>, these activation energies have been attributed to thermally activated non-radiative recombination or singlet fission. However, as singlet fission in PDIs is known to occur on a sub-ps<sup>1</sup> to ps<sup>2</sup> timescale and the time resolution of our photoluminescence setup is 50 ps, it may be that SF is too fast to be responsible for the observed activation energy. Therefore, it is unlikely that the calculated activation energies for the PDIs belong to the thermally activated singlet fission process. Therefore, we have investigated the effects of other possible non-radiative decay pathways to determine a possible relationship between the observed thermally activated behavior and SF. Firstly, thermal relaxation related to non-radiative losses has been considered. To that end, we studied the temperature dependence of the PL of isolated PDI molecules (in

which SF cannot occur) using a solution of a hexylheptyl-imide substituted PDI in the glassy solvent 2Me-THF. The PL lifetime of the dissolved molecule remained unaffected by temperature as shown in Figure B.6. This indicates that internal conversion and energy dissipation from the PDI to its surroundings are not responsible for the thermally activated decay process observed in the thin films. A second, more likely possibility is the formation of exothermic fluorescent excimers that are known to occur in closely packed PDIs.<sup>9,19,21</sup> Excimer emission is strongly red shifted compared to fluorescence from isolated which matches with the observations. Furthermore, the increased PL lifetimes at low temperatures for PDI-C1 and PDI-C8 points to the formation excimer states as the main contributor to the PDI photoluminescence and as such the found activation energies.

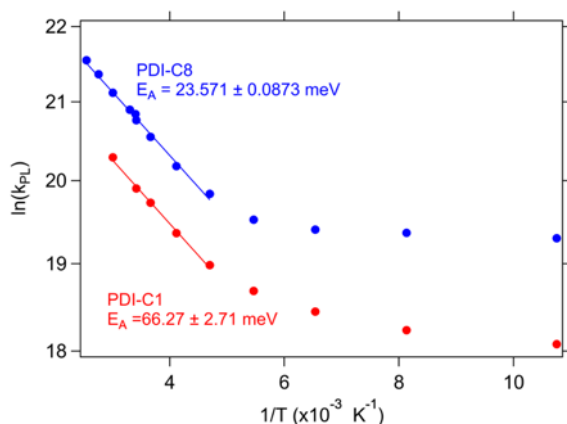


Figure 3.5: Plot of the natural logarithm of the inverse fluorescence decay time of the different PDIs as function of inverse temperature. The solid line represents the applied Arrhenius relation:  $k_{PL} = Ae^{-E_A/k_B T}$ .

### TRANSIENT ABSORPTION MEASUREMENTS ON PDI FILMS

While the thermally activated deactivation process is mainly related to the formation of excimers as argued above, PDIs are known to undergo SF with high efficiency in some cases. Therefore, we have performed femtosecond transient absorption (fs-TA) measurements on the thin films of the four model compounds considered here to establish whether triplets are formed. The results of these measurements are shown in Figure 3.6. We observe a strong ground state bleach (GSB) at short times that is reminiscent of the ground-state absorption spectrum (indicated by dashed lines). Furthermore, all PDIs show an absorption feature above 600 nm as will be discussed below. The triplet absorption in PDIs is known to occur in the same region as the GSB.<sup>24</sup> Such an induced absorption feature is exactly what we observe in the 520-550 nm region for PDI-C1, PDI-C1-Br<sub>2</sub> and PDI-C8 at times immediately after the excitation pulse. The assignment of this positive absorption feature to a triplet absorption is consistent with the long lifetime (> 2.7 ns) of this feature as shown in Figure 3.7.

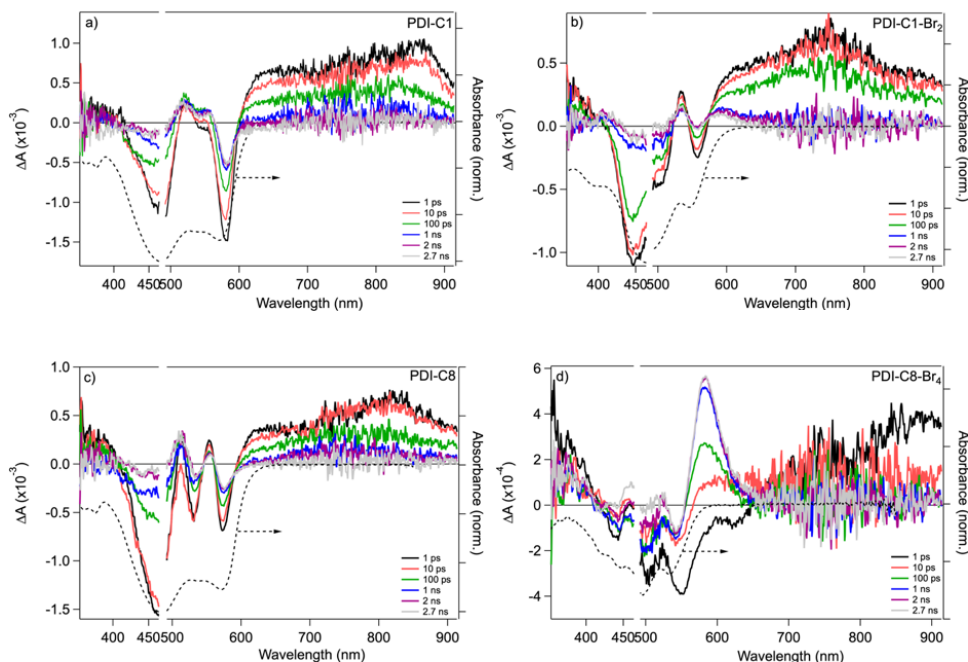


Figure 3.6: Transient absorption spectra at different times of thin films of a) PDI-C1, b) PDI-C1-Br<sub>2</sub>, c) PDI-C8 and d) PDI-C8-Br<sub>4</sub> on sapphire upon 480 nm excitation at  $1.86 \cdot 10^{12}$  ( $2.17 \cdot 10^{13}$  for PDI-C8-Br<sub>4</sub>) photons/cm<sup>2</sup>. The dashed line indicates the normalized absorption spectrum of the respective PDI thin films.

From the kinetics of the induced absorption above 600 nm we observe a full decay of singlet excited states within 3 ns. The overlapping TA features of triplet-triplet absorption and GSB at wavelengths shorter than 600 nm extend well beyond 3 ns. PDI-C8-Br<sub>4</sub> exhibits a distinctly different behaviour as the triplet-triplet absorption feature around 580 nm develops on much longer timescales than observed for the other three compounds. A positive transient absorption feature arises after 6 ps and continues to grow up to ~1 ns. This long lived state cannot be due to thermal heating artefacts<sup>25</sup> since the triplet absorption for this molecule is red-shifted, away from the ground state absorption spectrum. Moreover, the existence of long lived triplet species in analogous tetrabrominated PDIs<sup>12</sup> substantiate the triplet origin of this long-lived feature. In fact, the DFT calculations on triplet spectra, provided in Table 3.1, show that bromination leads to a red-shifted triplet absorption going from 2.31 eV (536 nm), to 2.19 eV (566 nm) and 2.14 eV (579 nm) for -Br<sub>0</sub>, -Br<sub>2</sub> and -Br<sub>4</sub> substituted PDIs, respectively, which is similar to the triplet-triplet absorption maximum observed in TA. The rising triplet signal for PDI-C8-Br<sub>4</sub> was approximated with a mono-exponential function and resulting in a singlet fission rise time of  $\tau_{SF} = 16.2$  ps ( $k_{SF} = 6.17 \cdot 10^{10} \text{ s}^{-1}$ ). To confirm the distinct behaviour of PDI-C8-Br<sub>4</sub>, we performed TA measurements on a similar tetrabrominated PDI, *i.e.* PDI-C1-Br<sub>4</sub>. Very similar kinetics were obtained as for PDI-C8-Br<sub>4</sub>, giving a characteristic time of  $\tau_{SF} = 19.7$  ps ( $k_{SF} = 5.08 \cdot 10^{10} \text{ s}^{-1}$ ), as shown in Figure B.7 in the Supporting Information. As the SF rise time and overall excited state kinetics of PDI-C1-Br<sub>4</sub> and PDI-



C8-Br<sub>4</sub> is very similar, it seems that bay-area bromination dominates the singlet fission behaviour more than the imid substitution.

The photoinduced absorption above 600 nm is commonly attributed to the S<sub>1</sub>-S<sub>n</sub> transition in PDIs.<sup>2</sup> However, taking into account the temperature dependent PL measurements, it is likely that the photoinduced absorption 600-900 nm region is at least partly due to excimer states. This also explains why the decay of this absorption feature does not correlate with the rise of the T<sub>1</sub>-T<sub>n</sub> absorption in PDI-C1, PDI-C8 and PDI-C1-Br<sub>2</sub>. This indicates that SF is not the only, or even the primary decay process for the S<sub>1</sub> states. Considering the temperature dependent fluorescence measurements presented above, we conclude that SF competes with excimer formation at short times. This results in the formation of a limited fraction of triplets formed by SF, while the remaining singlets transform into excimer states. These excimers have a lower energy and are not sufficiently energetic to undergo SF.<sup>26</sup> A notable exception to this behavior is PDI-C8-Br<sub>4</sub> as the decay of the S<sub>1</sub>-S<sub>n</sub> matches the growth of the T<sub>1</sub>-T<sub>n</sub> absorption. This indicates that excimer formation is prohibited in PDI-C8-Br<sub>4</sub> by the strong twisting of the core. Therefore, the decay of the singlet population correlates with the growth of the triplets as there is no competing process here. The transient absorption measurements presented here indicate that a reduced excitonic interaction between neighbouring molecules does not necessarily inhibit the occurrence of SF, but may be beneficial for SF because it prevents excimer formation. This shows that significant modifications to the PDI structure are possible leading to strongly enhanced solubility and reduced excitonic interactions while maintaining or even enhancing formation of triplet excited states.

The SF efficiency can be estimated via three main methods: 1) triplet sensitization to obtain a triplet extinction coefficient and subsequent subtraction from the spectrum, 2) global analysis using known extinction coefficients and spectra and 3) the singlet depletion method, *i.e.* GSB quantization.<sup>27</sup> All methods have their weaknesses and are not regularly in agreement, which is why we have chosen not to calculate a triplet yield but describe the triplet feature qualitatively. For PDI-C1 and PDI-C8 we observe a strong triplet absorption feature that persists after 2.7 ns as was shown previously for PDI-C8.<sup>25</sup>

In TA experiments, the pump fluences are typically high enough for singlet-singlet annihilation (SSA) to occur. The SSA leads to a hot singlet exciton that relaxes to the first excited singlet state during while releasing energy as heat to the surroundings. This thermal heating of the surroundings is known to induce a temporal change in the absorption spectrum of the PDI and may lead to a thermal heating artefact in the GSB region of the TA spectrum.<sup>25</sup> To address the issue of SSA leading to a thermal heating artefact, we compared the decay kinetics of T<sub>1</sub>-T<sub>n</sub> and S<sub>1</sub>-S<sub>n</sub> of the PDIs as function of the substrate, *i.e.* fused silica (dashed line) and sapphire (solid line) glass, shown in Figure 3.7. Since fused silica has an approximately 40 times lower thermal conductivity than sapphire, significant thermal heating artefacts due to SSA are expected, affecting both the absolute size and decay kinetics in the GSB region. As obvious from Figure 3.7, the decay kinetics of singlet and triplet absorption is close to identical on fused silica and sapphire for PDI-C8 and PDI-C8-Br<sub>4</sub>, while for PDI-C1 and PDI-C1-Br<sub>2</sub>, the TA features in the sapphire film have a slightly larger magnitude. From this we can conclude that the decay kinetics in PDIs at the used excitation fluence does not significantly affect the decay kinetics of the triplet as we should have seen an effect between fused silica and sapphire. The differ-



ence in absolute height may indicate a limited thermal heating effect, but the kinetics of the triplet absorption at 2.7 ns overlaps for both substrate-based samples making a triplet yield analysis via the singlet depletion method valid. To further study the effect of excitation fluence, we used an order of magnitude higher excitation fluence on the sapphire-based films and in Figure B.8 we observe a strong increase in the decay of all excited state species, indicative of SSA. This measurement shows how SSA can directly affect the excited state decay kinetics irrespective of thermal heating.

3

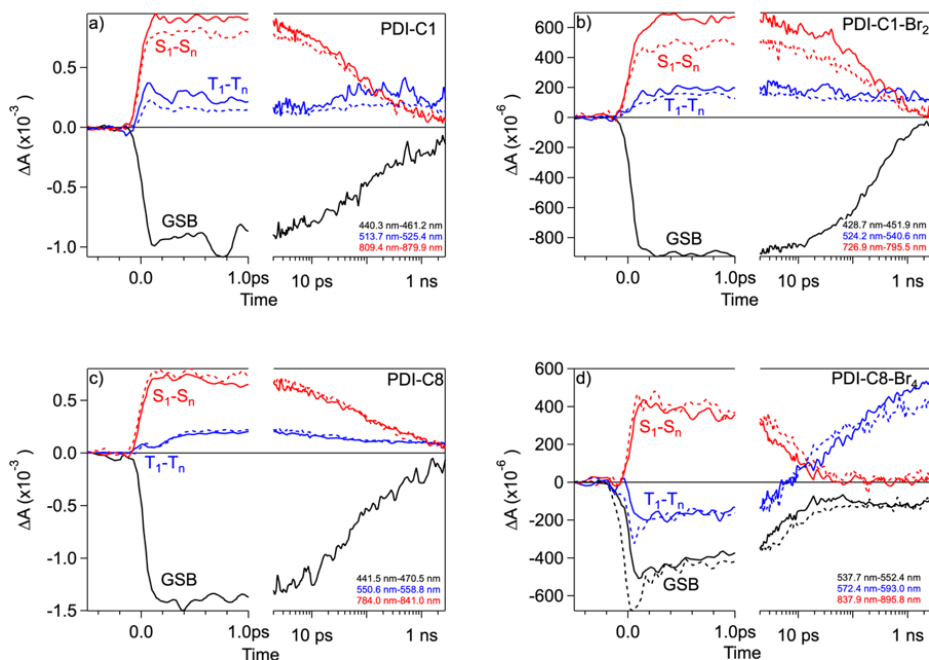


Figure 3.7: Kinetic traces of the ground state bleach (GSB), triplet absorption ( $T_1-T_n$ ) and the singlet absorption ( $S_1-S_n$ ) for a) PDI-C1, b) PDI-C1-Br<sub>2</sub>, c) PDI-C8 and d) PDI-C8-Br<sub>4</sub> on sapphire (solid lines) and fused silica (dashed lines) substrates. The traces are the average of a wavelength region as indicated in the lower right corner.

The lifetime of the triplet species generated by SF was studied using ns-TA experiments where we photoexcited the PDI samples on fused silica and sapphire at 480 nm, see Figure 3.8. The ns-TA measurement show a slower decay of the GSB and  $T_1-T_n$  of PDI-C1 and PDI-C8 in the case of a fused silica substrate, compared to sapphire which is in line with the dissipation of heat occurring after thermal heating of the sample (note that the excitation density in these experiments is much higher than in the fs-TA experiment). This clearly demonstrates the influence of SSA on the nano-to-microsecond excited state decay kinetics and the benefit of using sapphire substrates at high fluences. For PDI-C1-Br<sub>2</sub> there is a weaker effect of the substrate, and thus thermal heating, on the observed decay kinetics of GSB and triplets and in PDI-C8-Br<sub>4</sub> there is hardly any difference between the two substrates which may either be due to the low optical density of the film or the fact that the triplet absorption is not overlapping with the GSB region for

this compound. We can fit the triplet-triplet absorption with a biexponential decay and find a two-component triplet lifetime, provided in Table 3.2, where the short component has a lifetime of  $\tau_{T,1} = 30\text{-}80$  ns while the longer-lived component ranges from  $\tau_{T,2} = 270\text{-}600$  ns. The existence of multiple triplet lifetimes may stem from the highly disordered nature of even polycrystalline solid-state systems where a variety of non-radiative decay processes may exist. This is consistent with the significantly lower triplet lifetime compared to that of PDIs in solution ( $\tau_{T,s} > 30 \mu\text{s}$ ).<sup>28</sup> We also cannot rule out effect due to triplet-triplet annihilation.

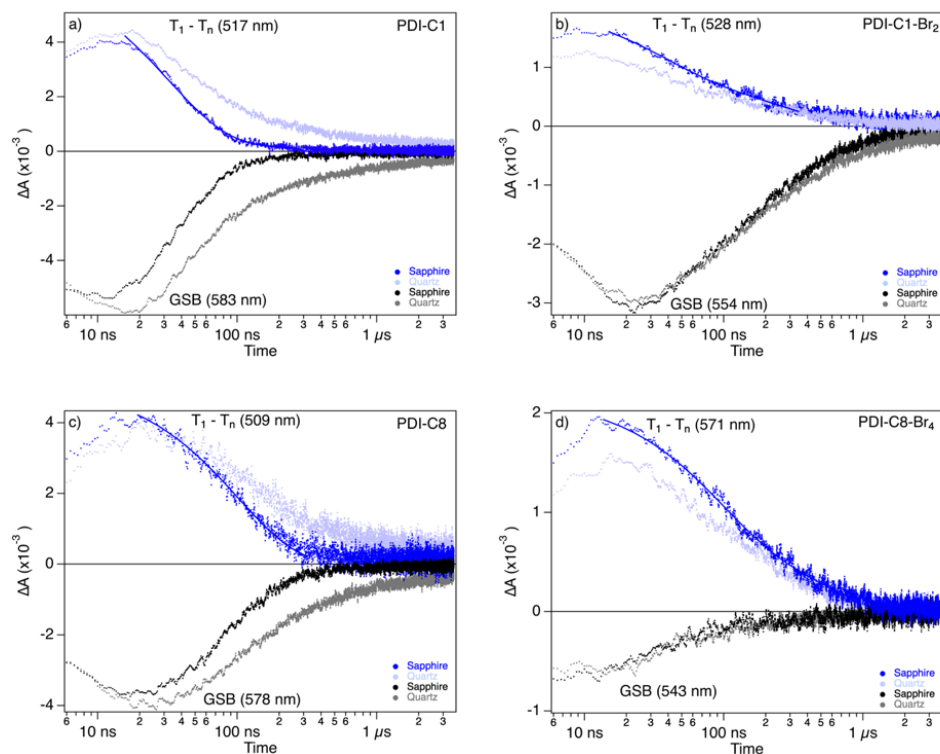


Figure 3.8: Kinetic traces of GSB on sapphire (black) and fused silica or 'quartz' (grey) and of the  $T_1 - T_n$  on sapphire (blue) and quartz (light blue) substrates with thin films of a) PDI-C1, b) PDI-C1-Br<sub>2</sub>, c) PDI-C8 and d) PDI-C8-Br<sub>4</sub> in the microsecond regime upon 480 nm excitation at a photon fluence of  $2.10 \cdot 10^{15}$  photons/cm<sup>2</sup>.

Table 3.2: Triplet lifetimes as obtained from a bi-exponential fit on the ns-TA triplet transient.

PDI	$T_1-T_n$	
	$\tau_{T,1}$ (ns)	$\tau_{T,2}$ (ns)
C1	32.3±0.5 (95%)	611.7±313.0
C1-Br <sub>2</sub>	33.7±2.0 (48%)	274.7±10.4
C8	109.4±1.0 (100%)	0
C8-Br <sub>4</sub>	83.4±1.9 (60%)	482.3±9.4

### 3.4. CONCLUSIONS

In this work we have examined the effect of bromination of the aromatic core of perylene diimide molecules on their excited state dynamics. We have measured the effect of bay-area bromination in PDIs on both the optical absorption, emission spectra and lifetime and found that bromination changes the molecular packing and thereby decreases the coupling between PDI chromophores. Temperature dependent measurements show the presence of a temperature activated process, which is attributed to excimer formation. Ultrafast (fs) transient absorption measurements show for all compounds, SF results in significant formation of triplet excited states, despite the pronounced changes in molecular packing on bromination. We conclude that in PDIs without bromines or only two bromines in the bay area, SF occurs in competition with excimer formation, resulting in relatively low SF yields. Introduction of four bromine atoms in the bay area results in significant distortion of the structure which prevent excimer formation. This shows that while bay area substitution of PDIs decreases the excitonic interactions between the neighbouring molecules, this is in fact beneficial for SF as it prevents the occurrence of the competing process, *i.e.* excimer formation.

## REFERENCES

- (1) Aulin, Y. V.; Felter, K. M.; Günbas, D.; Dubey, R. K.; Jager, W. F.; Grozema, F. Morphology independent efficient singlet exciton fission in perylenediimide thin films. *ChemPlusChem*.
- (2) Eaton, S. W.; Shoer, L. E.; Karlen, S. D.; Dyar, S. M.; Margulies, E. A.; Veldkamp, B. S.; Ramanan, C.; Hartzler, D. A.; Savikhin, S.; Marks, T. J. Singlet exciton fission in polycrystalline thin films of a slip-stacked perylenediimide. *J. Am. Chem. Soc.* **2013**, *135*, 14701–14712.
- (3) Le, A. K.; Bender, J. A.; Arias, D. H.; Cotton, D. E.; Johnson, J. C.; Roberts, S. T. Singlet Fission Involves an Interplay between Energetic Driving Force and Electronic Coupling in Perylenediimide Films. *J. Am. Chem. Soc.* **2018**, *140*, 814–826.
- (4) Singh-Rachford, T. N.; Nayak, A.; Muro-Small, M. L.; Goeb, S.; Therien, M. J.; Castellano, F. N. Supermolecular-chromophore-sensitized near-infrared-to-visible photon upconversion. *J. Am. Chem. Soc.* **2010**, *132*, 14203–14211.
- (5) Smith, M. B.; Michl, J. Singlet fission. *Chem. Rev.* **2010**, *110*, 6891–6936.
- (6) Feng, X.; Kolomeisky, A. B.; Krylov, A. I. Dissecting the effect of morphology on the rates of singlet fission: Insights from theory. *J. Phys. Chem. C* **2014**, *118*, 19608–19617.
- (7) Piland, G. B.; Bardeen, C. J. How morphology affects singlet fission in crystalline tetracene. *J. Phys. Chem. Lett.* **2015**, *6*, 1841–1846.
- (8) Basel, B. S.; Hetzer, C.; Zirzmeier, J.; Thiel, D.; Guldi, R.; Hampel, F.; Kahnt, A.; Clark, T.; Guldi, D. M.; Tykwinski, R. R. Davydov splitting and singlet fission in excitonically coupled pentacene dimers. *Chem. Sci.* **2019**.
- (9) Margulies, E. A.; Miller, C. E.; Wu, Y.; Ma, L.; Schatz, G. C.; Young, R. M.; Wasielewski, M. R. Enabling singlet fission by controlling intramolecular charge transfer in  $\pi$ -stacked covalent terrylenediimide dimers. *Nat. Chem.* **2016**, *8*, 1120.
- (10) Mirjani, F.; Renaud, N.; Gorczak, N.; Grozema, F. C. Theoretical Investigation of Singlet Fission in Molecular Dimers: The Role of Charge Transfer States and Quantum Interference. *J. Phys. Chem. C* **2014**, *118*, 14192–14199.
- (11) Renaud, N.; Grozema, F. C. Intermolecular vibrational modes speed up singlet fission in perylenediimide crystals. *J. Phys. Chem. Lett.* **2015**, *6*, 360–365.
- (12) Nagarajan, K.; Mallia, A. R.; Reddy, V. S.; Hariharan, M. Access to Triplet Excited State in Core-Twisted Perylenediimide. *J. Phys. Chem. C* **2016**, *120*, 8443–8450.
- (13) Mete, E.; Uner, D.; Cakmak, M.; Gulseren, O.; Ellialtıođlu, Ő. Effect of molecular and electronic structure on the light-harvesting properties of dye sensitizers. *J. Phys. Chem. C* **2007**, *111*, 7539–7547.
- (14) Duff, J. M.; Hor, A.-M.; Melnyk, A. R.; Teney, D. In *Hard Copy and Printing Materials, Media, and Processes*, International Society for Optics and Photonics; Vol. 1253, pp 183–192.

- (15) Hill, Z. B.; Rodovsky, D. B.; Leger, J. M.; Bartholomew, G. P. Synthesis and utilization of perylene-based n-type small molecules in light-emitting electrochemical cells. *Chem. Commun.* **2008**, 6594–6596.
- (16) Sengupta, S.; Dubey, R. K.; Hoek, R. W.; van Eeden, S. P.; Günbaş, D. D.; Grozema, F. C.; Sudhölter, E. J.; Jager, W. F. Synthesis of regioisomerically pure 1, 7-dibromoperylene-3, 4, 9, 10-tetracarboxylic acid derivatives. *J. Org. Chem.* **2014**, *79*, 6655–6662.
- (17) Chen, Z.; Baumeister, U.; Tschierske, C.; Würthner, F. Effect of Core Twisting on Self-Assembly and Optical Properties of Perylene Bisimide Dyes in Solution and Columnar Liquid Crystalline Phases. *Chem. - Eur. J.* **2007**, *13*, 450–465.
- (18) Würthner, F.; Thalacker, C.; Diele, S.; Tschierske, C. Fluorescent J-type aggregates and thermotropic columnar mesophases of perylene bisimide dyes. *Chem. - Eur. J.* **2001**, *7*, 2245–2253.
- (19) Kaufmann, C.; Kim, W.; Nowak-Król, A.; Hong, Y.; Kim, D.; Würthner, F. Ultrafast exciton delocalization, localization, and excimer formation dynamics in a highly defined perylene bisimide quadruple  $\pi$ -stack. *J. Am. Chem. Soc.* **2018**, *140*, 4253–4258.
- (20) Margulies, E. A.; Shoer, L. E.; Eaton, S. W.; Wasielewski, M. R. Excimer formation in cofacial and slip-stacked perylene-3, 4: 9, 10-bis (dicarboximide) dimers on a redox-inactive triptycene scaffold. *Phys. Chem. Chem. Phys.* **2014**, *16*, 23735–23742.
- (21) Son, M.; Park, K. H.; Shao, C.; Würthner, F.; Kim, D. Spectroscopic demonstration of exciton dynamics and excimer formation in a sterically controlled perylene bisimide dimer aggregate. *J. Phys. Chem. Lett.* **2014**, *5*, 3601–3607.
- (22) Burdett, J. J.; Gosztola, D.; Bardeen, C. J. The dependence of singlet exciton relaxation on excitation density and temperature in polycrystalline tetracene thin films: kinetic evidence for a dark intermediate state and implications for singlet fission. *J. Chem. Phys.* **2011**, *135*, 214508.
- (23) Li, J.; Chen, Z.; Zhang, Q.; Xiong, Z.; Zhang, Y. Temperature-dependent singlet exciton fission observed in amorphous rubrene films. *Org. Electron.* **2015**, *26*, 213–217.
- (24) Ford, W. E.; Kamat, P. V. Photochemistry of 3, 4, 9, 10-perylenetetracarboxylic dianhydride dyes. 3. Singlet and triplet excited-state properties of the bis (2, 5-di-tert-butylphenyl) imide derivative. *J. Phys. Chem.* **1987**, *91*, 6373–6380.
- (25) Le, A. K.; Bender, J. A.; Roberts, S. T. Slow singlet fission observed in a polycrystalline perylenediimide thin film. *J. Phys. Chem. Lett.* **2016**, *7*, 4922–4928.
- (26) Dover, C. B.; Gallaher, J. K.; Frazer, L.; Tapping, P. C.; Petty II, A. J.; Crossley, M. J.; Anthony, J. E.; Kee, T. W.; Schmidt, T. W. Endothermic Singlet Fission Is Hindered by Excimer Formation. *Nat. Chem.* **2018**, *10*, 305.
- (27) Mauck, C. M.; Hartnett, P. E.; Margulies, E. A.; Ma, L.; Miller, C. E.; Schatz, G. C.; Marks, T. J.; Wasielewski, M. R. Singlet fission via an excimer-like intermediate in 3, 6-bis (thiophen-2-yl) diketopyrrolopyrrole derivatives. *J. Am. Chem. Soc.* **2016**, *138*, 11749–11761.
- (28) Yu, Z.; Wu, Y.; Peng, Q.; Sun, C.; Chen, J.; Yao, J.; Fu, H. Accessing the Triplet State in Heavy-Atom-Free Perylene Diimides. *Chem. - Eur. J.* **2016**, *22*, 4717–4722.

# 4

## SOLID-STATE INFRARED UPCONVERSION IN PDIs FOLLOWED BY DIRECT ELECTRON INJECTION

*In this contribution we demonstrate a solid-state approach to triplet-triplet annihilation upconversion for application in a solar cell device in which absorption of near-infrared light is followed by direct electron injection into an inorganic substrate. We use time-resolved microwave photoconductivity experiments to study the injection of electrons into the electron-accepting substrate (TiO<sub>2</sub>) in a trilayer device consisting of a triplet sensitizer (fluorinated zinc phthalocyanine), triplet acceptor (methyl substituted perylenediimide), and smooth polycrystalline TiO<sub>2</sub>. Absorption of light at 700 nm leads to the almost quantitative generation of triplet excited states by intersystem crossing. This is followed by Dexter energy transfer to the triplet acceptor layer where triplet annihilation occurs and concludes by injection of an electron into TiO<sub>2</sub> from the upconverted singlet excited state.*

---

This chapter is based on: Felter, K. M., Fravventura, M. C., Koster, E., Abellon, R. D., Savenije, T. J., and Grozema, F. C. (2020). *Solid-State Infrared Upconversion in Perylene Diimides Followed by Direct Electron Injection*. ACS Energy Letters, 5(1), 124-129.

## 4.1. INTRODUCTION

One of the major factors limiting the energy conversion efficiency of single junction solar cells to the Shockley-Queisser limit is the inability of the active materials to absorb photons with energies lower than their bandgap.<sup>1</sup> A promising approach to overcome this problem is the incorporation of an upconverter material that combines the energy of multiple low-energy photons into a single high-energy photon.<sup>2</sup> Theoretically, it has been predicted that this can increase the conversion efficiency of a single-junction solar cell to 50.7% for an ideal upconverter material.<sup>3</sup> The most commonly used upconverter materials are based on lanthanide compounds, for instance  $\text{NaYF}_4:\text{Er}^{3+}$ ,  $\text{Yb}^{3+}$  and  $\text{NaYF}_4:\text{Er}^{3+}$  with quantum efficiencies of 5% and 3% under monochromatic irradiation, respectively.<sup>4</sup> However, the upconversion efficiency of such materials is limited by their very narrow absorption spectrum and the fact that upconversion, being a higher-order process, requires high light intensities to be efficient.<sup>5,6</sup> An alternative approach is to exploit triplet-triplet annihilation upconversion (TTA-UC) using a combination of two different organic molecules as shown in Figure 4.1.<sup>6-9</sup> The process requires a chromophore, the triplet sensitizer (TS), that absorbs light in the near-infrared region and efficiently converts the initially formed singlet excited state into a triplet via intersystem crossing (ISC). These triplets are then transferred, by Dexter energy transfer, to a second molecule, the triplet acceptor (TA), with a lower-lying triplet state. If a sufficiently high concentration of excited triplet acceptors builds up, TTA-UC can occur, leading to the formation of a singlet excited state. Emission can then occur by the high-energy singlet. There are two distinct advantages to this approach over the use of rare earth materials. First, the absorption bands of organic chromophores are generally broad and can be tuned relatively easily by chemical modification. Second, the key intermediate is a triplet excited state that generally has a very long lifetime. The latter makes it possible to build up a sufficient concentration of excited states, even under low light conditions.<sup>9</sup>

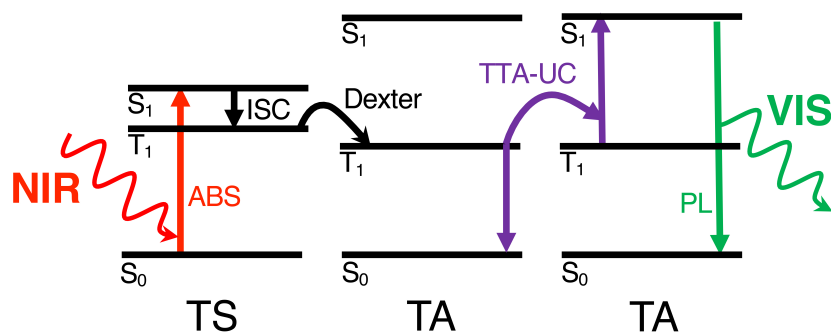


Figure 4.1: Scheme showing the TTA-UC process in a system composed of a triplet sensitizer (TS) and triplet acceptor (TA). Near-infrared light (NIR) is absorbed and creates a singlet excited state,  $S_1$ , that converts to a triplet state,  $T_1$ , via intersystem crossing (ISC). The triplet is transferred via Dexter energy transfer to the acceptor where it can undergo TTA-UC with a neighboring acceptor molecule in the  $T_1$  state. Emission of visible light (VIS) can then occur via photoluminescence (PL).

Upconversion by triplet-triplet annihilation has been extensively studied in solution, reaching quantum yields up to 32-38%.<sup>10-12</sup> While such efficiencies are impressive, it is

rather undesirable from a technological point of view to use a solution-based system for large-scale applications. There have been attempts to show the same type of upconversion in rubbery polymer matrices, but the efficiency is limited by their poor molecular diffusion.<sup>13,14</sup> An additional complication of the upconversion by triplet-triplet annihilation is that it usually relies on re-emission from the upconverted singlet state. This introduces an additional loss mechanism in solar cells because the emitted photons have to again be absorbed efficiently by the active semiconducting material. In this work, we show that both these problems can be overcome by using a system that consists of two layers of crystalline materials where triplet energy transfer and triplet-triplet annihilation rely on exciton diffusion rather than molecular diffusion. After TTA-UC, the resulting singlet excited state directly injects an electron into a TiO<sub>2</sub> substrate, bypassing the emission and reabsorption steps. A recent review on solid-state upconversion discussed the different strategies involving supramolecular, macromolecular and self-assembled systems to enable solid-state upconversion.<sup>9</sup> One strategy, explored by Hanson et al., involves the fabrication of a dye sensitized system with triplet sensitizer anchored to the triplet acceptor which, in turn, is anchored to the electron acceptor TiO<sub>2</sub>.<sup>15-17</sup> This upconverter architecture is similar to our approach, although there still is a dependence on the liquid medium containing electrolytes. One alternative solid-state upconversion system involves a spincoated film consisting of triplet acceptor molecules that are doped with triplet sensitizer molecules to provide triplets and highly fluorescent energy collectors that collect upconverted singlets and recombine them radiatively. The doping of the triplet acceptor by both sensitizer and energy collector acts to mitigate singlet back energy transfer from the triplet acceptor to the triplet sensitizer because of a lack of physical contact between the triplet sensitizer and energy collector.<sup>18</sup> This promising study showed that exciton motion can provide reasonable upconversion in the solid-state, although the system still relies on the emission of photons as a way to harvest the energy gained by upconversion. Similarly, another study on a solid-state upconversion system successfully demonstrated the prevention of singlet back-transfer from upconverted singlets in the triplet acceptor to the triplet sensitizer by using a neat layer of the triplet acceptor layer.<sup>19</sup>

The solid-state upconversion system that we demonstrate here consists of two crystalline layers (Figure C.1b) of fluorinated zinc phthalocyanine (F<sub>16</sub>ZnPc) and perylene-tetracarboxylic acid diimide (PDI-CH<sub>3</sub>) whose structures are shown in Figure 4.2a. The layers are deposited on top of a smooth polycrystalline titanium dioxide (TiO<sub>2</sub>) layer as shown in the atomic force microscopy image shown in Figure C.1a, that forms the trilayer system. F<sub>16</sub>ZnPc acts as the near-infrared absorber and very efficient triplet sensitizer that has a triplet energy level that is appropriate to facilitate downhill energy transfer to PDI-CH<sub>3</sub> that acts as triplet acceptor where upconversion occurs. Finally, electrons are directly injected from the upconverted singlet excited state of PDI-CH<sub>3</sub> into TiO<sub>2</sub>. The energy cascade leading to charge injection from upconverted singlets is schematically depicted in Figure 4.2b. Using this trilayer architecture, we show that near-infrared photon absorption at 700 nm photons can lead to charge injection into TiO<sub>2</sub> from PDI-CH<sub>3</sub>, while it does not absorb near-infrared photons by itself. Instead, selective optical absorption in the near-infrared by F<sub>16</sub>ZnPc, shown in Figure 4.2c, readily generates triplet states with high efficiency that transfer to PDI-CH<sub>3</sub> and undergo TTA-UC to singlet states



that can thus provide charge injection. The system does not rely on molecular diffusion but uses exciton motion, which is proven to be sufficiently efficient in the crystalline materials used. This trilayer architecture involving intraband exciton transfer between triplet sensitizer and acceptor can be regarded as an example of the photoactive part of an intermediate band solar cell.<sup>20</sup>

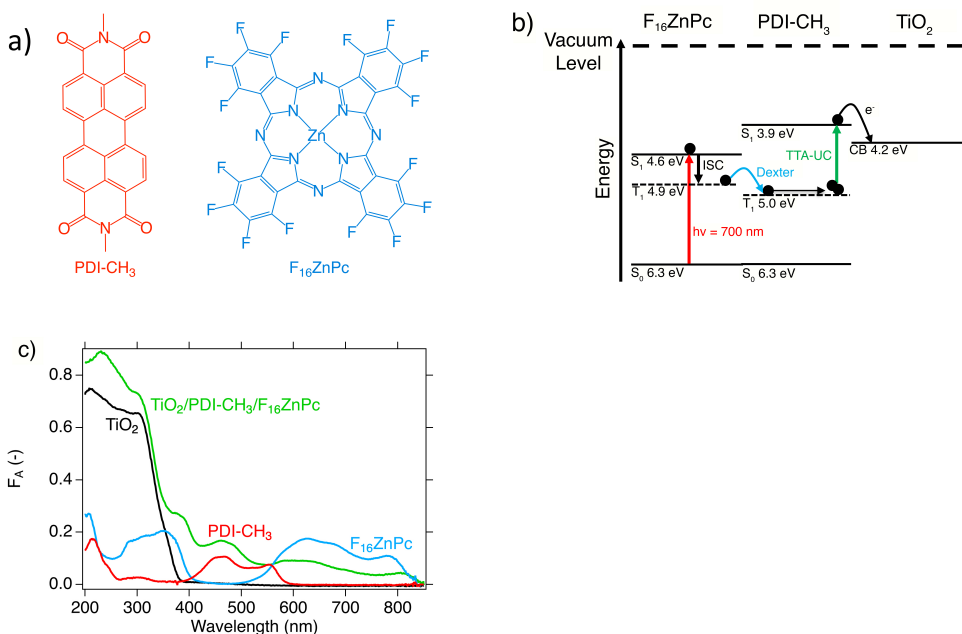


Figure 4.2: a) Molecular structures of PDI-CH<sub>3</sub> and F<sub>16</sub>ZnPc. b) Schematic representation of the trilayer sample structure with triplet and singlet (HOMO and LUMO) energy levels for F<sub>16</sub>ZnPc<sup>21</sup> and PDI-CH<sub>3</sub><sup>22–25</sup>, with respect to the conduction band edge (CB) of TiO<sub>2</sub>.<sup>26</sup> c) Attenuation spectra of the TiO<sub>2</sub>/PDI-CH<sub>3</sub>/F<sub>16</sub>ZnPc trilayer (green) and single-layer films of TiO<sub>2</sub> (black), PDI-CH<sub>3</sub> (red), and F<sub>16</sub>ZnPc (blue).

## 4.2. EXPERIMENTAL SECTION

N,N'-Dimethyl-3,4,9,10-perylenedicarboximide (PDI-CH<sub>3</sub>) and zinc 1,2,3,4,8,9,10,11,15, 16, 17,18,22,23,24,25-hexadecafluoro-29H,31H-phthalocyanine (F<sub>16</sub>ZnPc), powders were purchased from Sigma-Aldrich and used without further modification. The polycrystalline TiO<sub>2</sub> coated fused silica substrates (~90 nm thickness) were purchased from *Everest Coatings Inc.* and treated at 450°C for two hours in a furnace. A 15 nm layer of PDI-CH<sub>3</sub> and subsequently a 30 nm layer of F<sub>16</sub>ZnPc were thermally evaporated on top of TiO<sub>2</sub> films at 10<sup>-6</sup> mbar as outlined in Appendix C.

## 4.3. RESULTS AND DISCUSSION

In Figure 4.3a we show the time-resolved photoconductance of the trilayer system TiO<sub>2</sub>/PDI-CH<sub>3</sub>/F<sub>16</sub>ZnPc upon selective photoexcitation of the triplet sensitizer at 700 nm. The trilayer photoconductance exhibits a delayed rise over hundreds of microsec-

onds that we corrected for intrabandgap excitation of the  $\text{TiO}_2$ . The photoconductance due to intrabandgap excitation of the  $\text{TiO}_2$ , the original trilayer photoconductance and the subtracted trilayer photoconductance are shown in C.3 in Supporting information. In contrast, bilayer films of  $\text{TiO}_2/\text{PDI-CH}_3$  and

$\text{TiO}_2/\text{F}_{16}\text{ZnPc}$ , also shown in Figure 4.3a do not exhibit appreciable photoconductivity on the measured time scale, indicating that charge injection into  $\text{TiO}_2$  does not occur upon photoexcitation at 700 nm. The absence of electron injection in the  $\text{TiO}_2/\text{PDI-CH}_3$  bilayer is attributable to negligible optical absorption at 700 nm, although the electron affinity of  $\text{PDI-CH}_3$ , being 3.6 eV<sup>22–25</sup>, would allow charge injection into  $\text{TiO}_2$  with an electron affinity of 4.2 eV<sup>26</sup>. In the case of the  $\text{TiO}_2/\text{F}_{16}\text{ZnPc}$  bilayer, there is strong absorption by the  $\text{F}_{16}\text{ZnPc}$  at 700 nm, but its electron affinity of 5.1 eV<sup>21</sup> is larger than that of  $\text{TiO}_2$ , preventing direct charge injection into the  $\text{TiO}_2$  conduction band from either its lowest singlet or triplet state. Furthermore, we measured a trilayer system with reversed  $\text{PDI-CH}_3$  and  $\text{F}_{16}\text{ZnPc}$  ordering on the  $\text{TiO}_2$  substrate. As evident in Figure 4.3a, this trilayer does not show any delayed rise, indicating the necessity of the specific ordering of the trilayer structure, i.e. triplet sensitizer - triplet acceptor - electron acceptor. We conclude that a sequential stepwise mechanism must be operative in which 700 nm light is absorbed by  $\text{F}_{16}\text{ZnPc}$  forming an initial singlet excited state that is rapidly converted into a slightly lower-lying triplet state by intersystem crossing.<sup>27,28</sup> These triplet states are subsequently transferred to the  $\text{PDI-CH}_3$  layer by Dexter energy transfer, leading to an accumulation of low-lying triplet excited states in this layer. The energy of these triplet states is lower than in  $\text{F}_{16}\text{ZnPc}$ ; therefore direct injection into  $\text{TiO}_2$  is prohibited, as it is for  $\text{F}_{16}\text{ZnPc}$ .

However, in the  $\text{PDI-CH}_3$  layer triplet-triplet annihilation can occur, mediated by triplet exciton diffusion, leading to the formation of a singlet excited state with high enough energy to inject an electron into the  $\text{TiO}_2$  conduction band.<sup>29–31</sup> In a previous study we showed the injection of singlets in two  $\text{PDI}$  derivatives into  $\text{TiO}_2$  that was used to estimate exciton diffusion lengths.<sup>32</sup> It should be noted that a dynamic equilibrium exists between the singlet and triplet populations in  $\text{PDI-CH}_3$  that results from a balance in singlet fission and triplet-triplet annihilation upconversion. The dominant role of triplet exciton diffusion can be directly observed in the dynamics of charge injection in  $\text{TiO}_2$ .<sup>33</sup> This injection, and hence the growth of the photoconductivity, is seen to extend over hundreds of microseconds (see Figure 4.3a), much longer than the singlet lifetime.

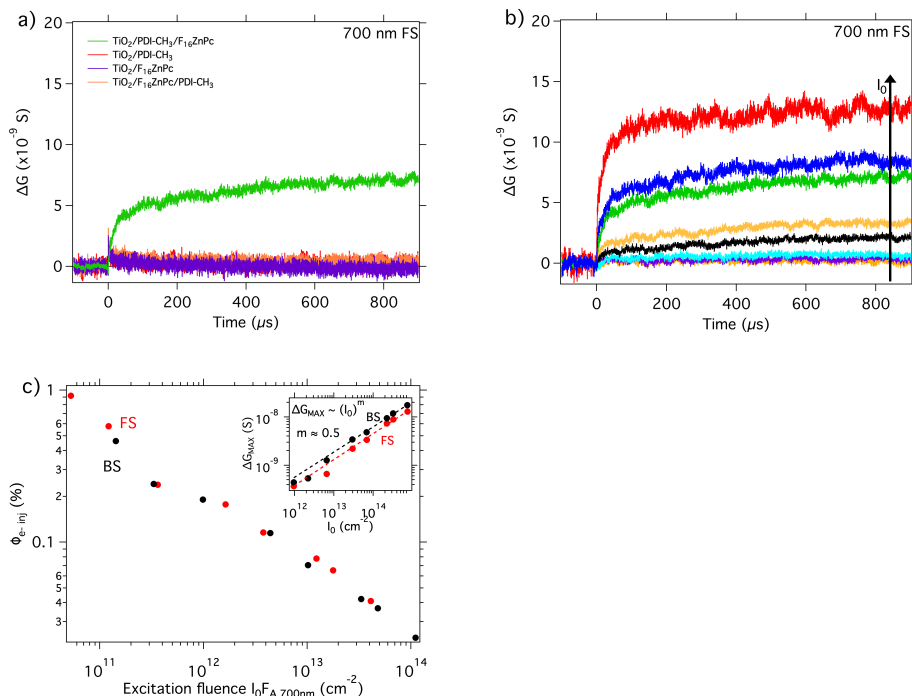


Figure 4.3: a) Photoconductivity transients of two trilayer systems,  $\text{TiO}_2/\text{PDI-CH}_3/\text{F}_{16}\text{ZnPc}$  (15/30 nm) and  $\text{TiO}_2/\text{F}_{16}\text{ZnPc}/\text{PDI-CH}_3$  (30/15 nm) and bilayer films of  $\text{PDI-CH}_3$  (15 nm),  $\text{F}_{16}\text{ZnPc}$  (30 nm), and  $\text{TiO}_2$  upon 700 nm excitation at an incident photon fluence of  $I_0 = 2.3 \cdot 10^{14}$  photons/ $\text{cm}^2$ . b) Fluence dependence of the  $\text{TiO}_2/\text{PDI-CH}_3/\text{F}_{16}\text{ZnPc}$  (15/30 nm) trilayer photoconductivity transients at 700 nm for  $I_0$  ranging from  $I_0 = 9.5 \cdot 10^{11} - 7.4 \cdot 10^{14}$  photons/ $\text{cm}^2$ . ac) Fluence-dependent yield of injection for the  $\text{TiO}_2/\text{PDI-CH}_3/\text{F}_{16}\text{ZnPc}$  trilayer. Inset: fluence dependence of the maximum signal  $\Delta G_{MAX}$ .

In Figure 4.3b we show the photoconductance in the trilayer as a function of the incident photon fluence upon excitation of the  $\text{F}_{16}\text{ZnPc}$  at 700 nm. An increase in the photon fluence increases the concentration of triplet states in the  $\text{F}_{16}\text{ZnPc}$ . This, in turn, leads to an increased  $\text{PDI-CH}_3$  triplet concentration after Dexter energy transfer from the  $\text{F}_{16}\text{ZnPc}$  that increases the formation of singlet states that can charge separate and inject an electron into the  $\text{TiO}_2$  conduction band. The maxima of the measured photoconductivity transients,  $\Delta G_{MAX}$ , are plotted logarithmically as a function of the incident photon fluence,  $I_0$ , in the inset of Figure 4.3c.  $\Delta G_{MAX}$  exhibits a square root dependence on the fluence over the entire fluence range. In contrast, solution-based triplet sensitizer and acceptor systems that involve monitoring the upconverter emission, display a quadratic-to-linear transition of emission intensity with excitation fluence.<sup>6</sup> The quadratic-to-linear transition is due to diffusion limited triplet-triplet encounters at low concentrations, while larger fluences saturate the triplet state concentration such that the TTA-UC becomes optimal and the emission intensity scales linearly with the fluence. The square root dependence of injection efficiency on excitation fluence can be attributed to a combination of two factors. First, the fluence range that we use to probe the photoconductivity is either not capable of saturating the  $\text{PDI-CH}_3$  with triplet states,

corresponding to the quadratic regime, or the lowest fluence used already ensures a saturated PDI-CH<sub>3</sub> triplet population, where all triplets find an annihilation partner and upconvert, corresponding to the linear regime. Second, the square root dependence indicates that a singlet decay process plays a role that may involve singlet fission which is known to occur effectively in PDI-CH<sub>3</sub>.<sup>34</sup> We exclude second-order exciton recombination processes in F<sub>16</sub>ZnPc as the cause of the square root fluence dependence as we do not observe a F<sub>16</sub>ZnPc exciton density dependence on the maximum photoconductance. We tested this by photoexciting the trilayer from the front side (FS) and the back side (BS), corresponding to an excitation profile with a maximum at the F<sub>16</sub>ZnPc/air and PDI-CH<sub>3</sub>/F<sub>16</sub>ZnPc interface, respectively. One would expect that excitation from the front, with creating a large concentration of F<sub>16</sub>ZnPc excitons at the F<sub>16</sub>ZnPc/air interface, allows for more exciton-exciton annihilation events to occur as excitons need to diffuse toward the PDI-CH<sub>3</sub>/F<sub>16</sub>ZnPc to transfer into the PDI-CH<sub>3</sub> in contrast to a reversed excitation profile in the back side excitation. However, we observe no such influence of excitation side on the  $\Delta G_{MAX}$  fluence dependence, implying that second-order exciton recombination is not playing a role in the F<sub>16</sub>ZnPc. Furthermore, diffusion limitations in the PDI-CH<sub>3</sub> and relatively low electron injection efficiency into the TiO<sub>2</sub> make it unlikely that second-order processes play a role in either PDI-CH<sub>3</sub> or TiO<sub>2</sub>.<sup>32</sup> From  $\Delta G_{MAX}$  we determined the yield of mobile electrons,  $\phi_{e-inj}$ , from absorbed photons as

$$\phi_{e-inj} = \frac{\Delta G_{MAX}}{\Sigma\mu\beta e I_0 F_A} \quad (4.1)$$

where  $\Sigma\mu = 2.3 \text{ cm}^2/(\text{Vs})$  is the mobility of electrons in the conduction band of TiO<sub>2</sub> measured upon front side illumination. We determined  $\Sigma\mu$  using the photoconductance values of bare TiO<sub>2</sub> as function of incident photon fluence as shown in Figure C.2.  $\beta$  is a geometrical factor,  $I_0$  the light intensity, and  $F_A$  the fraction of absorbed light at the wavelength of interest.<sup>35</sup> As shown in Figure 4.3c, the resulting  $\phi_{e-inj}$  reaches maxima of 0.92% upon front side excitation and 0.46% for back side excitation at the lowest fluence measured. The almost linear fluence dependence of  $\Delta G_{MAX}$  indicates that at the investigated excitation densities, all triplets find an annihilation partner and undergo TTA-UC, in analogy with the fluence dependence of the TTA-UC process in solution under high illumination conditions.<sup>6</sup> The observed trend for  $\phi_{e-inj}$ , *i.e.* decreasing upon increasing the fluence, can be explained by the occurrence of second-order recombination processes in the organic layers, *e.g.* singlet-singlet and/or triplet-triplet annihilation in PDI-CH<sub>3</sub>, and/or second-order interfacial recombination. The low  $\phi_{e-inj}$  is at least partially due to a low electron injection efficiency from PDI singlets that is commonly only a few percent.<sup>32</sup> We cannot determine the electron injection efficiency as photoexcitation of PDI-CH<sub>3</sub> leads to an unknown ratio of singlets and triplets and only singlets can charge separate. Therefore, we cannot quantify the amount of singlets that charge separate at the TiO<sub>2</sub> interface as function of the absorbed amount of photons, *i.e.* the singlet charge separation yield for this specific sample. As a result, isolation of the TTA-UC efficiency from  $\phi_{e-inj}$  by correcting for the singlet charge separation yield is also not possible. The presence of singlet fission in PDI-CH<sub>3</sub> also decreases the concentration of upconverted singlets and is another loss channel for the upconversion process. Finally, it is worth noting that TTA-UC requires two absorbed photons to generate one singlet

excited state in PDI-CH<sub>3</sub>, therefore defining the maximum number of injected electrons per absorbed photon to be 0.5. By setting this equal to 100% upconversion efficiency, we obtain an actual lower limit for the upconversion of 1.8%. In order to directly confirm the formation of low-lying triplet excited states in PDI-CH<sub>3</sub> upon 700 nm excitation of F<sub>16</sub>ZnPc, we have performed nanosecond transient absorption (TA) measurements. The changes in the optical absorption spectrum of PDI-CH<sub>3</sub> originating from ground-state bleach and triplet-triplet absorption are shown in Figure 4.4a. Upon 709 nm laser pulse excitation, a PDI-CH<sub>3</sub>/F<sub>16</sub>ZnPc bilayer on a sapphire substrate exhibits two characteristic transient absorption features: bleach of the ground-state absorption of PDI-CH<sub>3</sub> at 584 nm probe wavelength and a triplet-triplet absorption at 520 nm, as described previously.<sup>36</sup> This is corroborated by a decrease of the delayed rise in the photoconductance of the trilayer upon oxygen exposure that can be related to the well-known quenching of triplets by triplet oxygen (Figure C.4).<sup>36</sup> In the transient absorption spectra of the respective monolayers we do not observe any change in the optical absorption spectrum under identical conditions. In solution, the triplet lifetime of zinc phthalocyanines is on the order of hundreds of microseconds which makes the observation of a triplet absorption or ground-state bleach in the TA measurement likely.<sup>37</sup> However, the absence of a triplet absorption or ground-state bleach from F<sub>16</sub>ZnPc indicates that energy transfer is complete and occurs within a few nanoseconds. The temporal evolution of the PDI-CH<sub>3</sub> bleach in a PDI-CH<sub>3</sub> only upon 480 nm and a PDI-CH<sub>3</sub>/F<sub>16</sub>ZnPc film upon 709 nm excitation is shown in Figure 4.4b in red and black, respectively. The signal is characterized by an instrument-limited rise, indicating that the PDI-CH<sub>3</sub> triplets are formed on a sub-nanosecond time scale and have a lifetime of  $\tau_{T1} = 33$  ns.<sup>34</sup> The absence of an optical absorption caused by singlets or charge carriers at wavelengths above 620 nm indicates that triplets are the main photophysical species present in the PDI-CH<sub>3</sub> layer. This is corroborated by the identical decay of the bleach and triplet-triplet absorption shown in Figure C.5. The discrepancy between the 33 ns triplet lifetime from ns-TA and the microsecond rise in the photoconductance observed in TRMC can be explained by the fact that only a relatively small portion of triplet excitons can upconvert and inject charges on the microsecond time scale. These can easily be detected in the TRMC experiment but are below the detection limit in the time-resolved optical absorption experiment.

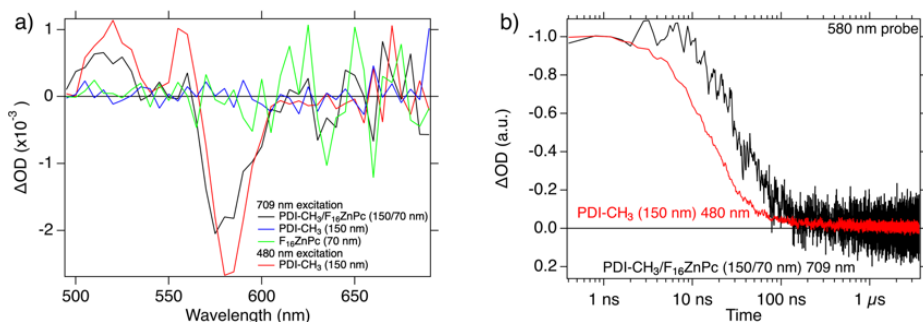


Figure 4.4: a) Transient absorption spectra at  $t = 26$  ns for a 150 nm thick PDI-CH<sub>3</sub> layer (blue), 70 nm thick F<sub>16</sub>ZnPc (green) and 150/70 nm PDI-CH<sub>3</sub>/F<sub>16</sub>ZnPc bilayer (black) excited at 709 nm, and 150 nm thick PDI-CH<sub>3</sub> excited at 480 nm (red). b) Temporal evolution of the PDI-CH<sub>3</sub> GSB in the PDI-CH<sub>3</sub> film upon 480 nm and PDI-CH<sub>3</sub>/F<sub>16</sub>ZnPc bilayer upon 709 nm excitation. The photon fluences upon excitation at 480 and 709 nm were  $2.1 \cdot 10^{15} \text{ cm}^{-2}$  and  $1.5 \cdot 10^{15} \text{ cm}^{-2}$ , respectively.

#### 4.4. CONCLUSIONS

In this work we have demonstrated the occurrence of the TTA-UC process in a TiO<sub>2</sub>/PDI-CH<sub>3</sub>/F<sub>16</sub>ZnPc trilayer, where the singlet excited state formed by upconversion directly injects into the TiO<sub>2</sub>. We show this by studying the photoconductance signal originating from selective 700 nm excitation of F<sub>16</sub>ZnPc and subsequent electron injection from PDI-CH<sub>3</sub> into the TiO<sub>2</sub> conduction band. We observe a delayed electron injection occurring over a millisecond time scale. From the agreement between transient absorption spectra of a PDI-CH<sub>3</sub> film and a PDI-CH<sub>3</sub>/F<sub>16</sub>ZnPc bilayer upon excitation of the sensitizer it is concluded that successful triplet energy transfer from the triplet sensitizer to the PDI acceptor occurs. The delayed rise of the TRMC signal is ascribed to PDI-CH<sub>3</sub> triplet states undergoing TTA-UC and resulting in upconverted PDI-CH<sub>3</sub> singlet states that charge separate at the TiO<sub>2</sub>/PDI-CH<sub>3</sub> interface. In our system the absorbed photon to injected electron efficiency reaches a maximum of 1.8%, the lower limit of the up-conversion efficiency. These results might be further improved by optimizing the thickness of the triplet sensitizer F<sub>16</sub>ZnPc and triplet acceptor PDI-CH<sub>3</sub>, in order to promote efficient exciton diffusion. Our experimental approach offers an effective tool to study the TTA-UC process in poorly luminescent materials, such as PDI-CH<sub>3</sub> thin films. The demonstrated trilayer structure may be tested in a photovoltaic device as the energy alignment would in principle allow hole and electron transport throughout the photoactive part.



## REFERENCES

- (1) Hanna, M.; Nozik, A. Solar conversion efficiency of photovoltaic and photoelectrolysis cells with carrier multiplication absorbers. *J. Appl. Phys.* **2006**, *100*, 074510.
- (2) Frazer, L.; Gallaher, J. K.; Schmidt, T. Optimizing the efficiency of solar photon up-conversion. *ACS Energ. Lett.* **2017**, *2*, 1346–1354.
- (3) Trupke, T.; Shalav, A.; Richards, B.; Würfel, P.; Green, M. Efficiency enhancement of solar cells by luminescent up-conversion of sunlight. *Sol. Energ. Mat. Sol. C.* **2006**, *90*, 3327–3338.
- (4) Hudry, D.; Howard, I. A.; Popescu, R.; Gerthsen, D.; Richards, B. S. Structure–Property Relationships in Lanthanide-Doped Upconverting Nanocrystals: Recent Advances in Understanding Core–Shell Structures. *Adv. Mater.* **2019**, 1900623.
- (5) Cheng, Y. Y.; Khoury, T.; Clady, R. G. C. R.; Tayebjee, M. J. Y.; Ekins-Daukes, N. J.; Crossley, M. J.; Schmidt, T. W. On the efficiency limit of triplet-triplet annihilation for photochemical upconversion. *Phys. Chem. Chem. Phys.* **2010**, *12*, 66–71.
- (6) Monguzzi, A.; Mezyk, J.; Scotognella, F.; Tubino, R.; Meinardi, F. Upconversion-induced fluorescence in multicomponent systems: Steady-state excitation power threshold. *Phys. Rev. B* **2008**, *78*.
- (7) Singh-Rachford, T. N.; Castellano, F. N. Photon upconversion based on sensitized triplet-triplet annihilation. *Coordin. Chem. Rev.* **2010**, *254*, 2560–2573.
- (8) Balushev, S.; Miteva, T.; Yakutkin, V.; Nelles, G.; Yasuda, A.; Wegner, G. Up-conversion fluorescence: Noncoherent excitation by sunlight. *Phys. Rev. Lett.* **2006**, *97*.
- (9) Gray, V.; Moth-Poulsen, K.; Albinsson, B.; Abrahamsson, M. Towards efficient solid-state triplet–triplet annihilation based photon upconversion: Supramolecular, macro-molecular and self-assembled systems. *Coordin. Chem. Rev.* **2018**, *362*, 54–71.
- (10) Hoseinkhani, S.; Tubino, R.; Meinardi, F.; Monguzzi, A. Achieving the photon up-conversion thermodynamic yield upper limit by sensitized triplet–triplet annihilation. *Phys. Chem. Chem. Phys.* **2015**, *17*, 4020–4024.
- (11) Khnayzer, R. S.; Blumhoff, J.; Harrington, J. A.; Haefele, A.; Deng, F.; Castellano, F. N. Upconversion-powered photoelectrochemistry. *Chem. Commun.* **2012**, *48*, 209–211.
- (12) Cao, X.; Hu, B.; Zhang, P. High upconversion efficiency from hetero triplet–triplet annihilation in multiacceptor systems. *J. Phys. Chem. Lett.* **2013**, *4*, 2334–2338.
- (13) Joarder, B.; Yanai, N.; Kimizuka, N. Solid-State Photon Upconversion Materials: Structural Integrity and Triplet–Singlet Dual Energy Migration. *J. Phys. Chem. Lett.* **2018**, *9*, 4613–4624.
- (14) Kim, J.-H.; Deng, F.; Castellano, F. N.; Kim, J.-H. High efficiency low-power upconverting soft materials. *Chem. Mater.* **2012**, *24*, 2250–2252.
- (15) Hill, S. P.; Dilbeck, T.; Baduelli, E.; Hanson, K. Integrated photon upconversion solar cell via molecular self-assembled bilayers. *ACS Energ. Lett.* **2016**, *1*, 3–8.



- (16) Hill, S. P.; Banerjee, T.; Dilbeck, T.; Hanson, K. Photon upconversion and photocurrent generation via self-assembly at organic–inorganic interfaces. *J. Phys. Chem. Lett.* **2015**, *6*, 4510–4517.
- (17) Dilbeck, T.; Hill, S. P.; Hanson, K. Harnessing molecular photon upconversion at sub-solar irradiance using dual sensitized self-assembled trilayers. *J. Mater. Chem. A* **2017**.
- (18) Ogawa, T.; Hosoyamada, M.; Yurash, B.; Nguyen, T.-Q.; Yanai, N.; Kimizuka, N. Donor–Acceptor–Collector Ternary Crystalline Films for Efficient Solid-State Photon Upconversion. *J. Am. Chem. Soc.* **2018**, *140*, 8788–8796.
- (19) Lin, Y. L.; Koch, M.; Brigeman, A. N.; Freeman, D. M.; Zhao, L.; Bronstein, H.; Giebink, N. C.; Scholes, G. D.; Rand, B. P. Enhanced sub-bandgap efficiency of a solid-state organic intermediate band solar cell using triplet–triplet annihilation. *Energ. Environ. Sci.* **2017**, *10*, 1465–1475.
- (20) Ekins-Daukes, N. J.; Schmidt, T. W. A molecular approach to the intermediate band solar cell: The symmetric case. *Appl. Phys. Lett.* **2008**, *93*, DOI: [Artn063507Doi10.1063/1.2970157](https://doi.org/10.1063/1.2970157).
- (21) Mayer, T.; Weiler, U.; Kelting, C.; Schlettwein, D.; Makarov, S.; Wohrle, D.; Abdallah, O.; Kunst, M.; Jaegermann, W. Silicon-organic pigment material hybrids for photovoltaic application. *Sol. Energ. Mat. Sol. C.* **2007**, *91*, 1873–1886.
- (22) Delgado, M. C.; Kim, E. G.; da Silva Filho, D. A.; Bredas, J. L. Tuning the charge-transport parameters of perylene diimide single crystals via end and/or core functionalization: a density functional theory investigation. *J. Am. Chem. Soc.* **2010**, *132*, 3375–87.
- (23) Danziger, J.; Dodelet, J. P.; Lee, P.; Nebesny, K. W.; Armstrong, N. R. Heterojunctions Formed from Phthalocyanine and Perylene Thin-Films - Photoelectrochemical Characterization. *Chem. Mater.* **1991**, *3*, 821–829.
- (24) Vivo, P.; Alekseev, A. S.; Kaunisto, K.; Pekkola, O.; Tolkki, A.; Chukharev, V.; Efimov, A.; Ihalainen, P.; Peltonen, J.; Lemmetyinen, H. Photoinduced electron transfer in thin films of porphyrin–fullerene dyad and perylenetetracarboxydiimide. *Phys. Chem. Chem. Phys.* **2010**, *12*, 12525–32.
- (25) Chis, V.; Mile, G.; Stiuflu, R.; Leopold, N.; Oltean, M. Vibrational and electronic structure of PTCDI and melamine-PTCDI complexes. *J. Mol. Struct.* **2009**, *924-26*, 47–53.
- (26) Gratzel, M. Photoelectrochemical cells. *Nature* **2001**, *414*, 338–44.
- (27) Frackowiak, D.; Planner, A.; Waszkowiak, A.; Boguta, A.; Ion, R. M.; Wiktorowicz, K. Yield of intersystem (singlet-triplet) crossing in phthalocyanines evaluated on the basis of a time in resolved photothermal method. *J. Photoch. Photobio. A* **2001**, *141*, 101–108.
- (28) Ruckmann, I.; Zeug, A.; Herter, R.; Roder, B. On the influence of higher excited states on the ISC quantum yield of octa- $\alpha$ -alkyloxy-substituted Zn-phthalocyanine molecules studied by nonlinear absorption. *Photochem. Photobiol.* **1997**, *66*, 576–584.
- (29) Brennaman, M. K.; Norris, M. R.; Gish, M. K.; Grumstrup, E. M.; Alibabaei, L.; Ashford, D. L.; Lapidus, A. M.; Papanikolas, J. M.; Templeton, J. L.; Meyer, T. J. Ultrafast,

- Light-Induced Electron Transfer in a Perylene Diimide Chromophore-Donor Assembly on TiO<sub>2</sub>. *J. Phys. Chem. Lett.* **2015**, *6*, 4736–4742.
- (30) Tachikawa, T.; Cui, S.-C.; Tojo, S.; Fujitsuka, M.; Majima, T. Nanoscopic heterogeneities in adsorption and electron transfer processes of perylene diimide dye on TiO<sub>2</sub> nanoparticles studied by single-molecule fluorescence spectroscopy. *Chem. Phys. Lett.* **2007**, *443*, 313–318.
- (31) Holman, M. W.; Liu, R.; Adams, D. M. Single-molecule spectroscopy of interfacial electron transfer. *J. Am. Chem. Soc.* **2003**, *125*, 12649–12654.
- (32) Felter, K. M.; Caselli, V. M.; Günbaş, D. D.; Savenije, T. J.; Grozema, F. C. Interplay between charge carrier mobility, exciton diffusion, crystal packing and charge separation in perylene diimide-based heterojunctions. *ACS Appl. Energ. Mater.* **2019**, DOI: [10.1021/acsaem.9b01490](https://doi.org/10.1021/acsaem.9b01490).
- (33) Kroeze, J. E.; Savenije, T. J.; Warman, J. M. Efficient Charge Separation in a Smooth-TiO<sub>2</sub>/Palladium-Porphyrin Bilayer via Long-Distance Triplet-State Diffusion. *Adv. Mater.* **2002**, *14*, 1760–1763.
- (34) Felter, K. M.; Dubey, R. K.; Grozema, F. C. Relation between molecular packing and singlet fission in thin films of brominated perylenediimides. *J. Chem. Phys.* **2019**, *151*, 094301.
- (35) Fravventura, M. C.; Deligiannis, D.; Schins, J. M.; Siebbeles, L. D. A.; Savenije, T. J. What Limits Photoconductance in Anatase TiO<sub>2</sub> Nanostructures? A Real and Imaginary Microwave Conductance Study. *J. Phys. Chem. C* **2013**, *117*, 8032–8040.
- (36) Ford, W. E.; Kamat, P. V. Photochemistry of 3,4,9,10-perylenetetracarboxylic dianhydride dyes. 3. Singlet and triplet excited-state properties of the bis(2,5-di-tert-butylphenyl)imide derivative. *J. Phys. Chem.* **1987**, *91*, 6373–6380.
- (37) Lang, K.; Mosinger, J.; Wagnerová, D. Photophysical properties of porphyrinoid sensitizers non-covalently bound to host molecules; models for photodynamic therapy. *Coordin. Chem. Rev.* **2004**, *248*, 321–350–1475.



# 5

## TRIPLET EXCITON DIFFUSION IN PDI THIN FILMS MEDIATED BY SINGLET FISSION

*There is an intimate link between unconventional photo-processes such as singlet fission (SF) and triplet-triplet annihilation upconversion (TTA-UC) and the diffusion of (triplet) excitons. There are considerable debates on these diffusion processes as it is not clear for instance how triplets move, as individual triplets or as correlated triplet pairs. In addition, there is very limited information about the temperature dependence of exciton diffusion, especially for triplet states. In this chapter we discuss the effect of temperature and molecular packing on exciton diffusion for thin films of a perylene diimide derivative. We have used the time resolved microwave photoconductivity technique to probe free mobile charge carriers that are generated at a planar heterojunction interface from excitons with a microsecond lifetime.*

## 5.1. INTRODUCTION

Exciton diffusion in organic semiconductors is a key process<sup>1</sup> in the design of optoelectronic devices based on organic semiconductors. A prime example where this plays a role is in organic photovoltaics (OPV) where generation of charge generally takes place at an interface between a donor and an acceptor material. This requires that excitons created far from this interface diffuse over longer distances to finally dissociate into charges. In many cases the relevant excitons are singlet excitons, as these are the ones that are initially formed on photoexcitation. However, recent developments in OPV<sup>2–4</sup> and silicon-based photovoltaics<sup>5</sup> aim to improve the device efficiency by the singlet fission process (SF). In SF the energy of a photo-excited molecule that is initially in the lowest singlet excited state ( $S_1$ ) splits up and distributes its energy between itself and a neighbouring ground-state molecule, with the net result two triplet first excited states ( $T_1$ ). This process therefore has the potential to exploit high-energy photons in the solar spectrum more efficiently by using the extra energy to generate an additional excited electron. Theoretically, SF can be a viable approach to overcome the Shockley–Queisser barrier. There are certain restrictions to the occurrence of SF in organic compounds. First of all, the  $S_1$  state should be at least twice as high in energy as  $T_1$ . In addition, the mutual orientation of neighboring molecules in the materials strongly affect the efficiency and rate of SF.<sup>6</sup> An important class of SF compounds in which the mutual orientation can be systematically varied are perylene diimides (PDIs). Theoretical<sup>7</sup> and experimental<sup>8–12</sup> studies, of which one is presented in Chapter 3, revealed that PDI compounds facilitate efficient SF in the solid-state owing to their favourably positioned energy levels and large electronic coupling values for SF. Quantum chemical simulations pointed to the relevance of the PDI imid substituent for the SF rate ( $k_{SF}$ ) and efficiency ( $\phi_{SF}$ ), as substituents in this position affect solid-state packing and the resulting electronic coupling of the dimer and morphology on a macroscale.<sup>7,11,13</sup> Upon utilizing the proper imid substituents, predicted  $k_{SF}$  as high as  $79 \text{ ps}^{-1}$  is achieved in PDIs, being at least one order of magnitude larger than what is observed in the well-known SF material anthracene, with efficiencies as high as 200%.<sup>11</sup> Such high efficiencies have been experimentally verified by fs-transient absorption spectroscopy measurements and appear quite common in PDIs.<sup>14</sup>

An important current question in the field of singlet fission is related to the diffusion of the excited state species that are formed. As discussed in Chapter 1, the initially formed  $S_1$  state is believed to be transformed into a correlated triplet pair state  $^1(TT)$  that is an overall singlet. This  $^1(TT)$  state can be a mixed state that still contains some singlet character and this coherent pair of triplets can diffuse as a single species. The  $^1(TT)$  state can eventually break up into two independent triplets that then diffuse according to the Dexter mechanism. A suitable measurement technique that can be used to indirectly probe exciton diffusion is the time resolved microwave photoconductivity (TRMC) technique that is based on the interaction of microwaves and a dielectric medium.<sup>15</sup> In TRMC we probe changes in conductivity of a sample by the formation of mobile free charge carriers that are formed upon diffusion of excitons towards an organic heterojunction interface of an electron or hole acceptor material where charge separation occurs. The TRMC technique has shown its use for determining exciton diffusion lengths ( $\Lambda_{EXC}$ ) in organic chromophores such as C60<sup>16</sup>, various porphyrins<sup>17,18</sup>, and for well-

packed PDIs ( $\Lambda_{EXC} = 60$  nm) as shown in Chapter 2. We recently performed a TRMC study on triplet-triplet annihilation upconversion (UC) in a trilayer heterojunction system composed of a smooth layer of the electron acceptor titanium dioxide ( $\text{TiO}_2$ ), a dimethyl imid substituted PDI derivative (PDI- $\text{CH}_3$ ) as triplet acceptor and a fluorinated zinc-phthalocyanine ( $\text{F}_{16}\text{ZnPc}$ ) as triplet sensitizer as discussed in Chapter 4. It is shown there, that photogenerated triplet excitons in  $\text{F}_{16}\text{ZnPc}$  transfer to PDI- $\text{CH}_3$  that subsequently upconvert to singlet states that, in contrast to the triplet states, charge separate at the  $\text{TiO}_2$ /PDI- $\text{CH}_3$  interface. A delayed rise is observed in the photoconductance signal on a time scale of hundreds of milliseconds that reflect the slow injection of electrons in  $\text{TiO}_2$ . This feature is attributed to long-lived triplet excitons in PDI- $\text{CH}_3$  that diffuse through the PDI layer and are transformed back into singlet states by triplet-triplet annihilation upconversion, upon which they charge separate.

In this chapter we examine the exciton diffusion process occurring in the PDI- $\text{CH}_3$  layer in more detail and investigate how the diffusion of photogenerated excitons in PDI- $\text{CH}_3$  is affected by temperature. Planar heterojunction bilayer systems of  $\text{TiO}_2$  and PDI- $\text{CH}_3$  are deposited and the injection of charges into  $\text{TiO}_2$  upon photoexcitation of PDI- $\text{CH}_3$  is followed in time by TRMC measurements. By observing the effect of temperature on the kinetics and yield of mobile and free electrons in  $\text{TiO}_2$ , we can indirectly obtain information on the temperature dependence of the exciton diffusion process after analysis of the carrier decay with a kinetic model of exciton dynamics.

A pronounced delayed rise is observed in the photoconductance in time scales of tens to hundreds of microseconds. This is way beyond the lifetime of singlet excited state and therefore has to involve other species, specifically triplets. We attribute the delayed injection of charges in  $\text{TiO}_2$  to charge separation of singlets that are in a dynamic equilibrium between singlet and electronically coherent triplet pair states as a result of the singlet fission. We propose that long lived triplet pair states are responsible for the observed microsecond singlet lifetime. We test our hypothesis with a one-dimensional kinetic model that includes exciton diffusion, singlet-singlet annihilation, singlet fission, triplet pair fusion and triplet pair decoherence. The model indicates that a triplet pair state may be responsible for the observed delayed growth in the photoconductance based on the value of the modelled exciton diffusion coefficient.

## 5.2. EXPERIMENTAL SECTION

### SAMPLE PREPARATION AND CHARACTERIZATION

We study planar heterojunction systems composed of a thin-film bilayer of 100 nm N, N'-dimethyl-3,4,9,10-perylenedicarboximide (PDI- $\text{CH}_3$ ) on top of a smooth polycrystalline  $\text{TiO}_2$  (~90 nm thickness) film on fused silica substrates (ESCO, 12 x 25 x 1 mm). The polycrystalline  $\text{TiO}_2$  coatings on fused silica were purchased from *Everest Coatings Inc.* and annealed for two hours at 450°C in a furnace to improve stoichiometry and conductivity prior to deposition. PDI- $\text{CH}_3$  was purchased from Sigma-Aldrich and used without further treatment. Prior to evaporation, the  $\text{TiO}_2$  film was plasma cleaned (two minutes, in air plasma) to clean and activate the surface. Thermal evaporation was carried out in an *AJA ATC Orion evaporator* during which the powders were heated beyond the sublimation temperature under high vacuum conditions ( $10^{-7}$ - $10^{-6}$  mbar) to the desired

evaporation rate of 0.3 Å/s. The deposition rate was monitored using a quartz micro-crystal balance and the sample holder was rotated at 25 rpm to ensure film homogeneity. The films were heated on a hotplate in a N<sub>2</sub> environment for 90 minutes to ensure the removal of oxygen and improve molecular packing. The thin film topology was measured using atomic force microscopy (AFM) on an *NTEGRA Prima AFM* operated in tapping mode, and the crystallinity was studied using X-ray diffraction measurements in Bragg-Brentano geometry with a *Brüker D8* X-ray diffractometer (Co K $\alpha$ 1 radiation,  $\lambda = 1.79$  Å) and analysed with the Brüker program *EVA*. The steady state optical absorption measurements were performed in a *Perkin Elmer Lambda 1050* spectrometer with the sample placed inside an integrating sphere to measure attenuation.

### FLASH PHOTOLYSIS MICROWAVE CONDUCTIVITY

The details and basic principles of the home-build TRMC setup that were used for this work have been described before.<sup>19</sup> In summary, in the TRMC setup, samples are photoexcited with a 3.5 ns wide laser pulse (tuneable from 250-2100 nm) under continuous exposure to an 8.5 GHz AC microwave field. Free mobile charge carriers that are generated upon photoexcitation absorb microwaves and giving rise to a temporal decrease in microwave power ( $\Delta P/P$ ) which is measured by a microwave detector.  $\Delta P/P$  can be related to a transient change in the sample photoconductivity  $\Delta G(t)$  using a predefined microwave dependent sensitivity factor  $K$ , giving:

$$\frac{\Delta P(t)}{P} = -K\Delta G(t) \quad (5.1)$$

The maximum in the photoconductivity  $\Delta G_{MAX}$  is related to the product of the separation yield  $\eta$  and mobility  $\mu_i$  of free and mobile charge carrier (*i.e.* electrons and holes), according to:

$$\frac{\Delta G_{MAX}}{\beta e I_0} = \eta \sum_i \mu_i \quad (5.2)$$

where  $\beta$  is the ratio between the inner width and length dimensions of the microwave cavity,  $e$  is the elementary charge and  $I_0$  the incident photon fluence. The sample is loaded into a nitrogen-filled microwave cavity cell that allows microwaves to resonate and interact optimally with the sample. Measuring under microwave resonant conditions in the cavity cell improves the signal-to-noise ratio of the photoconductivity signal, but increases the instrumental response time to 16 ns.

## 5.3. RESULTS AND DISCUSSION

### CHARGE SEPARATION AND EXCITON DIFFUSION IN THE TiO<sub>2</sub>/PDI-CH<sub>3</sub> HETEROJUNCTION

In order to investigate the diffusion of excitons in PDI-CH<sub>3</sub> and the subsequent charge separation at the interface we have performed microwave conductivity measurements on a bilayer heterojunction system composed of a 50 nm thick PDI-CH<sub>3</sub> layer on top of a smooth polycrystalline TiO<sub>2</sub> film. The schematic overview of the system and the relevant diffusion/kinetic processes is shown in Figure 5.1a. The lowest unoccupied orbital of PDI and the CB energy of TiO<sub>2</sub> have an energy offset of  $-3.6\text{ eV} - 4.25\text{ eV} = 0.65\text{ eV}$  that should ensure charge separation from PDI-CH<sub>3</sub> singlet excitons. We experimentally confirm charge separation at the heterojunction interface by measuring the photoconductance signal upon selective excitation of PDI-CH<sub>3</sub> at 500 nm of single layers of PDI-CH<sub>3</sub> and TiO<sub>2</sub> film and a TiO<sub>2</sub>/PDI-CH<sub>3</sub> bilayer. The bilayer is photoexcited from the side of the TiO<sub>2</sub>, which we refer to as the 'back' side (BS), so that the majority of excitons is created at the TiO<sub>2</sub>/PDI-CH<sub>3</sub> interface. As the mobility of holes in the organic layer is orders of magnitude lower than the electron mobility in TiO<sub>2</sub>, we exclusively probe the photoconductance due to mobile electrons in TiO<sub>2</sub>.<sup>20</sup> As shown in Figure 5.1b, we observe a negligible photoconductance in PDI-CH<sub>3</sub> (red) indicating that either no charges are formed, or that they have a very low mobility. Photoexcitation of the TiO<sub>2</sub> layer leads to a low conductance of  $1 \cdot 10^{-2}\text{ cm}^2/\text{Vs}$  in TiO<sub>2</sub> (blue) due to spurious absorption at 500 nm.<sup>17</sup> A dramatically different results is obtained for the bilayer, indicated as the black curve in Figure 5.1b. The maximum photoconductance in the TiO<sub>2</sub>/PDI-CH<sub>3</sub> bilayer (black) is roughly three times higher than in single layer TiO<sub>2</sub> and exhibits a significant rise in the photoconductance over tens of microseconds. The delayed rise of the photoconductance in the TiO<sub>2</sub>/PDI-CH<sub>3</sub> bilayer can be caused by three processes. The first is that an equilibrium between trapping and detrapping of electrons in TiO<sub>2</sub> occurs, where a gradual release of trapped electrons causes the photoconductance to increase over time as is observed in so called fluorescence blinking.<sup>21</sup> We discard this option however, because in previous TRMC measurements on TiO<sub>2</sub> based bilayers we never observed such delayed rise signals and this is supposed to be an intrinsic feature of the TiO<sub>2</sub>. Furthermore, the time scale of the blinking is commonly in the order of seconds, while we measure a rise on a microsecond time scale. The second explanation for the delayed rise is the injection of long-lived charge carriers, *i.e.* electrons in PDI-CH<sub>3</sub> that form upon photoexcitation and charge separate within the PDI-CH<sub>3</sub> itself. Electrons in PDIs are known to have microsecond lifetimes.<sup>22</sup> The slow charge carrier diffusion and long lifetime can therefore cause the delayed injection. However, the poor photoconductance and rapid decay of photo-generated charge carriers in the PDI-CH<sub>3</sub> single layer, as described above makes this option unlikely. The third and more likely cause is the existence of long-lived excitons that slowly migrate to the TiO<sub>2</sub>/PDI-CH<sub>3</sub> interface where electrons are injected into TiO<sub>2</sub>. This mechanism is confirmed by a previous TRMC study on a bilayer system of TiO<sub>2</sub> and a palladium based porphyrin that showed a delayed rise of the photoconductance over tens of microseconds and was attributed to long-distance triplet diffusion in the porphyrin to the heterojunction interface that led to successfully injected an electron into TiO<sub>2</sub> upon charge separation.<sup>23,24</sup> The porphyrin triplets were formed



after photoexcitation and subsequent intersystem crossing that occurs efficiently in the porphyrin due to the large spin orbit coupling induced by the heavy-metal palladium in the center. The delayed rise of the photoconductance in our bilayer system is also similar to what was observed in the  $\text{TiO}_2/\text{PDI-CH}_3/\text{F}_{16}\text{ZnPc}$  trilayer described in Chapter 4. In that system, triplet excitons were created in triplet sensitizer,  $\text{F}_{16}\text{ZnPc}$ , and transferred via Dexter energy transfer into the upconverter material  $\text{PDI-CH}_3$ . However, in the current experiment we directly photoexcite the  $\text{PDI-CH}_3$ . Therefore, we can only explain the delayed rise in the  $\text{TiO}_2/\text{PDI-CH}_3$  bilayer by assuming that triplets are formed in the  $\text{PDI-CH}_3$  itself, similar as in the palladium porphyrin. As previously shown in literature and in this thesis singlet fission occurs in  $\text{PDI-CH}_3$ , which is the likely process by which the  $\text{PDI-CH}_3$  triplets are formed,<sup>8,10</sup> since intersystem crossing has been shown to be negligible in PDIs.<sup>25</sup> As we previously attributed the delayed rise in the  $\text{TiO}_2/\text{PDI-CH}_3/\text{F}_{16}\text{ZnPc}$  trilayers in Chapter 4 to triplets in  $\text{PDI-CH}_3$  that upconvert on a time scale of hundreds of microseconds, we propose the following mechanism for the bilayer systems in this chapter: 1) Photoexcitation of  $\text{PDI-CH}_3$  generates singlet excitons, that 2) undergo rapid singlet fission (on a ps-time scale) to triplets; 3) these triplets, in turn can go back to the singlet state via UC resulting in a dynamic equilibrium between singlets and triplets. 4) Both singlets and triplets diffuse in the  $\text{PDI-CH}_3$  towards the  $\text{TiO}_2/\text{PDI-CH}_3$  interface, but 5) only singlets have enough energy to inject an electron into  $\text{TiO}_2$  giving rise to the photoconductance signal.

In Figure 5.1c the normalised photoconductance measured for the  $\text{TiO}_2/\text{PDI-CH}_3$  bilayer is shown as function of time for varying of the photon fluences. At low photon fluences the photoconductance rises over the first 80 microseconds after which the conductivity starts to decay. At higher photon fluences, the delayed component becomes less pronounced and almost complete disappears for the highest fluences used. The decrease at higher fluence is caused by increasingly dominant second-order recombination processes of both free charge carriers and excitons.

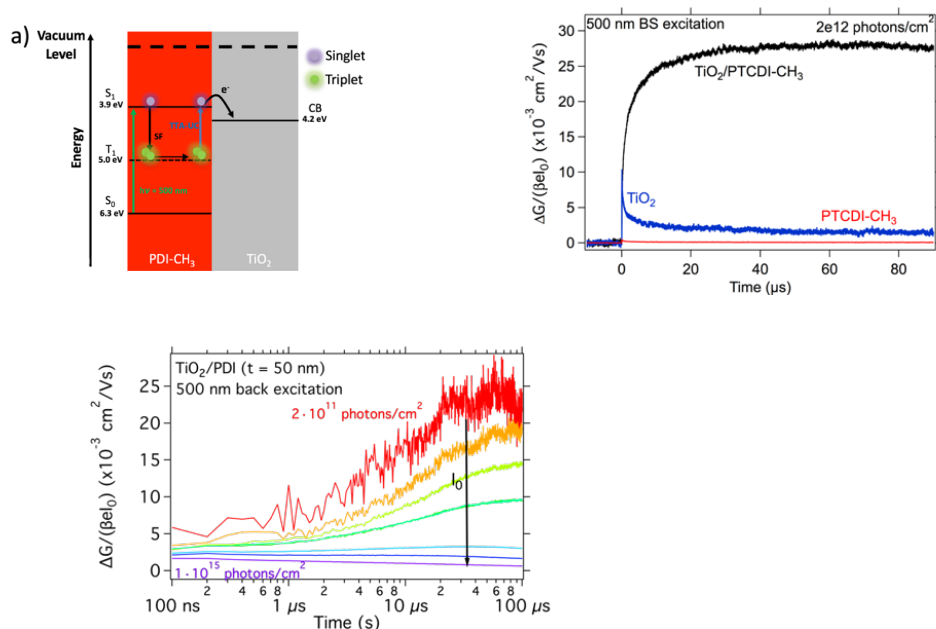


Figure 5.1: a) Energy diagram of the  $\text{TiO}_2$  CB level and singlet and triplet energy in PDI- $\text{CH}_3$ . b) TRMC transients of single  $\text{TiO}_2$  (blue), PDI- $\text{CH}_3$  (red) and  $\text{TiO}_2/\text{PDI-CH}_3$  (50 nm) bilayer (black) sample upon 500 nm backside photoexcitation at  $2 \cdot 10^{12}$  photons/ $\text{cm}^2$ . c) TRMC traces of the  $\text{TiO}_2/\text{PDI-CH}_3$  (50 nm) bilayer at different photon fluences, ranging from  $2 \cdot 10^{11}$  to  $1 \cdot 10^{15}$  photons/ $\text{cm}^2$ .

### TEMPERATURE DEPENDENT PHOTOCONDUCTANCE

In order to investigate the effect of temperature on diffusion, we have varied the temperature from  $-100$  to  $60^\circ\text{C}$ . The photoconductance transients belonging to an incident photon flux of  $1 \cdot 10^{12}$  photons/ $\text{cm}^2$  are shown for several temperatures in this range in Figure 5.2. Upon increasing the temperature from  $-100$  to  $60^\circ\text{C}$ , we observe an increase in the absolute photoconductance by almost an order of magnitude, which is accompanied by a shift of the maximum photoconductance  $\Delta G_{MAX}$  to shorter times. At  $60^\circ\text{C}$  the delayed growth in the photoconductance shows a maximum at 7 microseconds, after which the conductance starts decaying because of charge carrier recombination. We verified that the increasing trend is not caused by temperature dependent electronic properties of the  $\text{TiO}_2$  as the photoconductance in a single layer of  $\text{TiO}_2$  upon direct band gap excitation (300 nm) decreases upon increasing the temperature (Figure D.4). At low temperatures, sub-nanosecond formation of microsecond-lived self-trapped excitons (STEs) occurs that should decrease the amount of free charge carriers which is opposite to what we observe in single layer  $\text{TiO}_2$ .<sup>26</sup> It is therefore more likely that it is not the yield, but the mobility of the  $\text{TiO}_2$  charges that decreases upon increasing the temperature.<sup>27</sup> The increased photoconductance and decreased electron mobility in  $\text{TiO}_2$  point to a larger charge separation efficiency at higher temperatures, caused by a higher yield of excitons that reach the interface and inject charges. This can be due to a temperature effect on three different processes that are involved: temperature activated charge injection, a temperature effect on the singlet fission process leading to more triplets, or a thermal

effect on exciton diffusion. As the driving force for charge separation is already large, it is not likely that this is the cause of the increased photoconductance. An increased SF efficiency or rate would shift the singlet-triplet equilibrium to the triplet side. As triplets have a significantly lower diffusion constant than singlets this would move the maximum in the photoconductance to later times, contrary to what we observe. We therefore attribute the higher photoconductance and earlier maximum in  $\Delta G_{MAX}$  at higher temperatures to faster exciton diffusion, which readily follows from the temperature dependence of Dexter energy transfer of triplets<sup>28</sup> for two reasons: 1) larger diffusion coefficients increase the fraction of excitons that reach the  $\text{TiO}_2/\text{PDI-CH}_3$  interface and can charge separate, leading to a higher photoconductance, 2) and in addition, the majority of excitons has charge separated earlier for the same reason, shifting the maximum in conductivity to earlier times.

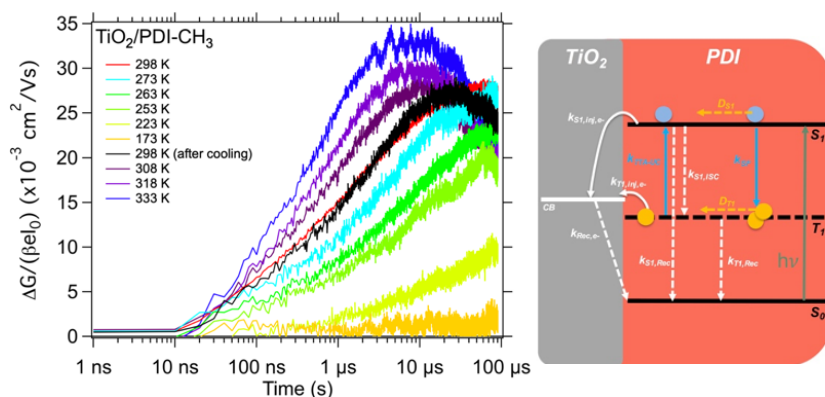


Figure 5.2: a) TRMC transients of a  $\text{TiO}_2/\text{PDI-CH}_3$  (50 nm) bilayer sample upon 500 nm backside photoexcitation at  $1 \cdot 10^{12}$  photons/ $\text{cm}^2$ . Schematic illustration of the singlet, triplet and electron processes considered in the model described by equations 5.3-5.5.

## KINETIC MODEL OF EXCITON DIFFUSION

In order to gain more insight in the temperature dependent processes that occur in the bilayer systems discussed above, we qualitatively analyse the observed trends using a one dimensional kinetic diffusion model in which the processes involving singlets, triplet pairs and electrons in  $\text{TiO}_2$  are described by the rate equations 5.3, 5.4, and 5.5. The model accounts for singlet diffusion and diffusion of the correlated triplet pair states characterized by the temperature dependent diffusion constant  $D_{S1}$  and  $D_{TT}$ , respectively. Electron injection into  $\text{TiO}_2$  from  $\text{PDI-CH}_3$  singlets is characterized by the rate  $k_{inj,S1,X=L}$ , where  $X = L$  indicates that electron injection only occurs at the  $\text{TiO}_2/\text{PDI-CH}_3$  interface. As argued in Chapter 4 for the  $\text{TiO}_2/\text{PDI-CH}_3/\text{F}_{16}\text{ZnPc}$  trilayer, triplets do not have sufficient energy to inject charges into  $\text{TiO}_2$ . Therefore, we only consider singlets being able to dissociate at the interface with  $\text{TiO}_2$ . Furthermore, we include rates for singlet fission ( $k_{SF}$ ), triplet pair fusion ( $k_{fusion}$ ), triplet pair dissociation ( $k_{TTdis}$ ), to transform the corrected triplet pair into two independent triplet excitons, and singlet-singlet annihilation ( $k_{SSA}$ ). We furthermore describe the decay of electrons injected into

TiO<sub>2</sub> as a first order decay process with rate  $k_{e,rec}$ .

$$\begin{aligned} \frac{\partial[S_1(x, t)]}{\partial t} = & G(x, t) + D_{S_1} \frac{\partial^2[S_1(x, t)]}{\partial x^2} - [S_1(x, t)]k_{inj,S_1,X=L} \\ & - [S_1(x, t)](k_{SF} + k_{s_1,rec} + [S_1(x, t)]k_{SSA}) + [T_{pair}(x, t)]k_{fusion} \end{aligned} \quad (5.3)$$

$$\begin{aligned} \frac{\partial[T_{pair}(x, t)]}{\partial t} = & D_{TT} \frac{\partial^2[T_{pair}(x, t)]}{\partial x^2} + [S_1(x, t)]k_{SF} - [T_{pair}(x, t)]k_{fusion} \\ & - [T_{pair}(x, t)]k_{TDis} \end{aligned} \quad (5.4)$$

$$\frac{\partial[e_{TiO_2}(t)]}{\partial t} = [S_1(x, t)]k_{inj,S_1,X=L} - [e_{TiO_2}(t)]k_{e,rec} \quad (5.5)$$

In Figure 5.3 we systematically explore the effects of the different kinetic parameters to obtain insight in the effects that play a deciding role in the temperature dependent conductivity experiments that we describe above. The full list of parameter values used can be found in Table D.1. In Figure 5.3a the decay rate of the initially formed singlet is varied, while all other parameters are kept the same. The decay rate obtained from fluorescence life time experiments at room temperature is 700 ps ( $1.4 \cdot 10^9 \text{ s}^{-1}$ ), while at 333 K and 93 K the fluorescence life time is 550 ps ( $1.8 \cdot 10^9 \text{ s}^{-1}$ ) and 14 ns ( $7.1 \cdot 10^7 \text{ s}^{-1}$ ), respectively, as based on the results presented in Chapter 3. Increasing the decay rate leads to a lower overall simulated conductivity because more singlets start to decay before they can transform into long-lived triplets, but no significant shift in the maximum is observed. Moreover, increasing the decay rate, as may be expected to happen on increasing the temperature (see also Chapter 3), leads to a lowering of the maximum conductivity. The latter is opposite to the observed experimental trend. The decay of singlets by second-order singlet-singlet annihilation can also be discarded as shown in Figure 5.2b. Typical parameters for singlet-singlet annihilation for singlet crystal tetracene, rubrene and TIPS-pentacene are  $k_{SSA} = 1.6 \cdot 10^{-9}$ ,  $1.6 \cdot 10^{-10}$  and  $2.4 \cdot 10^{-8} \text{ cm}^3/\text{s}$ .<sup>29</sup> For PDIs, a time dependent annihilation rate was found to be  $k_{SSA} = 1.90 \cdot 10^{-12}$  and  $1.55 \cdot 10^{-15} \text{ cm}^3/\text{s}$  at one femtosecond and from one second onwards, respectively.<sup>30</sup> We varied the second-order rate from  $k_{SSA} = 1.0 \cdot 10^{-15}$ - $1.0 \cdot 10^0 \text{ cm}^3/\text{s}$  but did not observe any influence on the simulated conductivity signal as the concentration of singlet is always very low. This is caused by the low excitation intensity and SF efficiency. In Figure 5.3c, the first-order rate for recombination of the electrons in TiO<sub>2</sub> is varied from  $k_{e,rec} = 5 \cdot 10^2$ - $5 \cdot 10^5 \text{ s}^{-1}$ . It is clear from this graph, that an increase of this decay rate, as might be expected at higher temperature, does lead to a shift of the maximum to earlier times, but this is also accompanied by an overall decrease in the magnitude of the conductivity. The latter is opposite to our experimental observations presented above and hence this can not be the sole reason for the trends observed in the TRMC measurements. We initially modelled a system in which separated triplet states were formed directly via singlet fission from singlets without the involvement of a triplet pair intermediate. In this approach, forming back the singlets would have to occur by homogeneous triplet-triplet annihilation of the separated triplets. However, this variant of the model did not result in values

that accurately predicted the overall kinetics of a delayed photoconductivity transients because of the unrealistic triplet-triplet annihilation rate constant that would have to be used for the low excitations densities that are used in the experiments. We instead assume a triplet pair state term that can diffuse but can not directly inject electrons at the interface. The triplet pair state can fuse to form back a singlet or dissociate forming two uncorrelated triplets that cannot undergo upconversion, *i.e.* second-order triplet recombination leading to the formation of the triplet pair state. The singlet fission and triplet pair fusion processes lead to an equilibrium that determines the overall ratio of singlets to triplet pair states. If the singlet fission rate is increased, relatively more triplet pair states are formed, while a larger triplet fusion rate increases the singlet concentration. In Figure 5.3d we show the effect of changing the absolute value of  $k_{SF}$  and  $k_{FUS}$  and their ratio. We increased  $k_{SF}$  from  $1 \cdot 10^6$  to  $1 \cdot 10^9 \text{ s}^{-1}$  at constant  $k_{FUS} = 1 \cdot 10^7 \text{ s}^{-1}$  leading to an decrease in the prompt rise in the electron concentration occurring  $< 10 \text{ ns}$ , while the electron kinetics from  $600 \text{ ns}$  and onwards remains unchanged. This change in the prompt contribution in the conductivity originates from a lower initial singlet concentration that undergoes charge separation on the nanosecond time scale. At later times, the kinetics remain unchanged because decay of the injected electrons occurs on a microsecond time scale, while the total triplet concentration remains similar in all cases and does not affect the growth in the electron concentration. Similarly, at a constant and high  $k_{SF} = 1 \cdot 10^{10} \text{ s}^{-1}$ , we observe the same trend but now more pronounced, as the singlet fission kinetics is greater than the used electron injection rate and competes with a negligible prompt photoconductivity when the equilibrium is strongly shifted to the triplet pairs. In Figure 5.3d we show the effect of changing the absolute value and ratio of the diffusion constants of the singlet and triplet pair state where we used singlet and triplet exciton diffusion constants that are typical for organic semiconductors.<sup>1</sup> Upon increasing the value of  $D_{S1}/D_{TT}$ , at  $k_{SF}/k_{FUS} = 1 \cdot 10^{10}/1 \cdot 10^7 \text{ s}^{-1}$  and fixed  $D_{TT} = 1 \cdot 10^{-11} \text{ m}^2/\text{s}$ , increases the maximum photoconductivity but does not alter the position of the maximum. This can be explained by considering the excitation profile that is maximal at the  $\text{TiO}_2/\text{PDI-CH}_3$  interface since we excited the sample from the backside, through the  $\text{TiO}_2$  layer. If the overall exciton diffusion coefficients are low, much of the large initial concentration of excitons remains at the interface and may participate in electron injection. However, when exciton diffusion coefficient is increased, the interfacial concentration drops fast owing to exciton diffusion away from the  $\text{TiO}_2/\text{PDI-CH}_3$  interface. Therefore, we observe the general trend that higher diffusion constants, irrespective of type, gives lower photoconductivity. A smaller  $D_{TT}$  ( $1 \cdot 10^{-13} \text{ m}^2/\text{s}$ ) and changing  $D_S$  gives more significant effects on the photoconductivity, compared to changing  $D_S$  with a large  $D_{TT}$  value ( $1 \cdot 10^{-8} \text{ m}^2/\text{s}$ ). This is attributed to a smaller overall diffusion coefficient that slows the formation of an equilibrium of singlet and triplet pair state concentration in the film. In this scenario, a smaller change in either  $D_S$  or  $D_{TT}$  is necessary to bring about a change in the overall conductivity. It is the formation of an equilibrium exciton concentration in the  $\text{PDI-CH}_3$  film that dominates the photoconductivity kinetics at microsecond lifetime making it identical within the used parameter space. Exciton diffusion in organic semiconductors, such as Dexter transfer, is known to be temperature activated.<sup>1</sup> Therefore, a higher temperature would lead to a larger triplet diffusion coefficient. We assume that the triplet pair state diffuses like an isolated triplet. However,

increasing the triplet diffusion constant in the model does not increase the photoconductivity nor does it shift the maximum. As such, varying the exciton diffusion coefficient does not account for the increased signal height at higher temperatures. This leads to the conclusion that also other parameters are temperature dependent. In addition, other processes than the ones included in this model may play an important role. One example of this was discussed in Chapter 3 where we observed the dominant presence of excimers in bay-area unsubstituted PDIs that affected singlet fission. We performed temperature dependent photoluminescence experiments and found that the formation of long lived excimer states is temperature dependent. As such, the question rises, how excimers can be included in this model. Excimers may form a dynamic equilibrium with singlets that is temperature dependent. Since the photoluminescence lifetime increases at lower temperatures, excimer formation seems exothermic, while singlet fission in PDIs is known to be endothermic. Increasing the sample temperature may therefore shift the equilibrium to singlets that undergo fast singlet fission. However, no sufficient knowledge about excimer diffusion in PDIs is currently available to incorporate this in a meaningful way in the model. It is uncertain whether excimers possess enough energy to charge separate, even though they are more stable states than singlets and are likely to do this slower than singlets. We simulated the effect of temperature on temperature activated exciton diffusion and temperature deactivated singlet lifetime, where we assumed that the increased photoluminescence lifetime at lower temperatures is related to a longer singlet lifetime, although this is not necessarily the case. We plot the results in Figure 5.3f and observe that a lower temperature, corresponding to a smaller  $k_{S1,rec}$  and  $D_S$  and  $D_{TT}$  gives a higher photoconductivity, contrary to what we experimentally observe. More experiments, such as transient absorption are required to obtain knowledge on temperature dependent exciton dynamics on a femto- to nanosecond time scale. Another approach to obtain more knowledge on the charge carrier and exciton dynamics is to perform temperature dependent measurements on a tetra-brominated PDI that does not form excimers. In addition, measuring the temperature dependence of PDI triplet states that originate from a triplet sensitized, may shed light on the temperature dependence of a system in which predominantly triplet states exist.

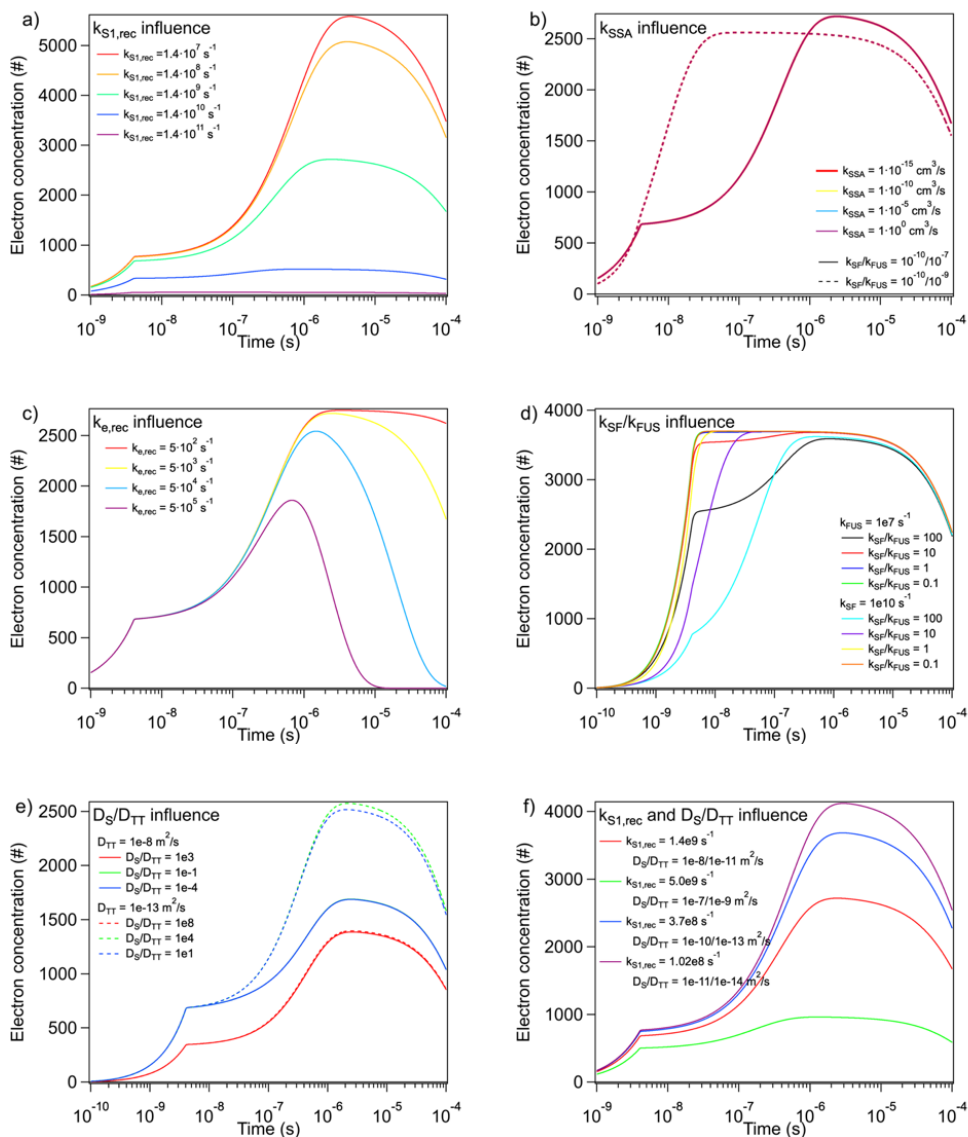


Figure 5.3: Modelled electron concentration kinetics in the  $\text{TiO}_2$  film based on equations 5.3-5.5 and using the input values provided in Table D.1 and varying values of  $k_{S1,rec}$ ,  $k_{SSA}$ ,  $k_{e,rec}$ , the ratio  $k_{SF}/k_{FUS}$ , the ratio  $D_S/D_{TT}$  and a mixture of varying  $k_{S1,rec}$  and  $D_S/D_{TT}$  ratio in Figures a-f, respectively.

## 5.4. CONCLUSIONS

In this study we investigated charge separation of excitons in a dimethyl-imid substituted perylene diimide derivative, PDI-CH<sub>3</sub> at the interface with smooth polycrystalline TiO<sub>2</sub>. Time resolved microwave conductivity measurements show a delayed rise of the photoconductance upon direct excitation of PDI-CH<sub>3</sub>. This is attributed to long-lived excitons that diffuse towards the interface on a microsecond time scale. These long-lived excitons are argued to contain triplet character as they are much longer lived than singlet. They are formed from singlets via the singlet fission process. Once the excitons arrive at the interface with the electron accepting TiO<sub>2</sub> layer, charge separation can take place, however, only the singlet excitons have sufficient energy to inject electrons. In order to unravel the mechanism of the exciton migration process, we have investigated how temperature affects the photoconductance. We observe an increased maximum photoconductance on increasing the temperature, which is accompanied by a shift in the maximum in photoconductance to earlier times. To gain more insight in the different processes that govern the photoinduced conductivity in these bilayer systems we have established a one-dimensional kinetic diffusion model for PDI-CH<sub>3</sub> excitons. This model only yields reasonable results if we assume that the triplets formed on singlet fission mainly exist as correlated triplet pairs rather than individual triplets. These triplet pairs are in equilibrium with the singlets that can inject into the TiO<sub>2</sub>. By varying the different parameters we conclude that the strong effect of temperature on the photoinduced conductivity is more complicated than involving a single temperature activated process such as exciton diffusion. It is more likely that more temperature dependent terms play a role, although we could exclude singlet recombination, electron recombination and singlet-singlet annihilation as the responsible temperature activated processes using our model.





## REFERENCES

- (1) Mikhnenko, O. V.; Blom, P. W.; Nguyen, T.-Q. Exciton diffusion in organic semiconductors. *Energ. Environ. Sci.* **2015**, *8*, 1867–1888.
- (2) Reuswig, P. D.; Congreve, D. N.; Thompson, N. J.; Baldo, M. A. Enhanced external quantum efficiency in an organic photovoltaic cell via singlet fission exciton sensitizer. *Appl. Phys. Lett.* **2012**, *101*, 113304.
- (3) Kawata, S.; Pu, Y.; Saito, A.; Kurashige, Y.; Beppu, T.; Katagiri, H.; Hada, M.; Kido, J. Singlet Fission of Non-polycyclic Aromatic Molecules in Organic Photovoltaics. *Adv. Mater.* **2016**, *28*, 1585–1590.
- (4) Busby, E.; Xia, J.; Wu, Q.; Low, J. Z.; Song, R.; Miller, J. R.; Zhu, X.; Campos, L. M.; Sfeir, M. Y. A design strategy for intramolecular singlet fission mediated by charge-transfer states in donor–acceptor organic materials. *Nat. Mater.* **2015**, *14*, 426.
- (5) Einzinger, M.; Wu, T.; Kompalla, J. F.; Smith, H. L.; Perkinson, C. F.; Nienhaus, L.; Wieghold, S.; Congreve, D. N.; Kahn, A.; Bawendi, M. G. Sensitization of silicon by singlet exciton fission in tetracene. *Nature* **2019**, *571*, 90.
- (6) Smith, M. B.; Michl, J. Singlet fission. *Chem. Rev.* **2010**, *110*, 6891–6936.
- (7) Renaud, N.; Grozema, F. C. Intermolecular vibrational modes speed up singlet fission in perylenediimide crystals. *J. Phys. Chem. Lett.* **2015**, *6*, 360–365.
- (8) Le, A. K.; Bender, J. A.; Arias, D. H.; Cotton, D. E.; Johnson, J. C.; Roberts, S. T. Singlet fission involves an interplay between energetic driving force and electronic coupling in perylenediimide films. *J. Am. Chem. Soc.* **2018**, *140*, 814–826.
- (9) Eaton, S. W.; Shoer, L. E.; Karlen, S. D.; Dyar, S. M.; Margulies, E. A.; Veldkamp, B. S.; Ramanan, C.; Hartzler, D. A.; Savikhin, S.; Marks, T. J. Singlet exciton fission in polycrystalline thin films of a slip-stacked perylenediimide. *J. Am. Chem. Soc.* **2013**, *135*, 14701–14712.
- (10) Felter, K. M.; Dubey, R. K.; Grozema, F. C. Relation between molecular packing and singlet fission in thin films of brominated perylenediimides. *J. Chem. Phys.* **2019**, *151*, 094301.
- (11) Mirjani, F.; Renaud, N.; Gorczak, N.; Grozema, F. C. Theoretical investigation of singlet fission in molecular dimers: the role of charge transfer states and quantum interference. *J. Phys. Chem. C* **2014**, *118*, 14192–14199.
- (12) Farag, M. H.; Krylov, A. I. Singlet fission in perylenediimide dimers. *J. Phys. Chem. C* **2018**, *122*, 25753–25763.
- (13) Sutton, C.; Tummala, N. R.; Beljonne, D.; Brédas, J.-L. Singlet fission in rubrene derivatives: impact of molecular packing. *Chem. Mater.* **2017**, *29*, 2777–2787.
- (14) Aulin, Y. V.; Felter, K. M.; Günbas, D. D.; Dubey, R. K.; Jager, W. F.; Grozema, F. C. Morphology-Independent Efficient Singlet Exciton Fission in Perylene Diimide Thin Films. *ChemPlusChem* **2018**, *83*, 230–238.

- (15) Savenije, T. J.; Ferguson, A. J.; Kopidakis, N.; Rumbles, G. Revealing the dynamics of charge carriers in polymer: fullerene blends using photoinduced time-resolved microwave conductivity. *J. Phys. Chem. C* **2013**, *117*, 24085–24103.
- (16) Fravventura, M. C.; Hwang, J.; Suijkerbuijk, J. W.; Erk, P.; Siebbeles, L. D.; Savenije, T. J. Determination of singlet exciton diffusion length in thin evaporated C60 films for photovoltaics. *J. Phys. Chem. Lett.* **2012**, *3*, 2367–2373.
- (17) Kroeze, J. E.; Savenije, T. J.; Vermeulen, M. J.; Warman, J. M. Contactless determination of the photoconductivity action spectrum, exciton diffusion length, and charge separation efficiency in polythiophene-sensitized TiO<sub>2</sub> bilayers. *J. Phys. Chem. B* **2003**, *107*, 7696–7705.
- (18) Huijser, A.; Suijkerbuijk, B. M.; Klein Gebbink, R. J.; Savenije, T. J.; Siebbeles, L. D. Efficient exciton transport in layers of self-assembled porphyrin derivatives. *J. Am. Chem. Soc.* **2008**, *130*, 2485–2492.
- (19) De Haas, M. P.; Warman, J. M. Photon-induced molecular charge separation studied by nanosecond time-resolved microwave conductivity. *Chem. Phys.* **1982**, *73*, 35–53.
- (20) Fravventura, M. C.; Deligiannis, D.; Schins, J. M.; Siebbeles, L. D.; Savenije, T. J. What limits photoconductance in anatase TiO<sub>2</sub> nanostructures? A real and imaginary microwave conductance study. *J. Phys. Chem. C* **2013**, *117*, 8032–8040.
- (21) Holman, M. W.; Liu, R.; Adams, D. M. Single-molecule spectroscopy of interfacial electron transfer. *J. Am. Chem. Soc.* **2003**, *125*, 12649–12654.
- (22) Günbaş, D. D.; Xue, C.; Patwardhan, S.; Fravventura, M. C.; Zhang, H.; Jager, W. F.; Sudhölter, E. J.; Siebbeles, L. D.; Savenije, T. J.; Jin, S. High charge carrier mobility and efficient charge separation in highly soluble perylenetetracarboxyl-diimides. *Chem. Commun.* **2014**, *50*, 4955–4958.
- (23) Kroeze, J. E.; Savenije, T. J.; Warman, J. M. Efficient Charge Separation in a Smooth-TiO<sub>2</sub>/Palladium-Porphyrin Bilayer via Long-Distance Triplet-State Diffusion. *Adv. Mater.* **2002**, *14*, 1760–1763.
- (24) Kroeze, J. E.; Koehorst, R. B.; Savenije, T. J. Singlet and Triplet Exciton Diffusion in a Self-Organizing Porphyrin Antenna Layer. *Adv. Funct. Mater.* **2004**, *14*, 992–998.
- (25) Nagarajan, K.; Mallia, A. R.; Reddy, V. S.; Hariharan, M. Access to Triplet Excited State in Core-Twisted Perylenediimide. *J. Phys. Chem. C* **2016**, *120*, 8443–8450.
- (26) Fravventura, M. C.; Siebbeles, L. D.; Savenije, T. J. Mechanisms of photogeneration and relaxation of excitons and mobile carriers in anatase TiO<sub>2</sub>. *J. Phys. Chem. C* **2014**, *118*, 7337–7343.
- (27) Forro, L.; Chauvet, O.; Emin, D.; Zuppiroli, L.; Berger, H.; Levy, F. High mobility n-type charge carriers in large single crystals of anatase (TiO<sub>2</sub>). *J. Appl. Phys.* **1994**, *75*, 633–635.
- (28) Lin, S.-H.; Xiao, W.; Dietz, W. Generalized Förster-Dexter theory of photoinduced intramolecular energy transfer. *Phys. Rev. E* **1993**, *47*, 3698.
- (29) Zhu, T.; Wan, Y.; Guo, Z.; Johnson, J.; Huang, L. Two birds with one stone: tailoring singlet fission for both triplet yield and exciton diffusion length. *Adv. Mater.* **2016**, *28*, 7539–7547.
- (30) Le, A. K.; Bender, J. A.; Roberts, S. T. Slow singlet fission observed in a polycrystalline perylenediimide thin film. *J. Phys. Chem. Lett.* **2016**, *7*, 4922–4928.

# 6

## MAGNETIC FIELD EFFECTS ON TRIPLET PAIR STATES IN PERYLENE DIIMIDE THIN FILMS

*In the preceding chapters of this thesis we have extensively studied processes involving triplet excited states, including singlet fission, triplet-triplet annihilation and triplet diffusion. Due to the net magnetic moment of triplet state, an excellent approach to study the dynamics of triplets is to study their dynamics in magnetic fields. In this chapter an explorative study of magnetic field effects on singlet exciton fission (SF) in thin films of perylene diimide (PDI) is presented using the steady state and time resolved photoluminescence experiments. Most perylene diimides studied show a low magnetic field (0.4 T) effect in the steady state photoluminescence that can be characterized as a singlet fission or triplet-triplet annihilation upconversion curve depending on the PDI substitution, i.e. imid and bay area substitution. We do not observe a magnetic field effect in the photoluminescence lifetime at 0.7 T on a 150 ps time scale. At high magnetic fields (35 T) no specific signatures of a magnetic field effects in the steady state fluorescence are observed in the perylene diimides studied.*

## 6.1. INTRODUCTION

Singlet fission (SF) is a photo-physical process occurring in organic chromophores in which a photoexcited singlet state ( $S_1$ ) evolves into a correlated triplet pair state (TT). This  $^1(TT)$  state has overall singlet character and two-electron excited state with no net magnetic moment. After formation this  $^1(TT)$  state can decohere into two electronically and spin uncorrelated triplet states ( $T_1+T_1$ ).<sup>1</sup> The two formed  $T_1$  states can eventually dissociate into two electrons and holes that can be collected. In the ideal case the final result is the generation of two electrons in an external circuit upon absorption of a single photon. This two-for-one concept has been proposed as a promising strategy to optimize and surpass the theoretical photon-to-current conversion efficiency limit of single junction silicon photovoltaic cells in which a lot of energy is lost by thermalization upon absorbing high-energy photons.<sup>2</sup> Singlet fission has two main requirements to be able to occur: (1) the chromophore energetics obey  $E_{S_1} > E(T_1+T_1)$  and (2) there is sufficient orbital coupling between neighbouring molecules, resulting from molecular packing. These requirements are used to design novel SF chromophores with optimal efficiency and fast rates.<sup>1</sup> Perylene diimides (PDIs) are excellent model systems to study SF owing to the controlled tuneability of their energetic and packing structure upon side groups substitution, as has been shown in theoretical studies.<sup>3-5</sup> The common experiment to study SF experimentally is transient optical absorption (TA) spectroscopy, which has its drawbacks for PDIs specifically since the triplet photoinduced absorption feature overlaps with the ground-state absorption. This complicates the analysis and makes it hard to avoid secondary experimental artefacts such as singlet-singlet annihilation. As a result, a wide variety of SF properties, *i.e.* rates and yields, have been reported for similar PDIs.<sup>6-10</sup> An alternative experimental approach to study singlet fission that was used very early on to confirm the occurrence of SF in 1965 in anthracene crystals<sup>11</sup> is the study of magnetic field effects in the photoluminescence (PL).<sup>12,13</sup> Magnetic field effect measurements were actually used to study the inverse singlet fission process, upconversion.<sup>14</sup> Magnetic field dependent measurements offer an unambiguous method to confirm the existence and key properties of singlet fission in chromophores. The applied magnetic field (solely) affects singlet fission, the  $S_1$  to (TT) conversion. The properties that can be extracted from such measurement depend on the field strength. At low magnetic fields (<1 T), values can be obtained for the singlet fission rate and quantum mechanical parameters, like the zero-field splitting parameters as discussed below.<sup>15</sup> At high fields (>1 T) however, it is possible to extract actual exchange energies for the triplet pair states that allows their identification and study in diffusion related studies. Currently, only one study on magnetic field effects in PDIs is known, in which a low magnetic field effect (0.45 T) shows the existence of triplet states in thin films of N, N'-dimethyl perylene tetracarboxylic acid diimide (PDI-CH<sub>3</sub>).<sup>16</sup> More information on magnetic field effects in PDIs could for example show how the balance between singlet fission and excimer formation in PDIs plays a role.<sup>17,18</sup> More importantly, high magnetic field measurements may shed light on the effect of tuning the excited state energetics and electronic coupling in PDIs upon substitution on the triplet pair state exchange energies and thereby the rate of singlet fission.

In this chapter report we describe the results of our explorative study of the presence of magnetic field effects on the steady state and time-resolved PL in thin films of the

perylene diimide molecules shown in Figure 6.1. Most perylene diimides studied show a low magnetic field (0.4 T) effect in steady state PL. The magnetic field dependence for some PDIs shows a dip at low very low fields and then an increase, that is reminiscent of the SF process, while others show the opposite trend, that is characteristic of up-conversion (UC) of triplet excitons to singlets via triplet-triplet annihilation. Interestingly, we observe both types of behaviour in a single PDI derivative depending on the extent of crystallization. We attempted to measure the PL lifetime at 0.7 T on a 150 ps time scale using a streak camera, but did not detect a magnetic field effect. High magnetic field sweeping measurements (up to 35 T) of the steady state PL at 1.4 K also did not reveal reliable signatures of SF or UC.

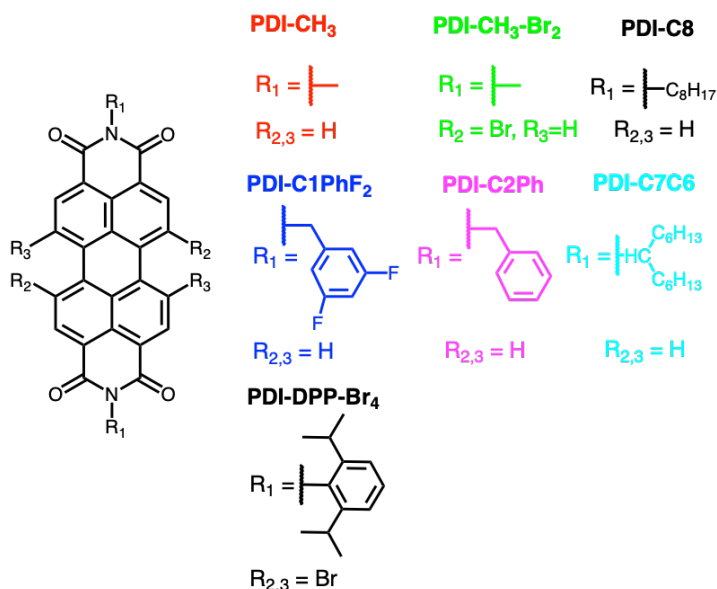


Figure 6.1: Molecular structures of the seven PDI derivatives studied.

## 6.2. THEORY

As mentioned above, an applied magnetic field (solely) affects singlet fission, the  $S_1$  to (TT) conversion and it does so in two ways<sup>19</sup>: 1) by influencing the spin wavefunctions  $\Psi_j(t)$  of the triplet excitons comprising the triplet pair states and 2) by changing the energy of the triplet pair spin states. The spin wavefunctions of the triplet excitons in the pair are constructed from 16 eigenstates  $\Psi_j(t)$  ( $j=16$ ) for the triplet pair state that can be found by arranging the four unpaired electrons in the triplet pair over the four energy levels of the pair.<sup>19</sup> The spin of these triplet pair eigenstates allows categorization into two spin states with singlet spin, nine states with triplet spin that are grouped into three triplet manifolds and five states with quintet spin that are grouped together within one quintet manifold. The states that are lowest in energy and which are therefore considered in measurements are a singlet state, one triplet manifold and the quintet manifold.

As mentioned, a magnetic field effect can alter the spin wavefunction of triplets and is described by considering the expression for the spin Hamiltonian of a triplet pair with a simplified representation of two single-particles:

$$\hat{H}_{spin} = g\mu_B H(S_1 + S_2) + D(S_{1z}^2 S_{2z}^2) + E(S_{1z}^2 + S_{2x}^2 - S_{2y}^2 - S_{2y}^2) \quad (6.1)$$

Where the first term is the Zeeman term including the g-factor  $g$ , the Bohr magneton  $\mu_B$ , the externally applied magnetic field  $H$  and the spin operators of the unpaired electrons  $S_1$  and  $S_2$ . The second and third term represent the zero-field splitting or fine structure terms that arise from the magnetic dipolar interaction of the two unpaired electrons of the triplet with  $D$  and  $E$  being the zero-field splitting parameters. These zero-field splitting terms are present even in the absence of an external magnetic field and their effect is best described by considering the expression for an eigenstate of the spin Hamiltonian  $\Psi_j(t)$ :

$$\Psi_j(t) = e^{-i(E_j/\hbar)t} \Psi_j(0) \quad (6.2)$$

Here,  $E_j$  is the eigen energy of state  $j$ ,  $i$  is  $(-1)^{0.5}$  and  $t$  is time. The time factor involves the 'spin precession motion' that is responsible for the conversion of the pure singlet triplet pair into other pairs.<sup>20</sup> As such, if the existence of the triplet pair, *i.e.* the triplet pair correlation time, is shorter than the time required for the spin to carry out its precession, then no magnetic field is observed. When  $H$  is zero, only three out of nine eigenstates display singlet character. At intermediate  $H$ , the Zeeman interaction together with the fine structure term lets the singlet character of more spin eigenstates evolve, so that five spin eigenstates obtain singlet character. When  $H$  is high, the Zeeman interaction is much larger than the fine structure term and the latter term cannot mix the triplet pair states any longer. Such low magnetic field effects have been shown magnetic field dependent fluorescence measurements in anthracene<sup>14,15,21</sup>, tetracene<sup>12,21,22</sup> and rubrene<sup>18</sup>. At very high magnetic fields however, the Zeeman interaction can split the energies of the spin eigenstates so much, that excited-state avoided crossings occur where triplet pair states with triplet or quintet spin become degenerate with the singlet spin state. At that particular  $H$ , the exchange interaction energy or splitting of the singlet-triplet or singlet-quintet state, is reached and the pure singlet state becomes hybridized with a triplet or quintet pair state. Note that this is a different kind of crossing than that which occurs because of the fine structure term discussed above. At very high  $H$ , the avoided pair state crossings are energy crossings between a singlet and a nonpure singlet pair state. Recent theoretical<sup>23</sup> and experimental<sup>24</sup> work on TIPS-tetracene crystals and 1,6-diphenyl-1,3,5-hexatriene<sup>25,26</sup> prove this principle where strong photoluminescence oscillations at high magnetic fields were observed due to these excited-state avoided crossings and exchange energies, characteristic for separate triplet pairs could be obtained. The processes described above are visualized in Figure 6.2.

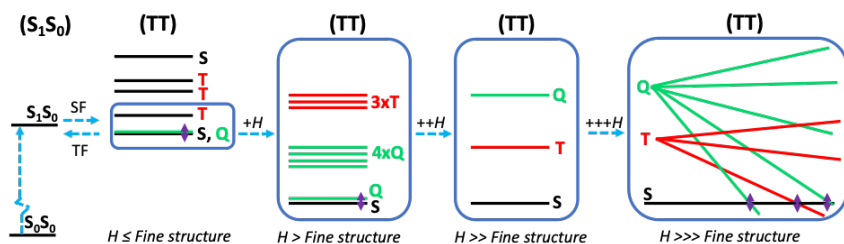


Figure 6.2: Schematic of the relative height of energetic levels of singlet,  $S_1$  and  $S_0$ , and triplet pair (TT) excited states as function of the externally applied magnetic field strength  $H$  on a material displaying singlet fission SF and triplet pair fusion TF.

## 6.3. EXPERIMENTAL SECTION

### SAMPLE PREPARATION AND CHARACTERIZATION

We studied thin films of seven PDI molecules deposited on fused silica substrates (ESCO, 12 x 25 x 1 mm). The un-brominated compounds were synthesized from perylene-3,4,9,10 tetracarboxylic acid dianhydride as purchased from Sigma-Aldrich using procedures published elsewhere.<sup>27</sup> PDI-C1-Br<sub>2</sub> and PDI-DPP-Br<sub>4</sub> respectively, were synthesized from 1,7- dibromoperylene dianhydride and 1,6,7,12-tetrabromoperylene dianhydride as described previously.<sup>9,28,29</sup> The films were deposited by thermal evaporation, resulting in the following thicknesses; PDI-CH<sub>3</sub>: 100 nm, PDI-C1PhF<sub>2</sub>: 50 nm, PDI-C2Ph: 300 nm, PDI-C8: 100 nm, PDI-C7C6: 150 nm, PDI-C1-Br<sub>2</sub>: 100 nm and PDI-DPP-Br<sub>4</sub>: 50 nm. Prior to evaporation, the fused silica substrates were plasma cleaned (two minutes, 1000 mtorr in air plasma) to clean and activate the surface. Thermal evaporation was carried out in an *AJA ATC Orion evaporator* during which the powders were heated above the sublimation temperature under high vacuum conditions ( $10^{-7}$ - $10^{-6}$  mbar) to the desired evaporation rate of 0.3 Å/s. The deposition rate was monitored using a quartz micro-crystal balance and the sample holder was rotated at 25 rpm to ensure film homogeneity. Thin films of PDI-C7C6 were spincoated from a saturated chloroform solution. The spincoated film was annealed at 60°C in a N<sub>2</sub> atmosphere to remove any solvents and improve the crystallization.

### MAGNETIC FIELD MEASUREMENT AT 0.7 T OF THE STEADY STATE PHOTOLUMINESCENCE

The magnetic field effects in the steady state PL spectrum of PDI thin films were measured in a home-build setup with a horseshoe permanent magnet that could slide reproducibly, such that the sample was located in the internal space. The permanent magnet had an effective field strength at the position of the sample of 0.7 T. The thin film was photoexcited with a *CPS405 Thorlabs* compact laser diode with a wavelength of 405 nm and power of 4.5 mW of which the intensity was decreased using an OD1 filter. The laser spot size is 3.8 mm x 1.8 mm as indicated by the supplier. The excitation was done under a 45 degrees angle with the substrate. The detector was placed under an angle. All measurements were performed in a N<sub>2</sub> filled glovebox.



### LOW MAGNETIC FIELD SWEEP MEASUREMENT 0.0-0.4 T OF THE STEADY STATE PHOTOLUMINESCENCE

Variable magnetic field measurement with field ranging from 0-0.4 T of the fluorescence spectrum were made on a home-build setup comprised of a *3470 Electromagnet of GMW*. Between the poles an aluminium structure. The sample was placed in an air-tight plastic cell. The sample was excited with a Thorlabs laser diodes of 405 nm and 520 nm wavelength and an excitation density of around  $3.4 \text{ mW/cm}^2$  and a spot size of  $3 \times 3 \text{ mm}$ .

### HIGH MAGNETIC FIELD SWEEP MEASUREMENT 0.0-35 T OF THE STEADY STATE PHOTOLUMINESCENCE

The steady state photoluminescence measurements in high magnetic fields (up to 35 T) were measured at variable temperatures (1.4 K - 300 K) at the High Field Magnetic Laboratory (HFML) in Nijmegen, The Netherlands. The thin film sample was mounted on an insert and mounted in a Helium4-bath cryostat to 4.2 K. The helium-bath could be pumped to further cool the sample to 1.4 K. The helium-bath in cryostat is isolated by a liquid nitrogen compartment and vacuum layers. The cryostat was placed in the center of a 38 T (resistive coil) water cooled Bitter magnet with the sample placed in Faraday Geometry (sample normal parallel with magnetic field). In order to probe the sample temperature, a heater and thermometer (Cernox,  $R = 32.7576 \text{ Ohm}$  at  $T = 298.88 \text{ K}$ ) were soldered on a piece of uncoated substrate. The excitation source was a *Genesis MX488-SLM* laser tuned at 490 nm with a power of 1 mW. The excitation light was guided into the cryostat with optical fibers. The emission was detected using an *Acton SpectraPro-300i* spectrometer (300 grooves/mm, blazed at 400 nm) coupled to a *Princeton Instruments PyLoN®:400* cryogenically-cooled CCD camera (imaging array was  $1340 \times 100$  pixels with  $20 \times 20$  micron pixels). A 488 nm short-pass filter was placed in front of the detector to cut off excitation light.

### MAGNETIC FIELD MEASUREMENT AT 0.7 T OF THE PHOTOLUMINESCENCE LIFETIME

Time and spectrally resolved measurements of the photoluminescence of the polycrystalline PDI films were performed on a picosecond time scale using a streak camera. In this setup, 140 fs (FWHM) laser pulses ( $680 \mu\text{W}$ ) were produced by a *Ti:Sapphire* laser (*Coherent Chameleon* laser 80.2 MHz) of which the repetition rate was decreased using an *APA GmbH* pulse picker. The fluorescence was spectrally resolved using a *Princeton Instruments* spectrograph (slit of  $50 \mu\text{m}$ ) and temporally resolved using a *Hamamatsu C5680* synchroscan streak camera unit (slit of  $20 \mu\text{m}$ ). The magnetic field was applied by placing a small permanent magnet against the back of the substrate such that a field strength of 0.22-0.25 T could be achieved. In this situation, the magnetic field was oriented parallel to the normal of the sample (Faraday orientation). The zero-field measurement was performed by simply removing the permanent magnet. To minimize air exposure during the measurements, a constant stream of  $\text{N}_2$  gas was blown against the films during measurements.

## 6.4. RESULTS AND DISCUSSION

### MAGNETIC FIELD EFFECTS AT ONE FIELD IN THE STEADY STATE AND TIME RESOLVED PL

We have performed exploratory measurements of a magnetic field effect on the PL from PDI films. In Figure 6.3 the steady state PL spectra of PDI-CH<sub>3</sub> (a), PDI-C1PhF<sub>2</sub> (b), and an unannealed (c) and an annealed film (d) of PDI-C2Ph are shown at zero field and a field of a 0.7 T. The calculated difference in the integrated emission intensity in the presented wavelength region is within 10% for most PDIs, while the unannealed film of PDI-C2Ph shows a large magnetic field effect of 31.0%. Interestingly, the applied magnetic field in some cases leads to an increase in the PL intensity (PDI-C1PhF<sub>2</sub> and unannealed PDI-C2Ph), while for other (PDI-CH<sub>3</sub> and PDI-C2Ph) a decrease is observed. These results show that there is a reproducibly measurable magnetic field effect on the PL, which suggest that triplets are present in the film, as the fluorescence from pure singlets should not be affected by a magnetic field. A further analysis of these magnetic field effects requires varying the field strength.

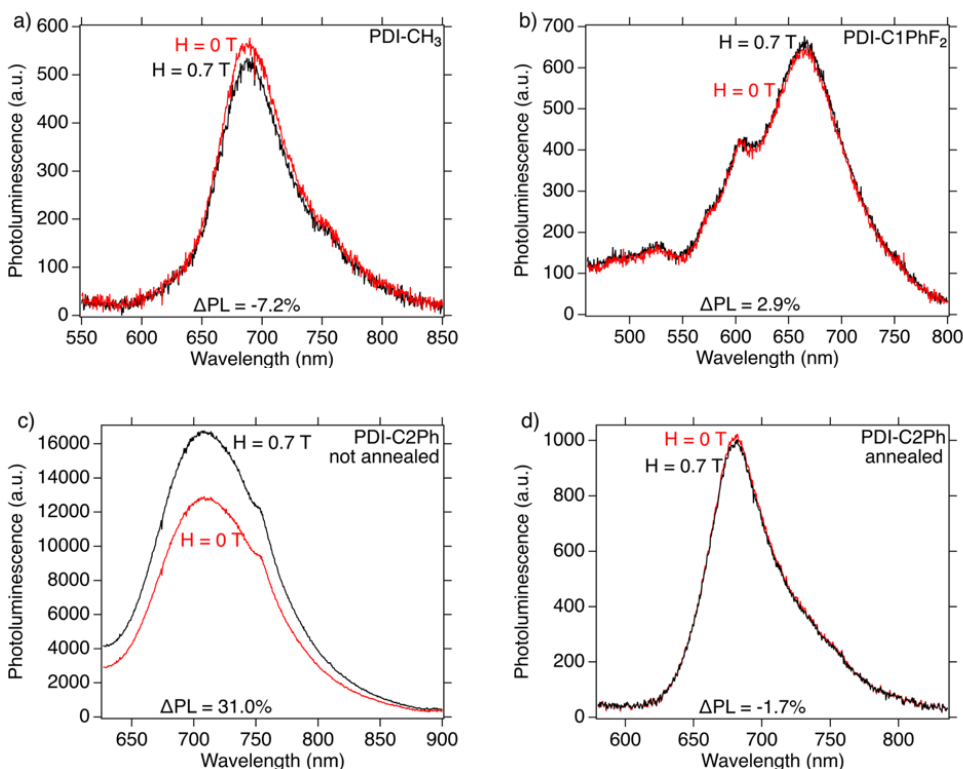


Figure 6.3: Magnetic field dependent photoluminescence measurements at  $T = 260$  K in a glovebox of various PDI thin films upon 405 nm photoexcitation and displayed as  $\Delta PL = (PL_H - PL_0) / PL_0$ . The thin films are a) PDI-CH<sub>3</sub> (100 nm), b) PDI-PhF<sub>2</sub> (50 nm), c) PDI-C2Ph (300 nm) not annealed and d) PDI-C2Ph (300 nm) annealed.

In order to gain insight in the effect of magnetic fields on the fluorescence lifetime we performed PL lifetime measurements on time scales up to 150 ps using streak camera. On this time scale, the fluorescence is dominated by directly photogenerated singlet states. The results are shown in Figure 6.4. Attempts were made to perform such measurements for all PDIs for which the steady state PL is shown in Figure 6.3, however, for several samples the fluorescence intensity was too low to do a meaningful measurement. For none of the PDIs investigated we observed an effect of a magnetic field at field strengths of  $\sim 0.25$  T. This is remarkable as we did observe a clear magnetic field effect in the steady state measurement. This difference may be caused by an effect on a time scale that is much shorter than the time resolution of the setup ( $\sim 10$  ps), *i.e.* decoherence of the triplet pair state has already occurred and no further magnetic field effect is present. An alternative, more likely explanation is that magnetic field effects occur at later times, corresponding to a delayed fluorescence. This would imply that the delayed fluorescence from triplet states are responsible for the magnetic field effect via the formation of a triplet pair state and the reverse process, triplet fusion.

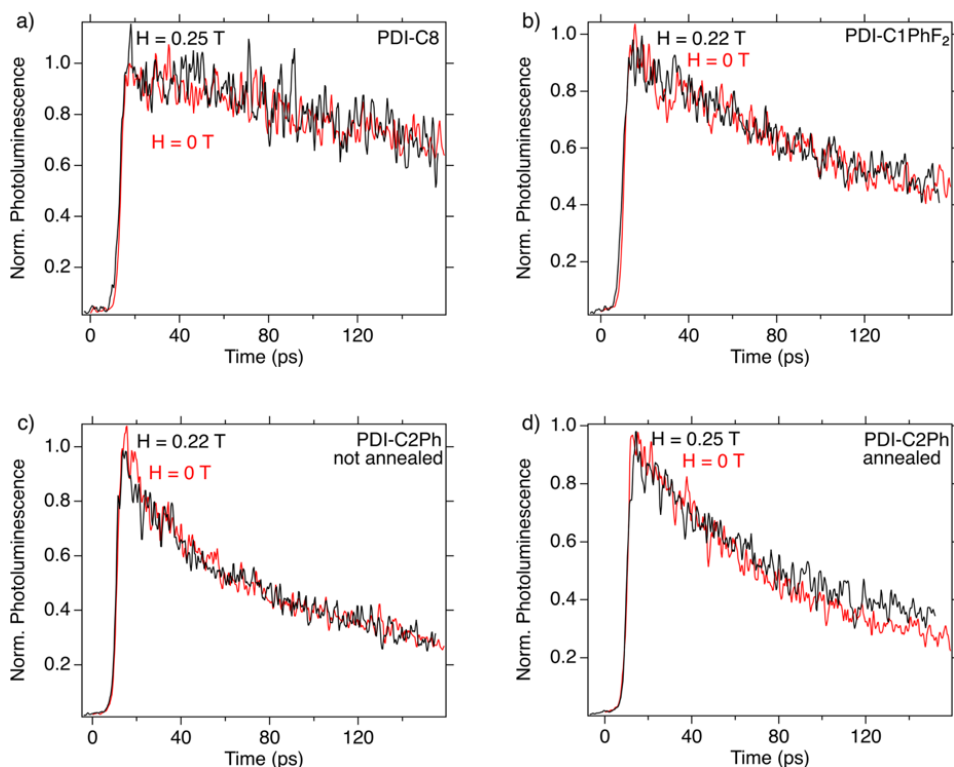


Figure 6.4: Magnetic field dependent time resolved photoluminescence measurements of various PDI thin films upon 490 nm photoexcitation at  $T = 0$  and  $T = 0.22$ - $0.25$ . The thin films are a) PDI-C8 (100 nm), b) PDI-C1PhF<sub>2</sub> (50 nm), c) PDI-C2Ph (300 nm) not annealed and d) PDI-C2Ph (300 nm) annealed. The laser power was  $680 \mu\text{W}$  and measurements were performed in air but samples were blown with N<sub>2</sub>.

### MAGNETIC FIELD EFFECTS AT LOW FIELDS IN PDI PL

As noted above, in order to get a clearer insight into the effects of magnetic field on the PL from PDI films, it is interesting to examine the trends in PL intensity as a function of the magnetic field strength. Therefore, we have measured the integrated steady state PL intensity of PDI films for magnetic field ranging from the 0 T to 0.4 T, as shown in Figure 6.5. The results in this figure show a clear trend in the magnetic field effect. At low fields the difference in PL  $\Delta$ PL first decreases and reaches a minimum slightly below 0.1 T, after which it increases again and stabilizes at 0.3 T for PDI-C1-Br<sub>2</sub> (a), PDI-DPP-Cl<sub>4</sub> (b), PDI-C7C6 (c) and un-annealed PDI-C2Ph (d). This trend observed for low magnetic fields corresponds with what is commonly observed in 'traditional' SF chromophores such as tetracene<sup>13</sup> and more novel compounds such as 1,6-diphenyl-1,3,5-hexatriene<sup>25</sup> and implicates a magnetic field effect on the formation of the correlated triplet pair upon photoexcitation through SF. In contrast to the behavior of unannealed PDI-C2Ph, the annealed PDI-C2Ph film shows the opposite trend in the magnetic field effect, *i.e.* for small fields the PL intensity first increases and then decreases again until it reaches a plateau at 0.3 T with a lower PL intensity than in absence of a magnetic field. This trend corresponds to a magnetic field effect originating from triplets that collide and form a magnetic field active correlated triplet pair, that may upconvert depending on the magnetic field strength to give a singlet. These singlets formed on longer times are responsible for delayed fluorescence. Similar observations have been made for fluorescence measurements in anthracene<sup>11</sup> and photocurrent measurements in devices including the SF material pentacene.<sup>30</sup>

In accordance with the steady state PL measurements described in section 4.1,  $\Delta$ PL at  $T > 0.4$  T is positive for unannealed PDI-C2Ph while it is negative for annealed PDI-C2Ph. It is remarkable that a change in the crystallinity, can give rise to such a difference in the magnetic field effect, while the singlet fission efficiency and rate seem similar.<sup>8</sup> This is probably caused by subtle effects of morphology on the energetics of the singlet and the correlated triplet pair state. Small changes in these energetics can move the equilibrium populations from the singlet side to the correlated triplet pair side, resulting in opposite magnetic field effects. Further modelling of the trend in the magnetic field dependence of  $\Delta$ PL may result in values for the rates and balance involving singlet fission, triplet pair fusion and triplet pair dissociation, but this is beyond the scope of this explorative study.<sup>12,14,20,30</sup>

### MAGNETIC FIELD EFFECTS AT HIGH FIELDS IN PDI PL

As mentioned in the theory section above, high magnetic fields, above several Tesla, in principle have very different effects on the PL intensity and may provide information on the energy splitting or the exchange energy of the distinct triplet pair states. The results of PL measurements on PDI films in magnetic fields ranging from 0 to 35 T are shown in Figure 6.6. This is the magnetic field range where very distinct features were observed previously for TIPS-pentacene.<sup>25</sup> Measurements were performed at various temperatures down to 1.4 K in order to minimize the effects of thermal vibrations that may blur the sharp dips in the fluorescence intensity that were previously observed for other compounds. In Figure 3.6a the magnetic field dependence is shown for PDI-CH<sub>3</sub> at 3.4 K, but we do not observe a magnetic field effect over the entire 35 T range. For the

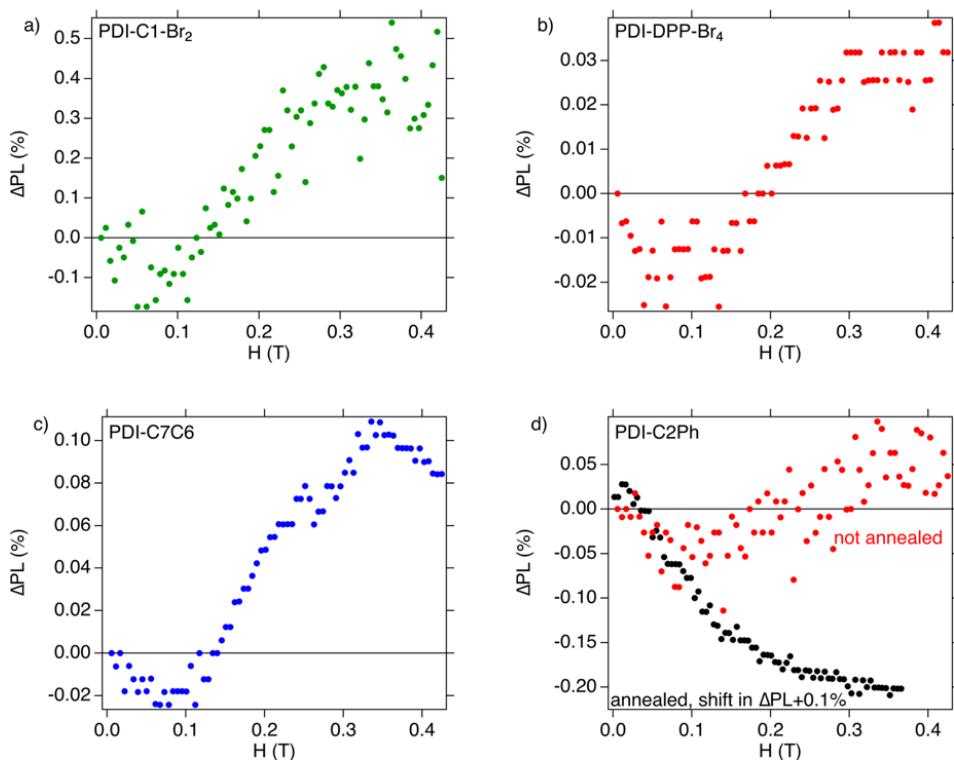


Figure 6.5: Magnetic field dependent photoluminescence measurements of various PDI thin films upon 405 nm photoexcitation and displayed as  $\Delta PL(\%) = (PL_H - PL_0) / PL_0$ . The thin films are a) PDI-C1-Br<sub>2</sub> (100 nm), b) PDI-DPP-Br<sub>4</sub> (50 nm), c) PDI-C6C7 (spincoated) and d) PDI-C2Ph (300 nm) unannealed (red) and annealed (black).

annealed PDI-C2Ph film at 1.4 K a small initial increase in  $\Delta PL$  is observed for magnetic fields up to 5 T, as shown in Figure 3.6b. This increase is followed by a decrease that stabilizes at 25 T and then appears to return to zero difference. The backward sweep, lowering the magnetic field down from 35 T leads to the same observations, confirming the observed field trend. The downward trend in fluorescence upon increasing the field strength is in accordance previous measurements for TIPS-tetracene and was attributed to a spin mixing process.<sup>24</sup> If we increase the temperature of this film to 30 and 90 K, the trends observed at 1.4 T are not observed anymore and any changes in  $\Delta PL$  that we do see are caused by non-stable temperature heating effects on the emission intensity. These temperature effects were shown to be significant in PDIs, see Chapter 3. In these measurements we did not observe any sharp dips in the fluorescence intensity as previously observed for TIPS-pentacene which allow determination of the exchange energy splitting of the triplet pair states. This can be caused by a variety of reasons. One is that the exchange energy is too high to be observed in the 35 T magnetic field range and even higher fields need to be used. Another possibility is that the direction of the magnetic field with respect to the sample is not optimized for observation of the effect

of string magnetic fields. This is possible since PDIs are known to crystallize in certain preferred orientations on a substrate, so no random orientation of crystalline domains is present. An additional complication may be the relatively low fluorescence quantum yield of PDIs in the solid-state, which decreases the signal-to-noise ratio and may hide the specific sharp feature. Future studies should involve more careful evaluation of the crystallization direction of the samples and possibly the choice of a different PDI compound that shows better fluorescence in the solid-state. In addition, it would be useful to have an estimate of the effect of packing geometry on the exchange splitting, for instance from electronic structure calculations. This would allow a more reasoned selection of a PDI derivative for studying these magnetic field effects.

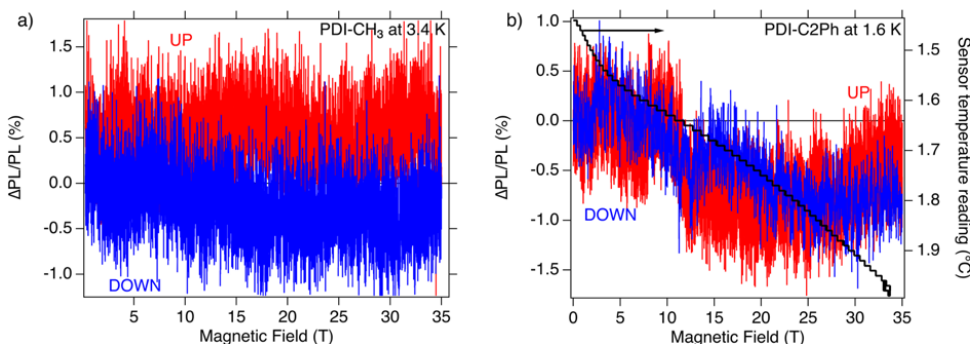


Figure 6.6: High magnetic field sweep measurements of integrated steady state PL, presented as the change in PL,  $\Delta$ PL. a) Magnetic field dependence of  $\Delta$ PL of PDI-CH<sub>3</sub> (100 nm) at 3.4 K from 0 - 35 T and back. b) Magnetic field dependence of  $\Delta$ PL of annealed PDI-C2Ph at 1.4 K from 0 - 35 T.

## 6.5. CONCLUSIONS

In this preliminary study we investigated the magnetic field effect on SF in thin films PDI molecules. We show that distinct magnetic field effects can be observed, proving that triplet are formed in these materials on photoexcitation. At low magnetic fields ( $<1$  T) signatures of triplet pair state modulation from either singlet or triplet side are observed that are dependent on the extent of crystallization. The majority of the PDIs show a singlet curve, indicating that the triplet pair state formed from singlet fission is responsible for the magnetic field effect. The lack of a low field effect in the PL lifetime of the PDIs indicates that the correlated triplet pair is not present in the 150 ps time scale studied. High field measurements were partially successful by showing a magnetic field effect in PDI-C2Ph. However, no clear dips in the  $\Delta$ PL were observed that are reminiscent of excited state avoided crossings of singlet with triplet or quintet character pair states. Therefore, no exchange energy for the PDIs could be determined. This preliminary study provides promising results for future, more detailed experiments and analysis involving magnetic field effects in order to gain relevant information on singlet fission properties of PDIs, in particular in relation to the dissociation of the triplet pairs.

## REFERENCES

- (1) Smith, M. B.; Michl, J. Singlet fission. *Chem. Rev.* **2010**, *110*, 6891–6936.
- (2) Hanna, M.; Nozik, A. Solar conversion efficiency of photovoltaic and photoelectrolysis cells with carrier multiplication absorbers. *J. Appl. Phys.* **2006**, *100*, 074510.
- (3) Renaud, N.; Grozema, F. C. Intermolecular vibrational modes speed up singlet fission in perylenediimide crystals. *J. Phys. Chem. Lett.* **2015**, *6*, 360–365.
- (4) Mirjani, F.; Renaud, N.; Gorczak, N.; Grozema, F. C. Theoretical investigation of singlet fission in molecular dimers: the role of charge transfer states and quantum interference. *J. Phys. Chem. C* **2014**, *118*, 14192–14199.
- (5) Farag, M. H.; Krylov, A. I. Singlet fission in perylenediimide dimers. *J. Phys. Chem. C* **2018**, *122*, 25753–25763.
- (6) Eaton, S. W.; Shoer, L. E.; Karlen, S. D.; Dyar, S. M.; Margulies, E. A.; Veldkamp, B. S.; Ramanan, C.; Hartzler, D. A.; Savikhin, S.; Marks, T. J. Singlet exciton fission in polycrystalline thin films of a slip-stacked perylenediimide. *J. Am. Chem. Soc.* **2013**, *135*, 14701–14712.
- (7) Le, A. K.; Bender, J. A.; Arias, D. H.; Cotton, D. E.; Johnson, J. C.; Roberts, S. T. Singlet fission involves an interplay between energetic driving force and electronic coupling in perylenediimide films. *J. Am. Chem. Soc.* **2018**, *140*, 814–826.
- (8) Aulin, Y. V.; Felter, K. M.; Günbas, D. D.; Dubey, R. K.; Jager, W. F.; Grozema, F. C. Morphology-Independent Efficient Singlet Exciton Fission in Perylene Diimide Thin Films. *ChemPlusChem* **2018**, *83*, 230–238.
- (9) Felter, K. M.; Dubey, R. K.; Grozema, F. C. Relation between molecular packing and singlet fission in thin films of brominated perylenediimides. *J. Chem. Phys.* **2019**, *151*, 094301.
- (10) Conrad-Burton, F. S.; Liu, T.; Geyer, E.; Costantini, R.; Schlaus, A. P.; Spencer, M. S.; Wang, J.; Hernández Sánchez, R.; Zhang, B.; Xu, Q. Controlling Singlet Fission by Molecular Contortion. *J. Am. Chem. Soc.* **2019**.
- (11) Singh, S.; Jones, W.; Siebrand, W.; Stoicheff, B.; Schneider, W. Laser generation of excitons and fluorescence in anthracene crystals. *J. Chem. Phys.* **1965**, *42*, 330–342.
- (12) Geacintov, N.; Pope, M.; Vogel, F. Effect of magnetic field on the fluorescence of tetracene crystals: exciton fission. *Phys. Rev. Lett.* **1969**, *22*, 593.
- (13) Merrifield, R.; Avakian, P.; Groff, R. Fission of singlet excitons into pairs of triplet excitons in tetracene crystals. *Chem. Phys. Lett.* **1969**, *3*, 386–388.
- (14) Johnson, R.; Merrifield, R.; Avakian, P.; Flippen, R. Effects of magnetic fields on the mutual annihilation of triplet excitons in molecular crystals. *Phys. Rev. Lett.* **1967**, *19*, 285.
- (15) Johnson, R.; Merrifield, R. Effects of magnetic fields on the mutual annihilation of triplet excitons in anthracene crystals. *Phys. Rev. B* **1970**, *1*, 896.
- (16) Lifshitz, E.; Kaplan, A.; Ehrenfreund, E.; Meissner, D. Magneto-optical studies of perylene tetracarboxylic acid diimide thin films. *Opt. Mater.* **1998**, *9*, 295–298.



- (17) Brown, K. E.; Salamant, W. A.; Shoer, L. E.; Young, R. M.; Wasielewski, M. R. Direct observation of ultrafast excimer formation in covalent perylene diimide dimers using near-infrared transient absorption spectroscopy. *J. Phys. Chem. Lett.* **2014**, *5*, 2588–2593.
- (18) Piland, G. B.; Burdett, J. J.; Kurunthu, D.; Bardeen, C. J. Magnetic field effects on singlet fission and fluorescence decay dynamics in amorphous rubrene. *J. Phys. Chem. C* **2013**, *117*, 1224–1236.
- (19) Scholes, G. D. Correlated pair states formed by singlet fission and exciton–exciton annihilation. *J. Phys. Chem. A* **2015**, *119*, 12699–12705.
- (20) Avakian, P. In *Mol. Spectrosc.–XI*; Elsevier: 1974, pp 1–19.
- (21) Katoh, R.; Kotani, M. Fission of a higher excited state generated by singlet exciton fusion in an anthracene crystal. *Chem. Phys. Lett.* **1992**, *196*, 108–112.
- (22) Einzinger, M.; Wu, T.; Kompalla, J. F.; Smith, H. L.; Perkinson, C. F.; Nienhaus, L.; Wieghold, S.; Congreve, D. N.; Kahn, A.; Bawendi, M. G. Sensitization of silicon by singlet exciton fission in tetracene. *Nature* **2019**, *571*, 90.
- (23) Bayliss, S. L.; Weiss, L. R.; Rao, A.; Friend, R. H.; Chepelianskii, A. D.; Greenham, N. C. Spin signatures of exchange-coupled triplet pairs formed by singlet fission. *Phys. Rev. B* **2016**, *94*, 045204.
- (24) Bayliss, S. L.; Weiss, L. R.; Mitioglu, A.; Galkowski, K.; Yang, Z.; Yunusova, K.; Surrente, A.; Thorley, K. J.; Behrends, J.; Bittl, R. Site-selective measurement of coupled spin pairs in an organic semiconductor. *P. Natl. A. Sci.* **2018**, *115*, 5077–5082.
- (25) Yago, T.; Ishikawa, K.; Katoh, R.; Wakasa, M. Magnetic field effects on triplet pair generated by singlet fission in an organic crystal: application of radical pair model to triplet pair. *J. Phys. Chem. C* **2016**, *120*, 27858–27870.
- (26) Wakasa, M.; Kaise, M.; Yago, T.; Katoh, R.; Wakikawa, Y.; Ikoma, T. What can be learned from magnetic field effects on singlet fission: Role of exchange interaction in excited triplet pairs. *J. Phys. Chem. C* **2015**, *119*, 25840–25844.
- (27) Duff, J. M.; Hor, A.-M.; Melnyk, A. R.; Teney, D. In *Hard Copy and Printing Materials, Media, and Processes*, International Society for Optics and Photonics; Vol. 1253, pp 183–191.
- (28) Hill, Z. B.; Rodovsky, D. B.; Leger, J. M.; Bartholomew, G. P. Synthesis and utilization of perylene-based n-type small molecules in light-emitting electrochemical cells. *Chem. Commun.* **2008**, 6594–6596.
- (29) Sengupta, S.; Dubey, R. K.; Hoek, R. W.; van Eeden, S. P.; Gunbaş, D. D.; Grozema, F. C.; Sudhölter, E. J.; Jäger, W. F. Synthesis of regioisomerically pure 1, 7-dibromoperylene-3, 4, 9, 10-tetracarboxylic acid derivatives. *J. Org. Chem.* **2014**, *79*, 6655–6662.
- (30) Thompson, N. J.; Hontz, E.; Congreve, D. N.; Bahlke, M. E.; Reineke, S.; Van Voorhis, T.; Baldo, M. A. Nanostructured Singlet Fission Photovoltaics Subject to Triplet-Charge Annihilation. *Adv. Mater.* **2014**, *26*, 1366–1371.

# 7

## OUTLOOK

The fields of singlet fission and triplet-triplet annihilation upconversion research have significantly evolved over the last decade. The research started from basic characterizations of yield and kinetics of SF by time-resolved fluorescence and ultrafast transient absorption spectroscopy. This is also shown in Chapter 3 of this thesis, where we focused on the relation between singlet fission and the packing of molecules in the solid-state. Combined with theoretical studies, such studies have given a lot of insight in the efficiency of the initial step in SF, *i.e.* transforming a singlet state into a coherent combination of two triplets. This has also given some insight in the mechanism by which this occurs although in most cases this relies on comparisons of experiments and theory and no general picture including vibronic effects is currently available. Studies on how the coherent triplet pair dissociates into separately diffusing triplets have only recently appeared for some systems, however, these processes are instrumental in actual applications and therefore a detailed understanding is of prime importance.

As shown in this thesis, in all these processes, including triplet diffusion and charge injection, the relevant electronic coupling matrix elements play a key role. This is why more insight into the effect of solid-state morphology and polycrystallinity in particular is important and SF chromophores where the crystal packing can be tuned are of particular interest. Systematic variation of the electronic coupling, as is possible for instance in perylene diimids, can be used to unravel the effect of the different coupling values in the different processes. In addition, systematic variations of the energetics of the different states involved can give insight in the nature of the triplet-pair states involved (singlet, triplet, quintet). The latter is possible by performing optical spectroscopy in high magnetic fields and such experiments should prove very valuable in gaining more insight in the SF dynamics and subsequent processes. We have made some initial attempts to perform such experiments on crystalline perylene diimides, as described in Chapter 6.

In addition, the initial formation of a coherent triplet pair and its subsequent decoherence into individual triplet is an important aspect, which can be explicitly studied by two-dimensional coherent spectroscopy. In all these experiments, materials where the crystal structure can be systematically tuned are appropriate, especially in relation

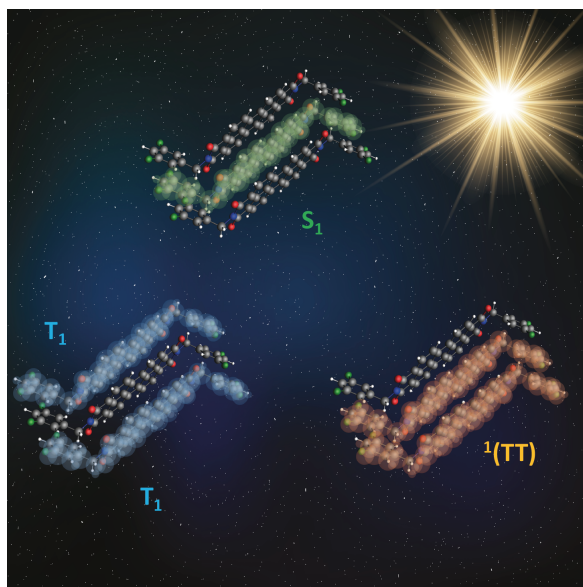


Figure 7.1: Artistic impression of the singlet fission process involving the formation of a photoexcited singlet state  $S_1$  that is equivalent to the triplet pair state intermediate with overall singlet character  $^1(TT)$ . The dissociation of  $^1(TT)$  leads to the formation of two separated triplets  $T_1$ .

with theory since high-level quantum chemical calculations invariably require information on the crystal structure. From the theory side it is important to continue to move beyond the initial step of forming a triplet pair in a dimer, but to study the dynamics in larger aggregates with an explicit description of decoherence and triplet diffusion. The application of methods such as high magnetic field measurements and 2D spectroscopy on samples with well-defined interchromophore geometry will ultimately lead to a more detailed and general understanding of SF and paves the way for improved design rules for SF chromophores that go beyond simple energy arguments.

# A

## APPENDIX CHAPTER 2

### DEKTAK – TARGET AND MEASURED PDI FILM THICKNESSES

The thickness of the evaporated PDI thin films were measured with a Dektak profilometer. Ten scans were made and averaged for every sample and consisted of measuring over the step from clean silica to the PDI layer. The height offset indicates the film thickness. We call the thickness set in the evaporator the nominal thickness and the measured film thickness the real film thickness.

Table A.1: Summary of the calculated optical properties of bay area substituted PDIs using DFT.

PDI-octyl thickness		PDI-hexhep thickness	
Nominal (nm)	Real (nm)	Nominal (nm)	Real (nm)
15	17.5	30	49.2
30	26.5	50	49.9
50	41.9	100	82.8
100	67.6	150	166.8
150	112.8	250	232.9
250	167.9		
500	326.7		

## THIN FILM CRYSTALLITE DOMAIN SIZE ESTIMATION USING THE SCHERRER EQUATION

We estimated the domain size of crystallites  $\tau$  from our XRD measurements using the Scherrer equation:

$$\tau = \frac{K\lambda}{\beta \cos\theta} \quad (\text{A.1})$$

Where  $K$  is the shape factor which is a function of crystallite shape and assumed to be 0.94,  $\lambda$  is the wavelength of the X-ray radiation (0.179 nm),  $\beta$  (in radians) is the Full Width Half Maximum (FWHM) location of the analysed reflection minus broadening caused by the instrument and  $\theta$  (in radians) is the angle of reflection. Using this equation on the reflection observed in the XRD spectra of the thin films shown in Figure 2.3 we can calculate the crystallite domain size values shown in Table S2. The crystallite packing of PDI-octyl is shown in Figure A.1 and is the molecular cell containing the intact contents of one unit cell. For PDI-hexhep this image cannot be shown as its crystalline structure is not available.

Table A.2: Crystallite grain sizes for the thin films of various thickness of PDI-octyl and PDI-hexhep as determined using the Scherrer equation.

Film thickness (nm)	PDI-octyl			PDI-hexhep		
	$\beta$ (°)	$\theta$ (°)	$\tau$ (nm)	$\beta$ (°)	$\theta$ (°)	$\tau$ (nm)
30	0.370	4.971	27.7	0.358	5.829	28.6
50	0.316	5.063	32.5	0.238	5.845	43.2
100	0.169	5.091	60.9	0.128	5.846	80.2
150	0.127	5.096	80.8	0.091	5.846	113.0
250	0.106	5.112	97.0	0.078	5.862	131.3

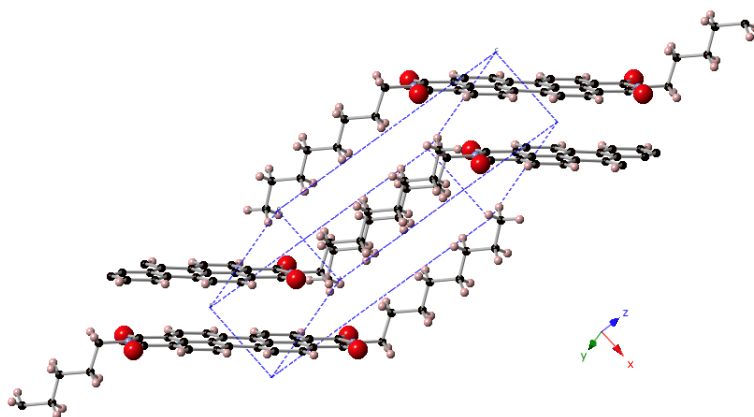


Figure A.1: Image of the molecular cell of PDI-octyl showing the unit cell (blue dash) and the molecule unit it contains in an intact shape.

## SEM IMAGES OF 30 NM AND 100 NM THICK ANNEALED PDI LAYERS ON FUSED SILICA

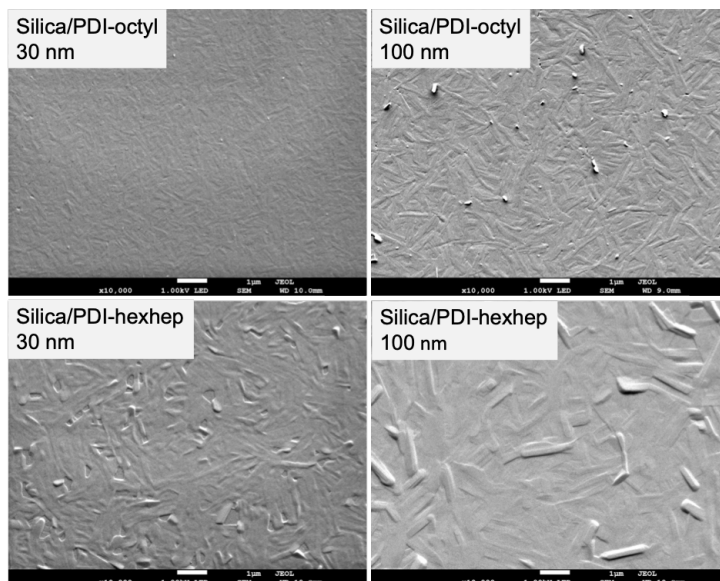


Figure A.2: SEM images of a 30 and 100 nm annealed thin film of PDI-octyl (left panel) and PDI-hexhep (right panel). Scale bars indicate the size of the features at 10.000X magnification. The samples are coated with a 3 nm Pt layer.

## SEM IMAGES OF UNCOATED FUSED SILICA AND TiO<sub>2</sub> LAYERS ON FUSED SILICA

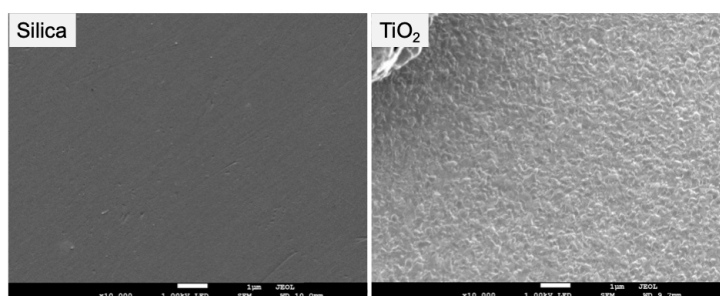


Figure A.3: SEM images of an uncoated fused silica substrate and a TiO<sub>2</sub> coated fused silica substrate as used in this study at 10.000X magnification. The samples are coated with a 3 nm Pt layer.

## OPTICAL PROPERTIES OF PDI-OCTYL, PDI-HEXHEP AND ZnPc

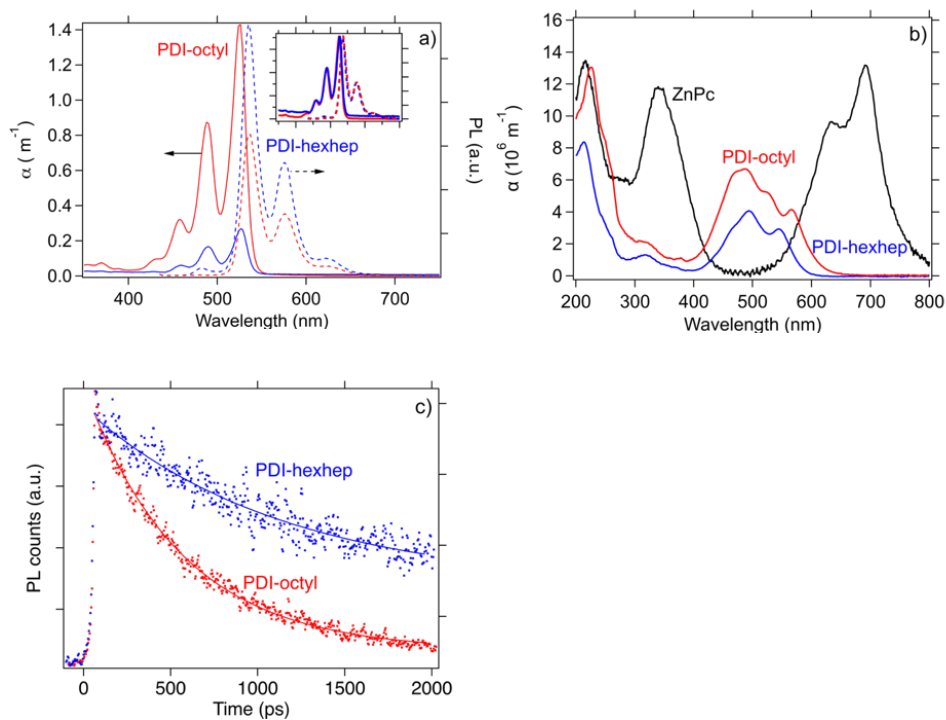


Figure A.4: a) Absorption spectra of PDI-octyl and PDI-hexhep in a  $1 \cdot 10^{-5}$  M  $\text{CHCl}_3$  solution and b) solid-state absorption spectra of a PDI-octyl (50 nm), PDI-hexhep (50 nm) and ZnPc (30 nm) individual layers. c) Fluorescence decays of annealed thin films of PDI-octyl (emission at 687 nm) and PDI-hexylheptyl (emission at 630 nm) (dots) upon 460 nm photoexcitation (300  $\mu\text{W}$ ) and their monoexponential fit (solid lines).

## XRD OF TiO<sub>2</sub>/PDI HETEROJUNCTIONS

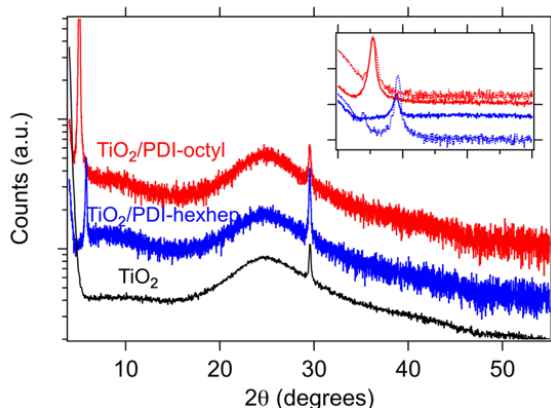


Figure A.5: XRD diffractograms of a TiO<sub>2</sub>/PDI-octyl (red) and TiO<sub>2</sub>/PDI-hexhep (blue) heterojunction and a TiO<sub>2</sub> sample. The reflection at 29° originates from the TiO<sub>2</sub>. The inset shows that the PDI reflection on TiO<sub>2</sub> (solid line) has an identical width and position as on fused silica (dotted line).

## TRMC PHOTON FLUENCE DEPENDENCE CHARGE CARRIER KINETICS FOR PDI-OCTYL

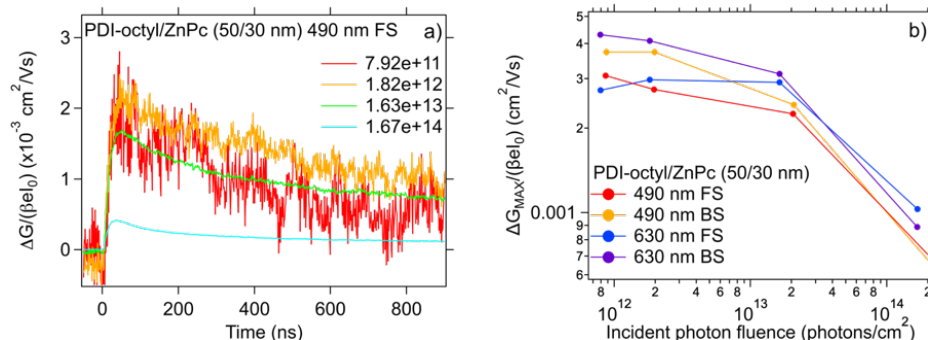


Figure A.6: a) Photoconductivity transients for a 50/30 nm PDI-octyl/ZnPc bilayer at various photon fluences upon 490 nm FS excitation. b) The photon fluence dependence of  $\eta_0 \Sigma \mu$  for the same bilayer upon PDI (490 nm) and ZnPc (630 nm) at FS and BS.

## TABLE WITH KINETIC PARAMETERS OBTAINED FROM FITTING OF PDI-OCTYL TRMC TRANSIENTS

The estimation of the exciton diffusion length requires a correction for possible electron-hole recombination that occurs within the instrumental response time. This correction is carried out by fitting the transients with a tri-exponential function as described by 2.9. Some of the fitting parameters are time constants that describe charge carrier decay processes and are obtained with their respective weight. In addition, we obtain an estimate



for the intrinsic change in photoconductance  $\Delta G_0$ . We provide these fitting parameters in A.3 as function of film thickness, excitation side (front side FS, backside BS) and excitation wavelength (490 nm PDI excitation and 630 nm ZnPc excitation) for PDI-octyl. We use the  $\Delta G_0$  values to determine the exciton diffusion length.

Table A.3: Fitting parameters obtained from a tri-exponential fit on the photoconductivity transients of PDI-octyl/ZnPc as function of different PDI-octyl thicknesses and illumination side (FS = front side and BS = back side) dependence at 490 and 630 nm excitation.

PDI-octyl/ZnPc									
490 nm									
	Side	PF	$\tau_1$	$\tau_2$	$\tau_3$	$W_1$	$W_2$	$W_3$	$G_0$
15/30	FS	1.94E+12	6.0E-07	8.0E-05	5.0E-04	5.0E-01	3.0E-01	2.0E-01	5.1E-03
	BS	8.05E+11	6.0E-07	8.0E-05	5.0E-04	5.0E-01	3.0E-01	2.0E-01	6.4E-03
30/30	FS	8.77E+11	6.0E-08	9.0E-07	1.0E-06	5.0E-01	4.0E-01	1.0E-01	2.6E-03
	BS	8.67E+11	1.0E-07	8.0E-07	1.0E-05	5.0E-01	4.0E-01	1.0E-01	3.0E-03
50/30	FS	8.65E+11	6.0E-08	7.0E-07	1.0E-06	5.0E-01	4.0E-01	1.0E-01	2.8E-03
	BS	8.74E+11	1.5E-07	1.0E-06	1.0E-04	5.0E-01	4.0E-01	1.0E-01	3.7E-03
100/30	FS	8.59E+11	2.0E-07	1.0E-05	1.0E-04	5.0E-01	4.0E-01	1.0E-01	3.8E-03
	BS	8.36E+11	2.0E-07	5.0E-06	1.0E-05	5.0E-01	4.0E-01	1.0E-01	3.4E-03
150/30	FS	8.83E+11	2.0E-07	2.0E-05	1.0E-04	5.0E-01	4.0E-01	1.0E-01	4.7E-03
	BS	8.29E+11	2.0E-07	6.0E-05	1.0E-04	5.0E-01	4.0E-01	1.0E-01	2.6E-03
250/30	FS	8.35E+11	1.5E-07	1.5E-06	1.0E-04	5.0E-01	4.0E-01	1.0E-01	4.0E-03
	BS	8.26E+11	1.0E-07	6.0E-07	1.0E-05	5.0E-01	4.0E-01	1.0E-01	2.1E-03
500/30	FS	8.87E+11	2.0E-07	5.0E-06	1.0E-04	5.0E-01	4.0E-01	1.0E-01	4.0E-03
	BS	8.25E+11	2.0E-07	3.0E-07	1.0E-06	5.0E-01	4.0E-01	1.0E-01	1.2E-03
630 nm									
	Side	PF	$\tau_1$	$\tau_2$	$\tau_3$	$W_1$	$W_2$	$W_3$	$G_0$
15/30	FS								
	BS	6.48E+11	3.5E-07	8.0E-05	5.0E-04	5.0E-01	3.0E-01	2.0E-01	5.7E-03
30/30	FS	7.93E+11	7.0E-08	3.0E-07	1.0E-06	5.0E-01	4.0E-01	1.0E-01	2.5E-03
	BS	7.81E+11	2.0E-07	1.0E-06	1.0E-05	5.0E-01	4.0E-01	1.0E-01	2.2E-03
50/30	FS	7.92E+11	1.5E-07	2.0E-06	1.0E-05	5.0E-01	4.0E-01	1.0E-01	2.2E-03
	BS	7.90E+11	1.0E-07	1.0E-06	5.0E-06	5.0E-01	4.0E-01	1.0E-01	4.0E-03
100/30	FS	7.99E+11	1.5E-07	8.0E-06	1.0E-05	5.0E-01	4.0E-01	1.0E-01	2.8E-03
	BS	7.84E+11	2.0E-07	7.0E-06	1.0E-05	5.0E-01	4.0E-01	1.0E-01	4.6E-03
150/30	FS	7.99E+11	1.0E-07	2.0E-06	1.0E-05	5.0E-01	4.0E-01	1.0E-01	3.8E-03
	BS	8.16E+11	1.5E-07	7.0E-05	1.0E-04	4.0E-01	5.0E-01	1.0E-01	4.3E-03
250/30	FS	7.70E+11	1.0E-07	2.0E-06	1.0E-05	5.0E-01	4.0E-01	1.0E-01	3.8E-03
	BS	7.24E+11	1.0E-07	2.0E-06	1.0E-05	5.0E-01	4.0E-01	1.0E-01	5.5E-03
500/30	FS	7.91E+11	1.0E-07	3.0E-06	1.0E-04	5.0E-01	4.0E-01	1.0E-01	4.2E-03
	BS	7.74E+11	3.0E-07	3.0E-06	1.0E-04	5.0E-01	4.0E-01	1.0E-01	5.2E-03

## TRMC CHARGE CARRIER KINETICS FOR PDI-HEXHEP THIN FILMS OF VARIABLE THICKNESS

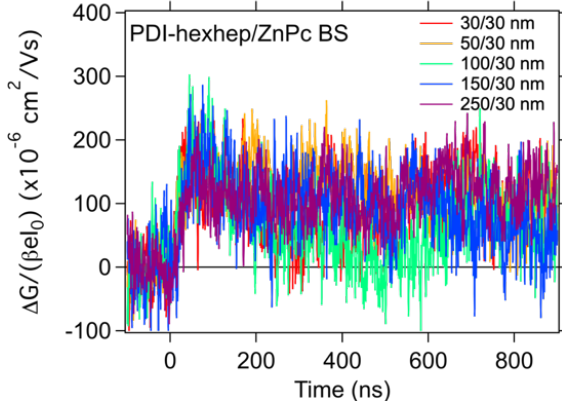


Figure A.7: Photoconductivity transients for PDI-hexhep/ZnPc heterojunctions of varying PDI thicknesses. The transients were obtained upon 495 backside excitation (BS) at a photon fluence  $I_0$  of  $9.2 \cdot 10^{12}$  photons/cm<sup>2</sup>.

### METHODOLOGY FOR EXCITON DIFFUSION LENGTH DETERMINATION

The fraction of charges that arrive at the interface S for the PDI/ZnPc heterojunction is described by the following two expressions assuming quenching of excitons at the PDI-fused silica interface:

$$S_{FS} = \left( \frac{\alpha^2 \Lambda_{exc}^2}{\alpha^2 \Lambda_{exc}^2 - 1} \right) \left[ 1 - e^{\alpha L} \operatorname{sech} \left( \frac{L}{\Lambda_{exc}} \right) - \frac{\tanh \left( \frac{L}{\Lambda_{exc}} \right)}{\alpha \Lambda_{exc}} \right] \quad (\text{A.2})$$

$$S_{BS} = \left( \frac{\alpha^2 \Lambda_{exc}^2}{\alpha^2 \Lambda_{exc}^2 - 1} \right) \left[ \operatorname{sech} \left( \frac{L}{\Lambda_{exc}} \right) - e^{\alpha L} \left( 1 + \frac{\tanh \left( \frac{L}{\Lambda_{exc}} \right)}{\alpha \Lambda_{exc}} \right) \right] \quad (\text{A.3})$$

For the TiO<sub>2</sub>/PDI heterojunction we use the following two expressions for S and assume exciton quenching occurs at the PDI-air interface.

$$S_{Q,FS} = \left( \frac{\alpha^2 \Lambda_{exc}^2}{\alpha^2 \Lambda_{exc}^2 - 1} \right) \left( \frac{\operatorname{csch} \left( \frac{L}{\Lambda_{exc}} \right) - e^{\alpha L} \operatorname{coth} \left( \frac{L}{\Lambda_{exc}} \right)}{\alpha \Lambda_{exc}} - e^{\alpha L} \right) \quad (\text{A.4})$$

$$S_{Q,BS} = \left( \frac{\alpha^2 \Lambda_{exc}^2}{\alpha^2 \Lambda_{exc}^2 - 1} \right) \left( 1 + \frac{e^{\alpha L} \operatorname{csch} \left( \frac{L}{\Lambda_{exc}} \right) - \operatorname{coth} \left( \frac{L}{\Lambda_{exc}} \right)}{\alpha \Lambda_{exc}} \right) \quad (\text{A.5})$$

The reflection corrected  $\eta_0 \Sigma \mu$  values obtained at different excitation wavelengths are plotted in Figure A.8a and A.8c as function of the corresponding absorption coefficient ( $\alpha$ ) for PDI-octyl and PDI-hexhep, respectively. Different datasets for front side and back

side illumination are fitted individually using Equations 2.11 and A.4, A.5 and are shown in the same figure. The fitting results are provided in Table 2.1. Figure A.8b and A.8d contain the fit trajectory at larger  $\alpha$  values that serve to check whether the fitting function displays the expected  $\eta_0 \Sigma \mu(\alpha)$  trend as function of illumination side.

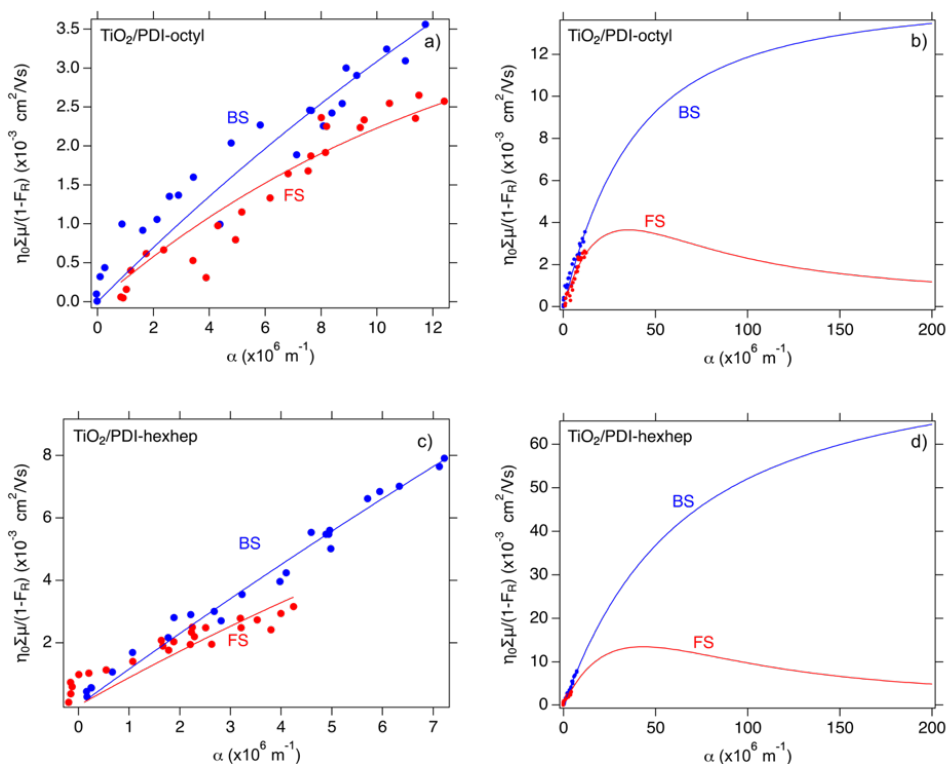


Figure A.8: a) A plot of  $\eta_0 \Sigma \mu$  vs. the absorption coefficient  $\alpha$  for a TiO<sub>2</sub>/PDI-octyl (100 nm) bilayer upon FS and BS excitation with a fit obtained from applying the exciton diffusion model. c) A plot of  $\eta_0 \Sigma \mu$  vs.  $\alpha$  for a TiO<sub>2</sub>/PDI-hexhep (30 nm) bilayer with a fit obtained from applying the exciton diffusion model. b) and d) A plot of the fits at extended values of  $\alpha$  to prove a viable exciton diffusion profile, similar to that of the organic bilayer for TiO<sub>2</sub>/PDI-octyl and TiO<sub>2</sub>/PDI-hexhep, respectively.

## DETERMINATION OF THE TiO<sub>2</sub> ELECTRON MOBILITY

Figure A.9a gives a demonstration how the TiO<sub>2</sub> electron mobility was determined. TRMC conductivity fluences were measured at 300 nm backside (BS) TiO<sub>2</sub> excitation. The maximum photoconductance signals at  $t = 0$  were plotted as function of fluence and corrected for the fraction of absorbed photons ( $F_{A,300\text{nm}} = 0.58$ ). The plateau region  $\phi \Sigma \mu$  value was then taken as indicated by the red dashed line in figure A.9b. By assuming full exciton charge separation efficiency ( $\phi = 100\%$ ) and neglecting any conductivity and thus mobility due to holes, the  $\mu_{e^-}$  in TiO<sub>2</sub> upon backside excitation was determined as  $2.09 \text{ cm}^2/\text{Vs}$ . In the study we used the average mobility determined upon FS and BS excitation.

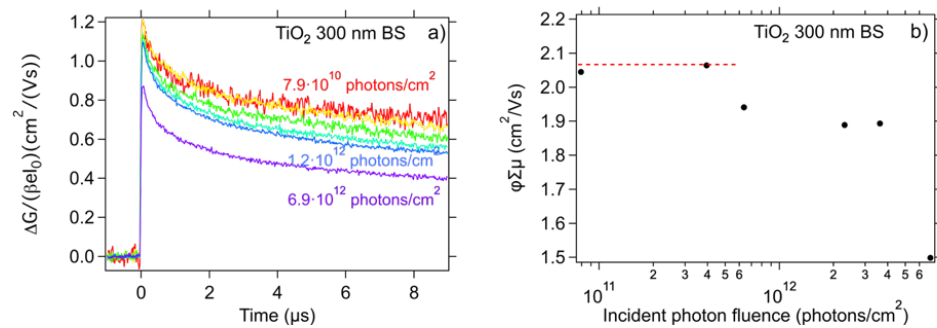


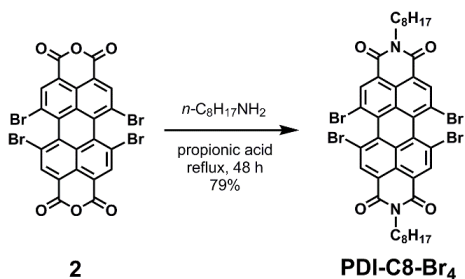
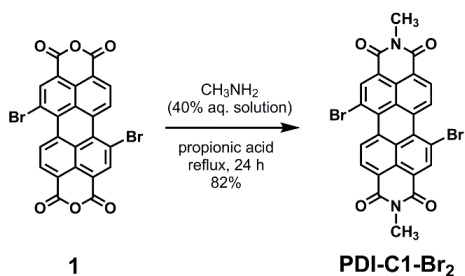
Figure A.9: a) TRMC transients of a TiO<sub>2</sub> film upon direct bandgap (300 nm) back side (BS) excitation for the fluence range  $1 \cdot 10^9$ - $1 \cdot 10^{12}$  photons/cm<sup>2</sup>. b) A plot of  $\eta \Sigma \mu$  vs.  $I_0$  for the TiO<sub>2</sub> single layer film. The dashed line shows the readout value for the electron mobility in the TiO<sub>2</sub> film.



# B

## APPENDIX CHAPTER 3

### PDI CHROMOPHORE SYNTHESIS



**Synthesis of N,N'-dimethyl-1,7-dibromoperylene diimide (PDI-C1-Br<sub>2</sub>):** Regioisomerically pure 1,7-dibromoperylene dianhydride<sup>1</sup> **1** (1.00 g, 1.82 mmol, 1 eq.) was suspended in propionic acid (40 mL) and, subsequently, 40% aqueous solution of CH<sub>3</sub>NH<sub>2</sub>

(1.26 mL, 14.54 mmol, 8 eq.) was added. The reaction mixture was refluxed under stirring for 24 h, cooled to room temperature and poured into ice-water mixture. The precipitate was filtered off, thoroughly washed with several portions of water and ethanol, and dried. The crude product was taken in chloroform (200 mL) and refluxed overnight under fast stirring. After being cooled to room temperature, the precipitate was collected by filtration and dried to get the pure product (0.86 g, 82%). The product was highly insoluble in common organic solvents. Therefore, it was characterized by  $^1\text{H}$  NMR in sulfuric acid- $\text{d}_2$  solution (96–98 wt. % in  $\text{D}_2\text{O}$ ).  $^1\text{H}$  NMR (400 MHz,  $\text{D}_2\text{SO}_4$ ):  $\delta$  = 9.83 (d,  $J$  = 8.1 Hz, 2H), 9.18 (s, 2H), 8.94 (d,  $J$  = 8.1 Hz, 2H), 3.85 (s, 6H).

**Synthesis of  $N,N'$ -dioctyl-1,6,7,12-tetrabromoperylene diimide (PDI-C8-Br<sub>4</sub>):** 1,6,7,12-tetrabromoperylene dianhydride<sup>2</sup> **2** (1.00 g, 1.41 mmol, 1 eq.) and *n*-octylamine (2.92 g, 22.60 mmol, 16 eq.) were taken in a round-bottomed flask equipped with a water-condenser. Thereafter, propionic acid (50 mL) was added. The reaction mixture was refluxed under stirring for 48 h, cooled to room temperature and poured into ice-water mixture. The precipitate was filtered off, thoroughly washed with several portions of water and ethanol, and dried to obtain the crude product. The crude product was chromatographed on silica with 2:1 DCM-hexane mixture to yield the pure product (1.04 g, 79%).  $^1\text{H}$  NMR (400 MHz,  $\text{CDCl}_3$ ):  $\delta$  = 8.81 (s, 4H), 4.18 (t,  $J$  = 8.0 Hz, 4H), 1.78–1.67 (m, 4H), 1.43–1.25 (m, 20H), 0.87 (t,  $J$  = 7.2 Hz, 6H).  $^{13}\text{C}$  NMR (100 MHz,  $\text{CDCl}_3$ ):  $\delta$  = 162.137, 136.055, 131.628, 131.393, 123.901, 122.679, 40.949, 31.784, 29.274, 29.162, 28.090, 27.044, 22.615, 14.069.

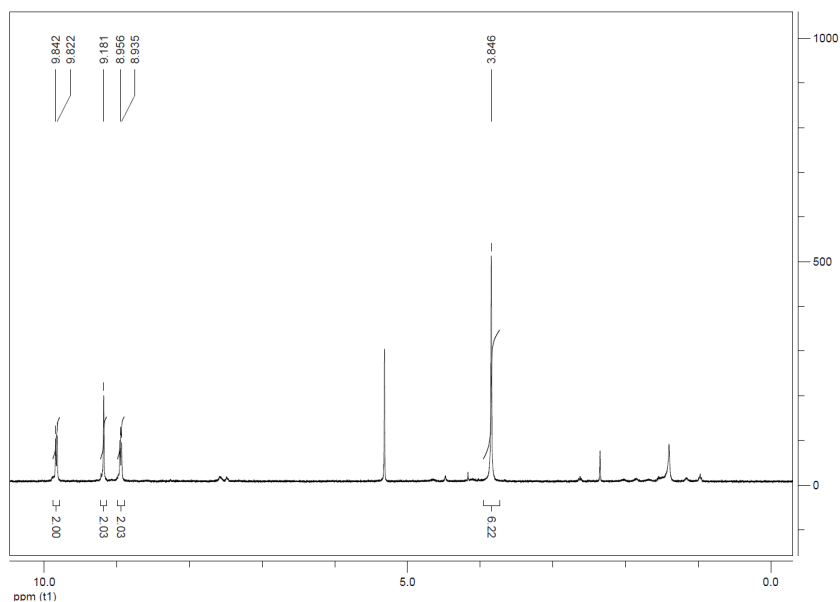


Figure B.2:  $^1\text{H}$  NMR spectrum of PDI-C1-Br<sub>2</sub> in 96–98%  $\text{D}_2\text{SO}_4$ .

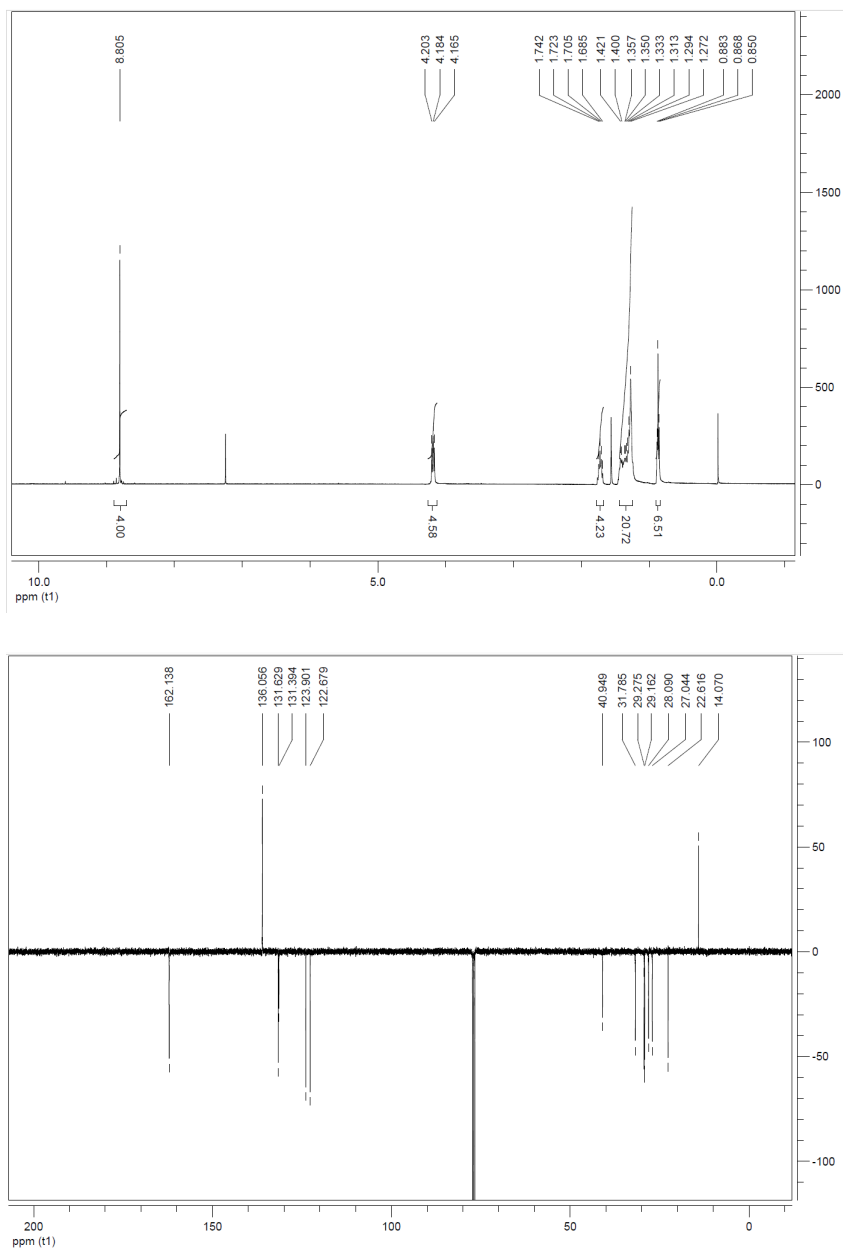


Figure B.3: <sup>1</sup>H and <sup>13</sup>C (APT) NMR spectra of PDI-C8-Br<sub>4</sub> in CDCl<sub>3</sub>.



## THIN FILM THICKNESSES

Table B.1: Thin films effective thicknesses

PDI	Effective Thickness (nm)
PDI-C1	$83 \pm 10$
PDI-C1-Br <sub>2</sub> *	$835 \pm 97$
PDI-C8	$67 \pm 5$
PDI-C8-Br <sub>4</sub>	$253 \pm 46$

\*Dektak measurements compromised by the high surface roughness.

## X-RAY DIFFRACTION ON PDI THIN FILMS

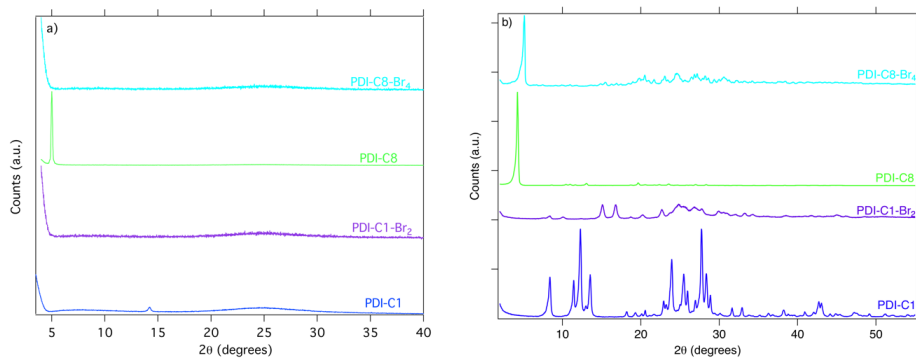


Figure B.4: XRD spectra of a) thin films and b) powders of PDI-C1, PDI-C1-Br<sub>2</sub>, PDI-C8, and PDI-C8-Br<sub>4</sub>.

## TEMPERATURE DEPENDENT STEADY STATE ABSORPTION AND PHOTOLUMINESCENCE DECAY

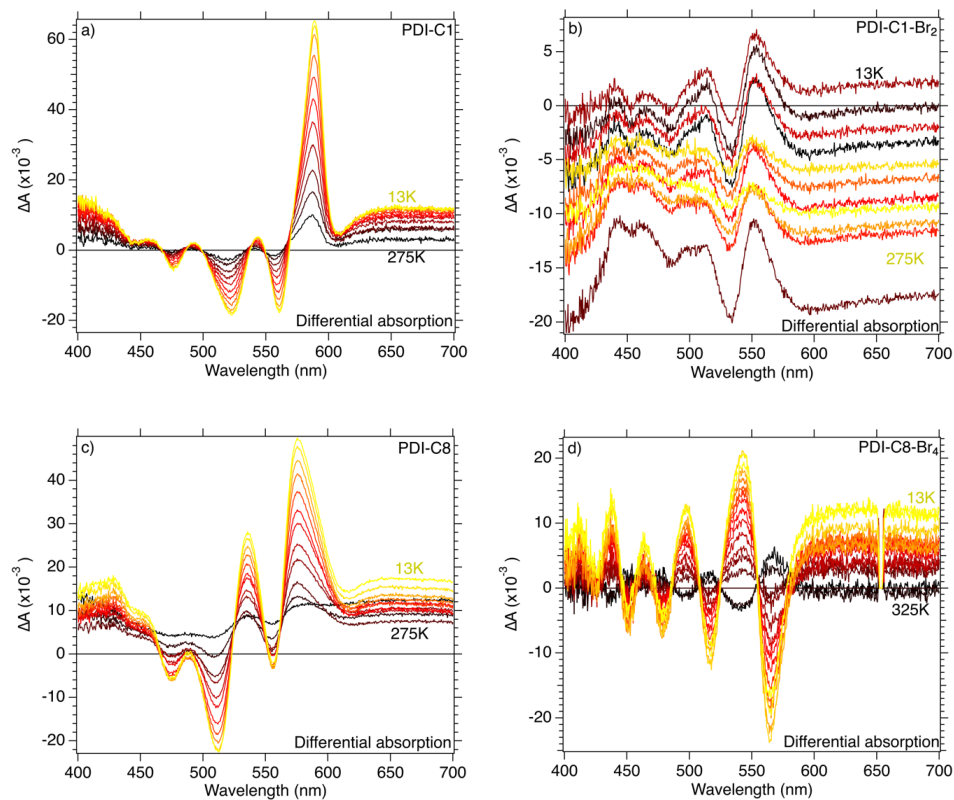


Figure B.5: Temperature dependent optical absorption of a) PDI-C1, b) PDI-C1-Br<sub>2</sub>, c) PDI-C8, and d) PDI-C8-Br<sub>4</sub>. The differential absorption is shown with 300 K as the base temperature.

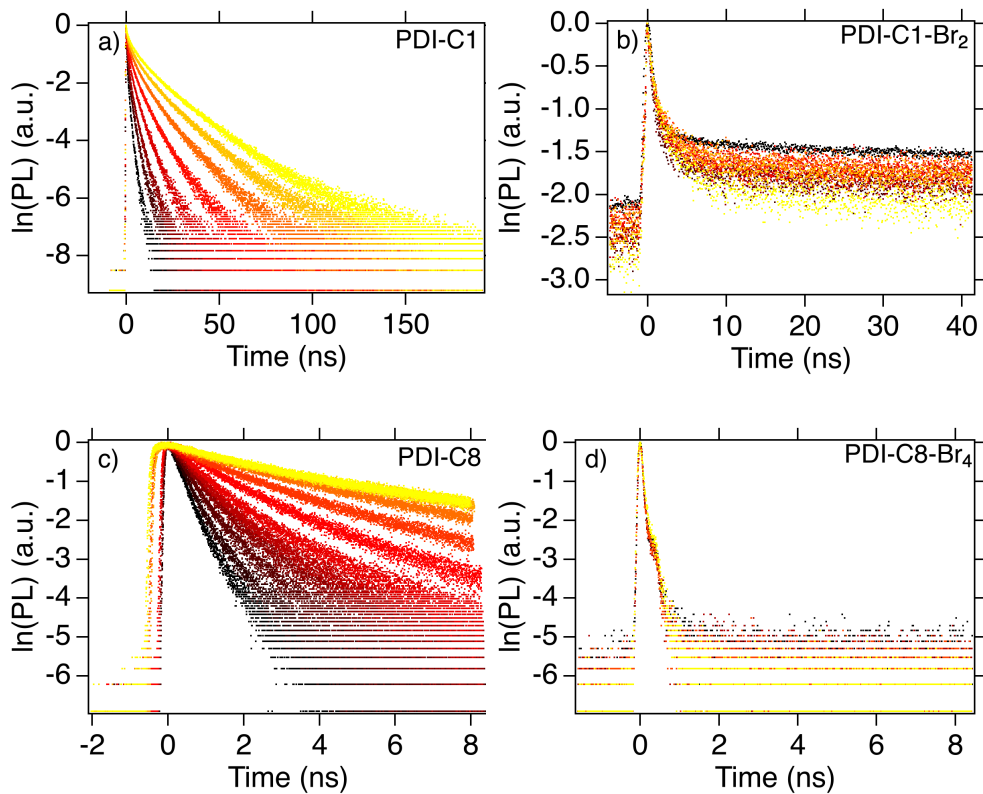


Figure B.6: Temperature dependent time resolved photoluminescence of a) PDI-C1, b) PDI-C1-Br<sub>2</sub>, c) PDI-C8, and d) PDI-C8-Br<sub>4</sub>.

## VIBRATIONAL MOTION

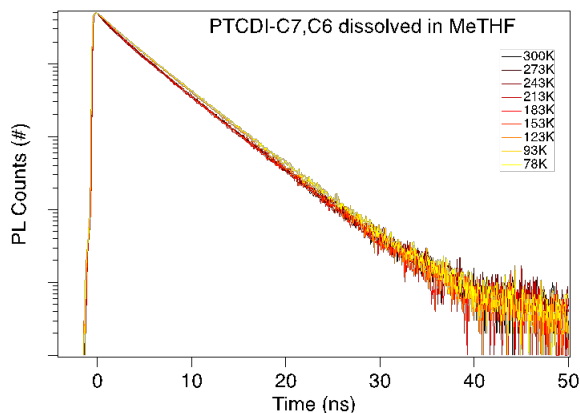


Figure B.7: Temperature dependent PDI-hexylheptyl in a MeTHF solution.

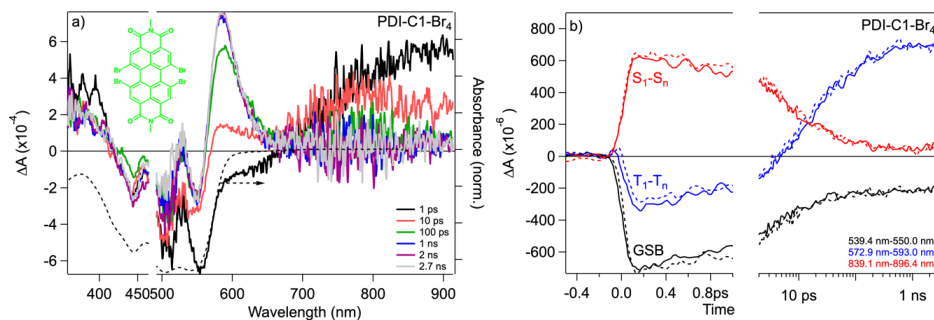
TRANSIENT ABSORPTION MEASUREMENTS ON A PDI-C1-Br<sub>4</sub> THIN FILM

Figure B.8: a) Transient absorption spectra at different times of a PDI-C1-Br<sub>4</sub> thin film on sapphire upon 480 nm excitation at  $1.86 \cdot 10^{12}$  photons/cm<sup>2</sup>. The dashed line indicates the normalized absorption spectrum of the thin film. The inset shows the molecular structure of PDI-C1-Br<sub>4</sub>. b) Kinetic traces of the ground-state bleach (GSB), triplet absorption ( $T_1-T_n$ ) and the singlet absorption ( $S_1-S_n$ ) of PDI-C1-Br<sub>4</sub>. The solid lines are kinetic traces from the sample on sapphire, while the dotted line belong to kinetic traces of a fused silica based film.

## PUMP POWER DEPENDENCE IN FS-TA

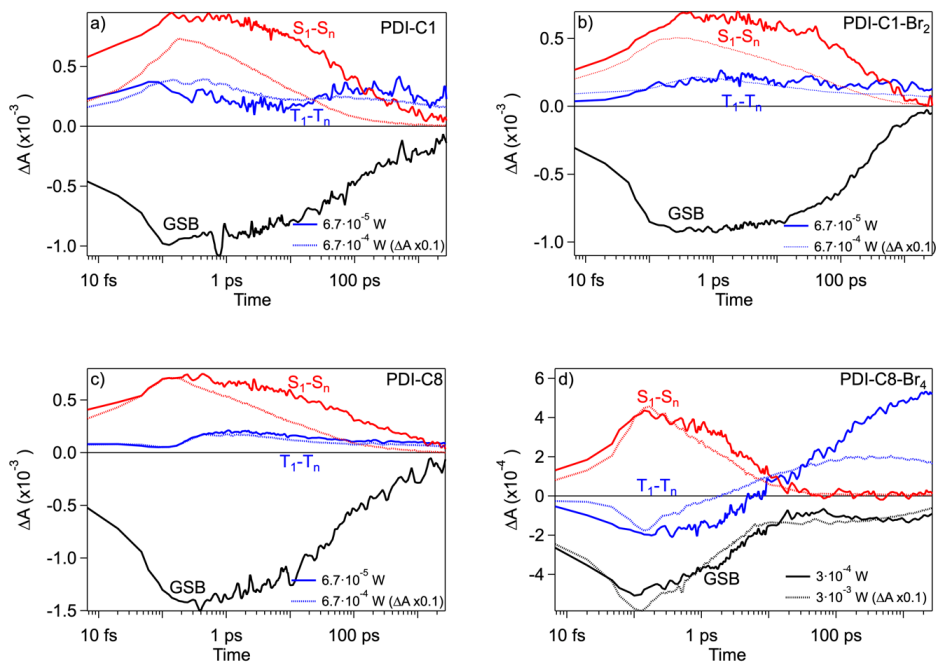


Figure B.9: Kinetic traces of the ground-state bleach (GSB), triplet absorption ( $T_1-T_n$ ) and the singlet absorption ( $S_1-S_n$ ) for a) PDI-C1, b) PDI-C1-Br<sub>2</sub>, c) PDI-C8 and d) PDI-C8-Br<sub>4</sub> at  $67 \mu\text{W}$  ( $1.86 \cdot 10^{12}$  photons/cm<sup>2</sup>, solid lines) and  $670 \mu\text{W}$  ( $1.86 \cdot 10^{13}$  photons/cm<sup>2</sup>, dashed lines). For PDI-C8-Br<sub>4</sub> the powers were  $300 \mu\text{W}$  ( $2.17 \cdot 10^{13}$  photons/cm<sup>2</sup>) and  $3 \text{ mW}$  ( $2.17 \cdot 10^{14}$  photons/cm<sup>2</sup>). The traces are the average of a wavelength region as indicated in the lower right corner.

## REFERENCES

- (1) Sengupta, S.; Dubey, R. K.; Hoek, R. W.; van Eeden, S. P.; Günbaş, D. D.; Grozema, F. C.; Sudhölter, E. J.; Jager, W. F. Synthesis of regioisomerically pure 1, 7-dibromoperylene-3, 4, 9, 10-tetracarboxylic acid derivatives. *J. Org. Chem.* **2014**, 79, 6655–6662.
- (2) Hill, Z. B.; Rodovsky, D. B.; Leger, J. M.; Bartholomew, G. P. Synthesis and utilization of perylene-based n-type small molecules in light-emitting electrochemical cells. *Chem. Commun.* **2008**, 6594–6596.



# C

## APPENDIX CHAPTER 4

### SAMPLE PREPARATION AND CHARACTERIZATION

Thin films of anatase  $\text{TiO}_2$  of  $90 \pm 10$  nm thickness were purchased from *Everest Coatings* (Delft, The Netherlands). The films were prepared by chemical vapor deposition on top of 1 mm thick quartz plates. Subsequently, annealing at  $450^\circ\text{C}$  for two hours in air was performed to improve stoichiometry. The resulting crystallite size is  $90 \pm 10$  nm (see Figure C.1). Thin films of PDI- $\text{CH}_3$  and  $\text{F}_{16}\text{ZnPc}$  powders were deposited on sapphire substrates by thermal evaporation in an *AJA ATC Orion evaporator*. Prior to deposition, the substrates and single layer  $\text{TiO}_2$  film on a fused silica substrate (*ESCO*, 12 x 25 x 1 mm) were cleaned by an air plasma for 2 min at 1000 mtorr. During thermal evaporation, the powders were heated to their sublimation temperature ( $180$ - $230^\circ\text{C}$ ) under high vacuum conditions ( $10^{-7}$ - $10^{-6}$  mbar) and was adjusted to an evaporation rate of  $0.3 \text{ \AA/s}$ . The deposition rate was monitored using a quartz micro-crystal balance and a substrate holder rotated the substrates at 25 rpm to ensure film homogeneity. The resulting tri-layer sample was annealed at  $70^\circ\text{C}$  for 1 hour. This preparation method ensures high reproducibility, homogeneity and controlled thickness of the PDI- $\text{CH}_3$  and  $\text{F}_{16}\text{ZnPc}$  films. In addition, following the PVD procedure described above, individual layers of  $\text{F}_{16}\text{ZnPc}$  and PDI- $\text{CH}_3$  and bilayers of  $\text{TiO}_2/\text{PDI-CH}_3$  and  $\text{PDI-CH}_3/\text{F}_{16}\text{ZnPc}$  were prepared for reference measurements.

The thin film surface morphology was probed with an *NTEGRA Prima AFM* atomic force microscopy (AFM) in tapping mode. X-ray diffractograms were acquired using a *Brüker D8* X-ray diffractometer (Co  $K\alpha 1$  radiation,  $\lambda = 1.79 \text{ \AA}$ ) and analysed with the Brüker program *EVA*. Steady state absorption spectra were obtained using a *Perkin Elmer Lambda 1050* spectrometer with the sample placed inside of an integrating sphere to measure attenuation. Nanosecond time resolved transient absorption spectra were acquired using an *LP920* transient absorption spectrophotometer of *Edinburgh Instruments* with pulsed probe light (7 ms) produced by a Xe lamp. The samples were excited by 4 ns (FWHM) laser pulses produced by an *Ekspla NT 342B OPO* pumped by a Q-switched Nd:YAG laser. To probe in the 495-690 nm region, we used a 495 nm long-pass filter when photoexciting the sample at 480 nm to neutralize scattered light, while



upon 709 nm photoexcitation we used a 700 nm short pass filter.

### FLASH PHOTOLYSIS MICROWAVE CONDUCTIVITY

The electron injection into TiO<sub>2</sub> was studied with the flash photolysis time resolved microwave conductivity (TRMC) technique. These TRMC measurements were performed on a home-built setup of which the operating principles are described elsewhere.<sup>1</sup> In this technique, optical excitation of the sample occurred via 3 ns full width half maximum (FWHM) laser pulses ( $\lambda = 240\text{-}2200$  nm). The sample was probed by continuous X-band microwaves ( $\sim 8.4$  GHz) in a microwave resonant cavity cell that limited the instrumental response time to 18 ns. The sample chamber in the cavity cell was filled with N<sub>2</sub> to avoid oxygen exposure. The fractional change in microwave power reflected ( $\Delta P/P$ ) is related to a change in photoconductance,  $\Delta G(t)$ , as:

$$\frac{\Delta P(t)}{P} = -K\Delta G(t) \quad (\text{C.1})$$

In equation C.1,  $K$  is the microwave frequency dependent sensitivity factor that has a predetermined value of  $40 \cdot 10^3 \text{ S}^{-1}$  for the current experimental conditions.<sup>2</sup>  $\Delta G(t)$  is directly proportional to the product of the charge carrier density  $n_i$  and mobility  $\mu_i$  according to:

$$\Delta G(t) = e\beta L \sum_i n_i(t)\mu_i \quad (\text{C.2})$$

In equation C.2,  $e$  is the elementary charge,  $L$  the film thickness and  $\beta$  the ratio between the inner width and length dimensions of the microwave waveguide. The index ' $i$ ' runs over all charged species present, *i.e.* electrons and holes both contribute to the photoconductance. The photoconductance transients can be deconvoluted for the instrumental response function using the cavity response function profile ( $LP(t)$ ):

$$\Delta G_{exp}(t) = LP(t) \otimes \Delta G_0 \left( \sum_i c_i e^{-t/\tau_i} \right) \quad (\text{C.3})$$

In equation C.3,  $\Delta G_0$  is the initial photoconductance prior to charge carrier decay and  $\otimes$  indicates the convolution between  $LP(t)$  and  $\Delta G_0$ .  $c_i$  and  $\tau_i$  are the exponent and decay time characteristic of the  $i$ -th transient decay component. The sum of all decay components account for all recombination processes occurring in the sample.  $\Delta G_0$  can be used to obtain a value for the product of the incident photon to charge carrier generation yield,  $\eta_0$ , and the sum of electron and hole mobility,  $\sum \mu$ , as<sup>3</sup>.

$$\frac{\Delta G_0}{\beta e I_0} = \eta \sum_i \mu_i \quad (\text{C.4})$$

In equation C.4,  $I_0$  is the measured incident photon fluence.

## SURFACE CHARACTERIZATION

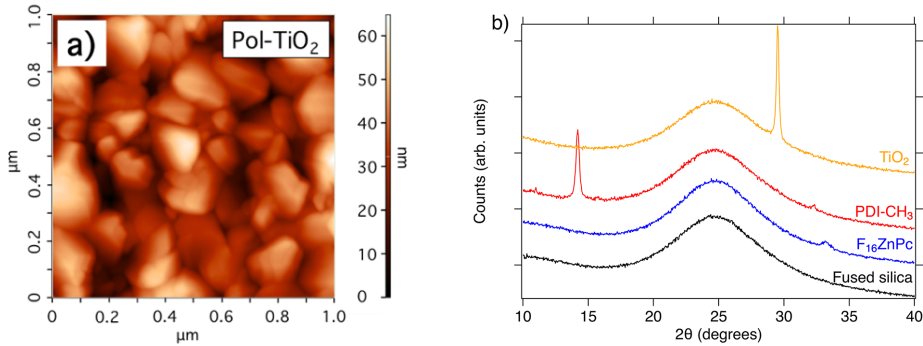


Figure C.1: a) AFM image of Pol-TiO<sub>2</sub>. The crystallite size is approximately 100 nm. b) XRD diffractograms of Pol-TiO<sub>2</sub>, a 100 nm PDI-CH<sub>3</sub> and a 200 nm F<sub>16</sub>ZnPc film on fused silica and the fused silica substrate. The sharp peak at  $2\theta = 29.8^\circ$  corresponds to a lattice spacing of 3.46 Å, typical for the anatase crystal unit.[4]

## TiO<sub>2</sub> ELECTRON MOBILITY DETERMINATION

We determined the electron mobility in TiO<sub>2</sub> using a previously used method.<sup>5</sup> In short, the maximum photoconductance signal at which no charge recombination has occurred,  $\Delta G_0$  is equal to the product of the charge carrier generation yield,  $\eta$ , and the sum of the electron and hole mobility,  $\Sigma \mu$ , by the proportionality factor  $\beta e I_0$ : as described by equation C.4. The hole mobility in TiO<sub>2</sub> is assumed to be negligible compared to the TiO<sub>2</sub> electron mobility,  $\mu_{e^-}$ . We calculate the  $\mu_{e^-}$  in TiO<sub>2</sub> by dividing the experimentally determined quantity  $\Delta G_0 / \beta e I_0$  by the fraction of absorbed photons at direct bandgap excitation in TiO<sub>2</sub> (300 nm),  $F_{A,300nm}$ , and by assuming that the absorbed photon-to charge carrier separation yield is unity,  $\phi=1$ :

$$\eta = \phi F_{A,300nm} \quad (C.5)$$

Therefore  $\mu_{e^-}$  can be calculated as:

$$\mu_{e^-} = \frac{\Delta G_0}{F_{A,300nm} \beta e I_0} \quad (C.6)$$

Figure C.2a and C.2d show a plot of  $\Delta G_0 / \beta e I_0$  values, that are obtained from Figure C.2a and C.2b, as function of photon fluence. Upon front (FS) and back (BS) side direct bandgap excitation of TiO<sub>2</sub>,  $\Delta G_0 / \beta e I_0$  amounts to 1.49096 and 1.4888 cm<sup>2</sup>/Vs, respectively. Using the  $F_{A,300nm}$  of 0.66 and 0.74 for FS and BS excitation gives  $\mu_{e^-,FS} = 2.3$  cm<sup>2</sup>/Vs and  $\mu_{e^-,BS} = 2.0$  cm<sup>2</sup>/Vs, respectively.

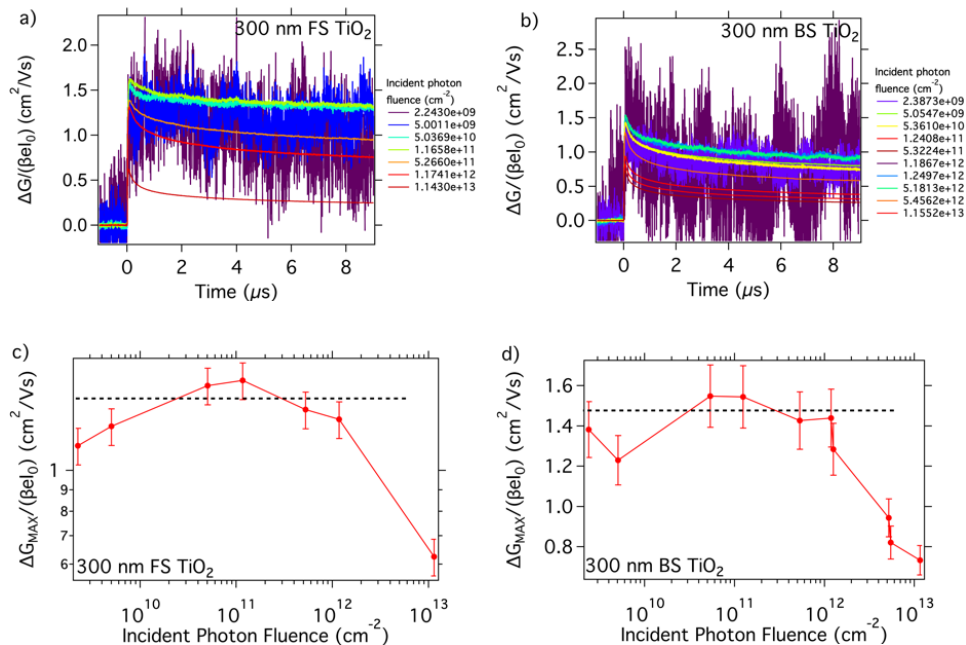


Figure C.2: TRMC photoconductance  $\Delta G$  transients as function of photon fluence upon 300 nm direct bandgap excitation of TiO<sub>2</sub> in a) front side and b) back side b) illumination. Plots of the maximum photoconductance  $\Delta G_0 / \beta e I_0$  as function of incident photon fluence. The dotted line, indicates the average maximum value that is used to determine the electron mobility in TiO<sub>2</sub>,  $\mu_{e^-}$ , upon c) front side and d) back side illumination.

### SUB-BANDGAP STATE CORRECTION IN SENSITIZED $\text{TiO}_2$ SAMPLES

We correct for intrabandgap state absorption in  $\text{TiO}_2$  at 700 nm photoexcitation by using a procedure used previously.<sup>5</sup> This method involves subtracting the photoconductance transient, shown in Figure C.3 of a single layer  $\text{TiO}_2$  at 700 nm excitation from its respective  $\text{TiO}_2/\text{PDI-CH}_3/\text{F}_{16}\text{ZnPc}$  trilayer under identical excitation conditions. We scale the single layer  $\text{TiO}_2$  trace with a weigh factor,  $F_{SB}$ , in order to match 100 ns kinetics. We note that the photoconductance transient of  $\text{TiO}_2$  at 700 nm excitation was recorded only until 10 microseconds. In order to subtract it from the 1 ms transient, we extrapolated the latter part of the decay kinetics using a mono-exponential decay function.

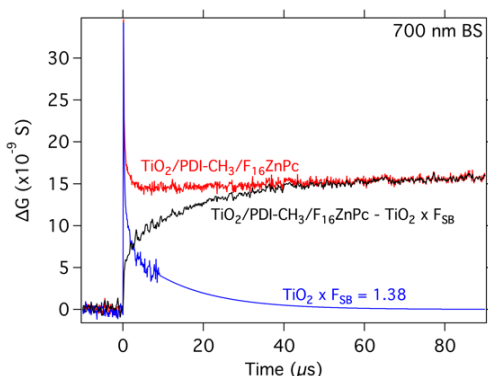


Figure C.3: Intrabandgap state correction of a trilayer photoconductance  $\Delta G$  transients (red) obtained upon 700 nm back side (BS) illumination by an  $\text{TiO}_2$  trace under identical illumination conditions (blue) that is scaled by a factor  $F_{SB}$ . The resulting trace is used to derive numbers for the electron injection efficiency (black).

### AIR INFLUENCE ON DELAYED GROWTH IN PHOTOCONDUCTANCE

We studied the effect of air on the photoconductance by measuring the trilayer sample in an air atmosphere under identical conditions as in the case of an  $N_2$  environment. In Figure C.4 we observe only a very minute delayed photoconductance signal in air, which is in agreement with previous observations of oxygen quenching triplet states in perylene derivatives.<sup>6</sup>

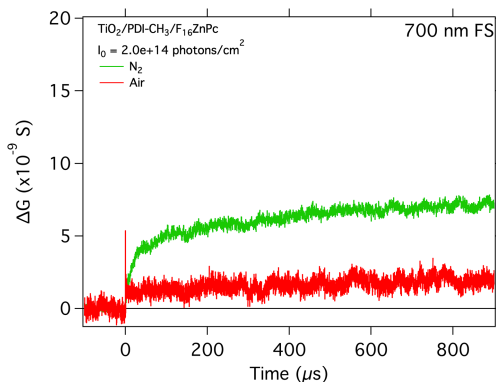


Figure C.4: Photoconductance  $\Delta G$  transient of a  $TiO_2/PDI-CH_3/F_{16}ZnPc$  (15/30 nm) trilayer in  $N_2$  (green) and in air (red) at 700 nm front side (FS) excitation ( $I_0 = 2.0 \cdot 10^{14}$  photons/cm<sup>2</sup>).

### NS-TA GROUND-STATE BLEACH AND TRIPLET ABSORPTION COMPARISON

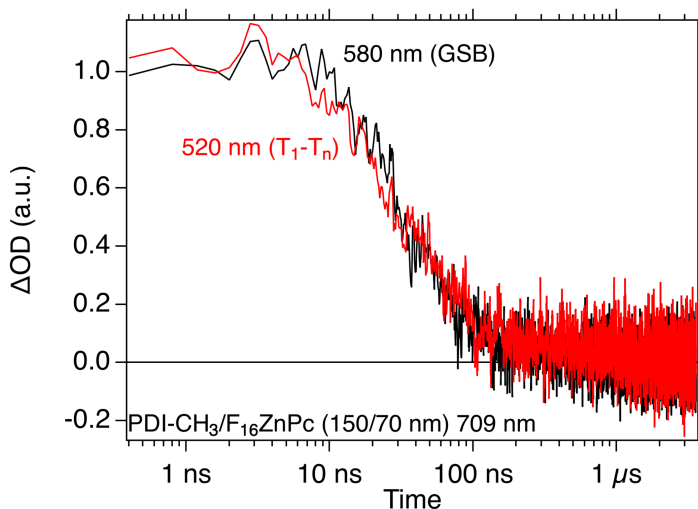


Figure C.5: Nanosecond TA transients of the trilayer at a probe wavelength of 520 nm (red) and 580 nm (black), corresponding to the triplet absorption feature ( $T_1-T_n$ ) and ground-state bleach (GSB), respectively.

## REFERENCES

- (1) Dehaas, M. P.; Warman, J. M. Photon-Induced Molecular Charge Separation Studied by Nanosecond Time-Resolved Microwave Conductivity. *Chem. Phys.* **1982**, *73*, 35–53.
- (2) Infelta, P. P.; Haas, M. P. D.; Warman, J. M. Study of Transient Conductivity of Pulse Irradiated Dielectric Liquids on a Nanosecond Timescale Using Microwaves. *Radiat. Phys. Chem.* **1977**, *10*, 353–365.
- (3) Savenije, T. J.; Ferguson, A. J.; Kopidakis, N.; Rumbles, G. Revealing the Dynamics of Charge Carriers in Polymer:Fullerene Blends Using Photoinduced Time-Resolved Microwave Conductivity. *J. Phys. Chem. C* **2013**, *117*, 24085–24103.
- (4) Tang, H.; Prasad, K.; Sanjines, R.; Schmid, P.; Levy, F. Electrical and optical properties of TiO<sub>2</sub> anatase thin films. *J. Appl. Phys.* **1994**, *75*, 2042–2047.
- (5) Kroeze, J. E.; Savenije, T. J.; Warman, J. M. Contactless determination of the efficiency of photo-induced charge separation in a porphyrin–TiO<sub>2</sub> bilayer. *J. Photoch. Photobio. A Chem.* **2002**, *148*, 49–55.
- (6) Ford, W. E.; Kamat, P. V. Photochemistry of 3,4,9,10-perylenetetracarboxylic dianhydride dyes. 3. Singlet and triplet excited-state properties of the bis(2,5-di-tert-butylphenyl)imide derivative. *J. Phys. Chem.* **1987**, *91*, 6373–6380.



# D

## APPENDIX CHAPTER 5

### SCANNING ELECTRON MICROSCOPY ON A SMOOTH POLYCRYSTALLINE $\text{TiO}_2$ FILM

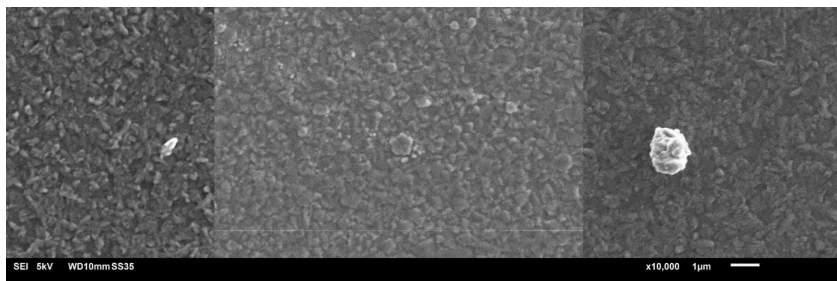


Figure D.1: Scanning electron microscope images of a single layer film of smooth polycrystalline  $\text{TiO}_2$ .

### ATOMIC FORCE MICROSCOPY ON A SMOOTH POLYCRYSTALLINE $\text{TiO}_2$ FILM

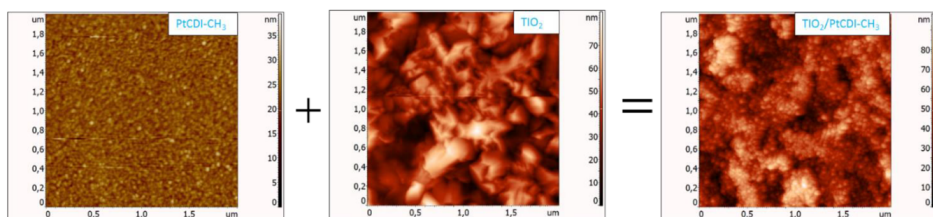


Figure D.2: Atomic force microscopy images of single layers of PDI- $\text{CH}_3$  (left),  $\text{TiO}_2$  (middle) and a bilayer of  $\text{TiO}_2$ /PDI- $\text{CH}_3$ .



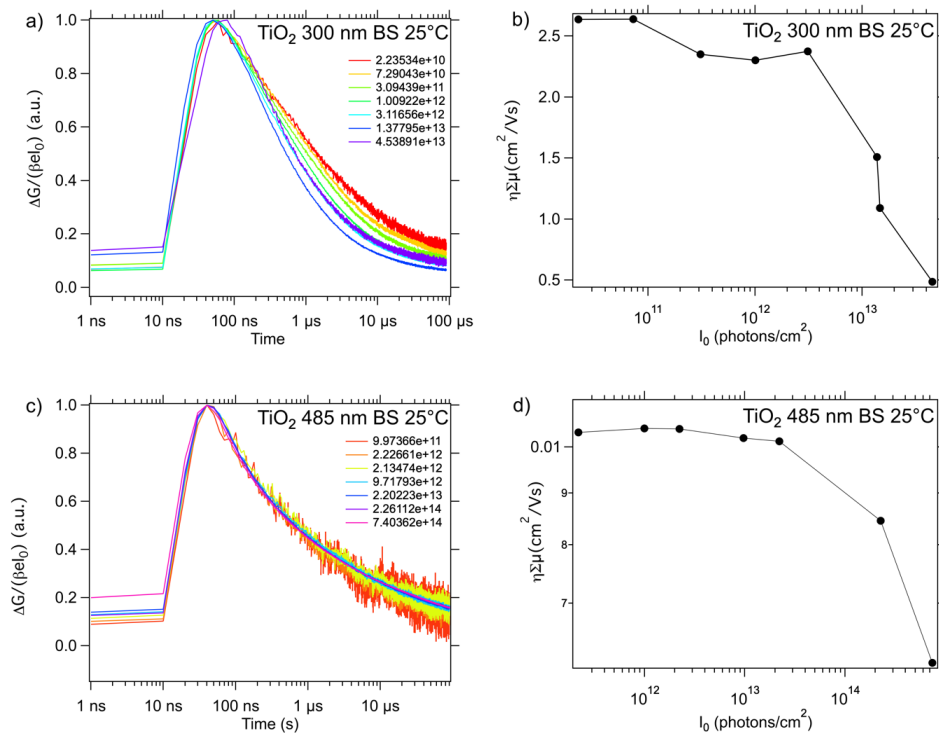
TiO<sub>2</sub> SINGLE LAYER PHOTOCONDUCTANCE

Figure D.3: a) Normalized photoconductance traces of TiO<sub>2</sub> excited at 300 nm at a photon fluence  $I_0$  ranging from  $2 \cdot 10^{10}$ – $4.5 \cdot 10^{13}$  photons/cm<sup>2</sup>. b) Maximum photoconductance signal  $\eta \Sigma \mu$  as function of  $I_0$ . c) and d) The same figures for TiO<sub>2</sub> upon 485 nm sub-band gap excitation.

## TiO<sub>2</sub> SINGLE LAYER PHOTOCONDUCTANCE AS FUNCTION OF TEMPERATURE AND FLUENCE

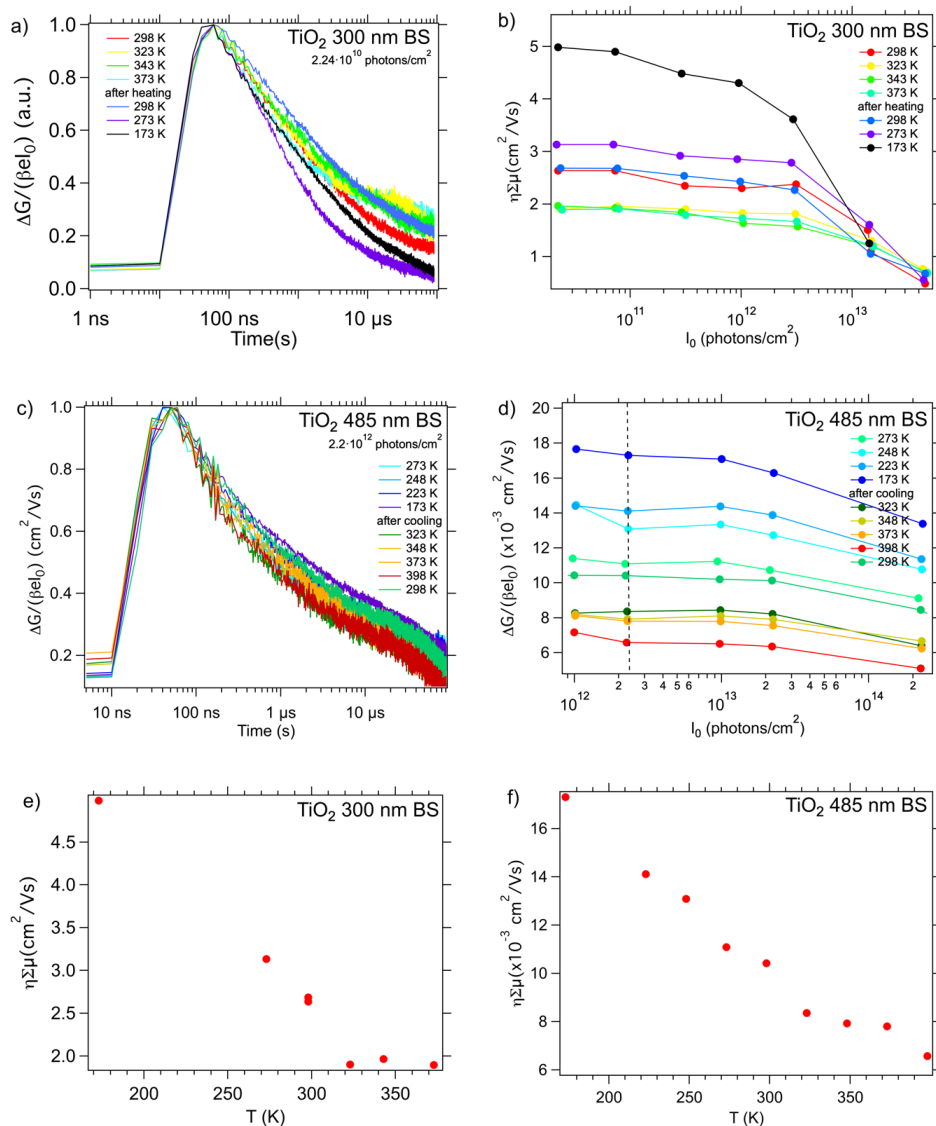


Figure D.4: Normalized photoconductance traces of TiO<sub>2</sub> excited at 300 and 485 nm at a photon fluence  $I_0$  ranging from  $2.2 \cdot 10^{10}$  and  $2.2 \cdot 10^{12}$  photons/cm<sup>2</sup> as function of temperature in a) and c), respectively. Maximum photoconductance signal  $\eta \Sigma \mu$  of TiO<sub>2</sub> excited at 300 and 485 nm as function of temperature and  $I_0$  in b) and d), respectively. Temperature dependence of  $\eta \Sigma \mu$  of TiO<sub>2</sub> excited at 300 and 485 nm in e) and f), respectively.

Table D.1: List of parameters used in the 1D exciton diffusion model to calculate the curves shown in Figure 5.3.

Parameter	Figure 5.3a	Figure 5.3b	Figure 5.3c	Figure 5.3d	Figure 5.3e	Figure 5.3f
Laser P (J)	8.35E-07	8.35E-07	8.35E-07	8.35E-07	8.35E-07	8.35E-07
$\lambda$ (m)	5.00E-07	5.00E-07	5.00E-07	5.00E-07	5.00E-07	5.00E-07
$k_{injS_1}$ ( $s^{-1}$ )	1.00E+09	1.00E+09	1.00E+09	1.00E+09	1.00E+09	1.00E+09
$k_{SF}$ ( $s^{-1}$ )	1.00E+10	1.00E+10	1.00E+10	<b>Varied</b>	1.00E+10	1.00E+10
$k_{FUS}$ ( $s^{-1}$ )	1.00E+07	1.00E+07	1.00E+07	<b>Varied</b>	1.00E+07	1.00E+07
$k_{TDis}$ ( $s^{-1}$ )	1.00E+06	1.00E+06	1.00E+06	1.00E+06	1.00E+06	1.00E+06
$k_{SSA}$ ( $m^3s^{-1}$ )	1.00E-15	<b>Varied</b>	1.00E-15	1.00E-10	1.00E-15	1.00E-15
$k_{s1,rec}$ ( $s^{-1}$ )	<b>Varied</b>	1.40E+09	1.40E+09	1.40E+09	1.40E+09	<b>Varied</b>
$k_{e,rec}$ ( $s^{-1}$ )	5.00E+03	5.00E+03	<b>Varied</b>	5.00E+03	5.00E+03	5.00E+03
$D_S$	1.00E-08	1.00E-08	1.00E-08	1.00E-09	<b>Varied</b>	<b>Varied</b>
$D_{TT}$	1.00E-11	1.00E-11	1.00E-11	1.00E-11	<b>Varied</b>	<b>Varied</b>

## SUMMARY

Conjugated organic materials are interesting for application in opto-electronic devices where they can act as a light absorbing layer, for instance in solar cells or as a light emitting layer in light-emitting diodes. In addition, they can also be used as the semiconducting materials in for instance field-effect transistors. Conjugated organic materials have certain desirable properties that are generally found in organic materials such as light weight, flexibility and cheap processing from solution. A particularly attractive aspects of such materials is that their solid-state properties can be tuned by making changes in the molecular structure by organic synthesis techniques. This also makes it possible to modify the materials so that they exhibit more uncommon processes that may be beneficial for solar cells. Two of such processes, singlet exciton fission (SF) and triplet-triplet annihilation upconversion (TTA-UC) are the main subjects of this thesis. The first (SF) is a process in which a singlet excited state, formed by absorption of light, is transformed into a combination of two triplet excited states each with half of the energy. This can, in principle, double the number of electrons that are injected in a solar cell device, and hence double the current from the device. The second (TTA-UC) is the reverse process of SF in which two triplet states with low energy can be combined into a single higher-energy singlet excited state from which an electron can be injected in a solar cells. Exploiting these two processes can in principle lead to considerable improvements in the efficiency of solar cells based on these devices. SF can be exploited to use the excess energy in photons with more than twice the bandgap energy to excite an additional electron. In this way, the excess energy that is otherwise lost as heat, is used to increase the current and therefore the overall energy efficiency of the device. TTA-UC addresses another energy-loss in solar cells, that of photons in the solar spectrum that have a lower energy than the bandgap of the active material of the solar cell. TTA-UC can be used to combined the energy of two of these photons, that are normally not absorbed by the solar cells, to generate a single higher-energy excited state that has sufficient energy to charge separate at an interface. Together, these two processes can address two of the factors that cause major energy losses in solar cells. In order to efficiently exploit these processes, a detailed fundamental understanding of these processes is required, with particular emphasis on the effect of molecular packing in the solid-state as this is the state where they are to be used in devices.

In order to efficiently use SF and TTA-UC, the materials in which they take place also have to exhibit good energy and charge transport properties and hence a good understanding of these processes is required. Therefore, in **Chapter 2**, we have investigated the relation between the solid-state molecular packing and the exciton diffusion length, charge carrier mobility, and charge carrier separation yield using two perylene diimide (PDI) derivatives which differ in their substitution. We have used the time resolved microwave photoconductivity technique and measured charge carrier mobilities of 0.32 and 0.02 cm<sup>2</sup>/Vs and determined exciton diffusion lengths of 60 nm and 18 nm for octyl-

and bulky hexylheptyl-imide substituted PDIs, respectively. This diffusion length is independent of substrate type and aggregate domain size. The differences in charge carrier mobility and exciton diffusion length clearly reflect the effect of solid-state packing of PDIs on their opto-electronic properties and show that significant improvements can be obtained by effectively controlling the solid-state packing.

In **Chapter 3** we have examined the relation between the molecular packing and singlet exciton fission in thin films of brominated perylenediimides. We explore how introduction of bulky bromine atoms in the so-called bay-area of PDIs, resulting in a non-planar structure, affects the solid-state packing and efficiency of singlet fission. We found that changes in the molecular packing have a strong effect on the temperature dependent photoluminescence, expressed as an activation energy. These effects are explained in terms of excimer formation for PDIs without bay-area substitution, which competes with singlet fission. Introduction of bromine atoms in the bay-positions strong-

ly disrupts the solid-state packing leading to strongly reduced excitonic interactions. Surprisingly, these relatively amorphous materials with weak electronic coupling exhibit stronger formation of triplet excited states by SF because the competing excimer formation is suppressed here.

In **Chapter 4** we describe an approach to use TTA-UC in a solar cell device by demonstrating upconversion on absorption of infrared light, followed by direct electron injection into an inorganic substrate. We use time-resolved microwave conductivity experiments to study the injection of electrons into the electron-accepting substrate ( $\text{TiO}_2$ ) in a trilayer device consisting of a triplet sensitizer (phthalocyanine), triplet acceptor (perylenediimide) and  $\text{TiO}_2$ . Absorption of light at 700 nm leads to the almost quantitative generation of triplet excited states by intersystem crossing. This is followed by Dexter energy transfer to the triplet acceptor layer where the annihilation process occurs, directly followed by injection of an electron in  $\text{TiO}_2$ . These experiments nicely demonstrate the principle, although the efficiency should still be improved before it can be applied in a sufficiently efficient way in devices.

To gain a more detailed understanding of the mechanism of triplet diffusion we have performed temperature dependent time-resolved microwave conductivity experiments of bilayers of perylenediimides and  $\text{TiO}_2$  in **Chapter 5**. The experiments show a delayed rise in the photoconductivity upon photoexcitation that is due to injection of electrons in  $\text{TiO}_2$ . This delayed rise is strongly influenced by temperature. At low temperatures the rise takes place on longer time scales or is almost completely suppressed, while at higher temperature the delayed rise becomes faster. This clearly shows a temperature activated mechanism which we attempted to analyse using a one-dimensional exciton diffusion model involving singlet, triplet pairs and free electrons. We found that conventional processes like exciton diffusion, exciton recombination and charge injection cannot solely account for the observed delayed rise kinetics as function of temperature in the perylenediimide layer.

The initial species that is formed upon SF is a coherent pair of triplet excited states that constitutes an overall singlet state. In order to harvest the energy from these states they must first transform into two independent triplet states that can inject charges into an external circuit. The decoherence of this triplet pair has received only very little atten-

tion. In **Chapter 6** we explore an approach to increase the understanding of the breaking up of the triplet pairs by studying the fluorescence in the presence of an externally applied magnetic field. In this way it is possible to characterize the energetics of the different triplet pairs states which can give insight in the dynamics of triplets after singlet fission has taken place.

Finally, in **Chapter 7**, we give a short outlook on the fields of TTA and SF and indicate some future research directions, especially focussing on SF.



## SAMENVATTING

Geconjugeerde organische materialen zijn interessant voor toepassingen in opto-elektronische 'devices' waar ze fungeren als licht-absorberende laag, bijvoorbeeld in zonnecellen, of als licht-emitterende laag in 'light-emitting diodes'. Bovendien kunnen ze ook worden gebruikt als halfgeleidende materialen, bijvoorbeeld in veldeffecttransistoren. Deze organische materialen hebben diverse gunstige eigenschappen, zoals een lage dichtheid, flexibiliteit en goedkope verwerking vanuit een oplossing. Een bijzonder aantrekkelijk aspect van dergelijke materialen is dat hun vaste-stofeigenschappen kunnen worden gemodificeerd door het aanbrengen van veranderingen in de moleculaire structuur middels organische synthese technieken. Dit maakt het mogelijk om de materialen zo aan te passen, dat ze meer ongewone processen vertonen die gunstig kunnen zijn voor zonnecellen. Twee van zulke processen, singlet exciton fission (SF) en triplet-triplet annihilatie upconversie (TTA-UC) zijn de hoofdonderwerpen van dit proefschrift. Het eerste proces, SF, is een proces waarin een singlet-geëxciteerde toestand wordt gevormd door de absorptie van licht, en vervolgens wordt omgezet in een combinatie van twee triplet-geëxciteerde toestanden met elk de helft van maximaal de singlet energie. Dit kan in principe het aantal elektronen dat in een zonnecel wordt geïnjecteerd verdubbelen, en daarmee dus ook de stroom van het apparaat. Het tweede proces dat kan worden geactiveerd, TTA-UC, is het omgekeerde proces van SF en hierbij worden twee triplet-toestanden met lage energie gecombineerd tot een enkele hogere-energie singlet-geëxciteerde toestand waaruit een elektron kan worden geïnjecteerd in zonnecellen. Het benutten van materialen die deze twee processen mogelijk maken, kan leiden tot aanzienlijke verbeteringen in de efficiëntie van zonnecellen. SF kan worden gebruikt om de overtollige energie in fotonen te gebruiken met meer dan twee keer de bandgap-energie om een extra elektron te exciteren. Op deze manier wordt de overtollige energie, die anders verloren gaat als warmte, gebruikt om meer stroom te genereren en dus de algehele energie-efficiëntie van de zonnecel te verhogen. TTA-UC pakt een ander energieverlies in zonnecellen aan, namelijk dat van fotonen in het zonnenspectrum die een lagere energie hebben dan de bandgap van het actieve materiaal van de zonnecel. TTA-UC kan worden gebruikt om de energie van twee van deze fotonen, die normaal niet worden geabsorbeerd door de zonnecellen, te combineren om een enkele hogere energie aangeslagen toestand te genereren die voldoende energie heeft om een elektron over de bandgap te exciteren. Samen kunnen deze twee processen twee van de factoren aanpakken die grote energieverliezen in zonnecellen veroorzaken. Om deze processen efficiënt te benutten, is een gedetailleerd en fundamenteel begrip van deze processen vereist. In het bijzonder moet worden gekeken naar de invloed van de pakking van moleculen in de vaste stof, aangezien dit de toestand is waarin ze in apparaten worden gebruikt.

Om SF en TTA-UC efficiënt te gebruiken, moeten de materialen waarin ze plaatsvinden ook goede energie- en ladingstransporteigenschappen vertonen en daarom is een goed begrip van deze processen vereist. Om deze reden hebben we in **Hoofdstuk**



2 de relatie onderzocht tussen de moleculaire pakking in vaste toestand en de exciton-diffusielengte, de mobiliteit van ladingsdragers en de opbrengst aan ladingsdragerscheiding met behulp van twee peryleendiimide (PDI) afgeleiden, die verschillen in hun zijketens. We hebben tijdsopgeloste microgolffeidingsexperimenten gedaan en daaruit ladingsdragermobiliteiten van  $0.32$  en  $0.02 \text{ cm}^2 / \text{Vs}$  en exciton-diffusielengten van  $60 \text{ nm}$  en  $18 \text{ nm}$  voor octyl- en omvangrijke hexylheptyl-imide-gesubstitueerde PDI's bepaald. De diffusielengte is onafhankelijk van het substraattype en de totale domeingrootte. De verschillen in ladingsdragermobiliteit en exciton-diffusielengte weerspiegelen het effect van de vaste-stofpakking van PDIs op hun opto-elektronische eigenschappen en tonen aan dat significante verbeteringen kunnen worden verkregen door de vaste-stofpakking effectief te controleren.

In **Hoofdstuk 3** hebben we de relatie tussen de moleculaire pakking en singlet exciton fission in dunne films van gebromeerde peryleendiimiden onderzocht. We onderzoeken hoe de introductie van grote broomatomen in de zogenaamde bay-area in PDI's, (resultierend in een niet-vlakke structuur) de vaste-stofpakking en efficiëntie van singlet-fission beïnvloedt. Veranderingen in de moleculaire pakking hebben een sterk effect op de temperatuursafhankelijke fotoluminescentie, uitgedrukt als een activeringsenergie. Deze effecten worden verklaard in termen van excimeerformatie in PDIs zonder bay-area substitutie, die concurreert met singlet fission. Introductie van broomatomen in de bay-posities verstoort de pakking in vaste toestand sterk, wat leidt tot sterk verminderde excitonische interacties. Verrassenderwijs vertonen deze relatief amorphe materialen met zwakke elektronische koppeling een sterkere vorming van triplet-geëxciteerde toestanden door SF omdat de concurrerende excimeerformatie hier wordt onderdrukt.

In **Hoofdstuk 4** beschrijven we een methode om TTA-UC in zonnecellen te gebruiken waarin upconversie plaatsvindt na absorptie van infrarood licht, wat vervolgens kan leiden tot directe injectie van elektronen in een anorganisch substraat. We gebruiken tijdsopgeloste microgolffeidingsexperimenten om de injectie van elektronen in het elektronen-accepterende substraat ( $\text{TiO}_2$ ) te bestuderen in een tripellaags structuur bestaande uit een triplet generator (ftalocyanine), tripletacceptor (peryleendiimide) en  $\text{TiO}_2$ . Absorptie van licht bij  $700 \text{ nm}$  leidt tot de bijna kwantitatieve generatie van triplet-geëxciteerde toestanden via intersystem crossing. Na dit proces verplaatsen de tripletten via Dexter-energieoverdracht naar de triplet-acceptorlaag waar het upconversieproces plaatsvindt. Dit proces wordt gevolgd door de injectie van een elektron in  $\text{TiO}_2$ . Deze experimenten geven een goede demonstratie van het principe, hoewel de efficiëntie verder moet worden verbeterd voordat het op een voldoende efficiënte manier in zonnecellen kan worden toegepast.

Om meer inzicht te krijgen in het mechanisme van tripletdiffusie hebben we temperatuurafhankelijke tijdsopgeloste microgolffexperimenten aan bilaag systemen van peryleendiimiden en  $\text{TiO}_2$  in **Hoofdstuk 5** uitgevoerd. De experimenten tonen aan dat het maken van een licht-aangeslagen toestand een vertraagde stijging van de fotogeleiding tot gevolg heeft door injectie van elektronen in  $\text{TiO}_2$ . Deze vertraagde stijging wordt sterk beïnvloed door de temperatuur. Bij lage temperaturen vindt de stijging plaats op langere tijdschalen of wordt bijna volledig onderdrukt, terwijl bij hogere temperatuur de vertraagde stijging sneller wordt. Dit toont het bestaan aan van een temperatuur geactiveerd mechanisme dat we hebben geanalyseerd met een een-dimensionaal exciton

diffusie model dat bestond uit singlet, tripletpaar en elektron termen. Conventionele processen zoals exciton diffusie, recombinatie en ladingsinjectie zijn niet individueel verantwoordelijk voor de stijging van de fotogeleiding op langere tijden wanneer het temperatuursgedrag van de peryleendiimide laag in aanschouw wordt genomen

De natuur van de aangeslagen toestand die direct na SF wordt gevormd is een coherent paar van triplet-geëxciteerde toestanden dat samen een algehele singlet-toestand vormt. Om de energieën uit deze toestanden te benutten, moeten ze eerst transformeren in twee onafhankelijke triplettoestanden die ladingen in een extern circuit kunnen injecteren. Het decoherentieproces van dit tripletpaar heeft tot nu toe slechts zeer weinig aandacht gekregen en er is nog niet veel informatie over bekend voor veel SF chromoforen. In **Hoofdstuk 6** onderzoeken we een methode om meer kennis te verkrijgen over het opsplitsen van de tripletparen door middel van het bestuderen van de fluorescentie in aanwezigheid van een extern aangelegd magneetveld. Op deze manier is het mogelijk om de energieën van de verschillende tripletpaar toestanden te karakteriseren die inzicht kunnen geven in de triplet dynamiek volgend op singlet fission.

Tot slot geven we in **Hoofdstuk 7** een kort overzicht op het vakgebied van TTA en SF en geven we enkele toekomstige onderzoeksrichtingen, met name gericht op SF.



# ACKNOWLEDGEMENTS

This dissertation resulted from more than four years of involvement and research at the opto-electronic materials section in Delft. Prior to the start of my PhD project, I worked on two projects in the group and was daily supervised by Deniz Gunbas, Natalie Gorczak and Maria Fravventura. They taught me the skills that I gratefully made use of during my PhD project.

Outside of the group I also received thorough and much appreciated mentoring from my bachelor thesis supervisor Fabai Wu.

I carried out all my projects in the opto-electronic materials section under the main supervision of Ferdinand Grozema, and with good reason. Besides a shared interest in research topics, I greatly value your flexibility and support in exploring my own research initiatives that you considered with an open mind and positive attitude. I also appreciated our way of conversing, whether it be about work or non-work related topics during office hours. Even more so, I enjoyed our time outside office hours in, for example, a Burgundian restaurant in Brussels, during a more satisfying lunch in the Hard Rock café in Gothenburg or during one of the annual Christmas dinners at your home with the family. I would not have been in the position that I am in now if it wasn't for your intermittent positive support over these, in total, eight years and I am very grateful for that.

More on the background, but also involved for a long time was Tom Savenije. Your extensive knowledge on microwave conductivity measurements and straightforward opinion guided me in my research. Arjan, Laurens, thank you for your views and comments on my work over these years as well.

Apart from my supervisors, I received a lot of training and support from the technicians in our section. Jos, your vast knowledge regarding to laser spectroscopy and the thoroughness with which you carried out your work made many of the articles in this dissertation possible and were improved by your instructions. I enjoyed our sessions in the laser labs where you always took care to explain the ins and outs of the laser setups, while simultaneously being focused on the work at hand. John, I also want to thank you for your patience and work in establishing the laborious numerical model to describe the microwave conductivity experiments used in chapter 4. I could also not forget Ruben, who introduced me to organic photovoltaics when I started studying at the university. Little did I know then, that the titanium dioxide films sensitized with chromophores that we made by mortaring fruit, during practicum basisvaardigheden, would be very similar to what I would be doing during my PhD project. I appreciated our since conversations that were amusing and sometimes serious and the help you gave me during all these years.

Another technician I should definitely not forget is Wiel. Although you are strictly speaking a technician, in my view you seem more of a super postdoc with technician responsibility (and knowledge). I have had a very good time sharing an office with you, despite dozens of occasions that I had to disappoint people who came to our office to meet

you. Besides your much appreciated critical reflection on my doubts about certain scientific hypothesis, you also helped me to enable my strange ideas for experiments such as building our small PL magnet setup. However, I appreciated most our non-scientific discussions that I (will) put to good use. Thank you for the nice two year of my PhD and I wish you all the best with your family.

Two other postdocs that became friends were Silke and Rajeev. Silke, I liked our regular lunches and talks. I am also happy I could contribute to your work in Delft. Rajeev, without your molecules there would not have been a thesis. It was very interesting and pleasant to learn the basics of perylene diimide synthesis from an expert. Thank you for your friendship and mentoring.

It was a pleasure to work with my fellow PhD Grozema team members Sudeep, Damla, Magnus, Maco and Cansel. We were part of the formal established of the Grozema group and even made our own logo! I will not forget the time we spent during nice conferences such as the Gordon conferences, the group dinners and numerous activities we did together after work. I hope you all find the place where you feel at home.



Dengyang, I enjoyed our excursions together, whether it involved being scared of my life in a soaring and diving small plane or saving ourselves out of an ice-cold lake. I have no worries you will end up having a fancy job that is to your liking. Davide, Aditya, Prashant, Solrun, Zimu, Gianluca, Jaco, Frank, Hamit, Ryan, Ward, Eline: I appreciate the time we spent together, the talks we had and wish you all the best.

Sourav, I have good confidence that you will successfully continue the singlet fission research in Delft. It was very interesting to be able to finally discuss singlet fission research with a peer in the group. I wish you much happiness together with your wife and daughter.

Fahimeh, it was a great comfort to talk with you while walking hundreds of meters over the campus with coffee in our hands. I appreciated your sincere kindness that you give to everyone around you.

This thesis was made with contributions from bachelor and master students who worked together with me during their thesis projects. I enjoyed working with Nick and Irene who were able to understand difficult concepts about singlet fission in a relatively short time for their bachelor thesis. I also had the pleasure of working together with Jetsabel on laborious microwave conductivity experiments on interesting materials. Jets, it was fun to experience our many humorous moments and I hope to make more of these in the future.

Most of all though, I want to thank someone who I worked closely with since the

start of my project. Vale, you have not only been a huge support at work, but have also become unmissable outside of it and I am very happy that we are building up our life together and experience having our first child. Finally, I want to thank my family and particularly my parents and sister for their continuing support in all my endeavours.



# CURRICULUM VITÆ

Kevin Felter was born in Dordrecht, The Netherlands on June 15<sup>th</sup> 1992. He followed his bachelor study Molecular Science and Technology at Delft University of Technology and Leiden University. As part of the bachelor he spent half a year in Trondheim, Norway where he followed a minorprogramme in sustainable energy at Norges-teknisk naturvitenskapelige universitetet. In parallel to his bachelor study he participated in the Honours College at Leiden University and was a board member of the student association of the Honours College. He followed his chemical engineering master programme in Delft while working parttime as researcher in the Cees Dekker Lab of the Bionanoscience department. He was also part of student group Ecolution for which he (co-)organized several activities related to promoting on-campus sustainability. After succesfully finishing his master thesis project at the Opto-Electronic Materials section of the Chemical Engineering department, he remained in the group to work under supervision of Dr. F. Grozema on his PhD project titled Exciton Dynamics in Organic Crystals. During this time he expanded his knowledge on spectroscopic techniques to study the opto-electronic properties of chromophores. His research focus lies on exploring the singlet fission and triplet upconversion process in perylene diimide chromophores by using time resolved microwave photoconductivity measurements and transient absorption spectroscopy.





# PUBLICATIONS

## In this dissertation:

Felter, K. M., Dubey, R. K., Grozema, F. C. (2019). *Relation between molecular packing and singlet fission in thin films of brominated perylenediimides*. The Journal of chemical physics, 151(9), 094301.

Felter, K. M., Caselli, V. M., Günbaş, D. D., Savenije, T. J., and Grozema, F. C. (2019). *Interplay between charge carrier mobility, exciton diffusion, crystal packing and charge separation in perylene diimide-based heterojunctions*. ACS Applied Energy Materials, 2(11), 8010-8021.

Felter, K. M. and Grozema, F. C. (2019). *Singlet Fission in Crystalline Organic Materials: Recent Insights and Future Directions*. The Journal of Physical Chemistry Letters, 10(22), 7208-7214.

Felter, K. M., Fravventura, M. C., Koster, E., Abellon, R. D., Savenije, T. J., and Grozema, F. C. (2020). *Solid-State Infrared Upconversion in Perylene Diimides Followed by Direct Electron Injection*. ACS Energy Letters, 5(1), 124-129.

## Other publications:

Bi, Y., Felter, K., Hoogland, S., Grozema, F. C., Dennler, G., Houtepen, A. J., Savenije, T. J. (2016). *Optical Generation and Transport of Charges in Iron Pyrite Nanocrystal Films and Subsequent Injection into SnO<sub>2</sub>*. The Journal of Physical Chemistry C, 120(39), 22155-22162.

Aphrham, S., Pan, Q., Zaccarine, S. E., Felter, K.M., Thieme, J., van den Nieuwenhuijzen, K. J. H., ten Elshof, J.E., Huijser, A. (2017). *Effect of Water Addition during Preparation on the Early-Time Photodynamics of CH<sub>3</sub>NH<sub>3</sub>PbI<sub>3</sub> Perovskite Layers*. ChemPhysChem, 18(23), 3320-3324.

Aulin, Y. V., Felter, K.M., Günbaş, D. D., Dubey, R. K., Jager, W. F., Grozema, F. C. (2018). *Morphology-Independent Efficient Singlet Exciton Fission in Perylene Diimide Thin Films*. ChemPlusChem, 83(4), 230-238.

Diedenhofen, S. L., Bernechea, M., Felter, K.M., Grozema, F. C., Siebbeles, L. D. (2019). *Charge Photogeneration and Transport in AgBiS<sub>2</sub> Nanocrystal Films for Photovoltaics*. Solar RRL, 3(8), 1900075.

Wu, F., Swain, P., Kuijpers, L., Zheng, X., Felter, K., Guurink, M., Solari, J., Jun, S., Shimizu, T.S., Chaudhuri, D., Mulder, B., Dekker, C. (2019). *Cell boundary confinement sets the size and position of the E. coli chromosome*. Current Biology, 29(13), 2131-2144.